Astrocyte volume regulation and implication in brain flow transport

Cuong Pham

Sorbonne Université

Ecole doctorale n°158

-Cerveau Cognition Comportement-

Institut de biologie Paris Seine, Neuroscience Paris Seine

ASTROCYTE VOLUME REGULATION AND IMPLICATION IN BRAIN FLOW TRANSPORT

Régulation du volume astrocytaire et implication dans le flux cérébral

DOCTORAL THESIS

By Cuong Pham

Supervised by Dr. Dongdong Li

Pr. Carine Ali	Reviewer
Dr. Bruno Gasnier	Reviewer
Dr. Gilles Bonvento	Examiner
Dr. Eirini Papagiakoumou	Examiner
Dr. Denis Le Bihan	Examiner
Dr. Dongdong Li	Superviser

Summary

Abstract

Brain fluid transport is mediated by cerebrospinal fluid (CSF) circulation. This process plays important roles in the function, therefore the health of brain network. For instance, it regulates the intracerebral pressure equilibrium, dynamic distribution of energy fuels such as glucose and lactate, and notably for the removal of waste molecules like amyloid beta. Disturbance in brain flow transport is being recognized as a factor exacerbating neurological pathologies like Alzheimer's disease.

As a major type of glial cells, astrocytes are distributed throughout the brain and strategically located between cerebral vasculature and brain parenchyma. The discovery of the critical involvement of astrocytes in brain fluid transport has led to the emergence of the concept of the glymphatic system. It has been suggested that astrocyte volume dynamics, via regulating the extracellular space, shapes the brain flow transport. Water flux underlies astrocyte volume regulation. Astrocytes express the bidirectional water channel Aquaporin 4 (AQP4) that has been suggested to modulate astrocyte volume change. However, the exact role of AQP4 in astrocyte volume regulation has been debated, causing unresolved controversy on the mechanistic understanding of brain fluid transport and the glymphatic system.

My PhD study acutely discerns the role of AQP4 in astrocyte volume regulation in basal conditions and in response to osmotic changes in brain parenchyma in mouse models. Interdisciplinary approaches have been adopted during the PhD study, including in vivo chemical astrocyte labeling, ex vivo cellular fluorescence imaging in acute brain slices, in vivo fiberphotometry recording in freely moving animals and by diffusion weighted magnetic resonance imaging (DW-MRI). The obtained results (Chapter I) lead to the finding that AQP4 tonically sculpts astrocyte volume homeostasis, perturbing of which interferes with brain water diffusion. My following study (Chapter II) probed the potential mechanisms implicated in the dysregulated astrocyte signals and volume regulations in pathological β amyloid conditions. A hyper-regulation in astrocyte calcium signaling was observed that could potentially disturb the activity-dependent astrocyte volume dynamics. The possibility that targeting astrocytes AQP4 in vivo to facilitate amyloid clearance is being tested in an Alzheimer's disease mouse model. These results together shed light on the fundamental role of AQP4 in tuning astrocyte volume

and therefore the extracellular route for molecular diffusion, helping to understand brain fluid transport and its implication in health and neurological disorders.

The scientific knowledge from my PhD study has also fostered collaborative works for understanding I) brain astrocyte activity remodeling in obesity-associated metabolic syndromes. The results of this part contribute to the discovery that the calcium signaling of hypothalamic astrocytes undergoes heterogeneous remodeling in anatomically defined nuclei implicated in systemic metabolism regulation. This work helps to delineate the important participation of astrocytes in energy balance control; and II) the molecular mechanisms underlying the trafficking of calcium-permeable transient potential receptor ion channels. This work suggests testable molecular targets for interrogating the calcium signaling mechanisms in nervous cells including astrocytes.

Résumé (Français)

Le transport du flux cérébral est médié par la circulation du liquide céphalo-rachidien (LCR). Ce processus joue un rôle important dans la fonction, et donc dans l'homéostasie du cérébrale. Il régule l'équilibre de la pression intracérébrale, la distribution dynamique des carburants énergétiques tels que le glucose et le lactate, et notamment l'élimination des déchets comme la bêta-amyloïde. La perturbation du transport du flux cérébral est reconnue comme un facteur aggravant des pathologies neurologiques comme la maladie d'Alzheimer.

Etant un type majoritaire de cellules gliales, les astrocytes sont répartis dans tout le cerveau et stratégiquement situés entre le système vasculaire et le parenchyme cérébral. La découverte de l'implication critique des astrocytes dans le transport des fluides cérébraux a conduit à l'émergence du concept de système glymphatique. Il a été suggéré que la dynamique du volume astrocytaire, via la régulation du volume de l'espace extracellulaire, façonne le transport du flux cérébral. Le flux d'eau cellulaire sous-tend la régulation du volume des astrocytes. Les astrocytes expriment le canal d'eau bidirectionnel Aquaporine 4 (AQP4) qui a été suggéré comme modulateur du changement de volume astrocytaire. Cependant, le rôle exact de l'AQP4 dans la régulation du volume des astrocytes a été débattu, provoquant une controverse non résolue sur la compréhension mécanistique du transport des fluides cérébraux et du système glymphatique.

Durant mon doctorat, j'ai étudié le rôle de l'AQP4 dans la régulation du volume astrocytaire dans des conditions basales et en réponse à des manipulations environnementales dans le parenchyme cérébral de modèles murins. Des approches interdisciplinaires ont été développées ou adoptées au cours de cette étude, notamment via ciblage chimiogénique in vivo des astrocytes, d'imagerie par fluorescence cellulaire ex vivo dans des tranches de cerveau ex-vivo, d'enregistrement in vivo par fibrophotométrie chez des animaux en mouvement libre et par imagerie à résonance magnétique de diffusion (DW-MRI). Les résultats obtenus (chapitre I) conduisent à la découverte que l'AQP4 sculpte de manière tonique l'homéostasie du volume des astrocytes dans le parenchyme cérébral, dont la perturbation interfère de manière significative avec le transport du liquide cérébral. J'ai ensuite étudié (chapitre II) a sondé les mécanismes potentiels impliqués dans les dérégulations du volume astrocytaire dans des conditions de pathologies à bêta-amyloïdes. Dans ces conditions, une hyper-régulation de la signalisation

calcique astrocytaire a été observée, ce qui pourrait perturber la dynamique du volume astrocytaire dépendant de l'activité. Afin de moduler et faciliter la clairance amyloide dans un contexte murin de la maladie d'Alzheimer, l'activité de l'AQP4 a été impactée in vivo afin de moduler l'homéostasie volumique astrocytaire. Ensemble, ces résultats mettent en lumière le rôle fondamental de l'AQP4 dans le réglage du volume des astrocytes, et donc de la voie extracellulaire du flux cérébral, aidant ainsi à concilier les aspects jusqu'ici débattus du système glymphatique et son implication dans la santé et les troubles neurologiques.

Les connaissances scientifiques issues de mon doctorat ont également favorisé des travaux collaboratifs pour comprendre I) le remodelage de l'activité des astrocytes cérébraux dans les syndromes métaboliques associés à l'obésité. Les résultats de cette partie contribuent à la découverte que la signalisation calcique des astrocytes hypothalamiques subit un remodelage hétérogène dans des noyaux anatomiquement définis impliqués dans la régulation du métabolisme systémique. Ces travaux ont permis de mettre en évidence l'importante participation des astrocytes au contrôle de la balance énergétique; et II) les mécanismes moléculaires sous-jacents au trafic des canaux ioniques récepteurs potentiels transitoires perméables au calcium. Ce travail suggère des cibles moléculaires testables pour interroger les mécanismes de signalisation du calcium dans les cellules nerveuses, y compris les astrocytes.

List of abbreviations

Aβ: amyloid β

aCSF: Artificial cerebrospinal fluid

AD: Alzheimer's disease

ADC: Apparent diffusion coefficient

AQP: Aquaporin

AQP4: Aquaporin-4

ATP: Adenosine triphosphate

BBB: Blood brain barrier

Ca^{2+}: Calcium ion

CSF: Cerebrospinal fluid

CNS: Central nervous system

MRI: Magnetic resonance imaging

DW-MRI: diffusion weighed magnetic resonance imaging

ISF: Interstitial fluid

IP: intraperitoneal

Cx: Connexin

FIT: Fluorescence intensity-related

GJ: Gap junctions

GS: Glymphatic system

HC: Hemichannel

PMCA: Plasma membrane Ca^{2+} ATPase

SRB: Sulforhodamine B

TGN-020: 2-(nicotinamido)-1,3,4-thiadiazole

TGN-073: (N-(3-benzyloxypyridin- 2-yl)-benzene-sulfonamide)

List of figures

Chapter I: Investigating the role of Aquaporin 4 in astrocyte volume regulation.

Water is the most prevalent molecule in living creatures, representing the major body component from the vegetal organisms to mammalian animals. For instance ~60% of the body mass of the adult human is made out of water (Popkin et al., 2010). Water is essential for living organism vitality as just a few days without it will prove to be lethal. Water plays crucial roles in physiology to maintain body internal environment. It is indispensable for thermoregulation to sustain a narrow range of temperature highly necessary for routine metabolism and enzyme activities. With very high heat capacity (~4184 $J \cdot kg^{-1} \cdot K^{-1}$ at 20 °C), water excellently stores heat, and its oscillation from one body compartment to another helps to maintain the temperature constancy. Water is also required as a medium for chemical reactions between, enzymes, ions and proteins due to its heat storage capacity and its stable pH neutrality of 7.0. So water is a key resource for all metabolic features in living organisms.

Another key feature for water is to protect and lubricate tissues, from the amniotic fluid for a pregnant woman's baby, the pleural fluid lubricating lungs for breath, to the cerebrospinal fluid surrounding the brain and the spinal cord.

Importantly, water serves as a transportation vehicle. Ions, amino acids, vitamins, minerals, and sugars all need be transported by water. Water circulation also appears indispensable for the clearance of waste molecules in the body thereby preventing the build-up of potential toxicities.

I.1 - The cerebrospinal fluid is important for brain homeostasis

Water is a rudimental factor sustaining body homeostasis. Particularly, the central nervous system (CNS) is globally surrounded with the cerebral spinal fluid (CSF). The CSF is a liquid that is found within the tissues of the CNS of all vertebrates, filling all the ventricular spaces in the brain, and the central canal of the brainstem and the spinal cord. Fluid presence in the brain

was known since ancient Greece times. Hippocrates described it as "water surrounding the brain" when studying congenital hydrocephalus, while Galen, the first anatomist, was referring to it as an "excremental liquid" (Hajdu, 2003). But discovery of the CSF is attributed to Emmanuel Swedenborg. In his manuscript: «**The brain: considered anatomically, physiologically and philosophically**" he referred to the CSF as a "spirituous lymph" and a "highly gifted juice" that is distributed from the roof of the fourth ventricle to the medulla oblongata (reference). We have to wait until 1912 for a clear description of the chemical properties of the CSF by William Metrezegat (Hajdu, 2003)

I.1.*1* - Cerebrospinal fluid synthesis

The CSF is synthesized by ependymal cells located in the choroid plexus from filtrated blood plasma. The filtrated fluid pass through fenestrated capillaries in the choroid plexus to enter the interstitial space. And then from to the epithelial cell aligned in the choroid plexus in the ventricles. Additional ions and molecules join the CSF from the plasma by being filtered by ionic transporters or co-transporters in the epithelial cells. Ionic transporters will filtered blood plasma and by exchanging different ions with different co transporters and the complete CSF will be then transported into the ventricular systems (**Fig. 1**) (Mitchell et al., 2019; Rasmussen et al., 2022). The CSF is composed of all necessary physiological ions, essential proteins and amino acids (**Table 1**). The CSF will then circulates within the ventricles of the brain and to the subarachnoid space and will enter the brain parenchyma via the periarterial space and leave it from the periveinous space, and be drained away by lymph nodes located in the subarachnoid space, as well as the spine.

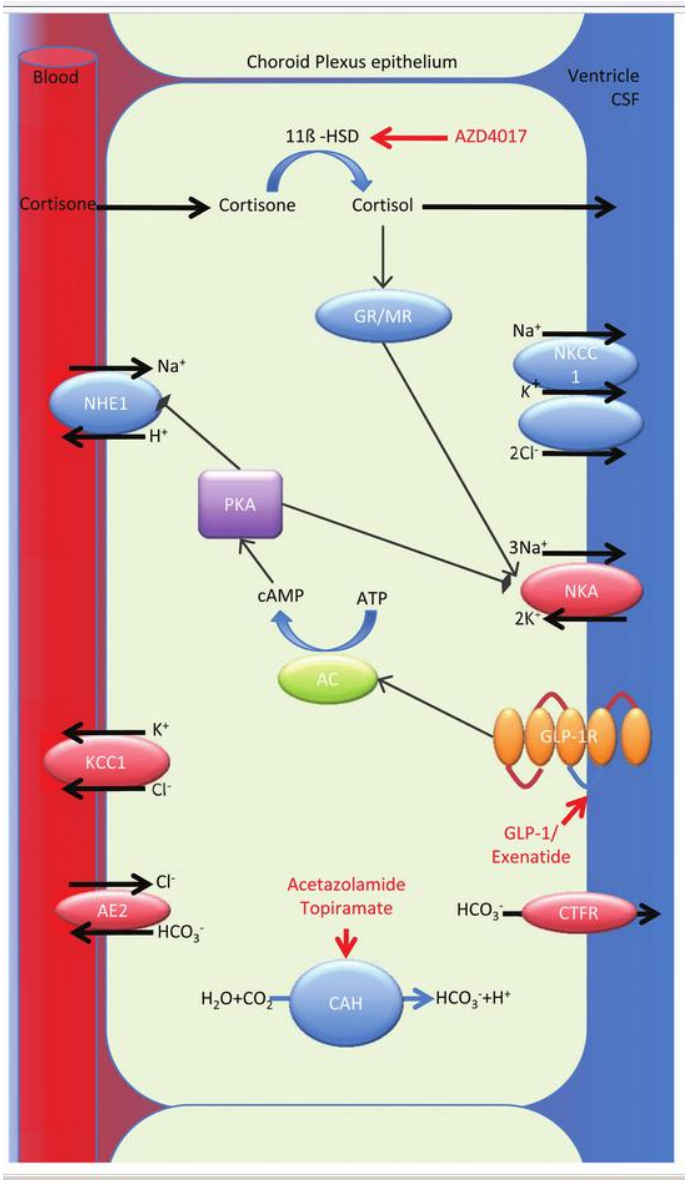

Figure 1: The major ion channels responsible for CSF secretion in the choroid plexus. *The major ion channels responsible for CSF secretion in the choroid plexus are shown with sites of action of acetazolamide, AZD4017 and exenatide. Cortisone is converted to the active cortisol by 11ß-HSD1, cortisol binds to the GR and MR receptors, which upregulate Na^+/K^+ ATPase activity; AZD4017 inhibits 11ß-HSD1 reducing local availability of cortisol. Exenatide binds and activates GLP-1R stimulating the conversion of ATP to cAMP by AC. cAMP activates PKA, which inhibits the Na^+ H^+ exchanger reducing Na^+ re-absorption and also inhibits the Na^+/K^+ ATPase reducing Na^+ excretion. Carbonic anhydrase catalyzes the conversion of H_2O and CO_2 to H^+ and HCO_3^- , which is important in the establishment of the osmotic gradient. Both acetazolamide and topiramate inhibit carbonic anhydrase function. AC, adenylate cyclase; AE2, anion exchange protein 2; cAMP, cyclic adenosine monophosphate; CSF,*

cerebrospinal fluid; CTFR, cystic fibrosis transmembrane conductance. Figure and legends from (Mitchell et al., 2019).

The composition of the CSF and plasma[a]

	Plasma	CSF
Na^+(mM)	155	151
K^+(mM)	4.6	3.0
Mg^{++}(mM)	0.7	1.0
Ca^{++}(mM)	2.9	1.4
Cl^-(mM)	121	133
HCO_3^-(mM)	26.2	25.8
Glucose (mM)	6.3	4.2
Amino acids (mM)	2.3	0.8
pH	7.4	7.4
Osmolality (mosmol.Kg H_2O^{-1})	300	305
*Protein (mg 100 g^{-1})	6500	25

The concentrations of the components in bold type are regulated by the choroid plexuses.

[a]Values are for dog CSF, except

*from rabbit, and are taken from the review by Davson et al. (1987).

***Table 1: CSF and blood plasma composition* (Brown et al., 2004)**

I.1.*2* - Cerebrospinal fluid functions

The CSF serves fundamental functions underpinning the function, integrity and waste clearance of the central nervous system (Cousins et al., 2022). As a delicately filtrated fluid, CSF sets the total ionic environment of the neural circuits, being extremely crucial for the operation of information processing in the nerve system (Sakka et al., 2011). Equally essential for the CNS function is the efficient diffusion of metabolic molecules throughout the neuron-glia networks (Magistretti and Allaman, 2018). For instance, as a highly energy-consuming organ, the brain relies exclusively on circulating glucose as an energy fuel, where the normal functionality of CSF tightly mediates the extracellular diffusion of glucose and its metabolic derivatives including the lactate (Magistretti and Allaman, 2018). Furthermore, as a wide spread liquid buffer, CSF critically protects the very complex yet super fragile nerve tissues (Spector et al., 2015). By being submerged by CSF, the brain exists in a neutral buoyancy enabling the brain to maintain its density and therefore its function during daily behaviors.

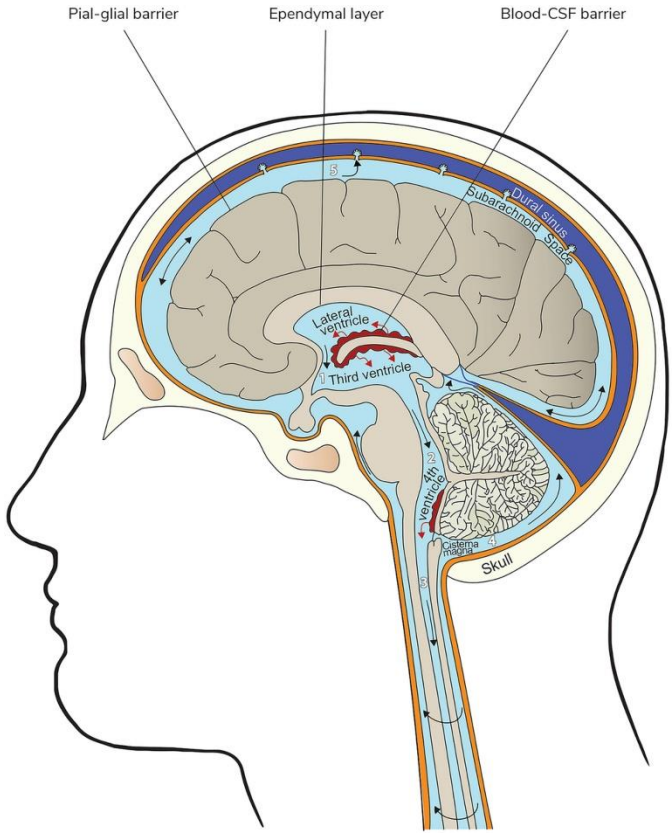

Figure 2: The classic model of cerebrospinal fluid (CSF) dynamics. *Ventricular CSF is produced from the blood via the choroid plexuses in the walls of each of the four ventricles (red arrows). CSF flows (black arrows) from the lateral into the third ventricle (1), then flows into the fourth ventricle (2) via the cerebral aqueduct. From the fourth ventricle CSF flow is either into the central canal of the spine (3) or into the subarachnoid space at the cisterna magna (4). CSF flows within the subarachnoid space and is cleared via the arachnoid villi into the dural venous sinuses (5). (Figure and legend from (Cousins et al., 2022).*

I.2 - Astrocytes, a key component in the Central nervous system

In the CNS, two type of cell are prevalent: the neurons and the glial cells. Neurons are electrically excitable cells, while glial cells are electrically non-excitable (Verkhratsky and

Nedergaard, 2018). The glial cells include oligodendrocytes, ependymal cells, microglia and astrocytes. They represent ~50 % of the cell population in the mammalian CNS, with an approximate of ~100 billion glial cells in the human brain (von Bartheld et al., 2016). **Among glial cells, astrocytes play important functions in regulating the development, function and homeostasis of the brain. My current study has been focused on brain astrocytes in mouse models.**

I.2.*1* - Historic

The initial description on glial cells neuroglia was from the pathologist Rudolf Virshow (1821-1902). In 1856, he introduced the term "Nervenkitt" (neuroglia) as a connective substance which forms in the brain, in the spinal cord and in the higher sensory nerve, in which the component of the nervous system are embedded. (**Fig. 3**). They were first thought of being mere structural cells, hence got their name from the word "glue", being referred as neuroglia. They were then considered as a mere glue holding neurons together. Astrocytes were found to be a major type of glial cells and initially observed in the 19th century along neurons (Verkhasky and Butt, 2013). The name astrocyte was introduced by Michaël von Lenhossék in 1895, coming from the greek astron and kytos, astron meaning star and kytos hollow vessel, later cell, so all together a star like cell.

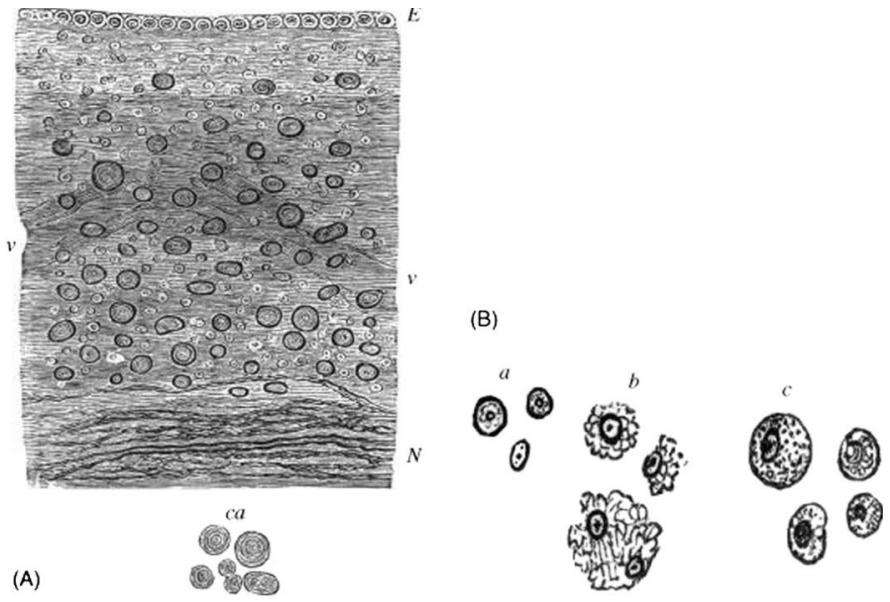

FIGURE 3: Virchow's illustrations of neuroglia*. (A) Ependyma and neuroglia in the floor of the fourth ventricle. Between the ependyma and the nerve fibers is "the free portion of the neuroglia with numerous connective tissue corpuscles and nuclei." Numerous corpora amylacea are also visible, shown enlarged below the main illustration (ca). E, ependymal epithelium; N, nerve fibers; v, blood vessels. (B) Elements of neuroglia from white matter of the human cerebral hemispheres. A, free nuclei with nucleoli; b, nuclei with partially destroyed cell bodies; c, complete cells. Source: Reproduced with permission from Verkhratsky A, Butt AM. Glial physiology and pathophysiology. Oxford, UK: Wiley-Blackwell; 2013 (Figure 1.14). (Figure and legends from astrocyte and epilepsy Hubbard et al Science 2016)*

I.2.*2* - Morphology, localisation and organization

They Astrocytes represent from ~20 to ~40% of the cell population of the brain and the most abundant type of glial cells in the CNS (Verkhratsky and Butt, 2013). Astrocyte are organized as individual domains and are interconnected via gap junctions between them as forming a syncytia network that help for involved in information propagation. Astrocytes are very heterogeneous in terms of following their functions, or their localization and molecular profiles. By general localization, they can be divided in two main subtypes: protoplasmic astrocytes, or fibrous astrocytes (**Fig. 4**). Protoplasmic astrocytes are found in the grey matter. They exhibit stem branches that give rise to many fine branch process. Fibrous astrocytes are found in the white matter and show a long fiber like processes morphology (Sofroniew and Vinters, 2010).

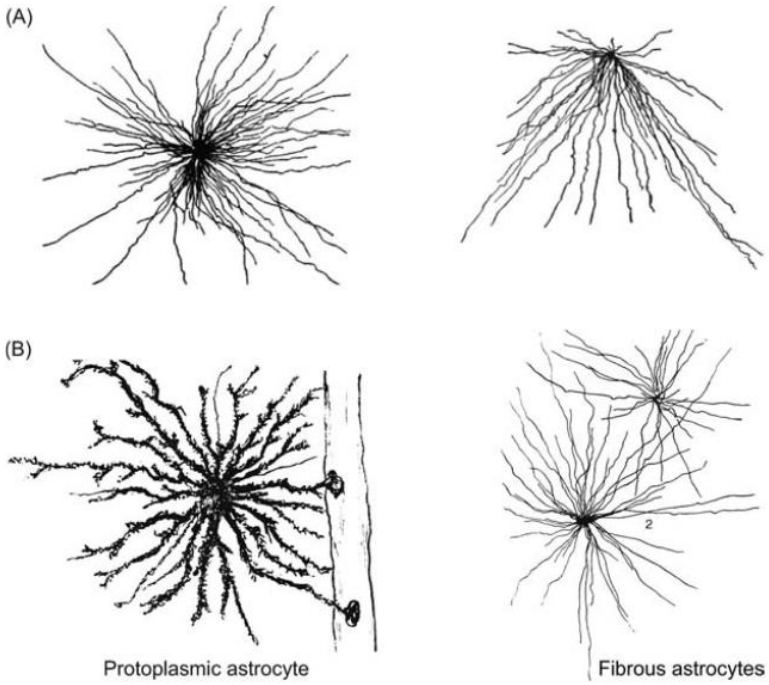

Figure 4: Two main type of astrocytes. *(A) Images of astrocytes drawn by Michael von Lenhossek (Lenhossek, 1895). (B) rotoplasmic and fibrous astrocytes drawn by William Andriezen (Andriezen, 1893).Both preparations were stained with Golgi technique. Figure and legends from (Verkhratsky and Butt, 2013)*

Astrocytes are widely distributed in the CNS, present in both grey and white matter. **They are organized in non-overlapping domains (Fig. 5)**. Protoplasmic astrocytes tend to have non overlapping domain in gray matter, so that only the most distal tips of their process are in contact to each other. Astrocytes communicate between each other by gap junctions expressed at the extremity of each domain (Wilhelmsson et al., 2006). Similar domains seem to exist in white matter but have not been reported extensively. Astrocyte are also aligned along blood vessels and part of the brain blood barrier (BBB) (Daneman and Prat, 2015).

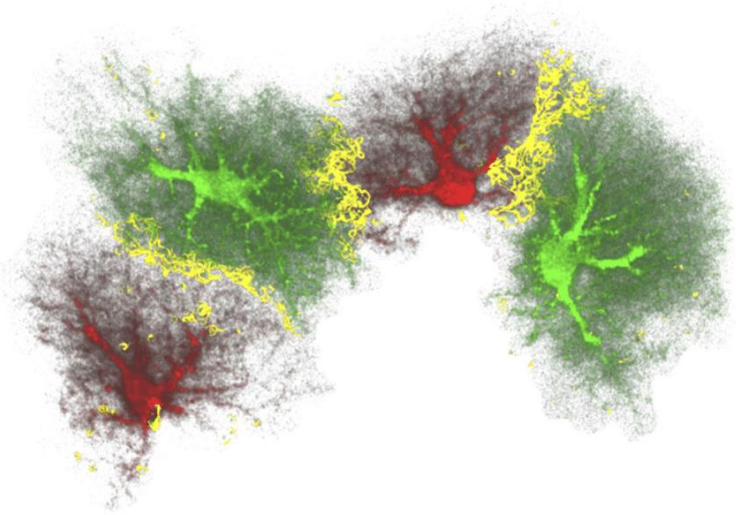

Figure 5: Astrocytes in the adult brain typically do not reach into domains of their astrocyte neighbors. *Interdigitation of fine cellular processes between adjacent astrocytes is shown here in a three-dimensional reconstruction of astrocytes in the dentate gyrus of the hippocampus of a mouse. Note the relatively limited overlap zone between adjacent astrocytes (shown in yellow) (Wilhelmsson et al., 2006).*

I.2.*3* - Functions

As one of the major glial cells, astrocytes have very important functions crucial for the homeostasis and the well-being of the CNS. Astrocytes are at close proximity with neuronal synapses and help for neurotransmission and ions and transmitter homeostasis at the synaptic level (Dallérac et al., 2018). Astrocytes also provide **metabolic support** to neurons. Indeed they provide to neurons the necessary nutrients (e.g., glucose, lactate) for the survival and function of neurons (Magistretti and Allaman, 2018). They also act as **repairing cells** to safeguard the microenvironment of neuropil and respond to pathological injuries. Indeed upon neuronal injury astrocytes are recruited and contribute to the neuronal repair by secreting neurotropic factors (O'Shea et al., 2017).

Hence, by occupying the strategic position in brain circuits, at the interface between blood vessels and neurons, astrocyte can **regulate synaptic activity, blood flow as well as energy metabolism**. Unlike neurons, astrocytes do not exhibit action **potentials**, but they display intracellular calcium (Ca^{2+}) signaling, thought to represent their dynamic activity (Khakh and

McCarthy, 2015) . They are part of the tripartite synapse, where their fine perisynaptic processes are adjoin the pre- and post-synaptic elements. This strategic position enables them to regulate synaptic activity; the local concentration of synaptic neurotransmitters is dynamically controlled by astrocytes, via either or both the transmitter uptake/recycling and the intracellular Ca^{2+} signaling by ion channels, neurotransmitter receptors and transporters. In turn astrocyte modulation of neuronal activity occurs via multiple mechanisms. For instance, neuroactive molecules (ATP, glutamate, lactate, peptides...) have been suggested to be released by astrocytic Ca^{2+} signaling to regulate neuronal excitability and synaptic transmission. Astrocytes also display changes in their morphology and synapse coverage, which set their proximity to synapses, and thus determine astroglial uptake capacity, released molecules availability and contact-mediated signaling (Pannasch et al., 2011; Kim et al., 2014). Intercellular astroglial networks are mediated by gap junction channels (GJ) composed of connexin (Cx) subunits, Cx30 and Cx43, which enable long-range exchange of ions, neuromodulators and metabolites mediating network- wide signaling and synchronization (Pannasch and Rouach, 2013; Chever et al., 2016). Cx also form channels, such as Cx43 hemichannels (HC), pannexin1 (Px1) or P2X7 (Chever et al., 2014; Abudara et al., 2018) channels, instrumental for the release of neuroactive molecules (**Fig. 6**). These molecules may also be released via vesicular exocytosis, although this remains controversial (Fiacco and McCarthy, 2018; Savtchouk and Volterra, 2018).. It is noteworthy that these astroglial molecules can be locally produced in the direct vicinity of neighboring synapses or alternatively they can originate from distal site of the astroglial network and be trafficked via GJ towards neuronal activity hotspots to fuel synapses, as shown for glucose and lactate delivery

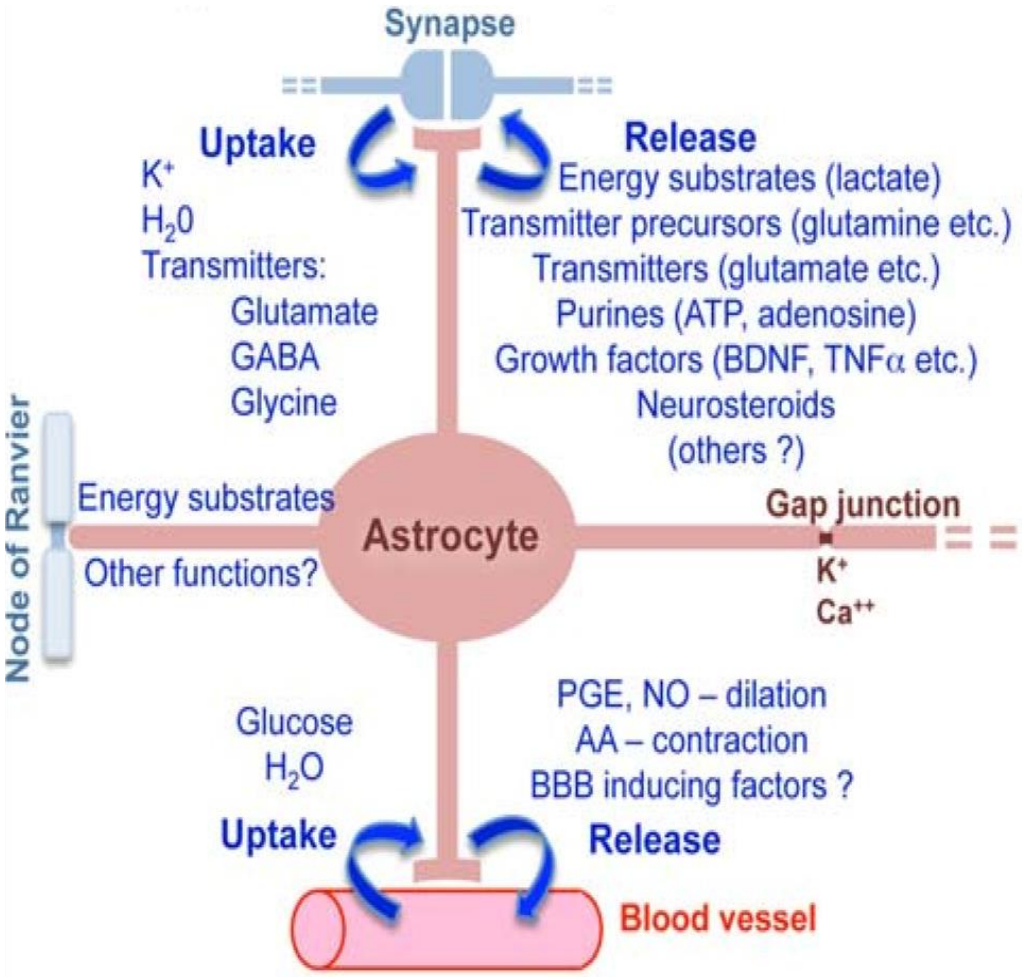

Figure 6: Astrocyte function in the CNS **(Sofroniew and Vinters, 2010)**

I.3 - Water transport by the Aquaporin 4 in astrocytes

Aquaporin (AQP) also called water channels, are a class of membrane protein part of the large family of channel proteins. Their main function is to facilitate water transport through cell membrane by forming pores enabling water molecules to pass. They play a crucial role in maintaining cell water homeostasis and by extension all body water homeostasis.

I.3.*1* - A brief historic on aquaporin research

Water is the most prevalent molecule in a cell, around 70% of the intracellular composition being water. Cells membrane delimits the interior cytoplasm from the outside of the cells. Cell membrane is made of lipid bilayer that is crucial for the cell integrity, and a strict control of how water can diffuse through a cell membrane is necessary to maintain this cell integrity.

Water can diffuse through plasma membrane by 2 different mechanisms. First by passive diffusion, and secondly via transporters or channels.

For long researchers hypothesized that passive diffusion was not the only mechanism enabling water molecule to cross cell membrane. As some type of cells were exhibiting higher water permeability than others. But for a long time these mechanisms remained unknown.

In 1957 Sidel and Solomon studied the hypothesis that maybe specialized proteins may exit in order to facilitate water diffusion though biological membrane (Sidel and Solomon, 1957). In 1984 Macey et al were able to block water selectivity of red blood cell, and revert it by applying a reducing agent (Macey, 1984)**.** But it was until 1992 that the first water permeable channel could be isolated by Peter Agre's lab, which awarded him the Nobel Prize in 2003. The isolated protein was then first named CHIP 28 for channel forming integral protein, and later renamed Aquaporin 1 (Agre, 2006).

I.3.*2* - Aquaporin classification

The AQP are divided in 13 families from aquaporin 0 to aquaporin 12. They are all expressed ubiquitously in mammalian tissues (**Table 2**). They can be subdivided in three different subgroup, first the ***Aquaporins*** "*purely water channel family*" (AQP0, 1, 2, 4, 5, 6 and 8); second, the ***Aquaglyceroporins*** (AQP3, 7, 9 and 10); and last and relatively new group of aquaporins the ***Super-aqua-porins*** (AQP11, 12) (Badaut et al., 2014).

AQP Subtypes	Transport molecules	Tissue distribution
AQP0	Water, anion	Fiber cells of the crystalline lens
AQP1	Water, gas, and possibly cations	Erythrocytes, eye, choroid plexuses, kidneys, heart, lungs, vascular endothelium, skin, gastrointestinal tract, salivary gland, liver, testes, ovaries, and uterus.
AQP2	Water	Renal collecting duct, ears, ductus deferens
AQP3	Water, urea, glycerol, ammonia,H_2O_2	Kidneys, leukocytes, erythrocytes, skin, eyes, respiratory tract, gastrointestinal tract, ovaries
AQP4	Water, CO_2, amonia	Brain, retinas, salivary and lacrimal glands, olfactory and auditory epithelium, gastrointestinal tract, kidneys, lungs, and skeletal muscle
AQP5	Water, CO_2	Epithelia of lacrimal, sweat, and salivary glands, alveolar, bronchial, and tracheal mucosa, ovaries, kidneys, and skin
AQP6	Water, urea, anions, glycerol, nitrate	ntracellular vesicles of the renal collector tubule and brain
AQP7	Water, urea, glycerol, ammonia, arsenite	Adipose tissue, carotid body, testes, kidneys, heart, skeletal muscle, and ovaries
AQP8	Water, ammonia, H_2O_2	Liver, pancreas, gastrointestinal tract, salivary glands, kidneys, lungs and trachea, testes, and ovaries
AQP9	Water,urea, glycerol, lactate, H_2O_2,mannitol, purines, pyramidines	Liver, leukocytes, erythrocytes, testes, ovaries, brain, kidneys, and splee
AQP10	Water, urea, glycerol	Small intestine, specifically in the duodenum and jejunum
AQP11	Water	Testes, heart, kidneys, ovaries, muscles, gastrointestinal tract, leukocytes, liver, brain
AQP12	Undertermined	Acinar cells of the pancreas

Table 2: Distribution and molecule transport of the different type of aquaporin in the CNS. Adapted from (Trillo-contreras et al 2022)

I.3.3 - The Aquaporin 4 is the major aquaporin in the CNS

The AQP4 is one of the main AQP present in the CNS, expressed mainly on astrocytes. The AQP-4 is enriched in astrocyte processes in close contact with blood vessels, being a main component of the glymphatic system. AQP4 was first discovered in 1994 in the rat brain (Jung et al., 1994). Verkman's and Agre's group independently reported that rat brain expresses a specific AQP cDNA. First named mercury insensitive water channel (MIWC) by Verkman's group but later named AQP4 (Nagelhus and Ottersen, 2013) (Morton et al., 2007) The polarized localization of AQP4 pool in astrocytes is maintained by anchoring proteins such as syntrophin (**Fig. 7**).

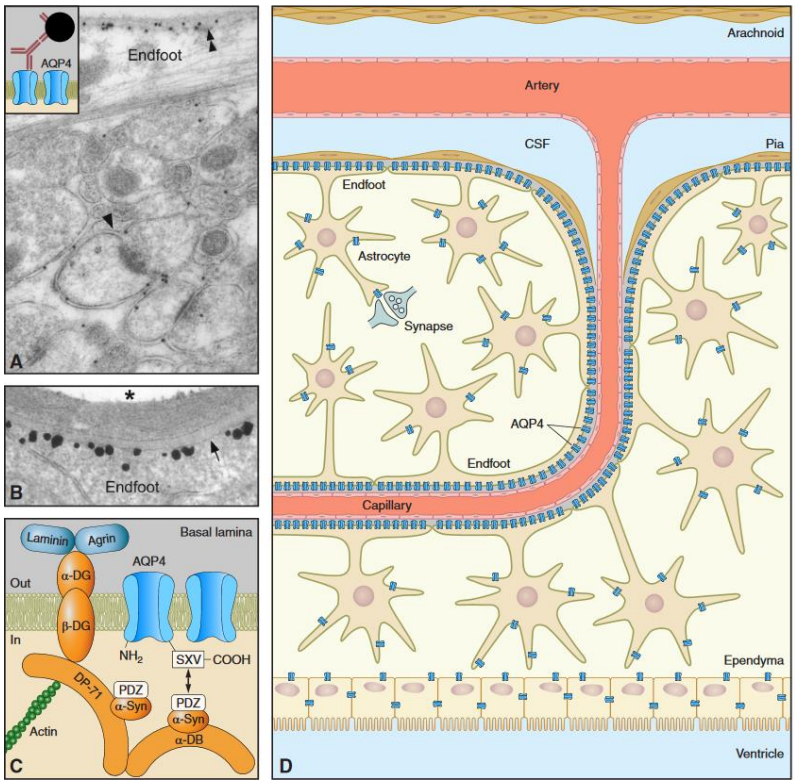

Figure 7: Distribution of AQP4 in the brain. *There is evidence accumulated to suggest that AQP4 is involved in such diverse functions as regulation of extracellular space volume, potassium buffering (references), cerebrospinal fluid circulation (references), interstitial fluid resorption, waste clearance,*

neuroinflammation, osmosensation, cell migration, and Ca^{2+} signaling. AQP4 is also required for normal function of the retina, inner ear, and olfactory system. From (Nagelhus and Ottersen, 2013)

I.4 - Glymphatic system, a recent concept for brain fluid circulation

The **glymphatic system** (GS) concept has emerged over the last decade. This concept is part of the theory of the intracerebral drainage system, and was first proposed by Iliff in 2012 (Iliff et al., 2012). Glymphatic system leans on the principle of fast pathway for inflow of CSF from the periarteriole space, and the outflow of interstitial fluid to the perivenous space (**Fig. 8**). **This system is featured by three dynamically interlinked aspects: (1) there exists a convective flow wide-spread in brain parenchyma (interstitial flow); (2) this flow is driven by the pulsation of infiltrated arterioles; (3) astrocyte AQP4 modulates the kinetics of glymphatic system.** Traditionally, it is known that the pulsation of arteriole creates a local convective flow in perivascular space (i.e., the VirchowRobin space). Glymphatic concept extends this scenario to the parenchyma, which is however still in debate (Smith and Verkman, 2019; Mestre et al., 2020b).

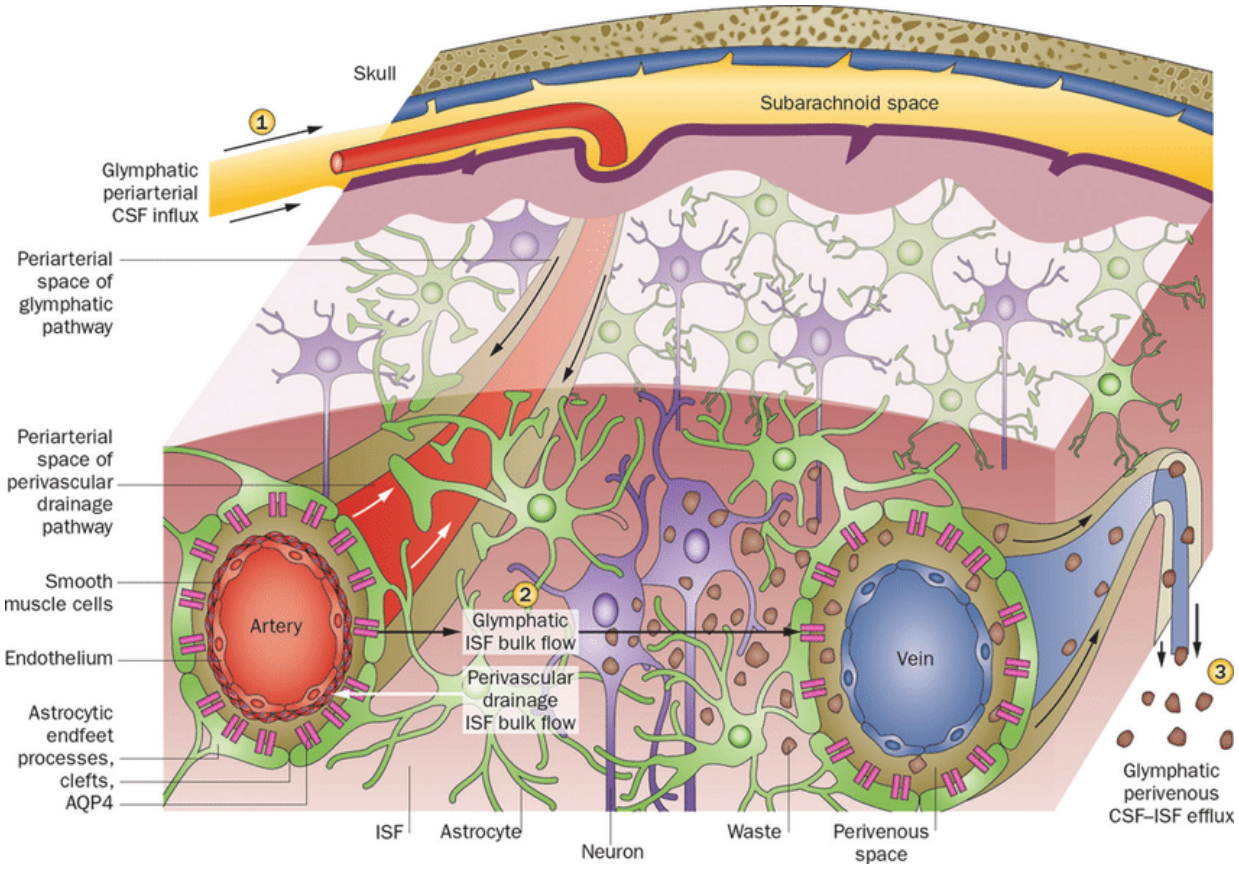

Figure 8: Outline of the glymphatic system. *This figure illustrates that perivascular clearance comprises perivascular drainage and glymphatic pathways. (1) Cerebrospinal fluid flows into the brain parenchyma via the periarterial space, which is the perivascular space surrounding the parenchymal arteries. From this perivascular space surrounding the artery, cerebrospinal fluid enters the interstitium of the brain tissue via aquaporin 4 (AQP4)-controlled water channels. These are distributed in the end feet of astrocytes that constitute the outer wall of the perivascular space. (2) Cerebrospinal fluid entering the interstitial fluid flows by convection, and the cerebral spinal fluid (CSF)-interstitial fluid (ISF) exchange within the brain parenchyma. (3) After washing the waste proteins from the tissue, it flows into the perivenous space, which is the perivascular space around the deep-draining vein, and is subsequently discharged outside the brain. (Reprinted by permission from Macmillan Publishers Ltd: Nat Rev Neurol [11:457-470], copyright [2015]). Figure and legend from (Nedergaard, 2013).*

I.4.*1* - Brain fluid study to glymphatic system

Study of brain fluid transport go along with the study of the brain itself. And the study of brain fluid transport is as old as the later. The earliest notions for brain fluid transport were found in ancient Greece. But those works were descriptive and often contained arbitrary postulates. It was until the renaissance, which is a period that saw the revival of science that led to many discoveries in many key component of the nervous system. Since then, the understanding for the brain fluid transport has been boosted by the all along scientific discoveries (**Fig. 9**).

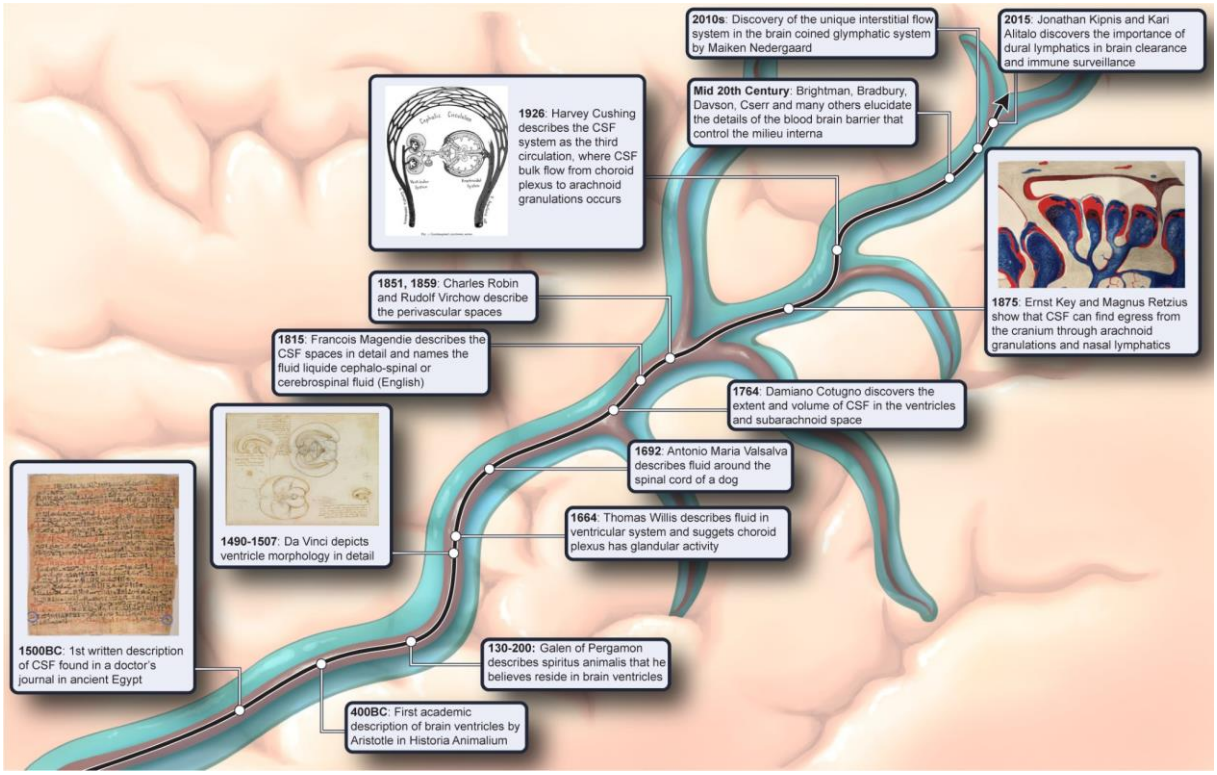

Figure 9. Timeline of significant events and discoveries pertaining to brain fluid transport. *The black arrow superimposed over the cerebral artery illustrates the passage of time. The timeline spans over millenniums and includes the first clinical description of cerebral spinal fluid (CSF) in ancient Egypt found in the Edwin Smith papyrus scroll from 1500 BC, the first morphologically correct drawing of the ventricular system by Leonardo da Vinci in 15th century, and the description of CSF flow as the third circulation by Harvey Cushing in the 20th century. Many other substantial discoveries extending beyond those illus- trated in the figure established the foundation to our modern understanding of brain fluid transport but due to space limitations cannot be included in the fig- ure (see FIGURE 3). Images are courtesy of The New York Academy of Medicine Library (Edwin Smith Papyrus scroll) and from Ref. 31 (Da Vinci drawings; with permission from Springer International), (schematic by Harvey Cushing; with*

permission from The Archives of Surgery), (Arachnoid granulations drawing by Key and Retzius))(Rasmussen et al., 2022)

The dynamics of glymphatic flow was first described in 2012 using bi-photon microscopy in mice by injecting fluorescent tracers into the cisterna magna in order to visualize CSF diffusion in real time (Iliff et al., 2012). Following injection, the tracers quickly flowed along the perivascular space of the cortical surface arteries and the penetrating arterioles, and from there entered the brain parenchyma. Brain fluid flow pathway in the parenchyma was defined by fluorescence imaging of fixed brain slices. A longer-time observation showed that the tracers have accumulated along capillaries and parenchymal venules. This imples that the interstitial fluid (ISF) were drained along the perivenous space surrounding large caliber draining veins. AQP-4 being localized near periarterial and periveinous space, **it was then also hypothesized that AQP4 may play a role in CSF and ISF exchange flux.**

Glymphatic system was proposed for the removal of the solute and protein wastes in the brain, sustained by the convective exchange between the CSF and ISF (**Fig. 10**) (Iliff et al., 2012; Louveau et al., 2015). As aforementioned, the CSF penetrates the astrocytes end-feet to reach the brain interstitial space through a water channel membrane composed with AQP-4, (Iliff et al., 2012). In the interstitial space, this CSF bulk flow can move brain metabolites and clear them through other perivascular spaces adjacent the cerebral veins. Then, the flow could travel through the cranial nerves, and in the recently described cerebral lymphatic vessels in the dura mater alongside the sinus veins (Aspelund et al., 2015; Louveau et al., 2015). Interestingly, the glymphatic activity is dramatically increased during sleep, which may have a role for brain waste clearance, a mechanism seemingly underlying the refreshing effect of sleep (Xie et al., 2013).

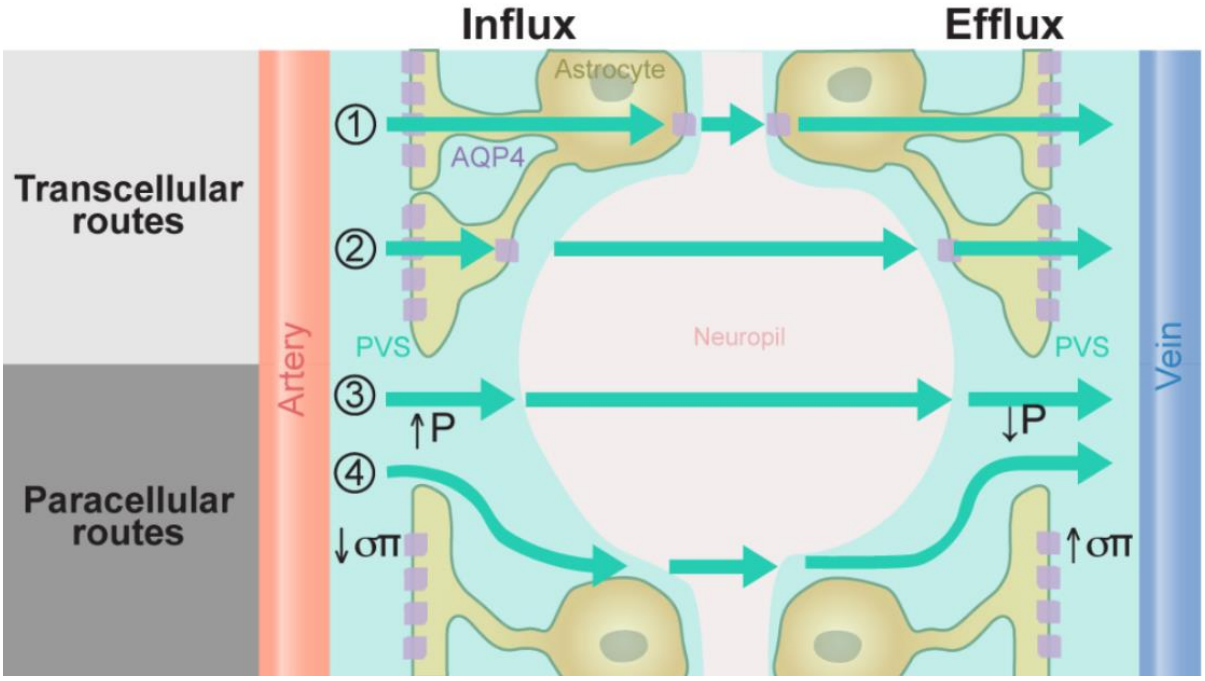

Figure 10: Plausible fluid transport routes and their dependence on the polarized expression of aquaporin 4 (AQP4) at perivascular astrocytic end- feet. *Directional fluid transport from arterial to venous vasculature would require differential conditions at the site of influx (left) and efflux (right) of fluid. Possible flow pathways can be largely divided into transcellular or paracellular transport routes. Transcellular routes (top row) would consist of direct entry of fluid through AQP4 channels, and could be subdivided into the following: 1: trans-astrocytic fluid transport, where fluid enters the astrocyte at the endfoot and continues through the soma and the greater glial syncytium following a largely intracellular pathway, or 2: trans-endfoot fluid transport, where fluid enters into the endfoot and rapidly exits into the extracellular space (ECS) without entering the soma, thus following a largely extracellular pathway interspersed with short segments of intracellular transport. Alternatively, fluid may also follow paracellular routes (bottom row), which would consist of fluid transport through the clefts formed by neighboring endfeet. This primarily extracellular transport route would rely indirectly on AQP4 water channel expression. 3: Hydrostatic pressure gradients, between the arterial and venous sides of the extracellular space could drive directional fluid flow toward the region of lower pressure (P artery > P ECS > P vein). 4: osmotic pressure gradients could be generated by astrocytic ionic fluxes (e.g., K1 spatial buffering) that in part depend on AQP4 polarization. Directional transport of extracellular osmoles could potentially drive fluid entry between endfeet toward efflux sites (rpvein > rpECS > rpartery). PVS, perivascular space. Figure and legends from (Rasmussen et al., 2022)*

I.4.*2* - Physiological functions of the glymphatic system

The glymphatic system plays roles in **brain fluid circulation, metabolite clearance, delivery of nutrient and in volume neurotransmission**. Glymphatic system thus helps the brain to get rid of excess of extracellular fluid, metabolite and protein waste products (**Fig. 11**).

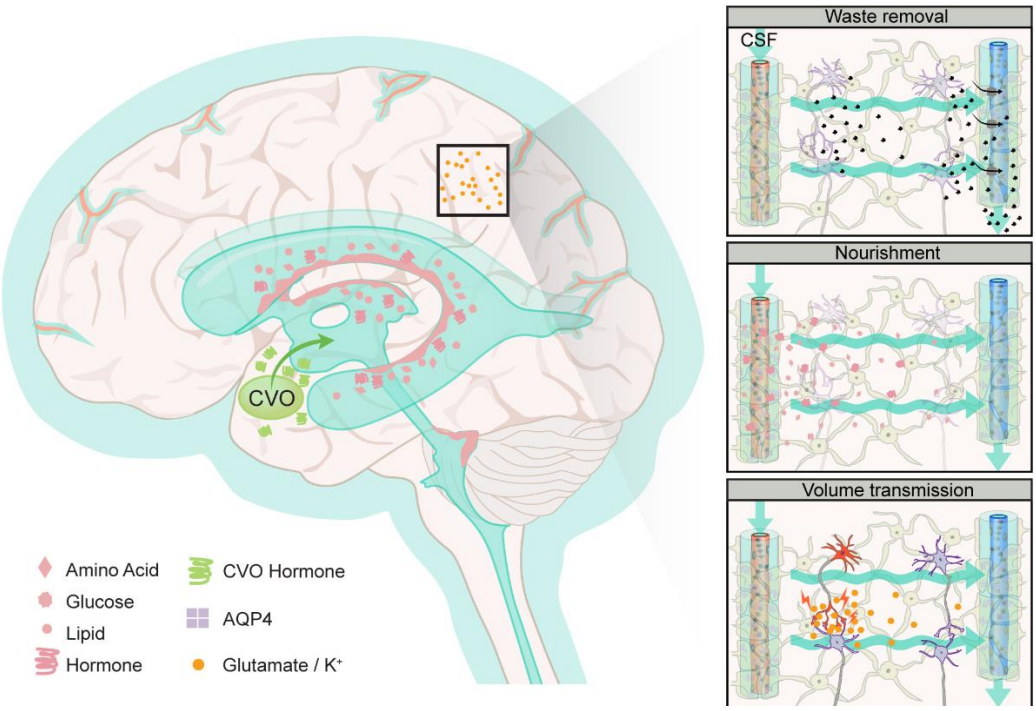

Figure 11. Glymphatic system and its role in clearance, nourishment, and volume transmission. *The glymphatic system serves various physiological functions. By establishing extracellular fluid efflux, the glymphatic system clears the brain parenchyma of extracellular metabolites and waste products. Furthermore, the influx of cerebrospinal fluid (CSF) to the brain along periarterial spaces also provides nourishment to the brain, whereby the glymphatic system distributes glucose to neurons and astrocytes, and delivers lipids and apolipoprotein E arising in the choroid plexus throughout the brain. Certain vitamins like folate and ascorbate are exclusively delivered to the brain parenchyma by CSF. Finally, the glymphatic sys- tem may play a role in local volume transmission, which refers to the transport of "spill-over" neurotransmitter from a synapse to neighboring non-post- synaptic cells. Glymphatic flow in the extracellular space would theoretically increase local volume transmission, as may occur during nonrapid eye movement (NREM) sleep, when large volumes of CSF wash through the neuropil. Interesting, NREM sleep is characterized physiologically by large scale synchrony of neuronal activity,*

which fits with the notion of widespread humoral action supported volume transmission, as opposed to the tight spatiotemporal coupling of neurotransmission during wakefulness. Global volume transmission refers to the brain-wide delivery of neuropeptides or hormones with CSF, arising in circumventricular organs or from the choroid plexus. CVO, circumventricular organs; AQP4, aquaporin 4. Figure and legend from (Rasmussen et al., 2022)

In this context, dynamic flowing of CSF plays critical roles in regulating brain function and in controlling diffusion of neurotransmitters and metabolic substrates, such as glucose and lactate, thereby shaping synaptic transmission and plasticity (Mestre et al.,2020.; Kessler, 2013; Rangroo Thrane et al., 2013; Xie et al., 2013; Lundgaard et al., 2015, 2017)

I.5 - Scientific question and technical challenges

Brain flow transport plays an important role in regulating extracellular molecular diffusion, therefore the health of brain network (Brinker et al., 2014; Mesquita et al., 2018). As a recently proposed concept, the glymphatic system extends an active brain flow transport across the parenchyma for physiological homeostasis maintenance as afore summarized. It controls the intracerebral pressure equilibrium, extracellular neurotransmitter diffusion and the dynamic distribution of energy fuels such as glucose and lactate in the brain. Disturbance in brain flow/fluid transport is being recognized as a severe factor exacerbating neurological pathologies like edema development and Alzheimer's disease (Tait et al., 2008; Louveau et al., 2015). As a major type of glial cells, astrocytes are distributed throughout the brain and strategically located between cerebral vasculature and brain parenchyma (Barres, 2008). **Astrocyte volume dynamics is implicated in regulating the extracellular architecture thereby brain flow transport** (Plog and Nedergaard, 2018). **Water flux underlies astrocyte volume regulation.** Aquaporins (AQP) represent a family of bidirectional water transport channels, with AQP4 being the major subtype expressed in brain astrocytes (Nagelhus and Ottersen, 2013; Papadopoulos and Verkman, 2013).

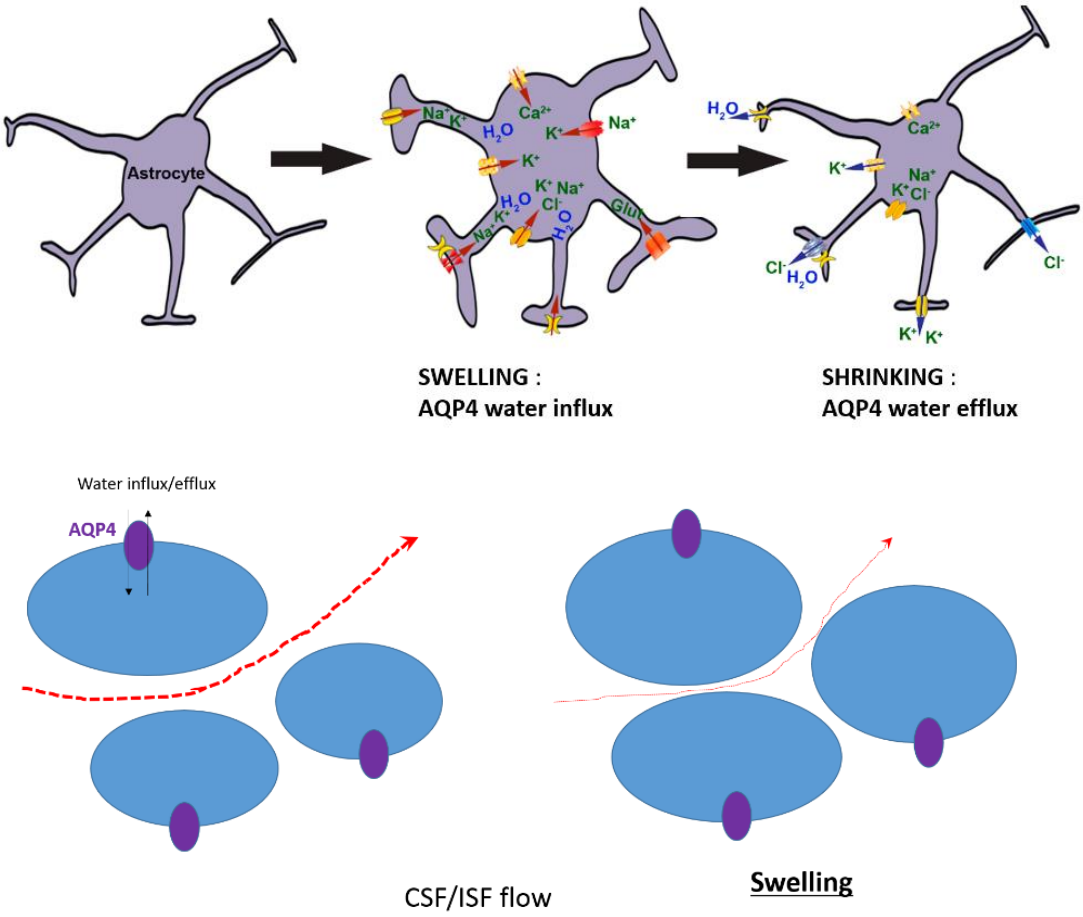

Figure 12: AQP4 is bidirectionally implicated in astrocyte volume regulation *(Simard and Nedergaard, 2004; Lafrenaye and Simard, 2019) and modulation of extracellular space thereby brain fluid transport.*

AQP4 has been implicated in brain fluid homeostasis, however its role in astrocyte volume regulation remains controversial. At the cellular level, early reports show controversial effects of AQP4 genetic inhibition on astrocyte swelling activity at cellular level; for instance, knocking out of AQP4 reduces astrocyte swelling as shown by (Benfenati et al., 2011),while in contrast Murphy et al. showed that AQP4 knocking out facilitated astrocyte swelling (Murphy et al., 2017). Also, reduced extracellular space was observed in AQP4-deficient mouse model (Binder et al., 2004; Zhang and Verkman, 2010), and in mouse model delocating AQP4 by knocking out its anchor protein syntrophin, implying that AQP4 deficiency may swell astrocytic endfeet (Amiry-Moghaddam et al., 2004). Not only being involved in astrocyte volume regulation, astrocyte AQP4 is implicated in brain pathologies such as the edema development.

Nevertheless, while AQP4 knock out ameliorates cytosolic brain edema that reflects the water accumulation in intact cells, deficiency of AQP4 exacerbates the brain swelling in vasogenic edema and hydrocephalus mouse model, which are observed during brain blood barrier disruption and the elevation of intraventricular pressures, respectively. (Bloch et al., 2006; Tait et al., 2008; Verkman et al., 2017). The presence of AQP4 has also been reported to alleviate perihematomal edema in intracerebral hemorrhage (Jeon et al., 2021)

Recently, dynamic exchange of brain fluid between CSF and parenchyma ISF is suggested to be important for clearing brain environment, leading to the emergence of the concept of glymphatic system (Mestre et al., 2020a). The importance of glymphatic system has been manifested by the removal of waste metabolites and harmful proteins (e.g., β amyloid) from the brain parenchyma. However, controversies exit about the operating mechanisms of glymphatic system (Smith and Verkman, 2019), with a major debate raised on the role of AQP4 water channel. Several lines of experiments utilizing different types of AQP4 KO mice and diffusible tracer imaging suggest an indispensable involvement of AQP4 in brain fluid transport (Mestre et al., 2018), However, it was also observed in AQP4 null mice that brain fluid transport is unafected (Smith et al., 2017a). In addition, selectively perturbing astrocyte AQP4 has led to distinct effects on water diffusion in the brain parenchyma as determined by the apparent diffusion coefficient using diffusion-weighted magnetic resonance imaging (DW-MRI) (Badaut et al., 2011; Debacker et al., 2020).

One reason underlying the aforementioned controversial observations (at the cellular, network and MRI level) on the role of astrocyte AQP4 in brain fluid transport, might be that chronically **inactivating astroctye AQP4 by genetic interventions have caused variable alterations in cerebral water environment, or induced unexpected cellular adaptation**. Indeed, it has been observed that in AQP4 KO mice, the water content in the brain parenchyma is significantly altered compared to intact animals (Haj-yasein et al., 2011); **Fig. 13**). This, likely have rendered it difficult to clarify the function of astrocyte AQP4 in brain fluid circulation. **Hence, acutely targeting AQP4 water channel is necessary to pinpoint its role in astrocyte volume regulation in brain physio- and pathology.**

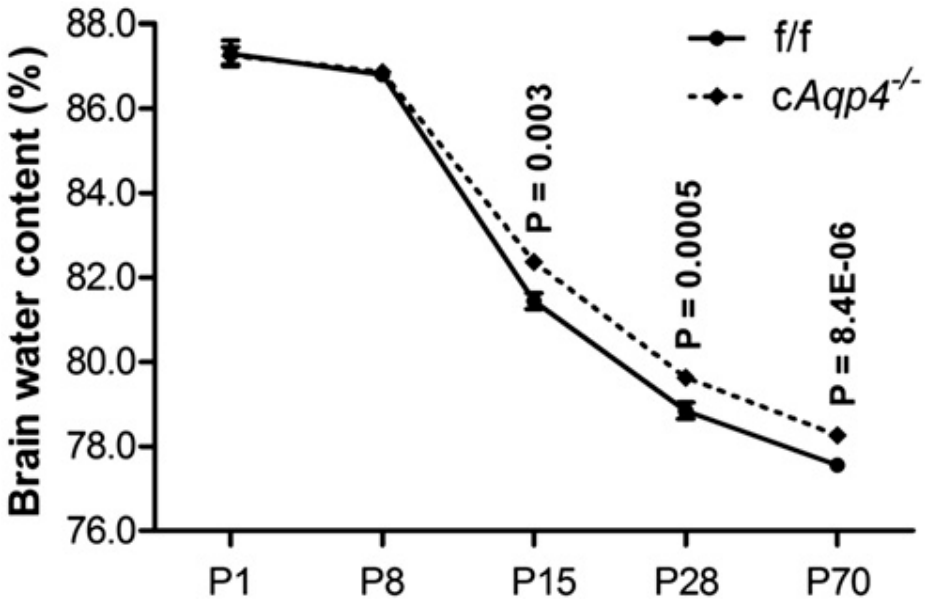

Figure 13: Water content in mouse brain in conditional AQP4 KO mice **(Haj-Yasein et al., 2011).**

The synthetic compound 2-(nicotinamido)-1,3,4-thiadiazole (TGN-020) is derived from the condensation of nicotinamide and thiadiazole derivatives (Burnett et al., 2015). TGN-020 has been identified as a selective and potent inhibitor of AQP4 water channel as testified using either the heterologous expression system (Toft-bertelsen and Larsen, 2020) or the AQP4 knockout mouse model (Igarashi et al., 2013.; Huber et al., 2009). Application of TGN-020 in vivo reduced ischemia-associated edema in mouse models as revealed by MRI (Igarashi et al., 2011). Using AQP4 knockout mice, TGN-020 has been engineered as an AQP4 selective ligand for preclinical positron emission tomography imaging to map brain AQP4 distribution (Nakamura et al., 2011). Blocking of AQP4 by TGN application augments the local cerebral blood flow, with effect of TGN-020 was absent in AQP4 knockout mice, indicating the specific targeting of AQP4 (Igarashi et al., 2013.).

Using mouse model and combining the selective targeting of AQP4 with TGN0-020, I developed ex vivo and in vivo fluorescent intensity-translated astrocyte volume imaging methodology and resorted to diffusion MRI to assess brain water diffusion. The results of my PhD study show that AQP4 water channel plays a tonic role in inhibiting astrocyte swelling, suggesting AQP4 mediating a constitutive water efflux from astrocytes. Acutely blocking AQP4 by TGN-020 caused astrocyte swelling in mouse somatosensory cortex. Accordingly,

AQP4 inhibition facilitated osmotically evoked astrocyte swelling while delayed the shrinking responses. I then observed that manipulating astrocyte AQP4 in vivo altered global water diffusion in mouse brain using diffusion-weighted MRI. **Together, my study proposes an asymmetric engagement of AQP4 in homeostatic astrocyte water flux which helps to maintain the brain water diffusion.** This finding provides an updated mechanism for understanding the cellular basis of astrocyte AQP4 in brain fluid transport and helps to better understand its involvement in brain glymphatic system.

I.6 - Material and methods

Brain slices preparation, and in vivo preparation

Experiments were undertaken in accordance with European Community guiding principles on the care and use of animals (86/609/CEE), and the rules of the host institute. Coronal slices comprising somatosensory cortex and hypothalamus were acutely prepared from C57BL/6 mice of both sexes at ages as indicated. Mice were deeply anesthetized by isoflurane (Axcience) evaporation in a closed plexiglass box. For mice less than 4 weeks old, the brain was taken out and placed in ice-cold artificial cerebrospinal fluid (aCSF, mM: 124 NaCl, 4.5 KCl, 1.2 NaH2PO4, 1 MgCl2, 2 CaCl2, 26 NaHCO3, and 10 D-Glucose), and cut into 300-μm thick slices by a vibratome (Leica VT1200S). For mice older than 4 weeks, the brain was placed in a modified aCSF for slicing (in mM: 30 NaCl, 4.5 KCl, 1.2 NaH2PO4, 1 MgCl2, 26 NaHCO3, 10 D-Glucose, and 194 sucrose) (Jiang et al., 2016) maintained at 4 °C during sectioning. Brain slices were recovered in normal aCSF at 37 °C for about 1 h. Mice of similar age were used also for in vivo labeling of astrocytes, sulforhodamine B (10 mg/ml, Sigma) was intraperitoneally injected into awake mice at a dose of10 μL/g (Appaix et al., 2012).

Fiberphotometry

4-6 week-old WT mice were implanted with optical fibers (200 mm core, NA = 0.37, Neurophotometrics) coupled to a stainless-steel ferule (1.25 mm) at S1 cortex coordinates, and fixed to the skull with dental cement (SuperBond, Sun medical). Mice were habituated to the

cage and fiber setup for 30 minutes, then fluorescence was recorded for 120 min (5 min of baseline, before SRB injection, saline solution or TGN-020 solution were injected by intraperitoneal injection 1 h after SRB injection). Fluorescence measurements of fluorescence volume translated intensity and calcium signals were recorded using a Neurophotometrics fiber photometry system (FP3002). A branched fiber optic patch cord (BFP_200/230/900-0.37_FC-MF1.25, Doric Lenses) connected to the fiber photometry apparatus was attached to the implanted fiber optic cannula using a cubic zirconia sleeve. To record fluorescence signals from SRB, light from 560-nm LED; for GCaMP6f, light from a 470-nm LED was band-pass filtered, collimated, reflected by a dichroic mirror and focused by a ×20 objective. LED light was delivered at a power that resulted in 50 µW of 560- and 470-nm light at the tip of the patch cord. Emitted SRB and GCaMP6f fluorescence was band-pass filtered and focused on the sensor of a CCD camera. To account for auto-fluorescence and possible motion artifacts during testing, a 410-nm light stimulation corresponding to isosbestic GCaMP6f signal was used. This signal was similarly directed into the brain and subsequently measured with the CCD camera. *Simultaneous recording of -560 470- and 410-nm channels was achieved through an integrated camera and image splitter (Flir Blackfly S series).* Signals were collected at a rate of 1 Hz for SRB and 16 Hz for GCaMP6f and visualized using the open-source software Bonsai 2.4 (http://bonsai-rx.org). Results of SRB recording were analyzed in Igor software (Wavemetrics), and results from GCaMP6f mice recording were analyzed using pMAT (Bruno et al., 2021).

Mice preparation and genotyping

The genetically encoded Ca^{2+} indicator GCaMP6 was expressed in astrocytes in vivo by crossing a Cre-dependent GCaMP6f mouse line (Ai95, The Jackson Laboratory) with an astrocyte-specific Glast-CreERT2 mouse line (Slezak et al., 2007). Tamoxifen (T5648, Sigma) was dissolved in ethanol 100 % (at 1 mg/250µL) and vortexed until tamoxifen is fully dissolved. Corn oil (sigma) were then added to have a final solution at 10% ethanol and 90% oil. Solution is then heated at 37°c for 15 min and vortexed, and put in sonicator for 15 min and then aliquoted. All procedures were made under light-proof protocols. Aliquots were stored at -20 °C until use. GCaMP6f/Glast-CreERT2 mice were injected at ~3–4 weeks of age, once a day (1 mg) for two consecutive days. Genotyping of the Cre-dependent GCaMP6f mouse line (Ai95, The Jackson Lab) used the standard primers and polymerase chain reaction protocols provided

by the supplier. Genotyping of GLAST-CreERT2 mouse line was performed using the primers for Cre recombinase (TK139/141) as reported (Slezak et al., 2007).

Imaging set up and procedures

Epifluorescence illumination was provided by a monochromator light source (Polychrome II, TILL Photonics, Germany) directly coupled to the imaging objective via an optical fiber. We used three water immersion imaging objectives: ×10 NA0.3, ×20 NA0.5 and ×40 NA 0.8 (ZEISS). The green fluorescence of GCaMP6 was separated from the red fluorescence of SRB, by spectrally exclusive double-band filters (Di03-R488/561-t3 and FF01- 523/610, Semrock). Fluorescence signal was collected using a digital electron-multiplying charge-coupled device (EMCCD Cascade 512B, Photometrics). The imaging chamber (20 × 30 × 46 mm width, height and length) was custom- designed using 3D modeling software (Trimble SketchUP), produced by a Mojo 3D printer (Stratasys). The chamber was mounted on a motorized PI stage (Physik Instrumente GmbH, Germany) for axial micro-manipulation. Laser excitation and image acquisition were controlled by MetaMorph (Molecular Devices).

In vivo diffusion MRI

Supported by an international exchange program JSPS-CNRS, I got the opportunity to go to the lab of Dr. Tomokazu Tsurugizawa in National Institute of Advanced Industrial Science and Technologies in Tsukuba, to carry out in vivo diffusion MRI experiments to test the effect of astrocyte AQP4 acute inhibition on the rate of brain fluid transport, where apparent diffusion coefficient (ADC) of cerebral water molecule was used.

Ten C57BL6 mice were used for the experiment. MRI experiment was performed with medetomidine anesthesia (0.6 mg/kg/h, i.v.). The mice were injected with TGN020 and saline at 4 weeks interval. For crossover test, the order of injection of TGN020 or saline was randomly determined. The respiration was monitored, and the body temperature was maintained at 36 °C by circulating hot water during the measurement.

The MRI experiments were conducted on a Bruker 7T scanner using a cryo-cooled mouse brain coil. After 10 min from the start of the scanning, TGN-020 (250 mg/kg body weight) or Saline

was injected. Then, scanning was continued for 60 min. The body temperature was maintained at 36 °C via the circulating hot water. The respiration rate was monitored and was confirmed within the range of 130-140 /min throughout the experiment. Mice were injected with 250mg/kg of TGN-020. We used a standard diffusion-weighted spin echo EPI sequence, with the following parameters: spatial resolution = 175 x 175 x 500 μm^3, 3 b-values (b = 0, 250 and 1800 s/mm^2), 6 directions, 1 segment, TE = 37.1 ms / TR = 5769 ms, bandwidth = 300 kHz, δ = 3 ms, Δ = 24 ms, total scan time = 5 min. The DWI scan was continued for 70 min (total 14 scans).

The ADC at each time point was calculated from DWI data using DSIstudio (https://dsi-studio.labsolver.org/). The percent change of ADC was then calculated following equation, $\Delta ADC_i = (ADC_i / ADC_2 - 1) \times 100$ (%). The ADC_i is the ADC at the i-th timepoint. We define the ADC at 2nd time-point as the baseline because saline injection was performed after 2nd DWI scan. The averaged ADC changes within the region of interests (ROIs) were calculated using a homemade program. The ROIs of the cortex, the hippocampus, and the striatum were created with reference to Allen mouse brain atlas.

Statistics

Experimental data are expressed as mean ± standard error unless otherwise mentioned. The t-test was performed for two-group comparisons, and significant difference was determined by p values less than 0.05. Mann-Whitney U test was also used to ascertain the significance level, in considering the deviation of the experimental data from the theoretical symmetrical distribution. In the present study, these two test methods yielded consistent results on statistical significance. Statistical tests were carried out in Matlab (The MathWorks). The significance levels are shown in figures by *$p < 0.05$, **$p < 0.01$, ***$p < 0.001$.

I.7 - Technical development establishing light sheet microscopy for high quality imaging of mouse brain astrocytes

To achieve high-quality dynamic imaging of astrocyte in situ, I first established light-sheet fluorescence microscope to image astrocytes in mouse acute brain slices. As a basis for astrocyte volume dynamics imaging, I took astrocyte morphology as an example to demonstrate the superior imaging performance of light-sheet microscope. In addition, as astrocytes Ca^{2+} represents a highly dynamic signaling underlying their physiology, I also showed that light-sheet microscopy is suitable to imaging astrocyte Ca^{2+} signals, which sets the basis for the following physiological experiments of activity-associated astrocyte volume adaptation and the physiopathological alterations. This part of the study has been published (Pham et al., 2020).

NeuroImage 220 (2020) 117069

Contents lists available at ScienceDirect

NeuroImage

journal homepage: www.elsevier.com/locate/neuroimage

Mapping astrocyte activity domains by light sheet imaging and spatio-temporal correlation screening

Cuong Pham [a], Daniela Herrera Moro [b], Christine Mouffle [a], Steve Didienne [a], Régine Hepp [a], Frank W. Pfrieger [c], Jean-Marie Mangin [a], Pascal Legendre [a], Claire Martin [b], Serge Luquet [b], Bruno Cauli [a], Dongdong Li [a,*]

[a] Sorbonne Université, Institute of Biology Paris Seine, Neuroscience Paris Seine, CNRS UMR8246, INSERM U1130, UPMC UMCR18, Paris, 75005, France
[b] Unité de Biologie Fonctionnelle et Adaptative, Centre National la Recherche Scientifique, Unité Mixte de Recherche 8251, Université Paris Diderot, Sorbonne Paris Cité, 75205, Paris, France
[c] Centre National de la Recherche Scientifique, Université de Strasbourg, Institut des Neurosciences Cellulaires et Intégratives, F-67000, Strasbourg, France

ARTICLE INFO

Keywords:
Fluorescence
Calcium
GCaMP
Brain

ABSTRACT

Astrocytes are a major type of glial cell in the mammalian brain, essentially regulating neuronal development and function. Quantitative imaging represents an important approach to study astrocytic signaling in neural circuits. Focusing on astrocytic Ca^{2+} activity, a key pathway implicated in astrocye-neuron interaction, we here report a strategy combining fast light sheet fluorescence microscopy (LSFM) and correlative screening-based time series analysis, to map activity domains in astrocytes in living mammalian nerve tissue. Light sheet of micron-scale thickness enables wide-field optical sectioning to image astrocytes in acute mouse brain slices. Using both chemical and genetically encoded Ca^{2+} indicators, we demonstrate the complementary advantages of LSFM in mapping Ca^{2+} domains in astrocyte populations as compared to epifluorescence and two-photon microscopy. Our approach then revealed distinct kinetics of Ca^{2+} signals between cortical and hypothalamic astrocytes in resting conditions and following the activation of adrenergic G protein coupled receptor (GPCR). This observation highlights the activity heterogeneity across regionally distinct astrocyte populations, and indicates the potential of our method for investigating dynamic signals in astrocytes.

1. Introduction

As a major type of glial cell, astrocytes form interconnected networks in mammalian central nervous system (Giaume et al., 2010). Long thought as solely supportive elements in nervous tissue, astrocytes are now being revealed as critical players in brain development and function (Dallerac et al., 2018). Astrocyte activity is encoded by dynamic intra- and intercellular signals that regulate synaptic microenvironment, communications within neural circuits and cognition (Santello et al., 2019). Spatio-temporal characterization of astrocytic signals in situ is the premise to understand their contribution to central information processing. With the continuous development of fluorescent indicators for specific signaling pathways (Deo and Lavis, 2018; Lin and Schnitzer, 2016; Lobas et al., 2019), dynamic imaging stands as an important approach to investigate astrocyte function.

As a highly dynamic signal, intracellular Ca^{2+} oscillation represents an important aspect of astrocyte activity that occurs spontaneously or downstream of GPCR activation by neurotransmitters (Agulhon et al., 2008; Khakh and McCarthy, 2015). Such Ca^{2+} signaling has been implicated in gliotransmitter release, neurotransmitter and ion homeostasis, neurovascular coupling and perisynaptic structural remodeling (Bazargani and Attwell, 2015; Cauli and Hamel, 2018; Khakh and McCarthy, 2015; Nedergaard and Verkhratsky, 2012). Recent evidence suggests the involvement of astrocyte Ca^{2+} signal in the central control of animal behaviors (Covelo and Araque, 2018; Robin et al., 2018). Furthermore, departing from the conventional view that astrocytes form a homogeneous cohort, recent studies also start to notice their heterogeneities in terms of gene expression, morphology and functional interaction with local neural circuits (Chai et al., 2017; Lanjakornsiripan et al., 2018; Martin-Fernandez et al., 2017). Nevertheless, both the cellular mechanism and the functional consequence of astrocytic Ca^{2+} signal still remain debated (Bazargani and Attwell, 2015; Fiacco and McCarthy,

* Corresponding author.
E-mail address: dongdong.li@inserm.fr (D. Li).

https://doi.org/10.1016/j.neuroimage.2020.117069
Received 3 April 2020; Received in revised form 12 June 2020; Accepted 15 June 2020
Available online 22 June 2020

2018; Savtchouk and Volterra, 2018). A better understanding of the spatial and temporal features of astrocytic Ca^{2+} signals in situ will help to dissect their functions in the nervous system.

Optical microscopes combined with high-affinity Ca^{2+} sensors have enabled dynamic imaging of astrocytic Ca^{2+} in various contexts (Otsu et al., 2015; Perez-Alvarez et al., 2014; Reeves et al., 2011). Epifluorescence (EPI) microscopy coupled with digital cameras allows fast wide-field imaging, whereas the image contrast is degraded by out-of-focus fluorescence due to the lack of optical sectioning. This problem could be ameliorated by computational deconvolution using theoretical or empiric point spread function (Li et al., 2004; Swedlow, 2013), yet this method usually requires off-line and time-consuming iterative computations. Direct optical sectioning has been achieved by laser scanning confocal and two-photon microscopy, which evidently improves the image quality (Otsu et al., 2015; Shigetomi et al., 2013), yet also imposes limitations on imaging speed due to the spatial scanning (Keller and Ahrens, 2015; Svoboda and Yasuda, 2006). Also, during laser scanning, the high local energy of the focused beam may disturb astrocyte Ca^{2+} homeostasis (Kuga et al., 2011; Schmidt and Oheim, 2018; Zhao et al., 2009). Moreover, the relatively high cost of the femtosecond pulsed lasers required for two-photon microscopy limits its wide application. It is therefore desirable to achieve optical sectioning in a scanless manner for in situ astrocyte Ca^{2+} imaging.

Light sheet of micron-scale thickness can be generated from continuous wave lasers by objectives of long focal depth (Keller and Dodt, 2012; Ritter et al., 2010). Aligning light sheet orthogonally to the focal plane of an imaging objective enables scanless wide-field optical sectioning and ultrafast image acquisition by digital cameras (Ahrens et al., 2013; Jemielita et al., 2013; Power and Huisken, 2017). Here, we adopted light sheet imaging to characterize astrocyte Ca^{2+} dynamics in acute mouse brain slices. In parallel, a computational principle based on spatio-temporal correlation screening was introduced to map active Ca^{2+} domains. Using chemical and genetically encoded indicators, we demonstrated the ability of light sheet imaging to resolve astrocyte Ca^{2+} activity. Video rate acquisition was achieved over wide field up to hundreds of microns with adapted objectives. Using this method, we observed distinct Ca^{2+} kinetics between cortical and hypothalamic astrocytes in resting condition and in response to GPCR activation, lending support to the activity heterogeneities associated with local astrocyte populations. Light sheet imaging therefore represents a useful tool to study astrocyte activity and its diversity in mammalian nerve tissues, and will complement the methods to investigate glial functions.

2. Materials and methods

2.1. Preparation of mouse brain slices

Experiments were undertaken in accordance with European Community guiding principles on the care and use of animals (86/609/CEE), and the rules of the host institute. Coronal slices comprising

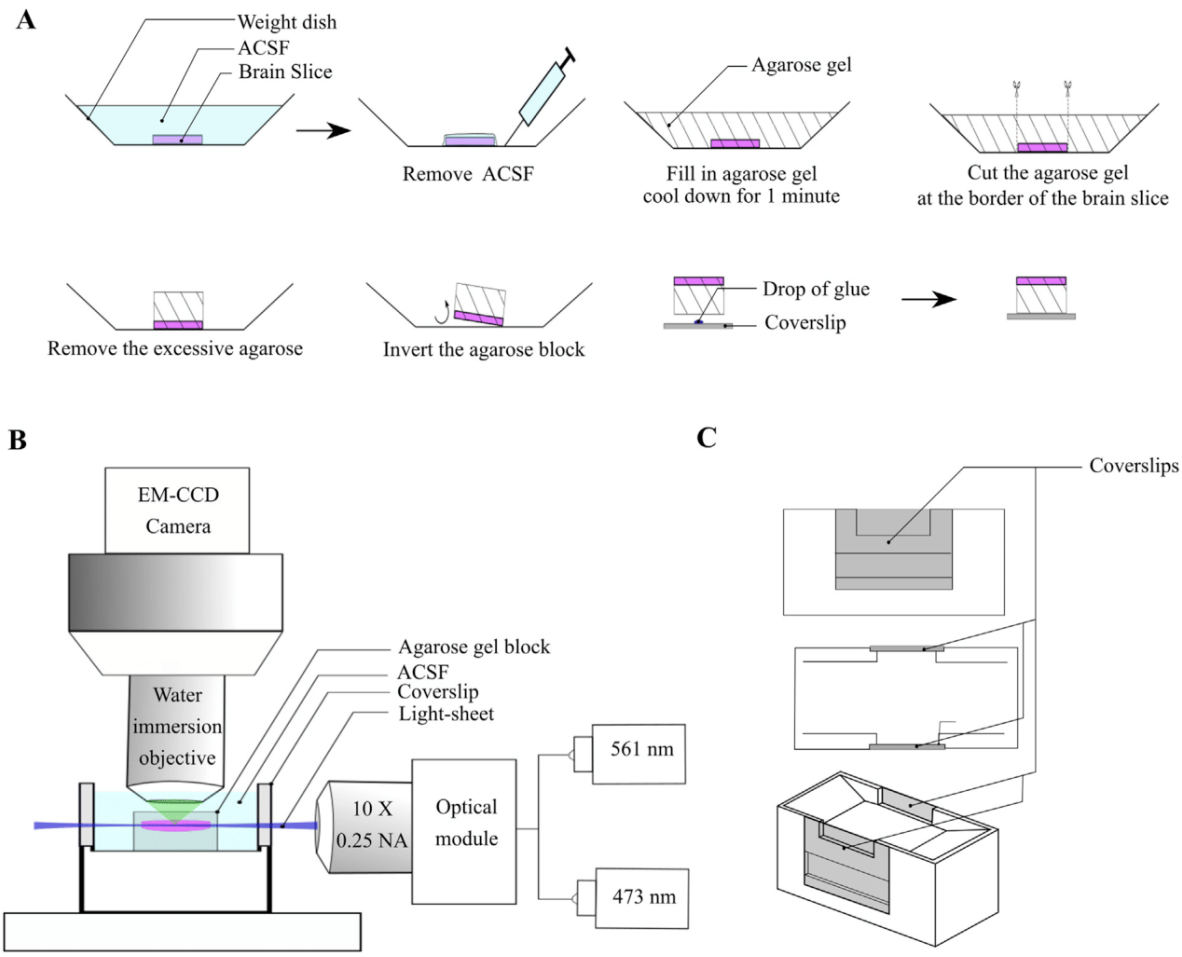

Fig. 1. Procedures and setup for light-sheet imaging. **(A)** Illustration of the placement of brain slices. **(B)** A light sheet optical module was orthogonally conjugated to an existing upright microscope. Two laser lines were coupled to the optical module via a fiber combiner. An air objective of long-working distance (× 10, 0.25 NA) was used to generate a thin and elongated light sheet for in-focus excitation. **(C)** The holding chamber designed for lateral light sheet excitation. From left to right: side, top and iso view.

somatosensory cortex and hypothalamus were acutely prepared from C57BL/6 mice of both sexes at ages as indicated. Mice were deeply anesthetized by isoflurane (Axcience) evaporation in a closed plexiglass box. For mice less than 4 weeks old, the brain was taken out and placed in ice-cold artificial cerebrospinal fluid (aCSF, mM: 124 NaCl, 4.5 KCl, 1.2 NaH_2PO_4, 1 $MgCl_2$, 2 $CaCl_2$, 26 $NaHCO_3$, and 10 D-Glucose), and cut into 300-μm thick slices by a vibratome (Leica VT1200S). For mice older than 4 weeks, the brain was placed in a modified aCSF for slicing (in mM: 30 NaCl, 4.5 KCl, 1.2 NaH_2PO_4, 1 $MgCl_2$, 26 $NaHCO_3$, 10 D-Glucose, and 194 sucrose) (Jiang et al., 2016) maintained at 4 °C during sectioning. Brain slices were recovered in normal aCSF at 37 °C for about 1 h. Prior to imaging, one single slice was mounted on a block of liquid-state transparent agarose (2% low melting agarose, Thermo Scientific). When cooled, the sample-containing agarose block was glued on 10-mm glass coverslip and then together placed in the light sheet imaging chamber (Fig. 1A). Fluorescent beads (#1851011, Thermo Fisher Scientific) were diluted 10-fold in distilled water and dispersed directly into a drop of agarose. Imaging was carried out at room temperature (21–23 °C) under constant perfusion (~3 ml/min) with aCSF. Solutions were saturated with a mixture of 95% O_2 and 5% CO_2.

2.2. Ex vivo and in vivo labeling of astrocytes

For ex vivo labeling, astrocytes were vitally stained by the red fluorescent dye sulforhodamine 101 (SR101) (Sigma-Aldrich) (Appaix et al., 2012; Nimmerjahn et al., 2004). Brain slices were incubated in aCSF containing 5 μM SR101 for 1 h in the dark and continuously bubbled with a mixture of 95% O_2 and 5% CO_2. After labeling, the slices were thoroughly washed in dye-free aCSF for at least 15 min prior to imaging. A similar procedure was used to load the Ca^{2+}-sensitive dye Fluo2 AM (TEF Labs; 5 μM, 1 h) in astrocytes in slices of ~3–4 weeks old mice. Mice of similar age were used also for in vivo labeling of astrocytes, sulforhodamine B (10 mg/ml, Sigma) was intraperitoneally injected into awake mice at a dose of 10 μL/g (Appaix et al., 2012; Perez-Alvarez et al., 2013). The genetically encoded Ca^{2+} indicator GCaMP6 was expressed in astrocytes in vivo by crossing a Cre-dependent GCaMP6f mouse line (Ai95, The Jackson Laboratory) with an astrocyte-specific Glast-CreER^{T2} mouse line (Slezak et al., 2007). Tamoxifen (T5648, Sigma-Aldrich) or its active metabolite 4-Hydroxytamoxifen (4-OHT) (Sigma-Aldrich or Tocris) were first dissolved in ethanol and aliquoted at 1 mg/50 μL. Corn oil (Sigma-Aldrich) was then added to each aliquot to reconstitute at 1 mg/250 μL, which was then warmed at 37 °C for 15 min and sonicated for 15 min until the solution was clear. Aliquots were stored at −20 °C until use. For 4-OHT, one dose of 1 mg was intraperitoneally injected in GCaMP6f/-Glast-CreER^{T2} bigenic mice at ~3–4 weeks of age. When using tamoxifen, mice were injected once a day (1 mg) for two consecutive days. Imaging experiments were carried out about two weeks after the last injection.

2.3. Imaging setups and procedures

Light sheet imaging was performed using a custom-built setup based on a wide-field upright microscope (Zeiss Axioskop 50, Germany) equipped with water-immersion objectives (Fig. 1B). EPI illumination was provided by a monochromator light source (Polychrome II, TILL Photonics, Germany) directly coupled to the imaging objective via an optical fiber. We used three water immersion imaging objectives: × 10 NA0.3, × 20 NA0.5 and × 40 NA0.8 (ZEISS). The green fluorescence of Fluo2 and GCaMP6 was separated from the red fluorescence of SR101, by spectrally exclusive double-band filters (Di03-R488/561-t3 and FF01-523/610, Semrock). Fluorescence signal was collected using a digital electron-multiplying charge-coupled device (EMCCD Cascade 512B, Photometrics).

The in-focus light sheet was generated from an independent optical module (Alpha3 light sheet add-on, Phaseview, France) equipped with an air objective (Zeiss EC EPIPlan × 10, 0.25NA). This optical module was orthogonal to the upright imaging pathway and coupled via a wavelength combiner (Thorlabs) to two continuous wave lasers (473-nm and 561-nm, CNI) (Fig. 1A). The center thickness (ω) of the generated light sheet was in the order of ~1–2 μm (Power and Huisken, 2017):

$$\omega = \frac{2\lambda}{\pi NA} \quad (1)$$

where λ denotes laser wavelength, NA the numerical aperture of excitation objective and π the Archimede's constant. The center of light sheet was orthogonally aligned to the focus of the imaging objective, so as to achieve wide-field optical sectioning (Fig. 1B). A chamber for light sheet imaging (20 × 30 × 46 mm width, height and length) was custom-designed using 3D modeling software (Trimble SketchUP; Fig. 1C), and produced by a Mojo 3D printer (Stratasys). Two 22 × 22 mm glass coverslips (#1, Erie Science Company, USA) were glued (Dow Corning GmbH, Germany) to each side of the chamber, thereby enabling the lateral illumination. The chamber was mounted on a motorized PI stage (Physik Instrumente GmbH, Germany) for axial micro-manipulation. Laser excitation and image acquisition were controlled by MetaMorph (Molecular Devices).

Two-photon imaging was performed using a custom-built setup as reported previously (Bonnot et al., 2014). It was based on an upright microscope (BX51WI, Olympus) equipped with a × 40 NA0.8 water immersion objective (Olympus) and a tunable femtosecond Ti:sapphire pulsed laser (MaiTai HP; Spectra Physics, Ellicot City, MD, USA). For SR101 and GCaMP6 imaging, two-photon excitation was set at 850 nm and at 880 nm, respectively (Appaix et al., 2012; Mutze et al., 2012). Fluorescence emitted by SR101 and GCaMP6 was split by a dichroic mirror at 590 nm, filtered subsequently by either a 535/50 nm or a 615/45 nm bandpass filter, respectively and collected by two independent photomultipliers (PMT H9305-03, Hamamatsu). Image acquisition was performed using the Matlab routine ScanImage (Pologruto et al., 2003). When × 40 NA0.8 water immersion objective was used, the lateral pixel size of two-photon imaging was set to 0.34 μm, comparable to EPI/LSFM CCD imaging (0.4 μm). To obtain fluorescence profiles along the *z*-axis, the sample was moved vertically in a step size of 0.5 μm.

2.4. Fluorescent immunohistochemistry and genotyping

Bigenic mice expressing GCaMP6 in astrocytes were anesthetized by intraperitoneal injection of pentobarbital at lethal dose (200 μl, Euthasol Vet, Dechra), and then subjected to intracardiac perfusion of phosphate buffer solution (PBS) for blood removal followed by infusion of 4% paraformaldehyde (PFA, Sigma-Aldrich). Harvested brains were fixed in 4% PFA overnight, prior to being washed in PBS containing 30% sucrose and 0.09% NaN_3. Tissues were next embedded in optimal cutting temperature compound (VWR, Fontenay-sous-bois, France) and quickly frozen at −50 °C in isopentane. Thirty μm thick floating coronal slices were cut using a cryostat (Leica, Wetzlar, Germany), washed in PBS and then incubated for 1 h in a blocking solution (0.25% fish gelatin with 0.4% Triton X-100 in PBS). Primary antibodies were diluted in the same solution, and added to slices overnight at 4 °C (rabbit monoclonal anti-S100β, ab52642, Abcam, Cambridge, UK, diluted at 1/500; chicken polyclonal anti-GFP, Aves Labs, Davis, CA, USA, diluted at 1/1000). After being washed in PBS, brain slices were incubated at room temperature for 2 h with the secondary antibodies diluted in the blocking solution (Alexa fluor 488- and 594-conjugated antibodies, Thermofisher, Waltham, MA, USA), to detect rabbit monoclonal and chicken polyclonal primary antibodies, respectively. After thorough washing, brain slices were dried and mounted in Mowiol medium (Millipore, Darmstadt, Germany). Fluorescent images of dual-color immunostaining were obtained using a standard confocal microscope (Zeiss LSM 800, Germany).

Genotyping of the Cre-dependent GCaMP6f mouse line (Ai95, The Jackson Lab) used the standard primers and polymerase chain reaction protocols provided by the supplier. Genotyping of GLAST-CreER^{T2} mouse line was performed using the primers for Cre recombinase (TK139/141)

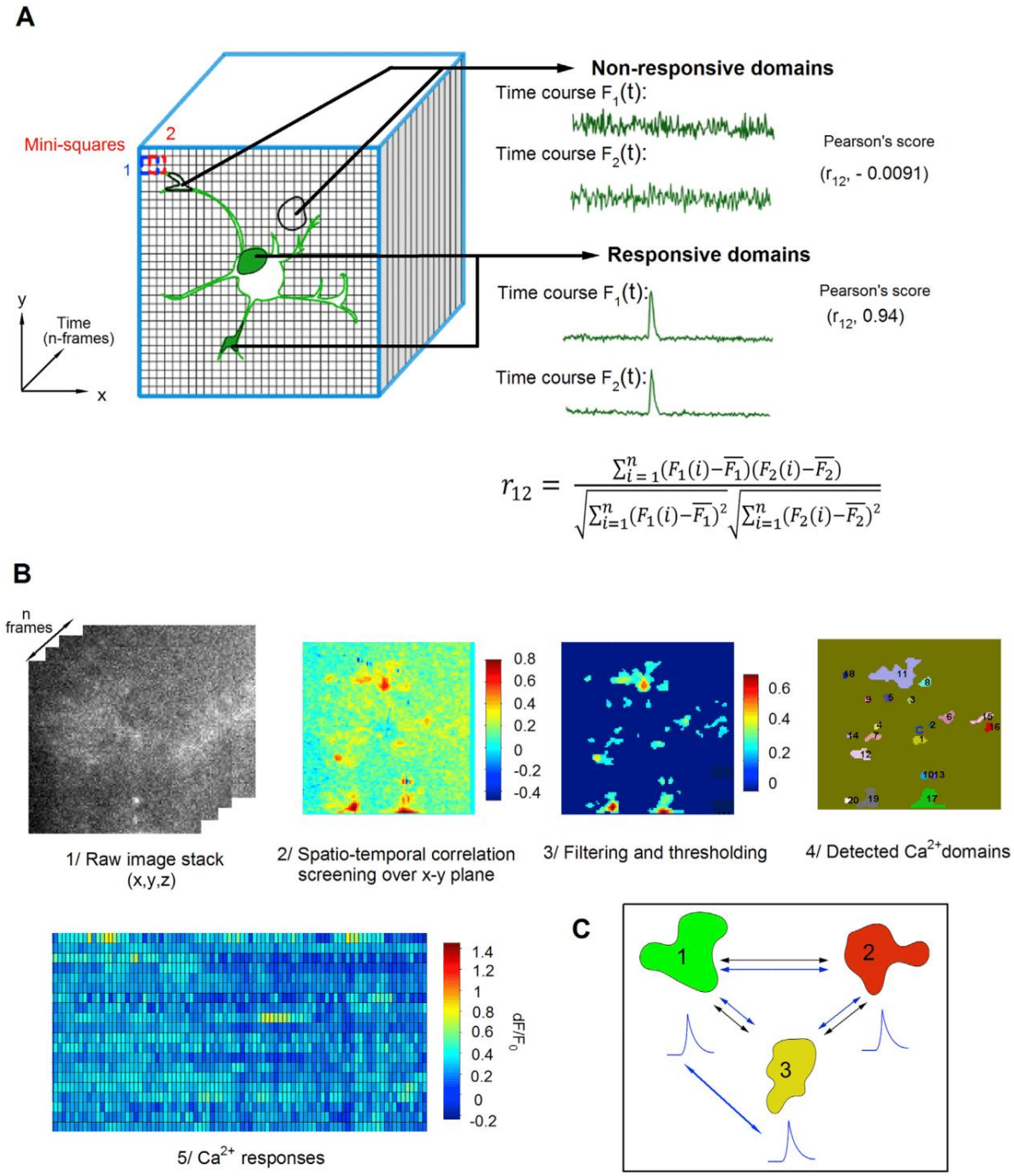

Fig. 2. Mapping astrocytic Ca^{2+} domains by screening locally correlated temporal signals. **(A)** Spatio-temporal correlation screening. Time-lapse image stack was obtained by acquiring consecutively the focal plane image of living nerve tissue. Time courses of contiguous pixels in Ca^{2+}-active domains (shaded in green) show higher correlation level than those of inactive domains and background regions. **(B)** Principal steps for C-Screen mapping. **(C)** Spatial and temporal parameters can be extracted following the identification of Ca^{2+}-active domains. For instance, the temporal correlation (r_{ij}) can be derived for Ca^{2+} signals between all paired combinations of active domains. Its distribution offers a global estimation on the synchronization degree of Ca^{2+} signals. In parallel, corresponding domain-domain distances (d_{ij}) can also be derived from their centroid coordinates.

as reported (Slezak et al., 2007).

2.5. Detection of Ca^{2+} domains by spatio-temporal correlation screening

Astrocyte Ca^{2+} signals acquired with current technology appear as local bursts or as wide-spread increases of fluorescence intensity over multiple pixels as previously observed (Otsu et al., 2015; Reeves et al., 2011; Shigetomi et al., 2010). Given that the time-dependent intensity changes of contiguous pixels within a defined Ca^{2+} domain are highly synchronized, we devised a computational method to screen for

temporally correlated Ca^{2+} signals so as to detect discrete Ca^{2+} domains. The Pearson's correlation coefficient r_{12} between time courses of half-overlapping mini-squares (2×2 pixel^2) was calculated in a running manner across the *x-y* image plane (Fig. 2A):

$$r_{12} = \frac{\sum_{i=1}^{n}(F_1(i) - \overline{F_1})(F_2(i) - \overline{F_2})}{\sqrt{\sum_{i=1}^{n}(F_1(i) - \overline{F_1})^2}\sqrt{\sum_{i=1}^{n}(F_2(i) - \overline{F_2})^2}} \quad (2)$$

where F_1 and F_2 representing the time courses derived from the two mini-squares and n representing the total number of image frames contained in a single movie. The time axis designates the third dimension in the movie (i.e., the time-lapse image stack). As expected, the r_{12} value between running mini-squares appeared higher in Ca^{2+}-active domains than areas showing no evident Ca^{2+} rises as dominated by background noises (exemplified in Fig. 2A). This approach enabled the detection of Ca^{2+} domains in time series images. Prior to analysis, we subtracted from the raw images the background signal as determined by the minimal intensity projection of the entire stack.

Computing temporal r_{12} correlation values of the overlapping mini-squares in a running manner across the *x-y* image plane (*z* as the time axis) gave rise to a 2D correlation map (Fig. 2B). This map was then segmented by an empirically determined correlation threshold (0.14–0.2) based on the match to the visual inspection of original movies. Subsequently, a low-pass median filter (3 - 5 pixel size) was applied to remove scattered solitary pixels. A signal threshold was further applied to determine Ca^{2+} domains, with their mean fluorescence time course comprising at least three consecutive data points exceeding three times standard deviation of the baseline. The baseline was searched by running a temporal segment (20 data points in length) across the full time course of single domains to find a period showing minimum mean intensity. The Ca^{2+} signal of single domains was then normalized as dF/F_0, with F_0 representing the mean baseline intensity (Fig. 2B). To quantify the signal strength, we calculated the temporal integral for normalized Ca^{2+} responses over a unitary time period (/minute). The detection of Ca^{2+}-active domains enables the further extraction of spatio-temporal information on astrocyte activity. This included the temporal correlations between Ca^{2+} signals across all combined detected domains (Fig. 2C), which indicates the degree of global signal synchronization. In addition, domain-domain distances could also be derived by their centroid coordinates (Fig. 2C). Since this method is based on correlation screening, we abbreviate it as C-Screen.

2.6. Fluorescent object analysis

The apparent size of fluorescent objects was derived from their center linescan profile obtained with ImageJ (NIH). The linescan profile was fitted with a Gaussian curve in Igor Pro (WaveMetrics), and the full width at half maximum (FWHM) served as size estimate. The minimal intensity of the image or the minimum projection of a temporal stack was used as background signal and subtracted from the raw images. Signal-to-background ratios (SBRs) of fluorescent objects were also derived from their linescan profile, calculated as the ratio of the peak against the basal level intensity.

2.7. Statistics

Experimental data are expressed as mean ± standard error unless otherwise mentioned. The *t*-test was performed for two-group comparisons, and significant difference was determined by *p* values less than 0.05. Mann-Whitney *U* test was also used to ascertain the significance level, in considering the deviation of the experimental data from the theoretical symmetrical distribution. In the present study, these two test methods yielded consistent results on statistic significance. Statistical tests were carried out in Matlab (The MathWorks). The significance levels are shown in figures by $^*p < 0.05$, $^{**}p < 0.01$, $^{***}p < 0.001$.

3. Results

3.1. Spatial performance of LSFM imaging

Prior to imaging astrocytes in brain tissue, we validated the performance of LSFM using micron-scale green fluorescent beads (core size, ~0.5 μm). Dispersed fluorescent puncta were observed in both LSFM and EPI images. Whereas EPI images appeared blurred due to out-of-focus fluorescence (Fig. 3A), LSFM images revealed single fluorescence beads at much higher contrast due to the optical sectioning (Fig. 3A). Linescan profiles confirmed the sharper fluorescence distribution obtained with LSFM (Fig. 3B). We next examined the fluorescence distribution of single beads along *z*-axis. An appreciable elongation along the *z*-axis was observed in EPI images, reflecting the low effective resolution along this axis (Li et al., 2004). This distortion was reduced by light sheet sectioning that revealed significantly shorter *z* profiles for single beads (Fig. 3C–D). To gain a comparative clue between our one-photon light sheet system and two-photon microscopy, we used both approaches to image the fluorescent beads. While two-photon microscope yielded the most contrasted image, the improvement provided by LSFM lied in the comparable range particularly along the *z*-axis (Fig. S1A-B). The out-of-focus fluorescence was further investigated using fluorescent beads (core size, ~4 μm) of similar size as astrocytic somata and their main branches (Shigetomi et al., 2013). In the *y-z* projection plane, the lateral (i.e., along *y*-axis) intensity was analyzed at both the focal and out-of-focus positions. Out-of-focus fluorescence at 10 μm above and below the focal plane was high in EPI images, but greatly reduced by LSFM (Fig. 3E). Hence, wide-field optical sectioning using LSFM ensures high spatial imaging performance.

3.2. Imaging astrocytes in acute brain tissues

Essential in regulating neural circuit function, astrocytes are widely distributed across brain regions (Giaume et al., 2010; Santello et al., 2019). They bear satellite branches and processes sitting in close contact to neuronal synapses and blood vessels, setting an architectural composition for neuroglial communication (Cauli and Hamel, 2018; Giaume et al., 2010). We then used LSFM to visualize astrocytes in acute mouse cortical slices after ex vivo labeling with astrocyte-specific fluorescent dye SR101 (Appaix et al., 2012; Nimmerjahn et al., 2004). Selective labeling was confirmed by colocalization with EGFP-positive astrocytes in the ALDH1L1-EGFP transgenic mouse line (Cahoy et al., 2008) (Fig. S2A). SR101-labeled astrocytes were well resolved by LSFM, whereas corresponding EPI images were blurred by out-of-focus signals (Fig. 4A and B). The signal-to-background ratio (SBR) was about three times higher with LSFM compared to EPI (Fig. 4C; $p < 0.01$). LSFM revealed SR101-labeled astrocytic branches (Fig. 4D), as observed also by two-photon microscopy in brain slices (Fig. S1C) and in vivo (Nimmerjahn et al., 2004), which however were barely visible in EPI images (Fig. 4D). The superior performance of LSFM was also evident when using a low-magnification objective to extend the field of view (Fig. 4E and F). To corroborate these observation, we also performed in vivo labeling of astrocytes through injection of the red fluorescent dye sulforhodamine B in awake mice, as reported previously (Appaix et al., 2012; Perez-Alvarez et al., 2013). The labeled astrocytes and their branches were also resolved by LSFM in the acute brain slice (Fig. S2B).

3.3. Light sheet imaging of astrocytic Ca^{2+} signal

We then used LSFM to image Ca^{2+} signals in astrocytes in acute mouse cortical slices. Chemical fluorescent Ca^{2+} indicators are convenient to use and allow sensitive optical detection of subcellular Ca^{2+} events (Lock et al., 2015). We used a green-fluorescent chemical indicator Fluo2 AM, a member of the membrane-permeable acetoxymethyl ester (AM) Ca^{2+} dyes that label astrocytes in slice preparations (Fiacco et al., 2007; Reeves et al., 2011). Indeed, Fluo2 labeling colocalized with

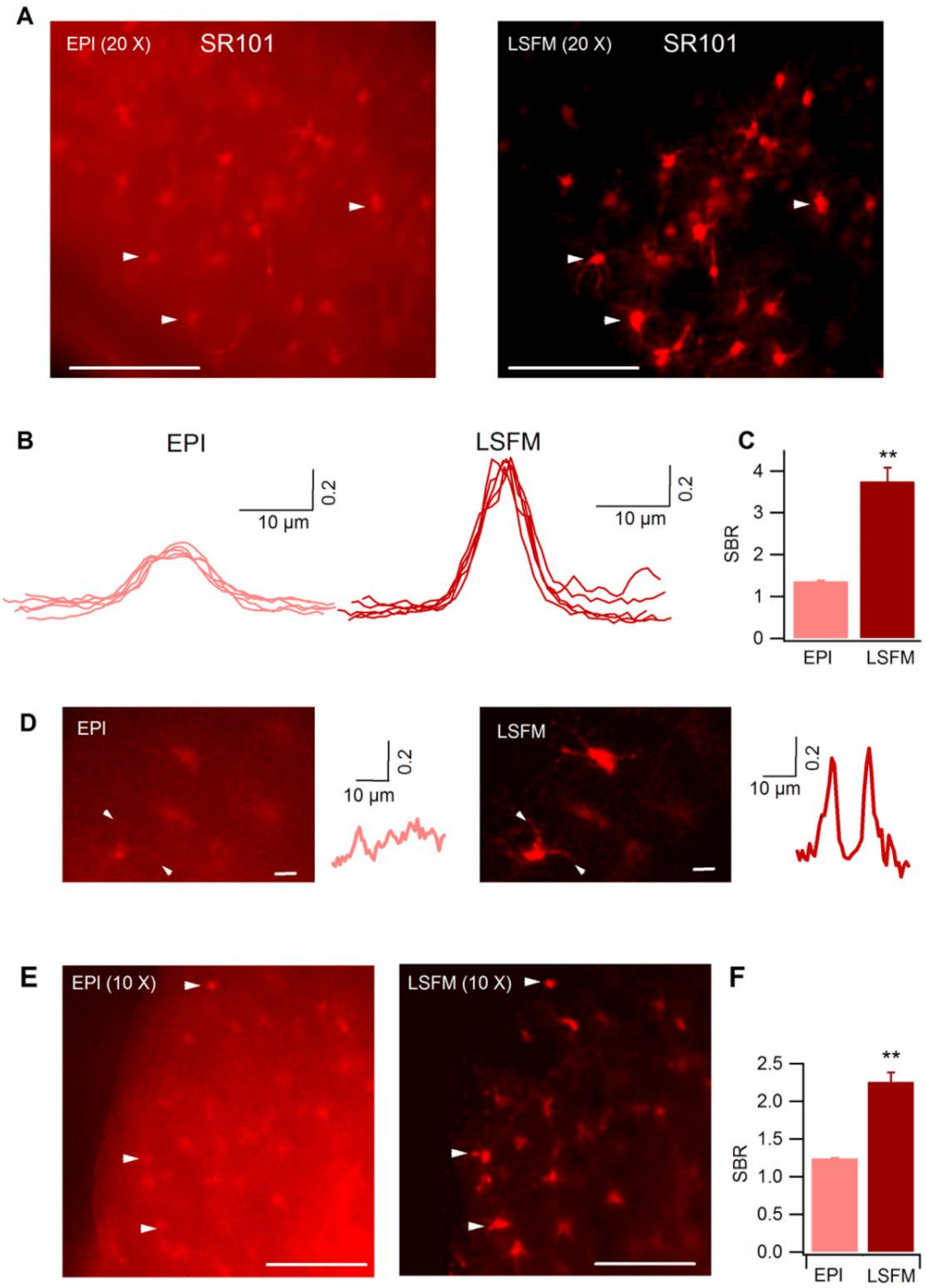

Fig. 4. Light sheet imaging of astrocytes in acute mouse brain slices. (A) SR101-stained astrocytes imaged by EPI and LSFM, respectively. A × 20 NA0.5 water immersion objective was used; arrow heads exemplify astrocytes visible in both conditions. **(B)** Linescan profiles of fluorescence distribution across the somata of single astrocytes (line position defined by the opposing arrowheads). **(C)** The signal to background ratio (SBR) quantified for single astrocytes ($p < 0.01$; $n = 20$ per condition). **(D)** Branches of SR101-stained astrocytes unveiled by LSFM, with linescan profiles shown aside. **(E-F)** Similar experiments carried out at lower-magnification (× 10 NA0.3; $n = 40$ per condition). Scale bars: 50 µm for *A*, 10 µm for *D*, and 100 µm for *E*.

SR101-positive astrocytes (Fig. S2C). In the absence of stimulus, the combination of LSFM and C-Screen revealed discrete active Ca^{2+} domains in astrocytes (Fig. 5A–B). LSFM-recorded Ca^{2+} signals displayed higher dynamic range and were twice as large on average relative to those detected by EPI imaging (Fig. 5C–D). The temporal correlations between Ca^{2+} signals of all active domains from light sheet imaging showed a broad distribution, suggesting a low-level of global synchronization ($r_{12} = 0.2 \pm 0.014$; Fig. 5E). Thanks to the wide-field configuration coupled with a digital camera, LSFM permitted astrocyte Ca^{2+} signals to be recorded at high acquisition rate (e.g., 20 Hz, Fig. 5F).

Complementary to chemical sensor, genetically encoded Ca^{2+} indicators enable calcium measurements in specific cell types (Akerboom

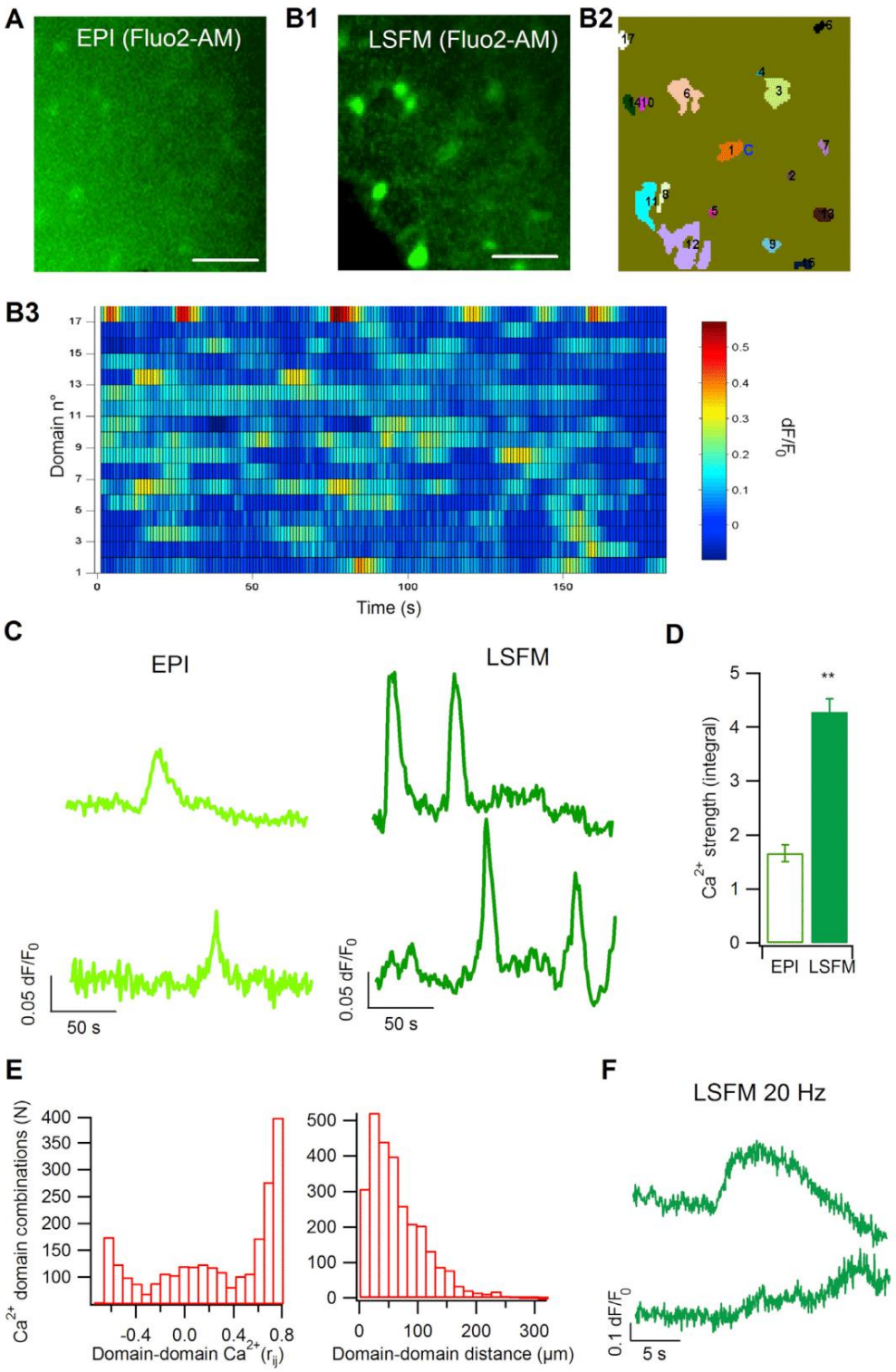

Fig. 5. Imaging astrocytic Ca^{2+} signals with chemical indicator. (A) Fluo2-labeled astrocytes viewed by EPI illumination in cortical slices. The same region was then imaged with LSFM **(B1)**. Ca^{2+}-active domains were detected by C-Screen analysis **(B2)**, with raster plot shown in **(B3)**. A × 10 NA0.3 water immersion objective was used. **(C)** Representative Ca^{2+} signals detected from EPI and LSFM time-lapse image stacks. **(D)** Comparison of Ca^{2+} signal strength quantified from temporal integral ($p < 0.01$; n = 188–299 responsive domains from 9 brain slices of 5 mice). **(E)** Distribution of temporal correlations between Ca^{2+} responses of all paired active domains (*left*), as an estimation of global synchronization. Right, histogram distribution of corresponding domain-domain distances (2775 paired domain combinations from 9 slices of 5 mice). **(F)** LSFM imaging of astrocytic Ca^{2+} signals at high acquisition rate (20 Hz). Representative movies from EPI and LSFM recordings are provided in the supplementary file. Scale bars: 50 µm.

et al., 2013) and are thought to influence less the intrinsic signals in targeted cells (Smith et al., 2018). We here used GCaMP6 that comprises circularly permuted GFP, the Ca^{2+}-sensitive protein calmodulin and the M13 fragment of the myosin light chain kinase (Baird et al., 1999; Nakai et al., 2001) (Chen et al., 2013). We expressed GCaMP6 selectively in astrocytes by crossing a Cre-dependent GCaMP6f mouse line (Madisen et al., 2015) with an inducible Glast-CreER^{T2} line where Cre recombinase is present in astrocytes (Slezak et al., 2007) (Fig. S3A). In bigenic GCaMP6/Glast-CreER^{T2} mice (Fig. S3B), tamoxifen induced apparent GCaMP6 expression in astrocyte-like cells (Fig. S3C). Dual-color fluorescent immunohistochemical statinging confirmed the colocalization of GCaMP6 with the astrocyte marker S100β (Fig. S3D).

Spontaneous Ca^{2+} dynamics in GCaMP6-expressing astrocytes were then imaged by LSFM. Compared to EPI illumination, light sheet excitation improved the dynamic range of Ca^{2+} signals and revealed more Ca^{2+}-active domains (Fig. 6A–C), echoing the observation with the chemical indicator. The global temporal correlation between Ca^{2+}-active domains was 0.16 ± 0.0073 (Fig. 6D), comparable to that derived from Fluo2 imaging (r_{12} = 0.2 ± 0.014), confirming that spontaneous Ca^{2+} signals are weakly correlated. Inhibition of neuronal activity with tetrodotoxin (TTX, 1 μM) failed to block the Ca^{2+} signals in astrocytes (Fig S4). For all combinations of Ca^{2+} domains, plotting domain-to-domain temporal Ca^{2+} correlations against their corresponding distances showed no dependence on distance (Fig. 6E). We also manually drew Ca^{2+} responsive domains by inspecting time-lapse images, which gave similar time courses as derived from C-Screen analysis (Fig S5). Finally, the wide-field optical sectioning of LSFM allowed to record GCaMP6 signal at high frame rates (e.g., 10 Hz, Fig. 6F), whereas the conventional two-photon setup reached only acquisition rate around 1 Hz using similar settings (pixel size 0.34 μm over a field of view ~170 × 170 μm) (Fig. S1D). High frequency LSFM imaging would help to observe Ca^{2+} events occurring at near-/sub-second levels, as exemplified in Fig. S6 (30 Hz) and reported previously (Di Castro et al., 2011; Gu et al., 2018; Panatier et al., 2011; Stobart et al., 2018). Together, these data show that LSFM enables high-sensitivity and high-speed imaging of astrocytic Ca^{2+} dynamics over a wide field of view.

3.4. Heterogeneous activity for cortical and hypothalamic astrocytes

Long considered as a homogeneous cellular population, astrocytes are being recognized to display heterogeneous properties across brain areas so as to coordinate the specific actions of local neural circuits (Chai et al., 2017; Covelo and Araque, 2018; Gourine et al., 2010). To gain insights into the functional heterogeneity of regionally defined astrocyte populations, we used LSFM to examine Ca^{2+} activities of astrocytes located in mouse somatosensory cortex and the paraventricular zone of hypothalamus, which are respectively engaged in the processing of sensory inputs and body metabolism signals (Clasadonte and Prevot, 2018; Giaume et al., 2009). Spontaneous Ca^{2+} signals were readily detected in GCaMP6-expressing astrocytes in acute brain slices (Fig. 7A), whereas signals in hypothalamic astrocytes showed more oscillatory changes than cortical astrocytes (Fig. 7B). Astrocytes respond to synaptically released neurontransmitters by GPCR signaling (Agulhon et al., 2008; Khakh and McCarthy, 2015). We then evoked astrocyte Ca^{2+} elevation by activating a Gq type GPCR, the α1 adrenergic receptor that is functionally expressed in astrocytes (Ding et al., 2013; Paukert et al., 2014). Application of α1 adrenergic receptor agonist phenylephrine (50 μM) to brain slices evoked distinct Ca^{2+} signals in cortical and hypothalamic astrocytes: the former responded with rises of few oscillations, whereas the latter showed more frequent transients during the evoked Ca^{2+} rise (Fig. 7C and E). Phenylephrine-evoked Ca^{2+} responses in astrocytes were inhibited by the α1 adrenergic receptor antagonist terazosin (Paukert et al., 2014) (Fig. S7), validating the involvement of this GPCR pathway. Ca^{2+} signals could be detected in both astrocytic somata and processes with LSFM (Fig. S8), as monitored by confocal and two-photon microscopy (Shigetomi et al., 2013; Srinivasan et al., 2015). While GCPR activation elevated astrocytic Ca^{2+} in both areas, hypothalamic astrocytes responded more strongly than cortical astrocytes (signal integral, 27.5 ± 2.3 vs. 21.5 ± 1.25 dF/F_0*s, $p < 0.01$; Fig. 7D). Furthermore, adrenergic GPCR activation increased the temporal correlation of Ca^{2+} signals for both cortical and hypothalamic astrocytes, indicating a higher degree of synchronization for evoked Ca^{2+} signals relative to spontaneous conditions (Fig. 7F). Together, these results show distinct Ca^{2+} kinetics between cortical and hypothalamic astrocytes.

4. Discussion

Here, we show that LSFM via wide-field optical sectioning allows for sensitive imaging of astrocyte Ca^{2+} signals in acute mouse brain slices. This approach revealed distinct Ca^{2+} signals between cortical and hypothalamic astrocytes, highlighting their activity heterogeneity. The light sheet configuration of two objectives separates the excitation and emission pathway, thereby facilitating the adjustment of the respective optical axes. For instance, imaging objectives of different magnifications and/or NA allow to select the field of view and the spatial resolution, while changing the excitation objective allows to tune the thickness and extent of the light sheet (Power and Huisken, 2017; Tian et al., 2019). Alternatively, LSFM can be also achieved by a single objective (Bouchard et al., 2015; Meddens et al., 2016), which facilitates imaging in conditions with limited spatial accessibility, but complicates the separate adjustment of the excitation and imaging pathway. Nevertheless, single-objective LSFM would facilitate in vivo recording to study astrocytes in a more native state (Zamanian et al., 2012). Since the light sheet plane can be digitally scanned (e.g., with a galvo mirror) along the z-axis (Bouchard et al., 2015; Power and Huisken, 2017; Tomer et al., 2015), LSFM will helpful for fast 3D imaging of astrocyte Ca^{2+} signals thus supporting on-going efforts to understand their physiological functions (Bindocci et al., 2017).

The continuous wave lasers used in the present study achieved penetration up to ~200 μm from the slice surface along the excitation direction. Nevertheless, the light sheet convergence within living mammalian tissues is inevitably affected by light scattering (Jacques, 2013). The use of pulsed infrared two-photon lasers and tunable acoustic gradient devices have increased tissue penetration of light sheet excitation (Wolf et al., 2015; Zong et al., 2015), at the expense of setup complexity and costs. LSFM can be coupled to different types of digital cameras to allow fast acquisition over a wide field of view (Keller and Dodt, 2012; Ritter et al., 2010). Moreover, the recent development of bright and ultrafast Ca^{2+} indicator (Dana et al., 2019) will help to reduce the exposure time for single images thus allow for higher acquisition rates. In this regard, light sheet imaging will help to follow over a wide field of view the fast Ca^{2+} events in astrocytes (Di Castro et al., 2011; Gu et al., 2018; Panatier et al., 2011; Stobart et al., 2018). On the other hand, the reliance on point-to-point scanning of conventional two-photon microscopy limits its use for fast image acquisition and may introduce artifacts in reconstituted images due to the desynchronized pixel sampling. Two-photon microscopes integrating newly designed scanning systems have improved the acquisition rate (Bindocci et al., 2017; Zong et al., 2017), though the additional components exacerbate the setup burden. Nevertheless, the digital scanning mode of two-photon microscope allows to zoom in regions of interest such as neuronal dendrites or single astrocytic processes for high speed acquisition, which is not provided by our LSFM approach. Considering the respective advantages of light sheet and two-photon excitation, the current study extends the method of choice for brain astrocyte activity imaging in specific experimental conditions.

Parallel to improving the quality of dynamic imaging, unbiased computational detection of Ca^{2+} domains in astrocyte networks is required. Maximal intensity projection of time-lapse images has been used as a rapid way to search astrocytic Ca^{2+} signals, where Ca^{2+} active domains in principle would imprint higher intensity in the projection image relative to inactive regions. Due to the uneven intracellular

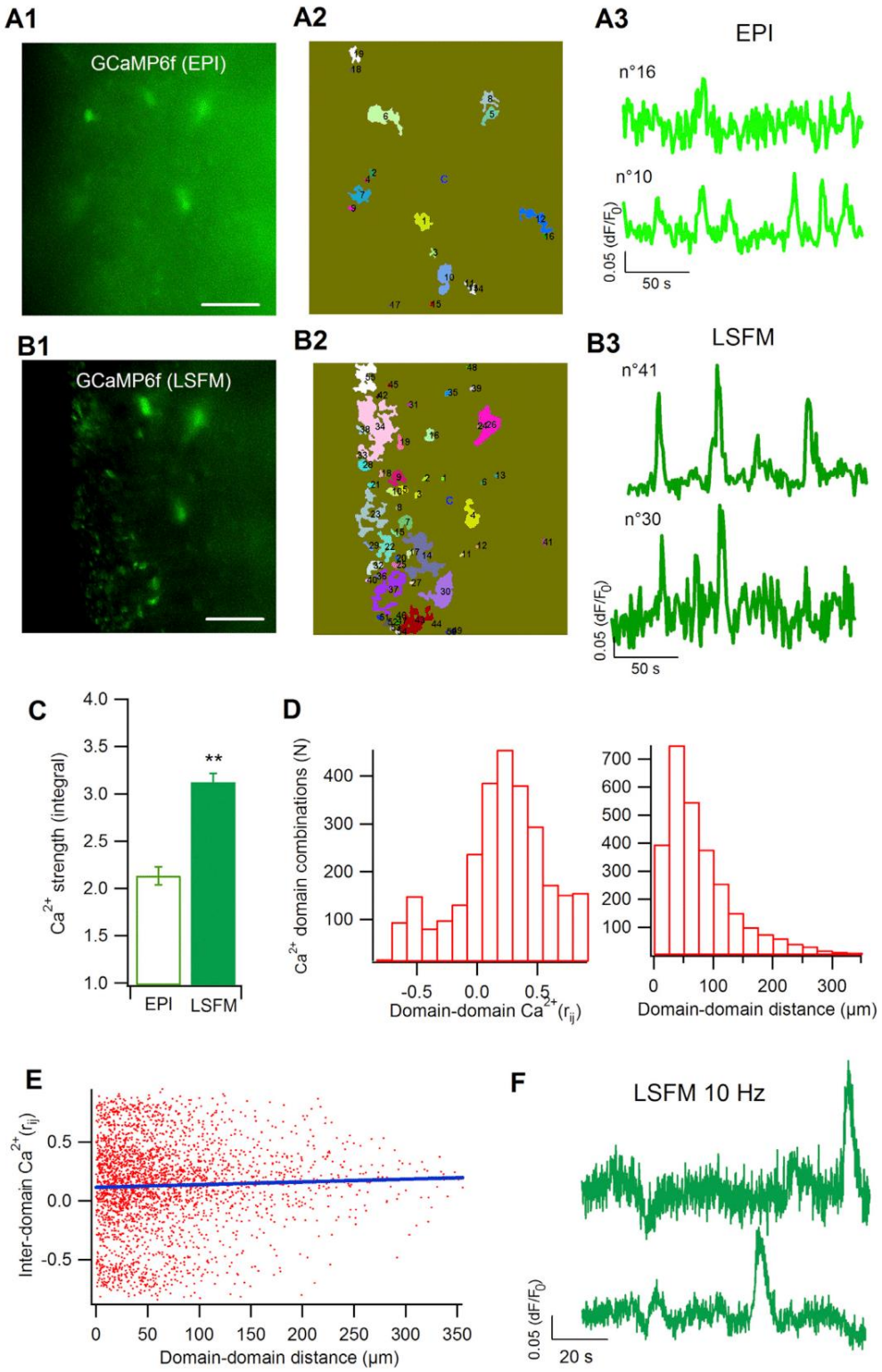

Fig. 6. Imaging astrocytic Ca^{2+} with genetically encoded sensor. Time-lapse imaging of GCaMP6-expressing astrocytes in acute cortical slices without (**A1-A3**, EPI) and with optical sectioning (**B1-B3,** LSFM). **(C)** Ca^{2+} signal strength compared for both conditions ($p < 0.01$; 220 - 359 active regions from 11 slices of 6–9 mice). **(D)** Histogram of temporal correlations for Ca^{2+} responses of paired domains (*left*), and their corresponding distances. Data were derived from 3156 pairs of Ca^{2+} domains from 11 slices of 9 mice. **(E)** Scatter plot depicting domain-domain Ca^{2+} correlations (i.e., synchronization level) against their distances. **(F)** Representative Ca^{2+} signals recorded at high frequency by LSFM (× 20 NA0.5 water immersion objective; 10 Hz). Representative movies for EPI and LSFM recordings are provided in the supplementary file. Scale bars: 50 µm.

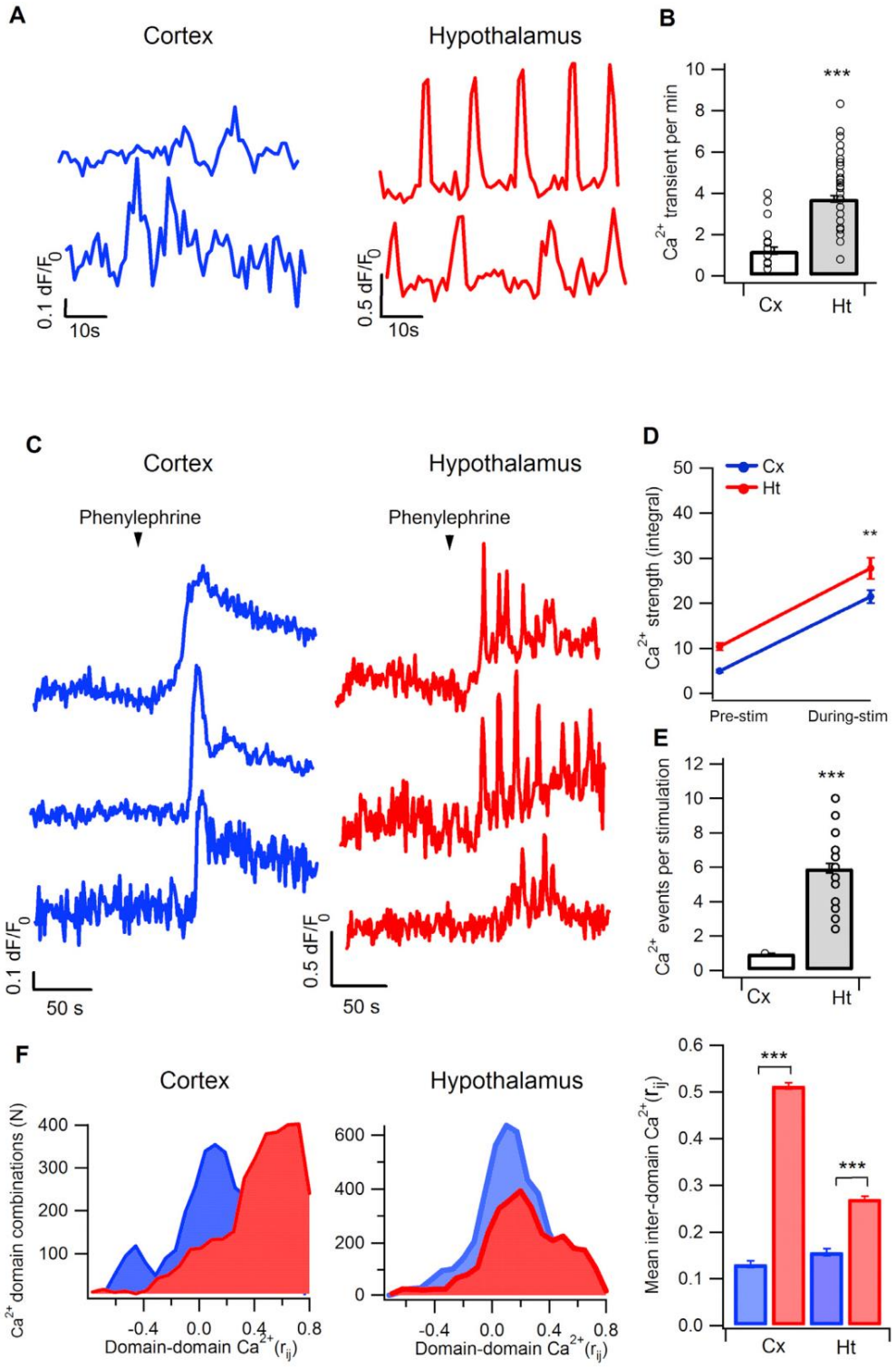

Fig. 7. Distinct features in Ca^{2+} signals in cortical and hypothalamic astrocytes. (A) Light-sheet imaging of spontaneous Ca^{2+} signals in astrocytes of mouse cortex and hypothalamus. GCaMP6 was expressed in astrocytes and the representative traces were from single Ca^{2+} domains. **(B)** Comparison of frequency of spontaneous Ca^{2+} oscillations for cortical (Cx) and hypothalamic (Ht) astrocytes (n = 57–67 cells from 15 slices of 11 mice per condition, $p < 0.001$). **(C)** Activation of adrenergic α1 receptors by phenylephrine (50 μM, bath perfusion for 60 s) evoked robust yet distinct Ca^{2+} elevations in astrocytes in cortex and hypothalamus. Representative traces were from different Ca^{2+} domains. **(D)** Signal strength of astrocytic Ca^{2+} signals pre- and during-stimulation as estimated by the temporal integral of normalized Ca^{2+} time courses (n = 314–345 active domains from 7-11 slices of 6 mice per condition). **(E)** Comparison of Ca^{2+} transients during phenylephrine stimulation (n = 44–72 cells from 11 slices of 8 mice, $p < 0.001$). **(F)** Phenylephrine stimulation enhanced the synchronization of astrocytic Ca^{2+} signals. Distributions of temporal correlations of Ca^{2+} signals from all active domains are shown in the histograms, blue denoting the data from spontaneous Ca^{2+} signals and red from phenylephrine-evoked signals (n = 3156–4415 pairs of Ca^{2+} domains from 7 - 15 slices of 6–9 mice per condition). Cx, cortex; Ht, hypothalamus; Pe, phenylephrine.

distribution of Ca^{2+} indicator, certain constantly bright areas showing no Ca^{2+} rises could also be registered that may mask the Ca^{2+}-active regions of lower intensity. We introduced here the principle of spatio-temporal correlation screening to detect locally correlated temporal signals. Clustered pixels showing synchronizing time courses were defined as responsive domains. Fluorescently visible structures that in fact showed no dynamic changes were excluded, while initially dim pixels that displayed later on fluorescence augmentation (i.e., Ca^{2+} rise) were picked up. Pearson's correlation coefficient relies mainly on the similarity of signal trends, while being relatively independent of the absolute intensity (Oheim and Li, 2007). Thus, screening of locally correlated signals helps to identify Ca^{2+} rises and improves their signal-to-noise ratio (Savtchouk et al., 2018; Wang et al., 2017). Ca^{2+} domains surrounding adjacent astrocytic structures may be merged together, which is due to the diffraction-limited fluorescence detection and the diffusion of Ca^{2+} bursts to nearby domains. A further step will be to incorporate temporal segmentation to isolate functional domains displaying activities at different time points. The computational time for C-Screen is in the order of tens of seconds and thus slower than the very rapid maximal intensity projection. Since imaging condition and quantification requirements vary in different contexts, a combination or an evaluation per se of different computational methods will help to improve the detection of astrocytic Ca^{2+} signals (Agarwal et al., 2017; Srinivasan et al., 2015) (Wang et al., 2019).

Astrocytes display Ca^{2+} activities spontaneously and in response to GPCR activation, as observed in brain slices (Di Castro et al., 2011; Shigetomi et al., 2018) and in vivo (Agarwal et al., 2017; Bindocci et al., 2017; Hirase et al., 2004; Paukert et al., 2014). Light sheet imaging unveiled distinct features in Ca^{2+} activities between cortical and hypothalamic astrocytes, thus reinforcing the evidence for heterogeneous astrocyte subpopulations that show different molecular, morphological and functional properties (Ben Haim and Rowitch, 2017; Chai et al., 2017; Lanjakornsiripan et al., 2018; Martin-Fernandez et al., 2017). Astrocyte heterogeneity appears necessary to coordinate the action of local neural circuits that are adapted to specific physiological inputs and outputs. Considering that astrocyte spontaneous Ca^{2+} activity is modulated by Ca^{2+}-permeable channels (Shigetomi et al., 2011) and the internal stores (Wang et al., 2006), the different spontaneous Ca^{2+} kinetics observed between cortical and hypothalamic astrocytes likely reflect the distinct recruitment of Ca^{2+} handling pathways. Accordingly, we observed that astrocytes of both regions differ also in their response to α1 adrenergic receptor activation in terms of kinetics and signal strength. Astrocyte Ca^{2+} kinetics is shaped by the intercellular communication of astrocyte populations (Gu et al., 2018), as well as the Ca^{2+} level in internal stores and their Ca^{2+} buffering capacity (Bazargani and Attwell, 2015; Li et al., 2012). Moreover, the distinct organization of local neuronal circuits may shape the astrocytic Ca^{2+} responses (Chai et al., 2017). To fully resolve the mechanisms underlying the heterogeneities in astrocyte Ca^{2+} signals will require further investigations. In view of the on-going challenge on understanding the function of astrocyte Ca^{2+} signaling in neurophysiology (Bazargani and Attwell, 2015; Fiacco and McCarthy, 2018; Savtchouk and Volterra, 2018), quantitative light sheet imaging represents a complementary strategy for mechanistic investigations. Moreover, beyond Ca^{2+} signals, this methodology will also helps to measure other dynamics signals by adopting pathway-specific fluorescent sensors.

Declaration of competing interest

The authors declare no competing interests.

CRediT authorship contribution statement

Cuong Pham: Methodology, Investigation, Formal analysis, Writing - original draft, Visualization, Writing - review & editing. **Daniela Herrera Moro:** Methodology, Validation, Resources, Writing - review & editing. **Christine Mouffle:** Resources. **Steve Didienne:** Resources. **Régine Hepp:** Methodology, Resources, Writing - review & editing. **Frank W. Pfrieger:** Resources, Writing - review & editing. **Jean-Marie Mangin:** Methodology, Resources. **Pascal Legendre:** Formal analysis, Resources, Writing - review & editing. **Claire Martin:** Resources, Writing - review & editing. **Serge Luquet:** Project administration, Resources, Writing - review & editing. **Bruno Cauli:** Project administration, Resources, Writing - review & editing. **Dongdong Li:** Conceptualization, Methodology, Investigation, Writing - original draft, Writing - review & editing, Supervision.

Acknowledgments

We thank the animal facility and imaging platform of the IBPS (Sorbonne Université, Paris, France). We also thank Gael Launay and Cyprian Wozniak for helping to set up the light sheet microscope, Anne-Cecile Boulay for ALDH1L1-EGFP mice and Ludovic Tricoire for help on two-photon setup, and Martin Oheim and Nicole Ropert for early discussions on the data analysis procedures. This work was supported by the Agence Nationale de la Recherche (ANR-15-CE14-0030; ANR-17-CE37-0010-03), National Natural Science Foundation of China (N° 31628005; N° 31929003), and Fondation pour la Recherche Médicale.

Appendix A. Supplementary data

Supplementary data to this article can be found online at https://doi.org/10.1016/j.neuroimage.2020.117069.

References

Agarwal, A., Wu, P.H., Hughes, E.G., Fukaya, M., Tischfield, M.A., Langseth, A.J., Wirtz, D., Bergles, D.E., 2017. Transient opening of the mitochondrial permeability transition pore induces microdomain calcium transients in astrocyte processes. Neuron 93, 587–605 e587.

Agulhon, C., Petravicz, J., McMullen, A.B., Sweger, E.J., Minton, S.K., Taves, S.R., Casper, K.B., Fiacco, T.A., McCarthy, K.D., 2008. What is the role of astrocyte calcium in neurophysiology? Neuron 59, 932–946.

Ahrens, M.B., Orger, M.B., Robson, D.N., Li, J.M., Keller, P.J., 2013. Whole-brain functional imaging at cellular resolution using light-sheet microscopy. Nat. Methods 10, 413–420.

Akerboom, J., Carreras Calderon, N., Tian, L., Wabnig, S., Prigge, M., Tolo, J., Gordus, A., Orger, M.B., Severi, K.E., Macklin, J.J., Patel, R., Pulver, S.R., Wardill, T.J., Fischer, E., Schuler, C., Chen, T.W., Sarkisyan, K.S., Marvin, J.S., Bargmann, C.I., Kim, D.S., Kugler, S., Lagnado, L., Hegemann, P., Gottschalk, A., Schreiter, E.R., Looger, L.L., 2013. Genetically encoded calcium indicators for multi-color neural activity imaging and combination with optogenetics. Front. Mol. Neurosci. 6, 2.

Appaix, F., Girod, S., Boisseau, S., Romer, J., Vial, J.C., Albrieux, M., Maurin, M., Depaulis, A., Guillemain, I., van der Sanden, B., 2012. Specific in vivo staining of astrocytes in the whole brain after intravenous injection of sulforhodamine dyes. PloS One 7, e35169.

Baird, G.S., Zacharias, D.A., Tsien, R.Y., 1999. Circular permutation and receptor insertion within green fluorescent proteins. Proc. Natl. Acad. Sci. U. S. A. 96, 11241–11246.

Bazargani, N., Attwell, D., 2015. Astrocyte calcium signaling: the third wave. Nat. Neurosci. 19, 182–189.

Ben Haim, L., Rowitch, D.H., 2017. Functional diversity of astrocytes in neural circuit regulation. Nat. Rev. Neurosci. 18, 31–41.

Bindocci, E., Savtchouk, I., Liaudet, N., Becker, D., Carriero, G., Volterra, A., 2017. Three-dimensional Ca(2+) imaging advances understanding of astrocyte biology. Science 356.

Bonnot, A., Guiot, E., Hepp, R., Cavellini, L., Tricoire, L., Lambolez, B., 2014. Single-fluorophore biosensors based on conformation-sensitive GFP variants. Faseb. J. 28, 1375–1385.

Bouchard, M.B., Voleti, V., Mendes, C.S., Lacefield, C., Grueber, W.B., Mann, R.S., Bruno, R.M., Hillman, E.M., 2015. Swept confocally-aligned planar excitation (SCAPE) microscopy for high speed volumetric imaging of behaving organisms. Nat. Photon. 9, 113–119.

Cahoy, J.D., Emery, B., Kaushal, A., Foo, L.C., Zamanian, J.L., Christopherson, K.S., Xing, Y., Lubischer, J.L., Krieg, P.A., Krupenko, S.A., Thompson, W.J., Barres, B.A., 2008. A transcriptome database for astrocytes, neurons, and oligodendrocytes: a new resource for understanding brain development and function. J. Neurosci. 28, 264–278.

Cauli, B., Hamel, E., 2018. Brain perfusion and astrocytes. Trends Neurosci. 41, 409–413.

Chai, H., Diaz-Castro, B., Shigetomi, E., Monte, E., Octeau, J.C., Yu, X., Cohn, W., Rajendran, P.S., Vondriska, T.M., Whitelegge, J.P., Coppola, G., Khakh, B.S., 2017. Neural circuit-specialized astrocytes: transcriptomic, proteomic, morphological, and functional evidence. Neuron 95, 531–549 e539.

Chen, T.W., Wardill, T.J., Sun, Y., Pulver, S.R., Renninger, S.L., Baohan, A., Schreiter, E.R., Kerr, R.A., Orger, M.B., Jayaraman, V., Looger, L.L., Svoboda, K., Kim, D.S., 2013. Ultrasensitive fluorescent proteins for imaging neuronal activity. Nature 499, 295–300.
Clasadonte, J., Prevot, V., 2018. The special relationship: glia-neuron interactions in the neuroendocrine hypothalamus. Nat. Rev. Endocrinol. 14, 25–44.
Covelo, A., Araque, A., 2018. Neuronal activity determines distinct gliotransmitter release from a single astrocyte. Elife 7, e32237.
Dallerac, G., Zapata, J., Rouach, N., 2018. Versatile control of synaptic circuits by astrocytes: where, when and how? Nat. Rev. Neurosci. 19, 729–743.
Dana, H., Sun, Y., Mohar, B., Hulse, B.K., Kerlin, A.M., Hasseman, J.P., Tsegaye, G., Tsang, A., Wong, A., Patel, R., Macklin, J.J., Chen, Y., Konnerth, A., Jayaraman, V., Looger, L.L., Schreiter, E.R., Svoboda, K., Kim, D.S., 2019. High-performance calcium sensors for imaging activity in neuronal populations and microcompartments. Nat. Methods 16, 649–657.
Deo, C., Lavis, L.D., 2018. Synthetic and genetically encoded fluorescent neural activity indicators. Curr. Opin. Neurobiol. 50, 101–108.
Di Castro, M.A., Chuquet, J., Liaudet, N., Bhaukaurally, K., Santello, M., Bouvier, D., Tiret, P., Volterra, A., 2011. Local Ca2+ detection and modulation of synaptic release by astrocytes. Nat. Neurosci. 14, 1276–1284.
Ding, F., O'Donnell, J., Thrane, A.S., Zeppenfeld, D., Kang, H., Xie, L., Wang, F., Nedergaard, M., 2013. alpha1-Adrenergic receptors mediate coordinated Ca2+ signaling of cortical astrocytes in awake, behaving mice. Cell Calcium 54, 387–394.
Fiacco, T.A., Agulhon, C., Taves, S.R., Petravicz, J., Casper, K.B., Dong, X., Chen, J., McCarthy, K.D., 2007. Selective stimulation of astrocyte calcium in situ does not affect neuronal excitatory synaptic activity. Neuron 54, 611–626.
Fiacco, T.A., McCarthy, K.D., 2018. Multiple lines of evidence indicate that gliotransmission does not occur under physiological conditions. J. Neurosci. 38, 3–13.
Giaume, C., Koulakoff, A., Roux, L., Holcman, D., Rouach, N., 2010. Astroglial networks: a step further in neuroglial and gliovascular interactions. Nat. Rev. Neurosci. 11, 87–99.
Giaume, C., Maravall, M., Welker, E., Bonvento, G., 2009. The barrel cortex as a model to study dynamic neuroglial interaction. Neuroscientist 15, 351–366.
Gourine, A.V., Kasymov, V., Marina, N., Tang, F., Figueiredo, M.F., Lane, S., Teschemacher, A.G., Spyer, K.M., Deisseroth, K., Kasparov, S., 2010. Astrocytes control breathing through pH-dependent release of ATP. Science 329, 571–575.
Gu, X., Chen, W., Volkow, N.D., Koretsky, A.P., Du, C., Pan, Y., 2018. Synchronized astrocytic Ca^{2+} responses in neurovascular coupling during somatosensory stimulation and for the resting state. Cell Rep. 23, 3878–3890.
Hirase, H., Qian, L., Bartho, P., Buzsaki, G., 2004. Calcium dynamics of cortical astrocytic networks in vivo. PLoS Biol. 2, E96.
Jacques, S.L., 2013. Optical properties of biological tissues: a review. Phys. Med. Biol. 58, R37–R61.
Jemielita, M., Taormina, M.J., Delaurier, A., Kimmel, C.B., Parthasarathy, R., 2013. Comparing phototoxicity during the development of a zebrafish craniofacial bone using confocal and light sheet fluorescence microscopy techniques. J. Biophot. 6, 920–928.
Jiang, R., Diaz-Castro, B., Looger, L.L., Khakh, B.S., 2016. Dysfunctional calcium and glutamate signaling in striatal astrocytes from huntington's disease model mice. J. Neurosci. 36, 3453–3470.
Keller, P.J., Ahrens, M.B., 2015. Visualizing whole-brain activity and development at the single-cell level using light-sheet microscopy. Neuron 85, 462–483.
Keller, P.J., Dodt, H.U., 2012. Light sheet microscopy of living or cleared specimens. Curr. Opin. Neurobiol. 22, 138–143.
Khakh, B.S., McCarthy, K.D., 2015. Astrocyte calcium signaling: from observations to functions and the challenges therein. Cold Spring Harbor Perspect. Biol. 7, a020404.
Kuga, N., Sasaki, T., Takahara, Y., Matsuki, N., Ikegaya, Y., 2011. Large-scale calcium waves traveling through astrocytic networks in vivo. J. Neurosci. 31, 2607–2614.
Lanjakornsiripan, D., Pior, B.J., Kawaguchi, D., Furutachi, S., Tahara, T., Katsuyama, Y., Suzuki, Y., Fukazawa, Y., Gotoh, Y., 2018. Layer-specific morphological and molecular differences in neocortical astrocytes and their dependence on neuronal layers. Nat. Commun. 9, 1623.
Li, D., Herault, K., Isacoff, E.Y., Oheim, M., Ropert, N., 2012. Optogenetic activation of LiGluR-expressing astrocytes evokes anion channel-mediated glutamate release. J. Physiol. 590, 855–873.
Li, D., Xiong, J., Qu, A., Xu, T., 2004. Three-Dimensional tracking of single secretory granules in live PC12 cells. Biophys. J. 87, 1991–2001.
Lin, M.Z., Schnitzer, M.J., 2016. Genetically encoded indicators of neuronal activity. Nat. Neurosci. 19, 1142–1153.
Lobas, M.A., Tao, R., Nagai, J., Kronschlager, M.T., Borden, P.M., Marvin, J.S., Looger, L.L., Khakh, B.S., 2019. A genetically encoded single-wavelength sensor for imaging cytosolic and cell surface ATP. Nat. Commun. 10, 711.
Lock, J.T., Parker, I., Smith, I.F., 2015. A comparison of fluorescent Ca(2)(+) indicators for imaging local Ca(2)(+) signals in cultured cells. Cell Calcium 58, 638–648.
Madisen, L., Garner, A.R., Shimaoka, D., Chuong, A.S., Klapoetke, N.C., Li, L., van der Bourg, A., Niino, Y., Egolf, L., Monetti, C., Gu, H., Mills, M., Cheng, A., Tasic, B., Nguyen, T.N., Sunkin, S.M., Benucci, A., Nagy, A., Miyawaki, A., Helmchen, F., Empson, R.M., Knopfel, T., Boyden, E.S., Reid, R.C., Carandini, M., Zeng, H., 2015. Transgenic mice for intersectional targeting of neural sensors and effectors with high specificity and performance. Neuron 85, 942–958.
Martin-Fernandez, M., Jamison, S., Robin, L.M., Zhao, Z., Martin, E.D., Aguilar, J., Benneyworth, M.A., Marsicano, G., Araque, A., 2017. Synapse-specific astrocyte gating of amygdala-related behavior. Nat. Neurosci. 20, 1540–1548.
Meddens, M.B., Liu, S., Finnegan, P.S., Edwards, T.L., James, C.D., Lidke, K.A., 2016. Single objective light-sheet microscopy for high-speed whole-cell 3D super-resolution. Biomed. Optic Express 7, 2219–2236.
Mutze, J., Iyer, V., Macklin, J.J., Colonell, J., Karsh, B., Petrasek, Z., Schwille, P., Looger, L.L., Lavis, L.D., Harris, T.D., 2012. Excitation spectra and brightness optimization of two-photon excited probes. Biophys. J. 102, 934–944.
Nakai, J., Ohkura, M., Imoto, K., 2001. A high signal-to-noise Ca2+ probe composed of a single green fluorescent protein. Nat. Biotechnol. 19, 137–141.
Nedergaard, M., Verkhratsky, A., 2012. Artifact versus reality-How astrocytes contribute to synaptic events? Glia 60, 1013–1023.
Nimmerjahn, A., Kirchhoff, F., Kerr, J.N., Helmchen, F., 2004. Sulforhodamine 101 as a specific marker of astroglia in the neocortex in vivo. Nat. Methods 1, 31–37.
Oheim, M., Li, D., 2007. Quantitative colocalisation imaging: concepts, measurements, and pitfalls. In: Shorte, S.L., Frischknecht, F. (Eds.), Imaging Cellular and Molecular Biological Functions. Springer, pp. 117–156.
Otsu, Y., Couchman, K., Lyons, D.G., Collot, M., Agarwal, A., Mallet, J.M., Pfrieger, F.W., Bergles, D.E., Charpak, S., 2015. Calcium dynamics in astrocyte processes during neurovascular coupling. Nat. Neurosci. 18, 210–218.
Panatier, A., Vallee, J., Haber, M., Murai, K.K., Lacaille, J.C., Robitaille, R., 2011. Astrocytes are endogenous regulators of Basal transmission at central synapses. Cell 146, 785–798.
Paukert, M., Agarwal, A., Cha, J., Doze, V.A., Kang, J.U., Bergles, D.E., 2014. Norepinephrine controls astroglial responsiveness to local circuit activity. Neuron 82, 1263–1270.
Perez-Alvarez, A., Araque, A., Martin, E.D., 2013. Confocal microscopy for astrocyte in vivo imaging: recycle and reuse in microscopy. Front. Cell. Neurosci. 7, 51.
Perez-Alvarez, A., Navarrete, M., Covelo, A., Martin, E.D., Araque, A., 2014. Structural and functional plasticity of astrocyte processes and dendritic spine interactions. J. Neurosci. 34, 12738–12744.
Pologruto, T.A., Sabatini, B.L., Svoboda, K., 2003. ScanImage: flexible software for operating laser scanning microscopes. Biomed. Eng. Online 2, 13.
Power, R.M., Huisken, J., 2017. A guide to light-sheet fluorescence microscopy for multiscale imaging. Nat. Methods 14, 360–373.
Reeves, A.M., Shigetomi, E., Khakh, B.S., 2011. Bulk loading of calcium indicator dyes to study astrocyte physiology: key limitations and improvements using morphological maps. J. Neurosci. 31, 9353–9358.
Ritter, J.G., Veith, R., Veenendaal, A., Siebrasse, J.P., Kubitscheck, U., 2010. Light sheet microscopy for single molecule tracking in living tissue. PloS One 5, e11639.
Robin, L.M., Oliveira da Cruz, J.F., Langlais, V.C., Martin-Fernandez, M., Metna-Laurent, M., Busquets-Garcia, A., Bellocchio, L., Soria-Gomez, E., Papouin, T., Varilh, M., Sherwood, M.W., Belluomo, I., Balcells, G., Matias, I., Bosier, B., Drago, F., Van Eeckhaut, A., Smolders, I., Georges, F., Araque, A., Panatier, A., Oliet, S.H.R., Marsicano, G., 2018. Astroglial CB1 receptors determine synaptic D-serine availability to enable recognition memory. Neuron 98, 935–944.
Santello, M., Toni, N., Volterra, A., 2019. Astrocyte function from information processing to cognition and cognitive impairment. Nat. Neurosci. 22, 154–166.
Savtchouk, I., Carriero, G., Volterra, A., 2018. Studying axon-astrocyte functional interactions by 3D two-photon Ca(2+) imaging: a practical guide to experiments and "big data" analysis. Front. Cell. Neurosci. 12, 98.
Savtchouk, I., Volterra, A., 2018. Gliotransmission: beyond black-and-white. J. Neurosci. 38, 14–25.
Schmidt, E.M., Oheim, M., 2018. Two-photon Imaging Induces Brain Heating and Calcium Microdomain Hyper-Activity in Cortical Astrocytes bioRxiv 321091.
Shigetomi, E., Bushong, E.A., Haustein, M.D., Tong, X., Jackson-Weaver, O., Kracun, S., Xu, J., Sofroniew, M.V., Ellisman, M.H., Khakh, B.S., 2013. Imaging calcium microdomains within entire astrocyte territories and endfeet with GCaMPs expressed using adeno-associated viruses. J. Gen. Physiol. 141, 633–647.
Shigetomi, E., Hirayama, Y.J., Ikenaka, K., Tanaka, K.F., Koizumi, S., 2018. Role of purinergic receptor P2Y1 in spatiotemporal Ca(2+) dynamics in astrocytes. J. Neurosci. 38, 1383–1395.
Shigetomi, E., Kracun, S., Sofroniew, M.V., Khakh, B.S., 2010. A genetically targeted optical sensor to monitor calcium signals in astrocyte processes. Nat. Neurosci. 13, 759–766.
Shigetomi, E., Tong, X., Kwan, K.Y., Corey, D.P., Khakh, B.S., 2011. TRPA1 channels regulate astrocyte resting calcium and inhibitory synapse efficacy through GAT-3. Nat. Neurosci. 15, 70–80.
Slezak, M., Goritz, C., Niemiec, A., Frisen, J., Chambon, P., Metzger, D., Pfrieger, F.W., 2007. Transgenic mice for conditional gene manipulation in astroglial cells. Glia 55, 1565–1576.
Smith, N.A., Kress, B.T., Lu, Y., Chandler-Militello, D., Benraiss, A., Nedergaard, M., 2018. Fluorescent Ca(2+) indicators directly inhibit the Na,K-ATPase and disrupt cellular functions. Sci. Signal. 11, eaal2039.
Srinivasan, R., Huang, B.S., Venugopal, S., Johnston, A.D., Chai, H., Zeng, H., Golshani, P., Khakh, B.S., 2015. Ca^{2+} signaling in astrocytes from Ip3r2(-/-) mice in brain slices and during startle responses in vivo. Nat. Neurosci. 18, 708–717.
Stobart, J.L., Ferrari, K.D., Barrett, M.J.P., Gluck, C., Stobart, M.J., Zuend, M., Weber, B., 2018. Cortical circuit activity evokes rapid astrocyte calcium signals on a similar timescale to neurons. Neuron 98, 726–735 e724.
Svoboda, K., Yasuda, R., 2006. Principles of two-photon excitation microscopy and its applications to neuroscience. Neuron 50, 823–839.
Swedlow, J.R., 2013. Quantitative fluorescence microscopy and image deconvolution. Methods Cell Biol. 114, 407–426.
Tian, Q., Hu, J., Xie, C., Mei, K., Pham, C., Mo, X., Hepp, R., Soares, S., Nothias, F., Wang, Y., Liu, Q., Cai, F., Zhong, B., Li, D., Yao, J., 2019. Recovery from tachyphylaxis of TRPV1 coincides with recycling to the surface membrane. Proc. Natl. Acad. Sci. U. S. A. 116, 5170–5175.

Tomer, R., Lovett-Barron, M., Kauvar, I., Andalman, A., Burns, V.M., Sankaran, S., Grosenick, L., Broxton, M., Yang, S., Deisseroth, K., 2015. SPED light sheet microscopy: fast mapping of biological system structure and function. Cell 163, 1796–1806.

Wang, T.F., Zhou, C., Tang, A.H., Wang, S.Q., Chai, Z., 2006. Cellular mechanism for spontaneous calcium oscillations in astrocytes. Acta Pharmacol. Sin. 27, 861–868.

Wang, Y., DelRosso, N.V., Vaidyanathan, T.V., Cahill, M.K., Reitman, M.E., Pittolo, S., Yu, G., Poskanzer, K.E., 2019. Accurate quantification of astrocyte and neurotransmitter fluorescence dynamics for single-cell and population-level physiology. Nat. Neurosci. 22, 1936–1944.

Wang, Y., Shi, G., Miller, D.J., Wang, C., Broussard, G., Tian, L., Yu, G., 2017. Automated functional analysis of astrocytes from chronic time-lapse calcium imaging data. Front. Neuroinf. 11, 48.

Wolf, S., Supatto, W., Debregeas, G., Mahou, P., Kruglik, S.G., Sintes, J.M., Beaurepaire, E., Candelier, R., 2015. Whole-brain functional imaging with two-photon light-sheet microscopy. Nat. Methods 12, 379–380.

Zamanian, J.L., Xu, L., Foo, L.C., Nouri, N., Zhou, L., Giffard, R.G., Barres, B.A., 2012. Genomic analysis of reactive astrogliosis. J. Neurosci. 32, 6391–6410.

Zhao, Y., Zhang, Y., Liu, X., Lv, X., Zhou, W., Luo, Q., Zeng, S., 2009. Photostimulation of astrocytes with femtosecond laser pulses. Optic Express 17, 1291–1298.

Zong, W., Wu, R., Li, M., Hu, Y., Li, Y., Li, J., Rong, H., Wu, H., Xu, Y., Lu, Y., Jia, H., Fan, M., Zhou, Z., Zhang, Y., Wang, A., Chen, L., Cheng, H., 2017. Fast high-resolution miniature two-photon microscopy for brain imaging in freely behaving mice. Nat. Methods 14, 713–719.

Zong, W., Zhao, J., Chen, X., Lin, Y., Ren, H., Zhang, Y., Fan, M., Zhou, Z., Cheng, H., Sun, Y., Chen, L., 2015. Large-field high-resolution two-photon digital scanned light-sheet microscopy. Cell Res. 25, 254–257.

Supplementary Data

Mapping astrocyte activity domains by light sheet imaging and spatio-temporal correlation screening

Cuong Pham, Daniela Herrera Moro, Christine Mouffle, Steve Didienne, Régine Hepp, Frank W. Pfrieger, Jean-Marie Mangin, Pascal Legendre, Claire Martin, Serge Luquet, Bruno Cauli, Dongdong Li

Abbreviation list:

4-OHT – 4-Hydroxytamoxifen

aCSF – artificial cerebrospinal solution

ALDH1L1 – Aldehyde Dehydrogenase 1 Family Member L1

AM – Acetoxymethyl ester

C-Screen – Correlative Screening

EPI – Epifluorescence

FWHM – Full width at half maximum

GPCR – G protein coupled receptor

LSFM – Light sheet fluorescence microscopy

NA – Numerical aperture

PBS – phosphate buffer solution

PFA – Paraformaldehyde

SBR – Signal-to-background ratio

SR101 – Sulforhodamine 101

TTX – tetrodotoxin

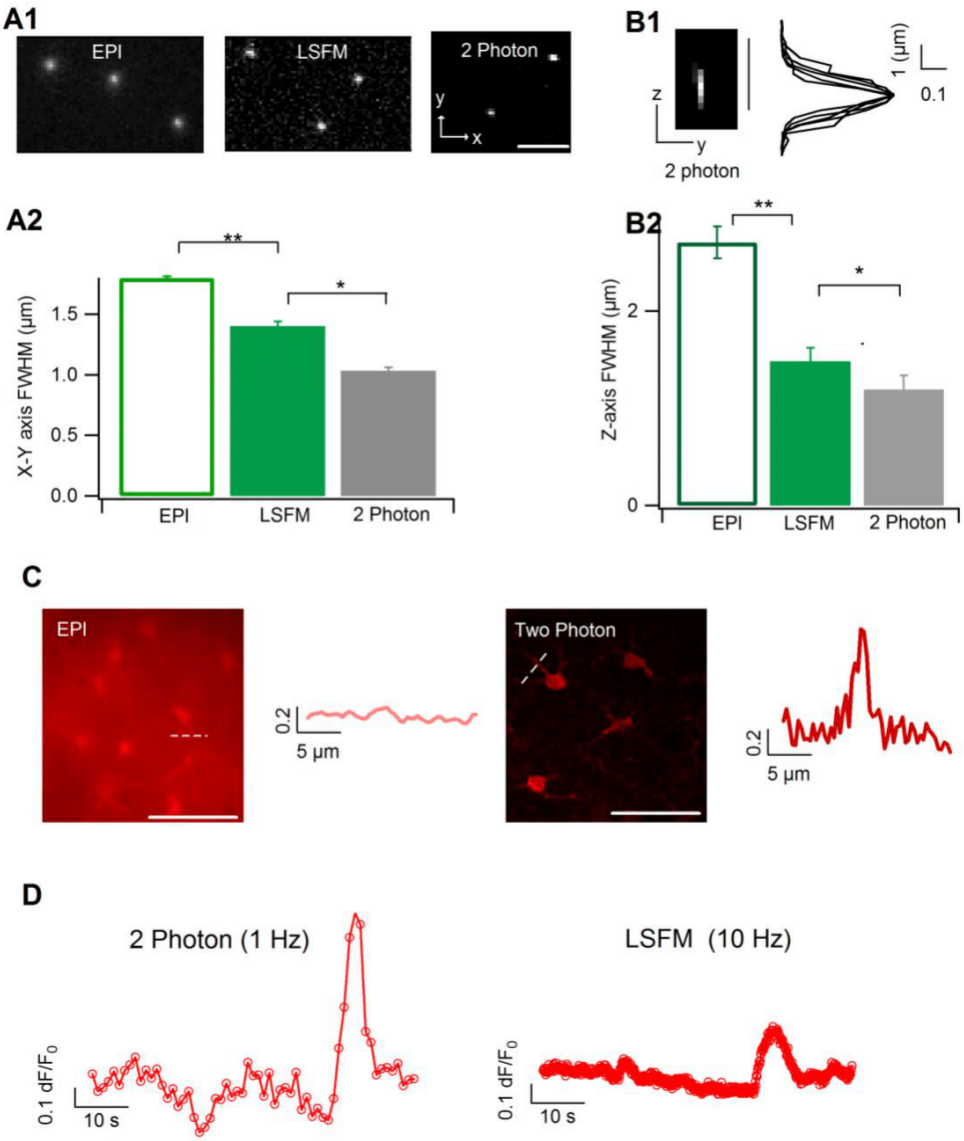

Figure S1. Comparison with two-photon microscopy. **(A)** Fluorescence images (*x*-*y* plane) of fluorescent beads of submicron size (core size, ~0.5 μm) acquired by EPI, LSFM and two-photon microscopy (A1). The apparent size of the beads in the fluorescent images was estimated by their FWHM (n = 5 for each, A2). **(B)** Representative *z*-axis profile of single bead imaged by two-photon microscopy (B1). The size of the *z* profile was evaluated by FWHM and compared to that obtained with EPI and LSFM (n = 5 per condition, B2). **(C)** Examples of SR101-labeled astrocytes in slices imaged by EPI and two-photon microscopy, respectively. The linescan profiles (along the dashed lines) show intersectional fluorescence intensity of astrocytic processes. **(D)** *Left*, representative time course of two-photon imaging at 1 Hz of astrocytic spontaneous GCaMP6 signal, across a field of view of 174 × 174 μm² at the pixel size of 0.34 μm. *Right*, 10 Hz LSFM recording at similar settings. Scale bars: 5 μm for A-B, and 50 μm for C.

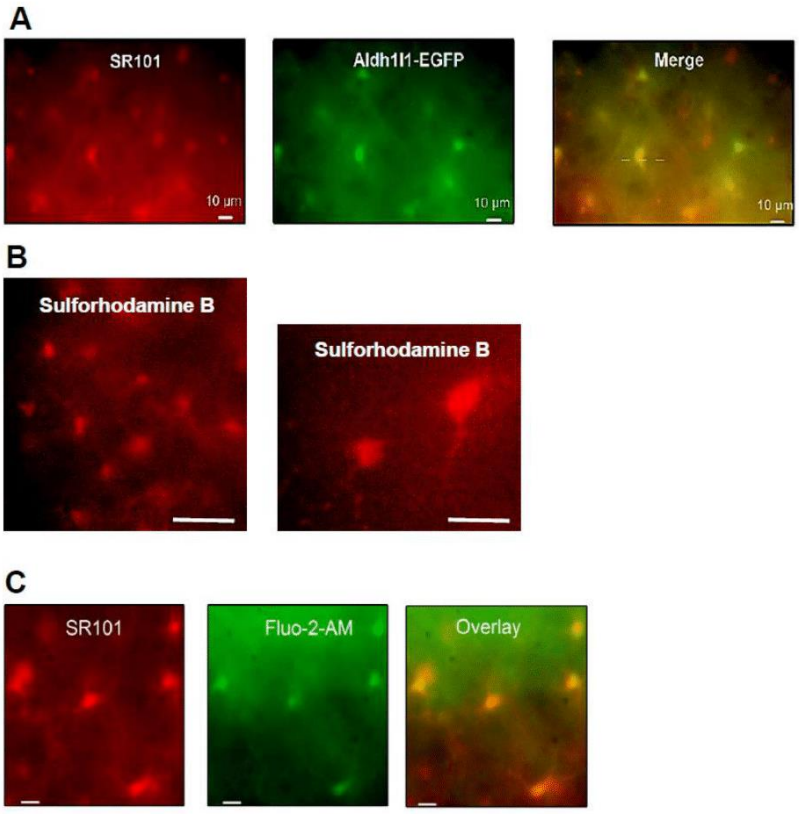

Figure S2. **(A)** Ex vivo labeling of astrocytes in acute mouse cortical slices. SR101 labeling colocalized with EGFP-positive astrocytes in slices prepared from ALDH1L1-EGFP transgenic mice. In this mouse line, EGFP is expressed under the astrocytic lineage promoter ALDH1L1 (Cahoy et al., 2008). Scale bars: 10 µm. **(B)** In vivo labeling of astrocytes via IP injection of Sulforhodamine B in awake mice (Appaix et al., 2012). Images were taken from acute slices with LSFM using ×20 (left) and ×63 objective (right), respectively. Scale bars: 50 µm for the left and 20 µm right. **(C)** The chemical Ca^{2+} indicator Fluo2 AM labels SR101-positive astrocytes, in line with early reports that the AM form of chemical Ca^{2+} dyes labels astrocytes in brain tissue (Fiacco et al., 2007; Reeves et al., 2011; Wang et al., 2006). Experiments were done in mice 3 - 4 weeks of age. Images in A and C were collected by epifluorescence imaging to integrate in-depth signals. Scale bars: 10 µm.

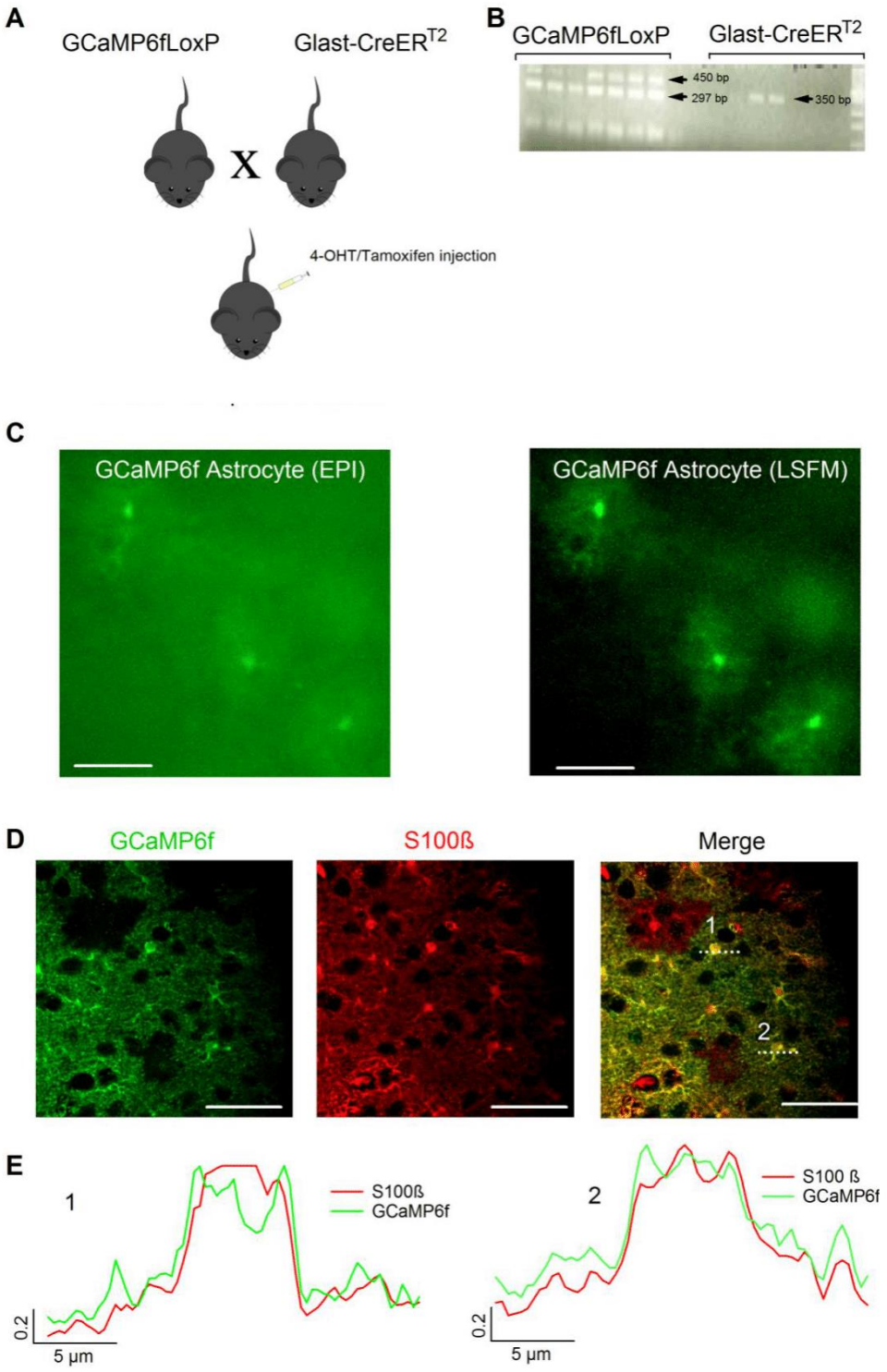

Figure S3. In vivo expression of GCaMP6 in astrocytes. (A) The Cre-dependent GCaMP6f (i.e., Loxp-GCaMP6f-Loxp) mouse line was crossed with the tamoxifen–inducible astrocyte-specific Glast-CreER^{T2} line. Intraperitoneal injection of tamoxifen into bigenic mice enabled selective expression of GCaMP6 in astrocytes. **(B)** Loxp-GCaMP6f-Loxp and Glast-

CreER^{T2} mutant was recognized at 450 bp and 350 bp band, respectively. **(C)** GCaMP6-expressing astrocytes visualized by EPI and LSFM in acute brain slices by a ×20 NA0.5 objective. **(D)** Astrocytic GCaMP6 expression validated by dual-color immunostaining. Colocalization was observed between GCaMP6 labeling identified by an anti-GFP antibody (green) and the astrcoytic marker S100β (red), as confirmed by the representative linescan profiles **(E)**. Scale bars: 50 μm.

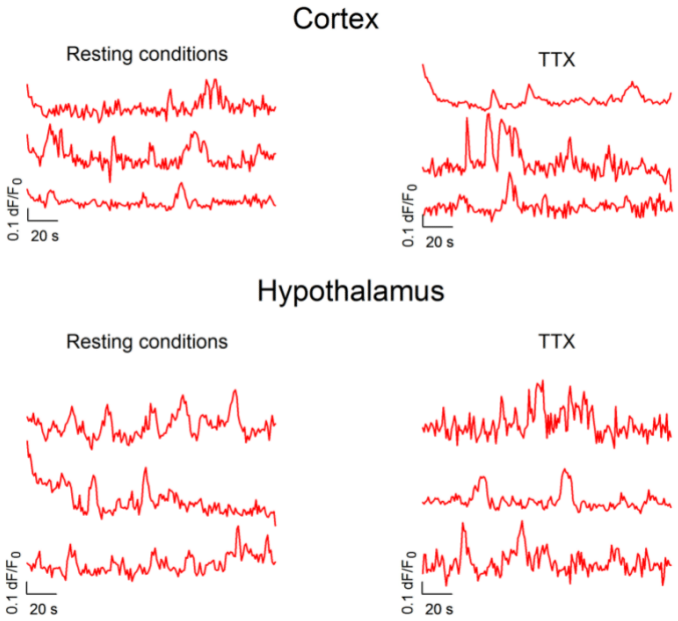

Figure S4. TTX failed to inhibit Ca^{2+} signals in astrocytes recorded in resting conditions. Representative Ca^{2+} time courses of light sheet imaging from both cortical **(A)** and hypothalamic **(B)** astrocytes genetically expressing the fluorescent indicator GCaMP6. Similar scenario was observed in 13 slices of 5 mice.

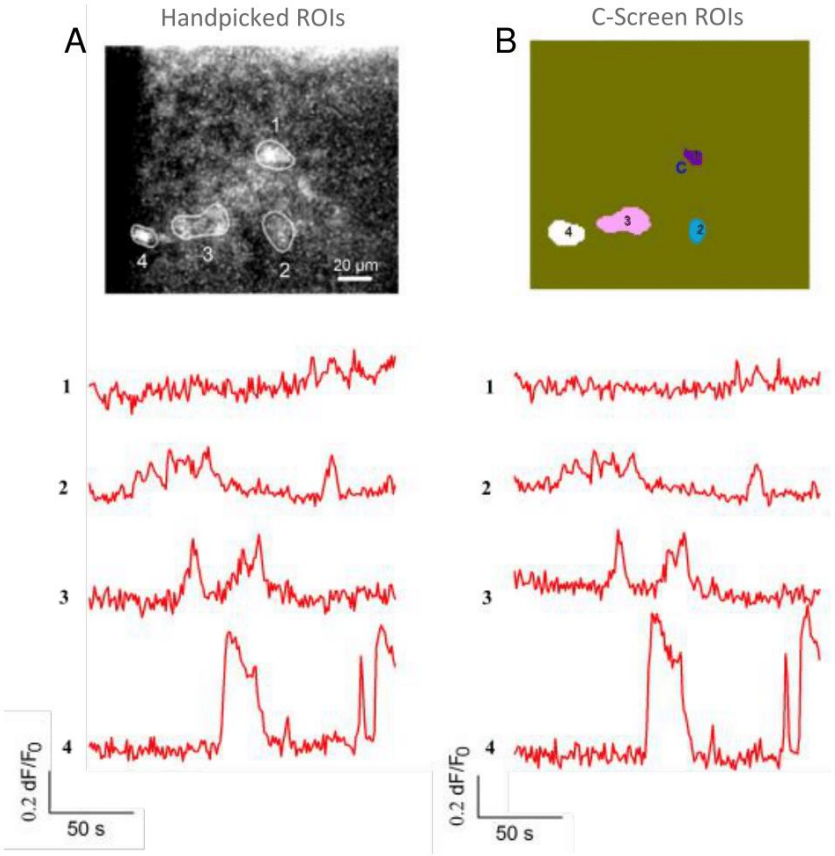

Figure S5. Ca^{2+} signals derived from regions determined by manual drawing (handpicked, A) and by C-Screen method (B). A ×20 NA0.5 water immersion objective was used for imaging GCaMP6-expressing astrocytes in mouse cortical slices. Signals were normalized as dF/F_0. For astrocytic Ca^{2+}-active domains, C-Screen analysis generated results in consistency with the manual detection.

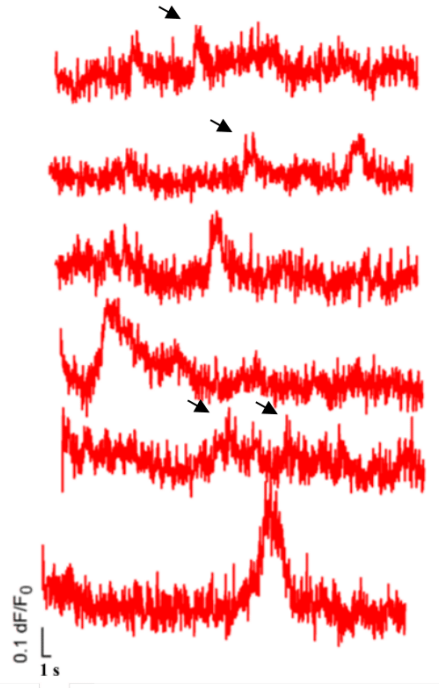

Figure S6. Ca^{2+} imaging at high acquisition rate. Hypothalamic astrocytes expressing GCaMP6 was imaged at 30 Hz with LSFM. Fast signals at near-second or sub-second scales were observed (exemplified by black arrows).

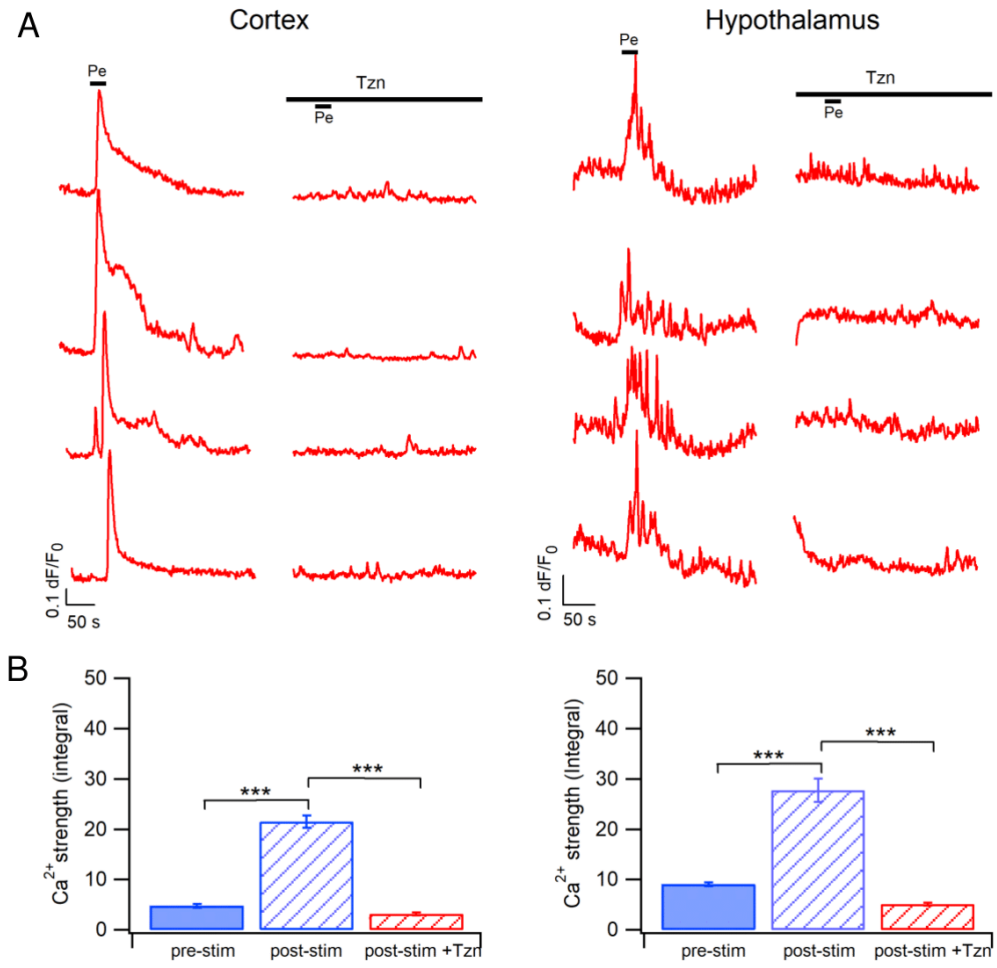

Figure S7. Phenylephrine-evoked astrocyte Ca^{2+} signals are mediated by α1 adrenergic receptor. (A) The α1 adrenergic receptor antagonist terazosin (Tzn, 10 μM) inhibited phenylephrine (Pe, 50 μM)-evoked Ca^{2+} signals in astrocytes. Signals were imaged by light sheet microscopy and GCaMP6. **(B)** Comparison of mean Ca^{2+} strength for cortical (left) and hypothalamic (right) astrocytes. Phenylephrine stimulation significantly boosted astrocyte Ca^{2+} strength which was inhibited by terazosin (370 - 390 active domains for cortical astrocytes, and 335 - 444 for hypothalamic astrocytes in the absence of terazosin; 50 active regions for cortex and 135 for hypothalamus when terazosin was present; 5-6 slices from 4 mice per condition; ***, $p < 0.001$).

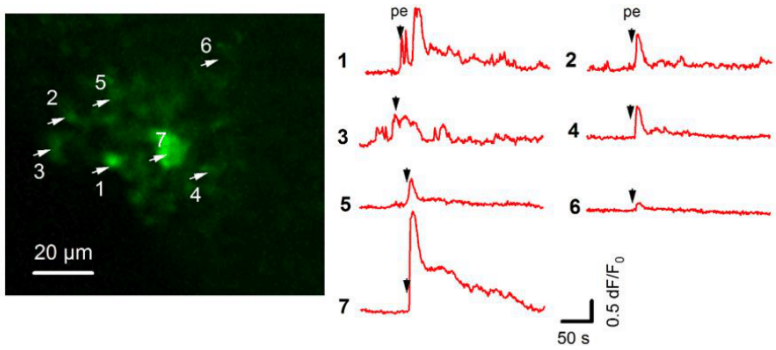

Figure S8. Ca^{2+} signals occur in both astrocytic somata and processes. Ca^{2+} signlas were imaged by LSFM in GCaMP6-expressing astrocytes in acute mouse cortical slices. ×20 NA0.5 water immersion objective was used for imaging at 1 Hz. Phenylephrine (pe, 50 µM) was applied by global perfusion. Localized Ca^{2+} signals were observed in astrocyte soma (ROI 7) and in microdomains located in ramified processes. Representative movie is provided in Supplementary file.

Supplemental References

Appaix, F., Girod, S., Boisseau, S., Romer, J., Vial, J.C., Albrieux, M., Maurin, M., Depaulis, A., Guillemain, I., van der Sanden, B., 2012. Specific in vivo staining of astrocytes in the whole brain after intravenous injection of sulforhodamine dyes. PLoS One 7, e35169.

Cahoy, J.D., Emery, B., Kaushal, A., Foo, L.C., Zamanian, J.L., Christopherson, K.S., Xing, Y., Lubischer, J.L., Krieg, P.A., Krupenko, S.A., Thompson, W.J., Barres, B.A., 2008. A transcriptome database for astrocytes, neurons, and oligodendrocytes: A new resource for understanding brain development and function. J. Neurosci. 28, 264-278.

Fiacco, T.A., Agulhon, C., Taves, S.R., Petravicz, J., Casper, K.B., Dong, X., Chen, J., McCarthy, K.D., 2007. Selective stimulation of astrocyte calcium in situ does not affect neuronal excitatory synaptic activity. Neuron 54, 611-626.

Reeves, A.M., Shigetomi, E., Khakh, B.S., 2011. Bulk loading of calcium indicator dyes to study astrocyte physiology: key limitations and improvements using morphological maps. J Neurosci 31, 9353-9358.

Wang, X., Lou, N., Xu, Q., Tian, G.F., Peng, W.G., Han, X., Kang, J., Takano, T., Nedergaard, M., 2006. Astrocytic Ca2+ signaling evoked by sensory stimulation in vivo. Nat Neurosci 9, 816-823.

I.8 - Results investigating the role of AQP4 in astrocyte volume regulation

In vivo astrocyte chemical labeling enables fluorescence intensity-translated volume imaging

To pinpoint the role of AQP4 in astrocyte volume regulation, we sought to image in situ in a real-time manner the astrocyte volume dynamics. Astrocytes bear extended three-dimensional morphology sitting in nanoscale distances with other cell types in the brain (Bindocci et al., 2017) (**Fig. 14**). Performing video-rate three-dimensional imaging at nanoscale resolution remains difficult. I therefore developed fluorescent intensity-translated (FIT) imaging to follow astrocyte volume change in high temporal resolution. In this method, selective delivery of a highly water soluble fluorescent dye in astrocytes can enable the imaging of its volume change by following the associated fluorescence oscillation. Fluorescence increases upon transient shrinking because it augments the astrocyte dye density in spatially limited focus depth and the field of view, while fluorescence signal decreases during swelling (**Fig. 15**).

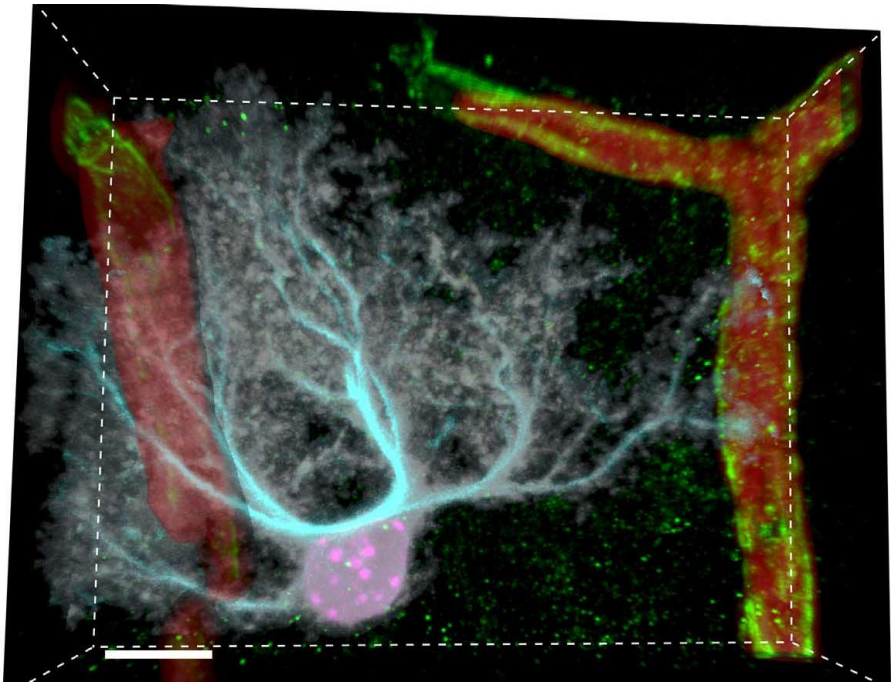

Figure 14: Complex morphology of mouse brain astrocyte (From bindocci et al 2017)

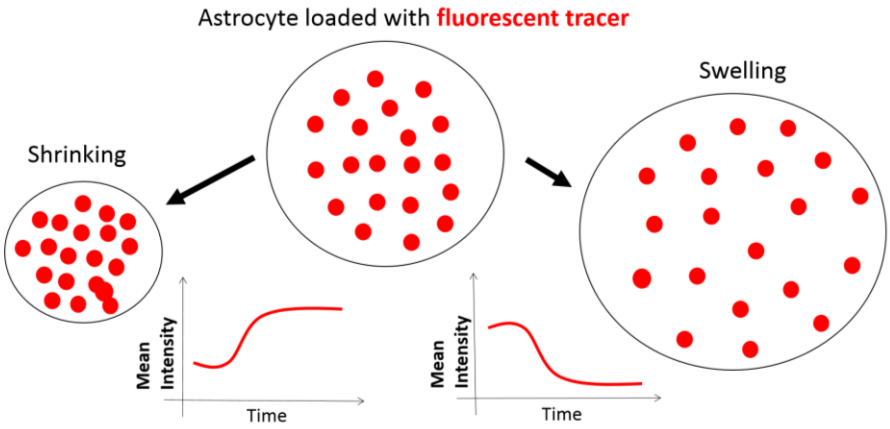

Figure 15: The principle of FIT imaging of astrocyte volume change.

To this end, I adopted a rapid in vivo astrocyte chemical labeling strategy where brain astrocytes were specifically labeled by the highly diffusible red fluorescent dye Sulforhodamine B (SRB) following an intraperitoneal injection in awake mice. In acute cortical slices, individual SRB-labeled astrocytes were resolved by a high numerical aperture objective (**Fig. 16**). This in vivo chemical labeling method labeled indeed widedly distributed astrocyte-like cells in mouse cortex (**Fig. 16**). The SRB labeling (red fluorescence) was validated to be astrocyte-specific using the fluorescent astrocyte reporter line GFAP-GFP mice (**Fig. 17**), thus corroborating the early report where an intravenous injection of another dye sulforhodamine 101 also results in the labeling of mouse brain astrocytes (Appaix et al., 2012). In order to follow the global volume dynamics of astrocytes, we then used the wide-file fluorescence microscopy configuration was used to perform single-section time lapse imaging of astrocytes in acute brain slices. This which collected not only the fluorescence signals distributed in the horizontal plane, but also the fluorescence along the axial axis, hence enabling the dynamic imaging of the overall fluorescence signals of single astrocytes in situ

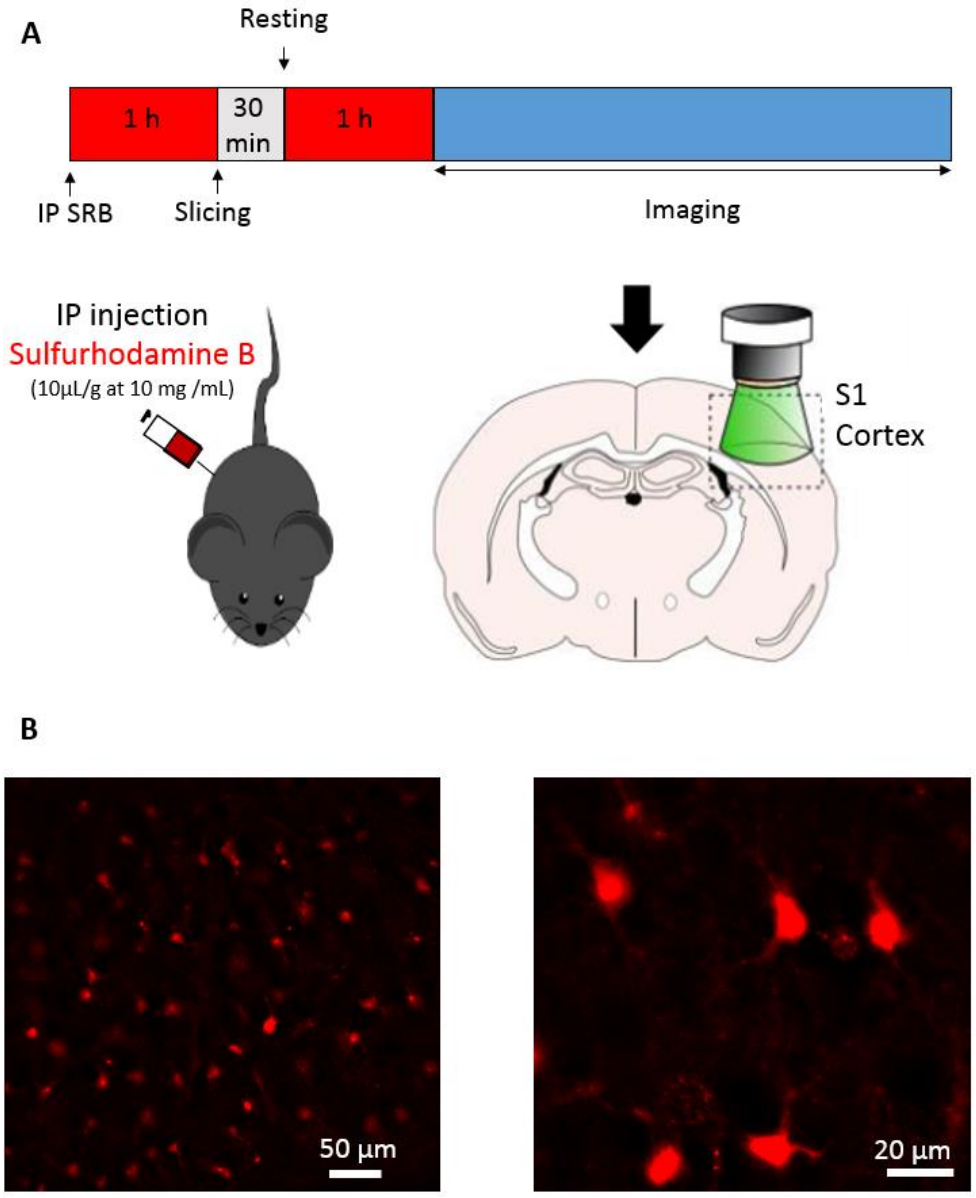

Figure 16: In vivo chemical labelling of astrocytes in mouse brain. *(A) Illustration of experimental protocol for in vivo astrocyte labelling by SRB. Coronal slices were prepared acutely for ex vivo imaging of astrocytes in S1 cortex using epifluorescence microscopy, which enables the acquisition of the fluorescence along the z-axis, so suitable for following the global fluorescence signals caused by volume changes. (B) Representative fluorescence images of astrocytes in S1 cortex labelled by SRB under low (×20) and high magnification (×63).*

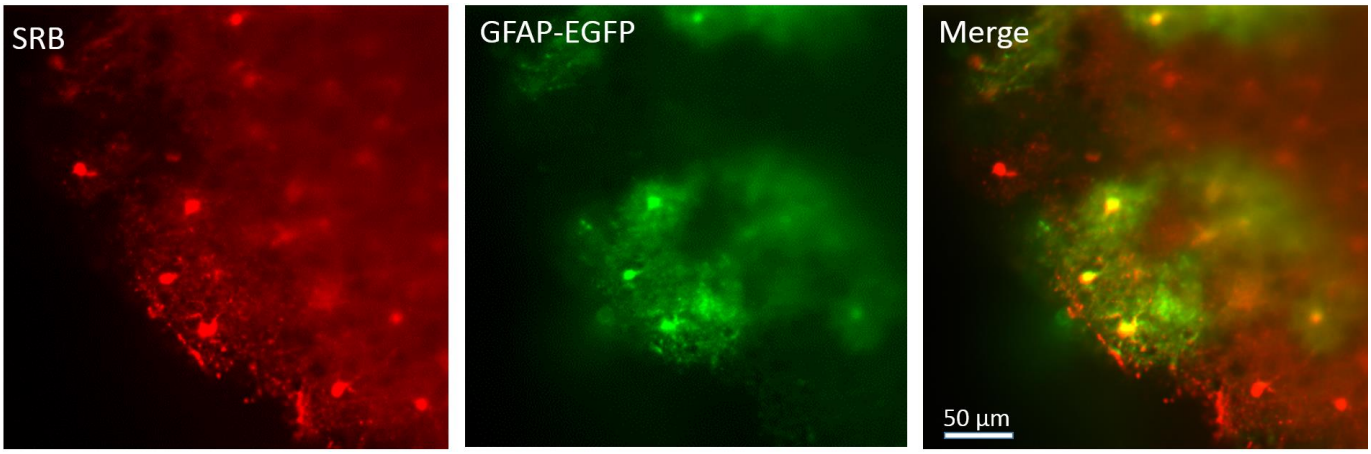

Figure 17: Validation of in vivo SRB labelling of mouse cortical astrocytes. *To resolve fine astrocytic structure dual-color, light-sheet fluoresce microscopy was used. Experiment was performed in the GFAP-EGFP mice. Colocalization was observed between the red fluorescence dye SRB and EGFP-positive astrocytes. Note that, in mouse cortex, just a subpopulation of astrocytes express GFAP, while SRB labels more astrocytes, which yields a sub-regional colocalization but meanwhile excluding any potential bleed through from the red SRB imaging channel to the EGFP channel.*

The average fluorescence intensity within defined regions of interest changes with astrocyte volume as its alteration influences the effective concentration of the fluorescent dye (**Fig. 15**) Indeed, applying hypo-osmotic solution to induce astrocyte swelling caused decreases in SRB fluorescence signal in a strength-dependent manner (**Fig. 18 A**), whereas the hyper-osmotically induced shrinking increased astrocyte fluorescence intensity (**Fig. 18 B**). Thus, by following time-lapse fluorescence signal, FIT imaging provided a selective and sensitive readout for astrocyte volume change.

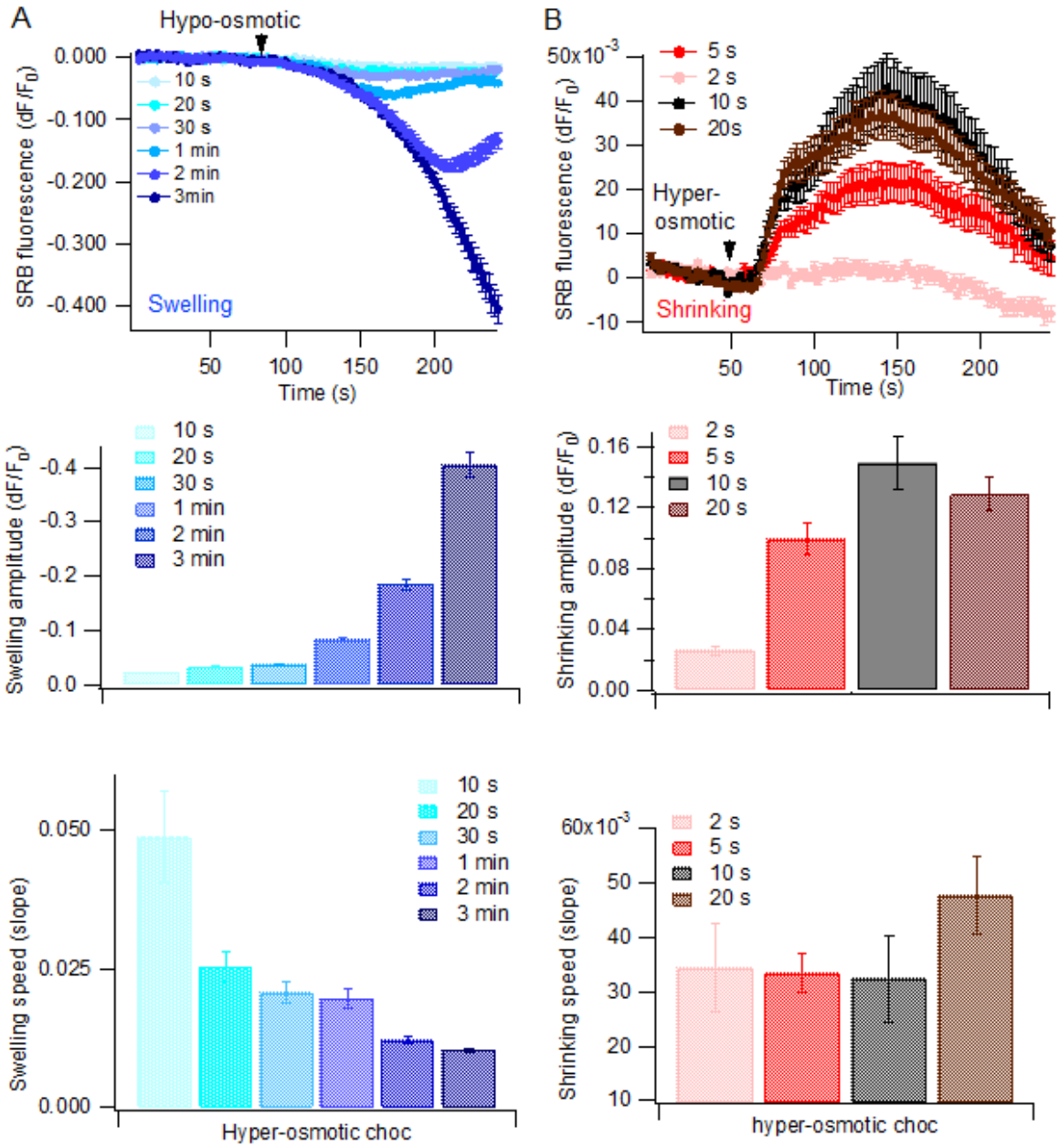

Figure 18: Experimental validation of The FIT imaging method of astrocyte volume dynamics. *(A) Top, time course of SRB fluorescence following hypo-osmotic solution application for different time periods. Bellow quantification of swelling amplitude (maximum fluorescence drop) and speed (temporal initial slope). (B) Top, time course of SRB fluorescence following hyper-osmotic solution application for different time periods. Bellow quantification of shrinking amplitude (maximum fluorescence peak) and speed (temporal initial slope). (n=52 astrocytes, from 8 slice from 4 mice).*

AQP4 plays a tonic role in restricting astrocyte swelling

To examine a potential role of AQP4 in maintaining the volume homeostasis in astrocytes, I then acutely inactivated AQP4 in basal conditions using this selective blocker TGN-020 (Huber et al., 2009).The specificity of TGN-020 in targeting AQP4 water channel has been demonstrated by in vitro using heterologous expression system and in vivo researches using AQP4 knockout mice (Nakamura et al., 2011; Igarashi et al., 2013) (**Fig. 19 and 20**).

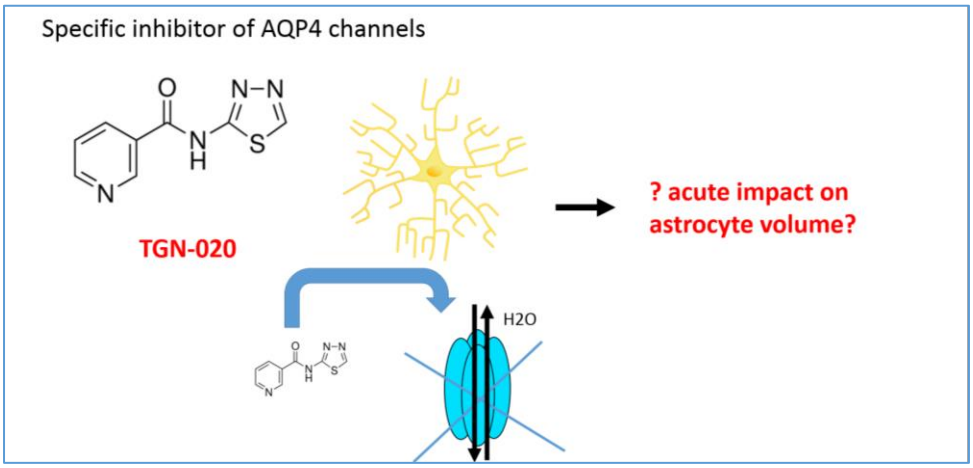

Figure 19: Protocol for acute blocking of astrocytic AQP4 by TGN-020.

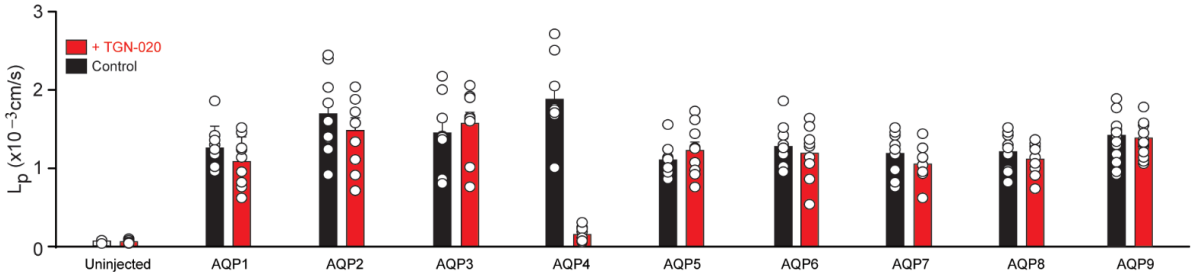

Figure 20: Selectivity of TGN-020 for AQP4 validated using oocytes expressing different type of aquaporin channels (Toft bertelsen et al 2020).

AQP4 is a bidirectional water channel (**Fig. 21A**). So, if AQP4 sustains a symmetric water influx and efflux across the astrocyte plasma membrane, acute pharmacological inhibition, in short time window, would not disturb astrocyte volume dynamics. Surprisingly, upon the

application of TGN-020 in acute brain slices (**Fig. 21B**), I observed a moderate yet significant swelling reflected by the drop in the intracellular SRB fluorescence in astrocytes as compared with the application of the control vehicle (**Fig. 20C**). **This result indicates that AQP4 tonically inhibits astrocyte swelling to maintain the volume homeostasis.** Intriguingly, this observation suggests that **AQP4 mediates a tonic water efflux from astrocytes** (**Fig. 22**), therefore exerting a net shrinking effect in basal conditions to sustain astrocyte volume stability. Hence, this line of data implies an imbalanced involvement of AQP4 in astrocyte water handling that facilitates the water efflux in the basal states.

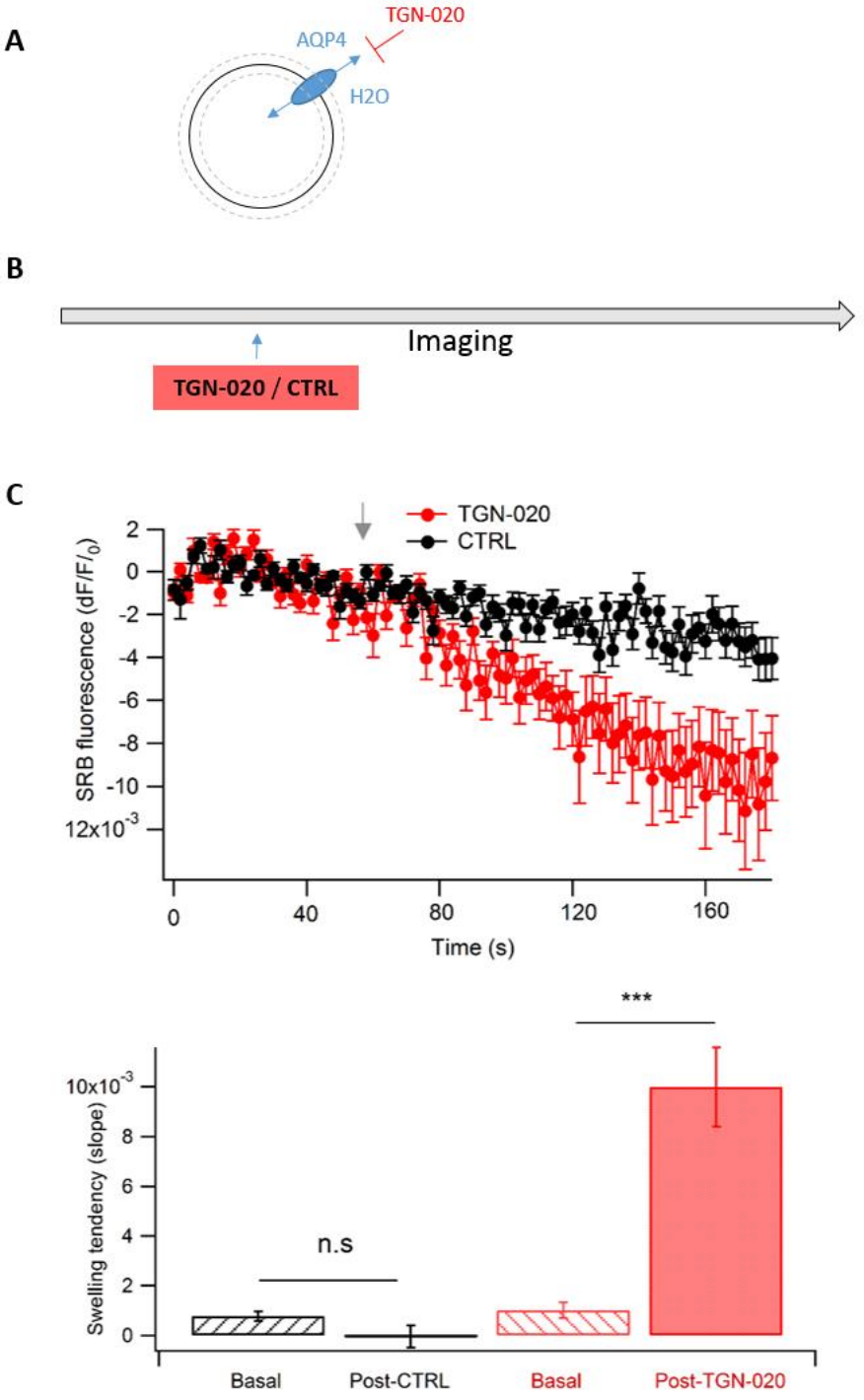

Figure 21: Acutely blocking AQP4 in astrocytes in situ in brain slices causes swelling. *(A) Acute blocking of astrocytic AQP4 should if equally bidirectional should not impact astrocytic volume. (B) Imaging protocol for acute blocking of AQP4 by TGN-020 (20 µM) or control (CTRL). (C) Time course of SRB fluorescence following TGN-020 application or CTRL solution*

(top). SRB fluorescence decreased following application of TGN-020, on the other hand CTRL solution application did not impact SRB fluorescence. Mean of astrocyte swelling tendency before and following TGN-020 application or CTRL solution (bottom). Astrocyte volume did not change following CTRL solution application, but increased following TGN-020 application. (n=53 astrocytes, from 10 slices from 6 mice).

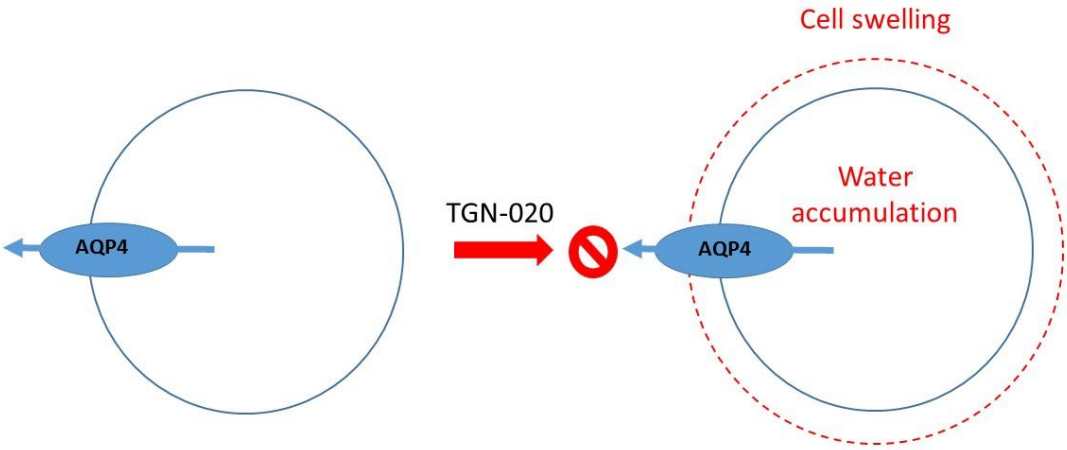

***Figure 22: Potential explanation for the tonic role of AQP4 in astrocyte volume homeostasis**. The results suggest that AQP4 mediates a net water efflux in basal conditions. This supports the observation that the acute AQP4 blocking by TGN-020 induces a transient swelling of astrocytes (right, from dotted line changing to the solid line).*

To validate the basal inhibition effect of AQP4 in astrocyte swelling, I checked the effect of TGN-020 on evoked astrocyte swelling and shrinking. First, I induced astrocyte swelling in acute mouse cortical slices by applying hypo-osmotic solution in the presence or absence of TGN-020 (**Fig. 23A**). Acute inhibition of AQP4 was observed to facilitate the rate of swelling reflected by a faster initiation time (namely, the shortened starting time) and the more rapid reaching of SRB fluorescence to the peak value (**Fig. 23B and C**). These results validates **the basal contribution of AQP4 for water efflux**, whereby (its inhibition enhances the intracellular water accumulation thus the swelling). Meanwhile, I noted that the maximal swelling extent was reduced (**Fig. 23B and C**). This observation confirms that AQP4 also

mediates water influx, hence inhibition of AQP4 over extended time windows reduces the total amount of water influx thereby the absolute swelling amplitude.

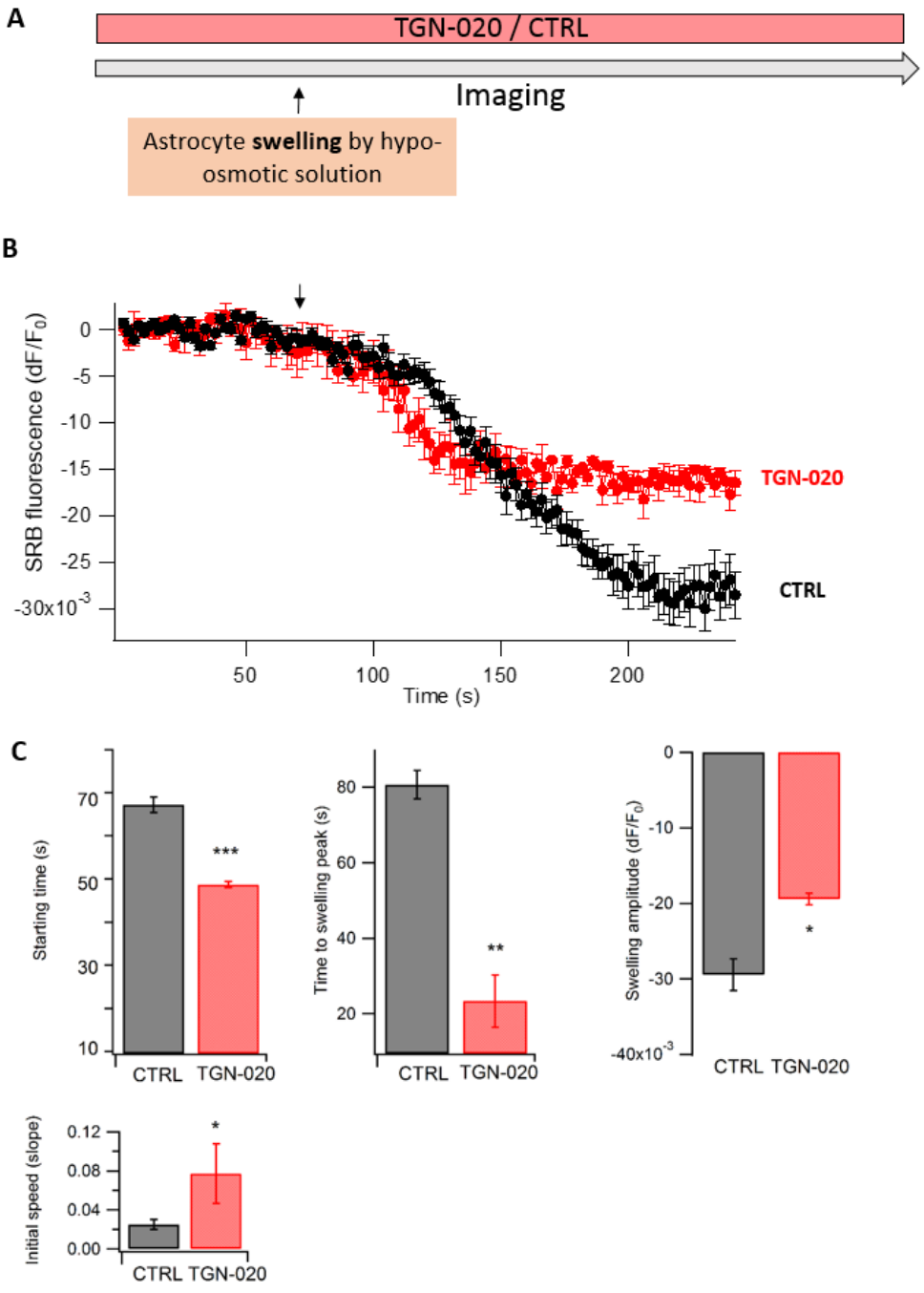

Figure 23: Blocking AQP4 facilitate astrocyte swelling. *(A) Imaging protocol for astrocyte swelling when blocking AQP4 by TGN-020 (20µM) or in control conditions (ACSF solution). Astrocyte swelling was triggered by application of a 100 mOsM solution. (B) SRB fluorescence time course following*

astrocyte swelling in presence of TGN-020 or control solution. Astrocyte swelling caused a decreased SRB fluorescence in both conditions. (C) Comparison between different swelling conditions in presence of TGN-020 or control solution. In presence of TGN-020 the swelling starting time (time between the reaching of the hypo-osmotic solution and the first changing pointing fluorescence curve), the time to swelling peak and the maximum swelling amplitude decreased compared to control. On the other hand initial astrocyte swelling speed was increased in presence of TGN-020 compared to control. (n=12 astrocytes, from 3 slices from 2 mice).

I also imaged the effect of blocking AQP4 on the shrinking activity of astrocytes induced by hypertonic solution in situ in brain slices (**Fig. 24A**). I observed shriking kinetics in astrocytes was altered by the presence of AQP4 blocker TGN-020 (**Fig. 24B**). Quantifying the shrinking kinetics parameters shows that AQP4 inhibition impairs astrocytes shrinking, reflected by a slower reaching to shrinking peak, and a reduced shrinking amplitude as compared with control conditions (**Fig. 24C**). Although TGN-020 tends to slow down the initiation reflected by the prolonged starting time, the effect is not yet significant. Overall inhibition of AQP4 limits the shrinking activities of astrocytes corroborating the preferential role of AQP4 mediating water efflux in astrocytes.

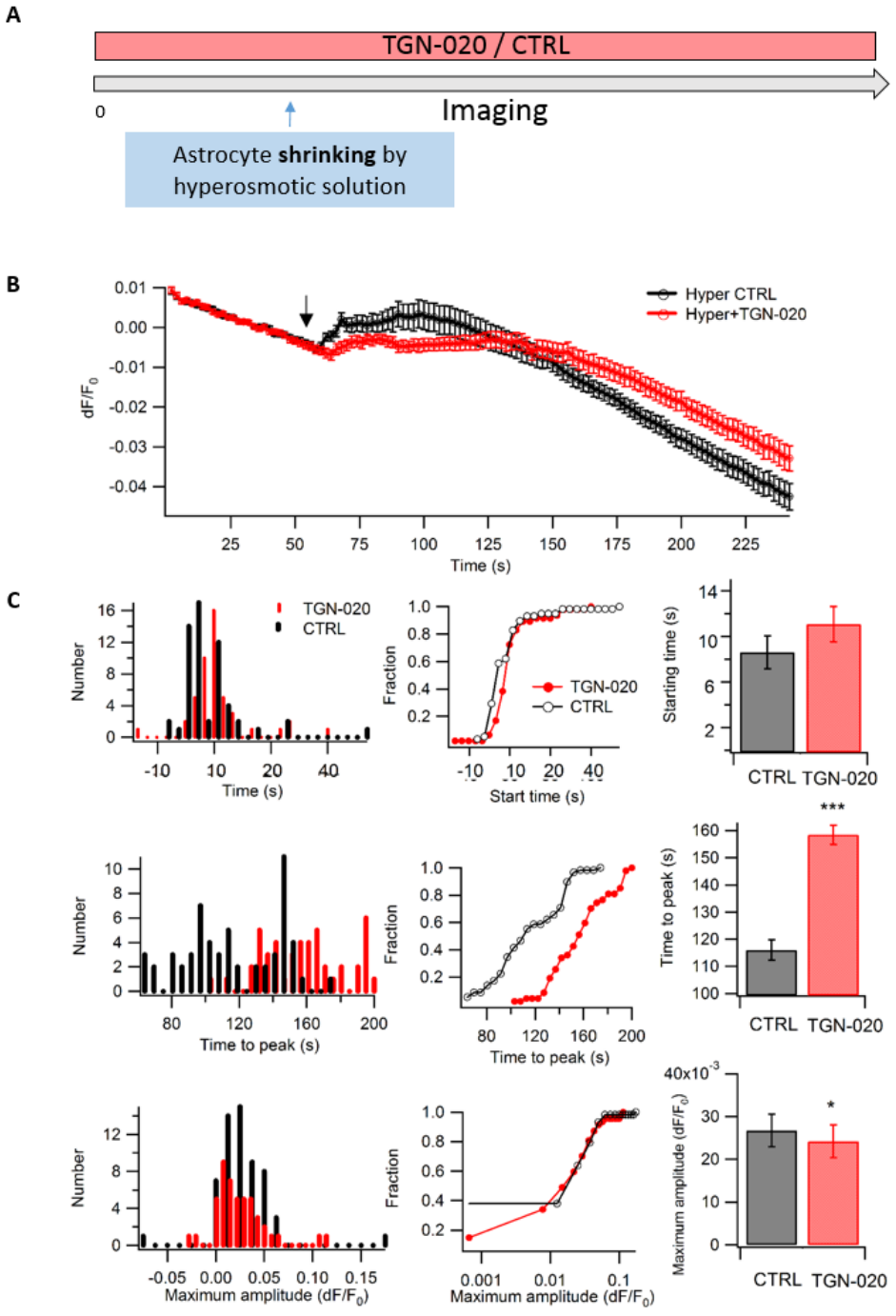

Figure 24: Blocking AQP4 acutely impaired astrocyte volume shrinking: *(A) Imaging protocol for astrocyte shrinking when blocking AQP4 by TGN-020 (20µM) or in control conditions (CTRL). Astrocyte shrinking was triggered by application of a 400 mOsM solution. (B) SRB fluorescence time course following astrocyte shrinking in presence of TGN-020 or CTRL. Astrocyte shrinking caused an*

increased SRB fluorescence in both conditions. (C) Histogram and comparison of the mean value for starting time, between the reaching of the hyper-osmotic solution and the first changing pointing fluorescence curve (top row), time to peak (middle row), and maximum amplitude (bottom row). (n=68 astrocytes, from 8 slice from 2 mice)

Together, these data confirm that AQP4 plays a tonic role in regulating astrocyte volume responses. Corroboratively, these results suggest that AQP4 in basal states mediates a net water efflux from cortical astrocytes, thereby constraining the basal swelling to maintain brain astrocyte volume stability.

Inhibition of astrocyte AQP4 causes swelling-associated Ca^{2+} transients

It is known that astrocyte swelling induces intracellular Ca^{2+} increases, likely due to the Ca^{2+} influx via the Ca^{2+} permeable transient receptor potential (TRPV) ion channels (Mola et al., 2016). Thus to furthermore validate that acute inhibition of basal AQP4 activity causes astrocyte swelling, I performed functional recording of astrocyte Ca^{2+} signaling using the GLAST-GCaMP6 mouse line where the genetically encoded Ca^{2+} sensor GCaMP6 is selectively expressed in astrocytes (Pham et al., 2020).

Using light-sheet imaging, I first validated that hypo-osmotically induced swelling indeed induced astrocyte Ca^{2+} signal increase (**Fig. 25A**), consistent with previous reports (Jarand et al., 2019). Next I checked the effect of AQP4 inhibition by TGN-020 effect on intracellular Ca^{2+} signals in astrocytes. I observed that application of TGN-020 induces significant Ca^{2+} increase in astrocytes, suggesting that acute blocking of AQP4 causes astrocyte swelling (**Fig. 25B**). This observation thus further supports the tonic inhibition role of AQP4 in astrocytes swelling (**Fig. 26**).

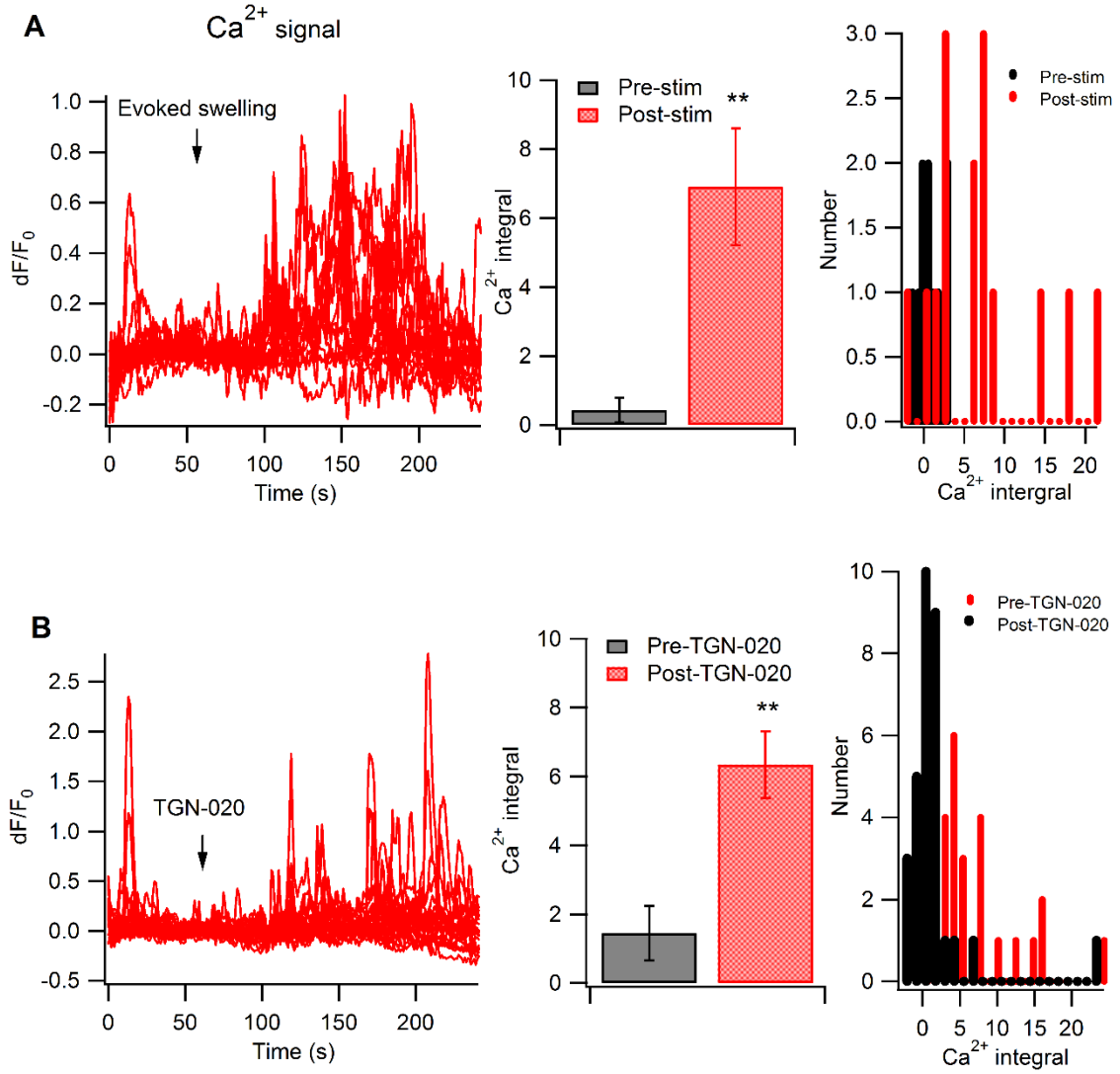

Figure 25: Acutely blocking AQP4 triggered swelling-associated astrocyte Ca^{2+} increase. *(A) Astrocyte swelling was triggered by application of a 100 mOsM solution, which triggered Ca^{2+} increase. Brain slices were taken from Glast-Cre^{ERT2}/GCaMP6^{floxP} mice where GCaMP6f is specifically expressed in astrocytes. Light-sheet fluoresce microscopy was used in order to sensitively track Ca^{2+} signals. Left, swelling induced Ca^{2+} signals time courses of individual responses regions. Middle to right, bar comparison between the signals integral values (area under the curve) and their histograms of the signals before and after hypo-osmotic solution challenge. (B) Left, TGN-020 induced Ca^{2+} signals time courses of individual responses regions. Middle to right, bar comparison between the signals integral values (area under the curve) and their histograms of the signals before and after TGN-020 application. (n=89 astrocytes, from 8 slices from 5 mice)*

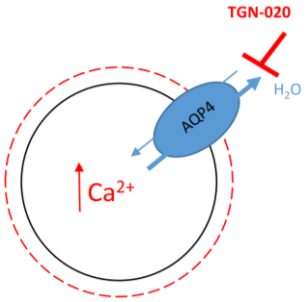

Figure 26: Swelling induced by AQP4 blocking elicits Ca^{2+} increase in astrocytes.

In vivo validation of the tonic inhibition role of AQP4 in astrocyte volume control

Following the observation in acute mouse brain slices, I have started to validate the observation in vivo using fiberphotometry. This technique allows the temporal recording of astrocyte population fluorescence in freely moving animals (**Fig. 27A**). First I monitored SRB temporal course into S1 cortex following its injection in vivo. An initial sharp entry of SRB into the cortex was noted, which was followed by a gradual fluorescence decrease over time in about 1 hour. Afterward, a long sustained SRB fluorescence plateau was observed lasting for a long time with much reduced decrease rate, indicating the accumulation of SRB in brain astrocytes (**Fig. 27B**). This time courses is consistent with SRB accumulation in astrocyte as validated by my slice imaging experiment, which is also comparable with the kinetics of the accumulation of sulforhodamine 101 following intravenous injection as previously previous reported (Appaix et al., 2012).

Then I tested the effect of TGN-020 on astrocyte swelling in this in vivo setting. TGN-020 was injected at the time when SRB is trapped in astrocytes. In parallel mice I injected saline control solution at the same time as TGN-020 (**Fig. 28B**).Given the tonic inhibitory effect of AQP4 blocking on astrocyte swelling it was expected that in vivo application of TGN-020 would induce a transient astrocyte swelling thereby a decrease in the SRB fluorescence. Along this line I observed that while the saline control showed no apparent (**Fig. 28A**), TGN-020 tended to cause a fluorescence decrease in astrocytes (**Fig. 28B**). Thus far the number of the experimental mice needs to be increased to establish statistical significance. I currently have experiments on going.

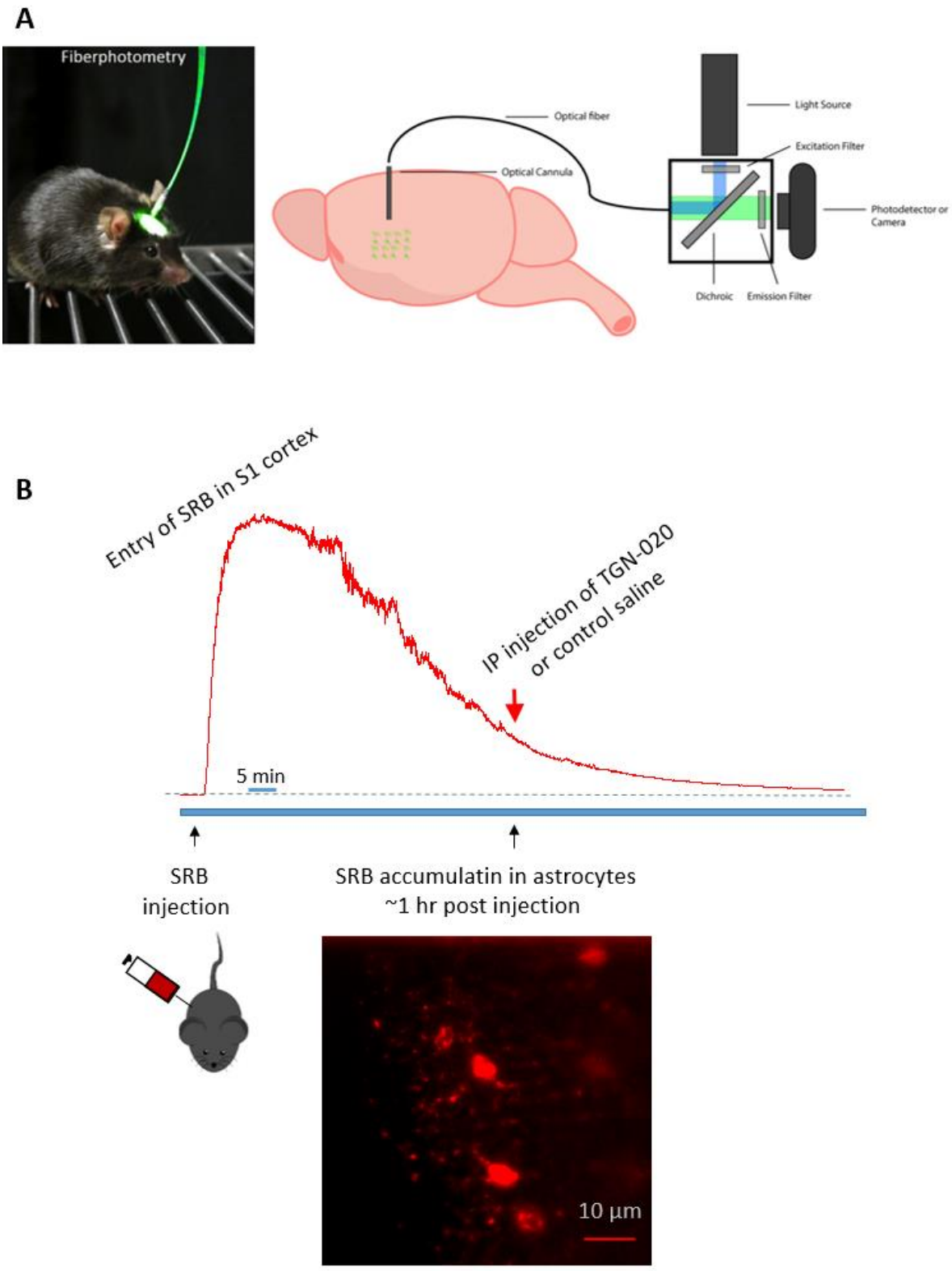

Figure 27: Fiberphotometry fluorescence recording of astrocyte volume in vivo. *(A)Fiberphotometry allows the recording of temporal fluorescence signals from populations of cells in freely moving animals.*

(B) Experimental protocol for in vivo recording with fiberphotometry of astrocyte volume changes using SRB fluorescence oscillation, FIT application in vivo. At the time point when SRB is trapped in S1 cortical astrocytes, TGN-020 (20 mg/kg) or saline control.

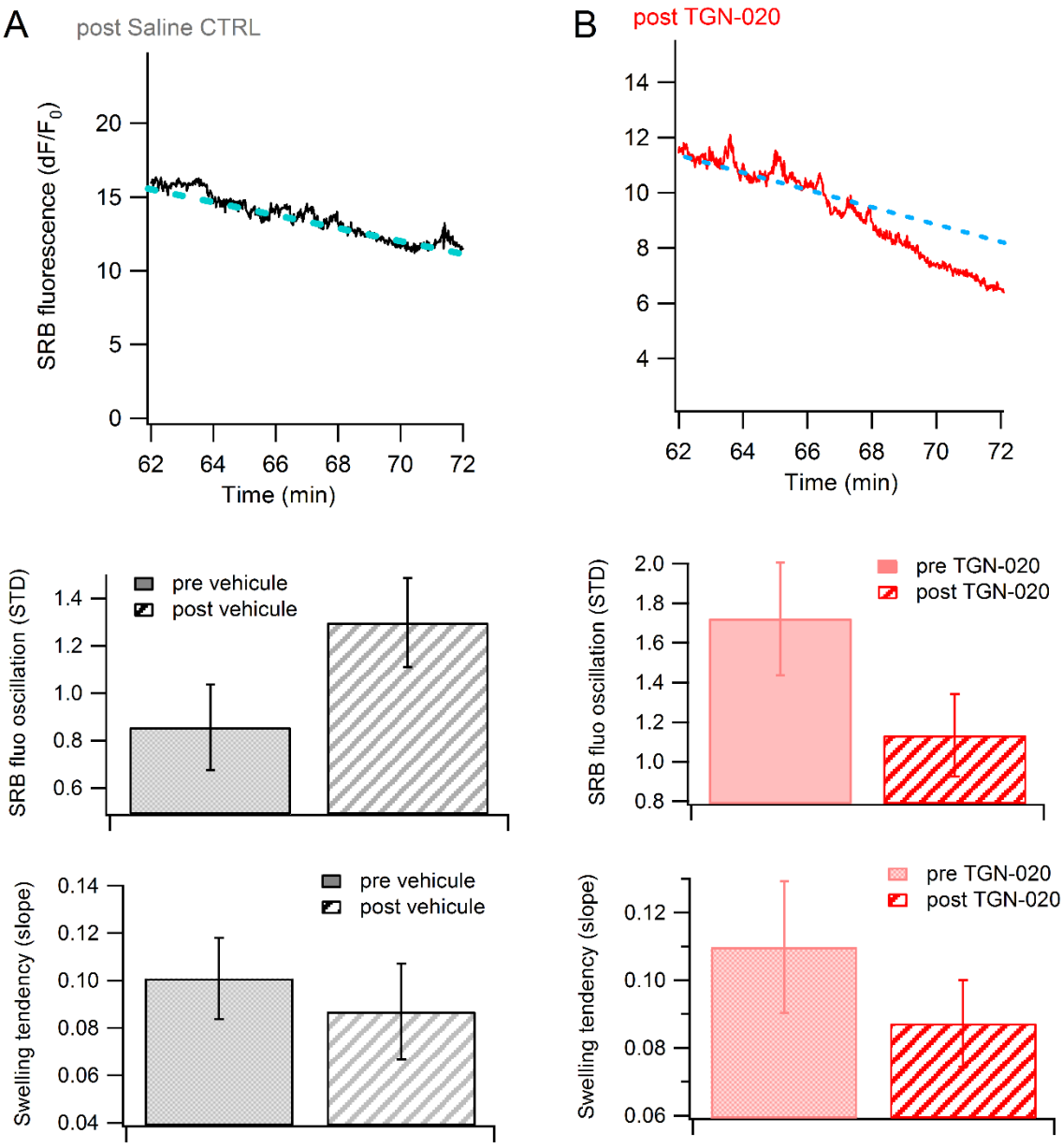

Figure 28: In vivo fiberphotometry suggest that AQP4 blocking shows a tendency to swell astrocytes. *(A) Astrocyte SRB fluorescence in response to saline control injection. Top, representative fiberphotometry recording following injection. Below, comparison of SRB fluorescence oscillation (derived from temporal standard deviation, STD) and swelling tendency (quantified by the curve slope)*

before and after the saline control injection. (B) Same experiments with TGN-020 injection. (n = 5 trials, from 3 mice)

In vivo diffusion MRI shows that acute AQP4 inhibition impacts water diffusion in mouse brain

My data from FIT volume recording show that AQP4 tonically confines the swelling of astrocytes thereby maintaining their volume homeostasis in the brain. These data suggest that AQP4 mediates a net water efflux from astrocytes under basal conditions. What is the contribution of astrocyte AQP4 to brain water diffusion per se?

The DW-MRI (DW-MRI) is a well-established technique for the diagnosis of diseases such as stroke and edema. **The DW-MRI uses the diffusion of water molecules to generate contrast: regions in which water molecules diffuse more freely appear darker** (**Fig. 29**) (Bihan and Iima, 2015). In biological tissues, the effective diffusion coefficient of water depends on several parameters, including the local diffusivity in intracellular and extracellular compartments, the relative volume fraction occupied by cells and the transport of water across the plasma membrane. To disentangle diffusion and relaxation effects on image contrast, one may obtain quantitative images of the "apparent" diffusion coefficient (ADC). The ADC concept is introduced to account for the fact that in biological tissues the diffusion process is complex and reflects several different mechanisms. The ADC incorporates the effects on water diffusion imparted by the cellular membrane and water permeability between intra-cellular and extra-cellular spaces at the voxel level.

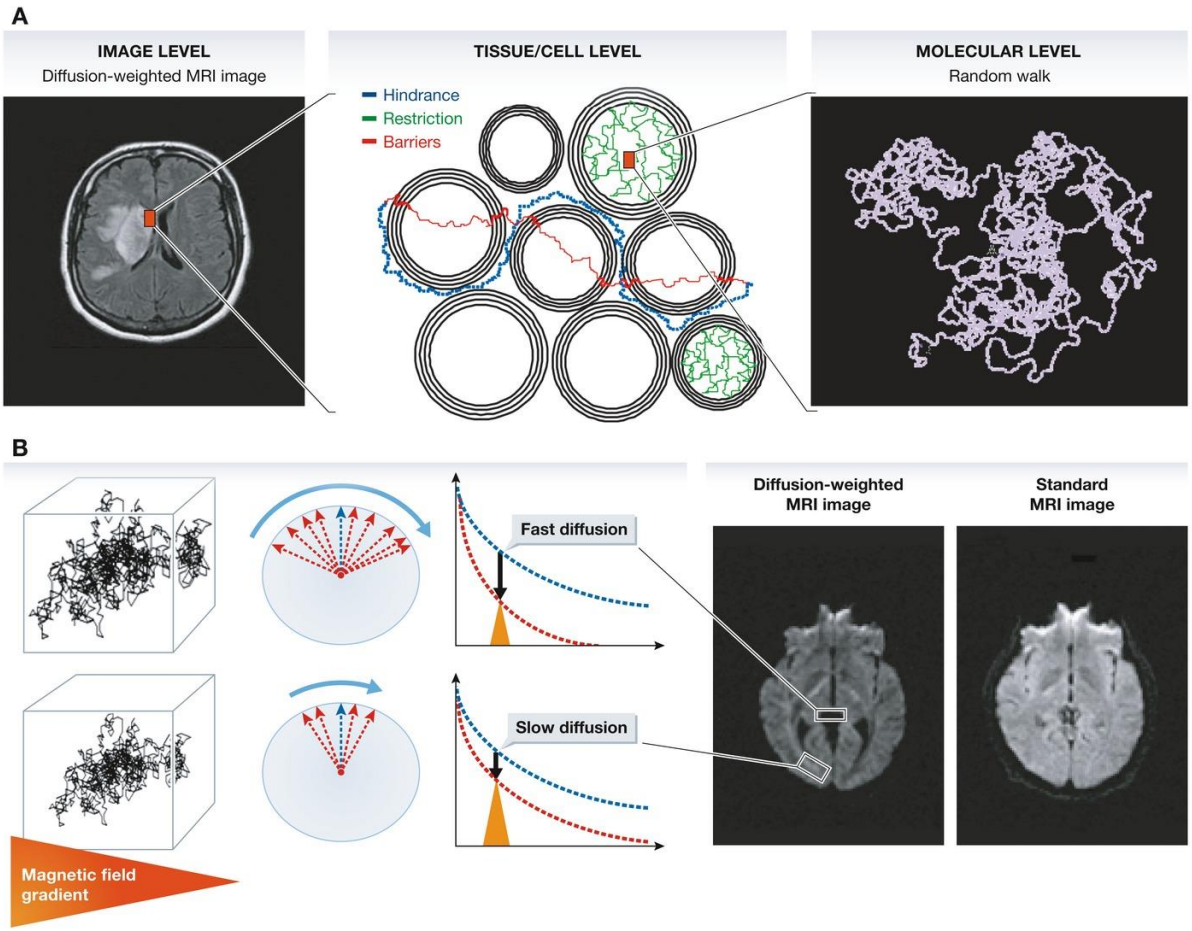

Figure 29: Diffusion weighted magnetic resonance imaging principles. *(A) Contrast and signal levels in the diffusion-weighted image (left) reflect water diffusion behavior (random walk) (right). Diffusion behavior is modulated by tissue structure at the cellular level (middle): For instance, diffusion can be restricted within cells, water may escape when cell membranes are permeable and might then experience a tortuous pathway in the extracellular space (hindrance). (B) In the presence of a magnetic field gradient (variation of the magnetic field along one spatial direction), magnetized water molecule hydrogen atoms are dephased. The amount of dephasing is directly related to the diffusion distance (a few micrometers) covered by water molecules during measurement (a few tens of milliseconds). Given the great many water molecules experiencing individual random walk displacements, the overall effect of this dephasing is an interference, which reduces MRI signal amplitudes. In areas with fast water diffusion (e.g. within ventricules), the signal is deeply reduced, while in areas of slow water diffusion (e.g. white matter bundles), the signal is only slightly reduced. This differential effect results in a contrast in the diffusion-weighted MRI images, which is not visible in standard MRI images. Figure and legends from (Le Bihan, 2014)*

During my Ph.D study I have obtained an international exchange grant between the CNRS and the Japanese Society for Promotion of Science (JSPS). This allowed me to perform in vivo DW-MRI experiment in the National institute of Advanced industrial Science and technologies (AIST) in Tsukuba, Japan in Dr. Tomokazu Tzurugizawa's lab. We used a 7T MRI to image the role of astrocyte AQP4 in brain water diffusion. The effect of AQP4 blocking by the water-soluble TGN-020 on brain water diffusion was examined in mildly anesthetized mice by medetomidine. We followed the water diffusion rate in the mouse brain at different time points following TGN-020 application (**Fig. 30**). Compared to the control saline injection in vivo application of TGN-020 significantly increased the water apparent diffusion coefficient (ADC) at different cerebral areas including the cortex, hippocampus and the striatum (**Fig. 31**). This result hence indicates that astrocytic AQP4 plays a critical role in mediating brain water diffusion, a process that can be imaged by the DW-MRI.

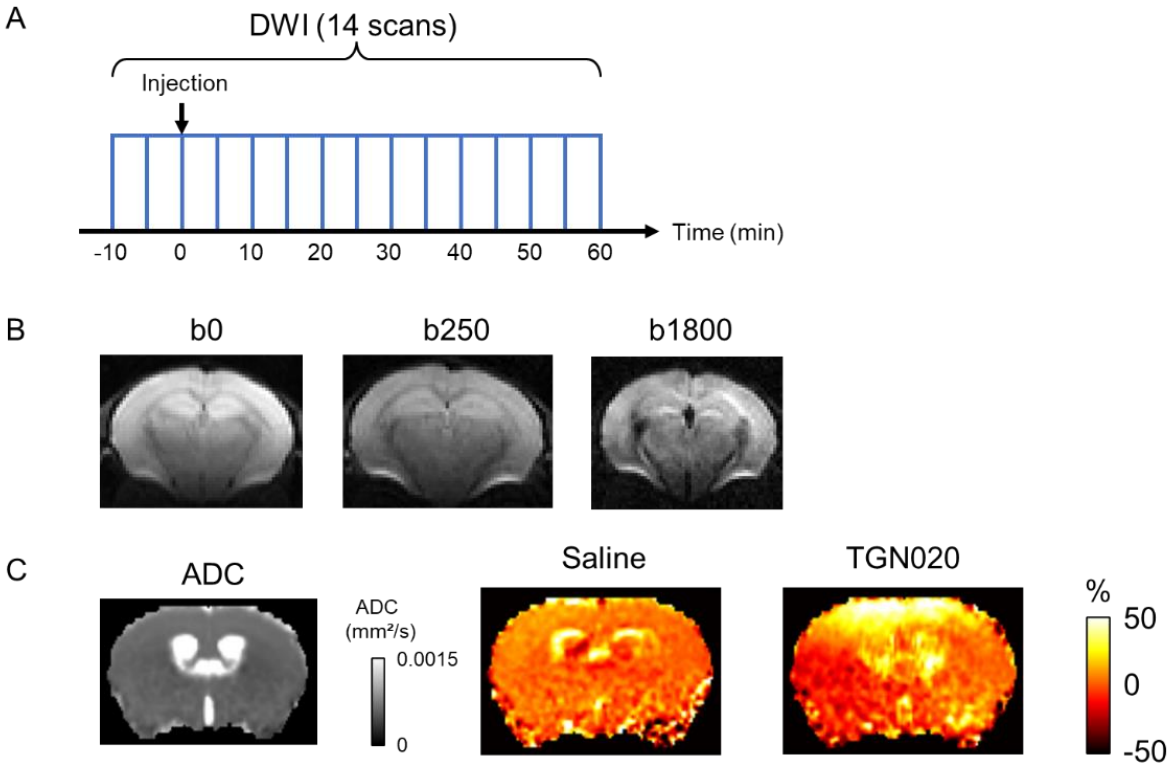

Figure 30: DW-MRI-detected water diffusion rate in mouse brain following the acute inhibition of astrocytic AQP4. *(A) Experimental design of DWI. Saline or TGN020 was injected at 10 min after the start of acquisition. DWI was acquired for 5 min in each scan. (B) Representative image of 3 b-values. (C Left) Calculated ADC image. (C Right) Representative image of percent change of ADC at 55-60 min after injection of saline or TGN020.*

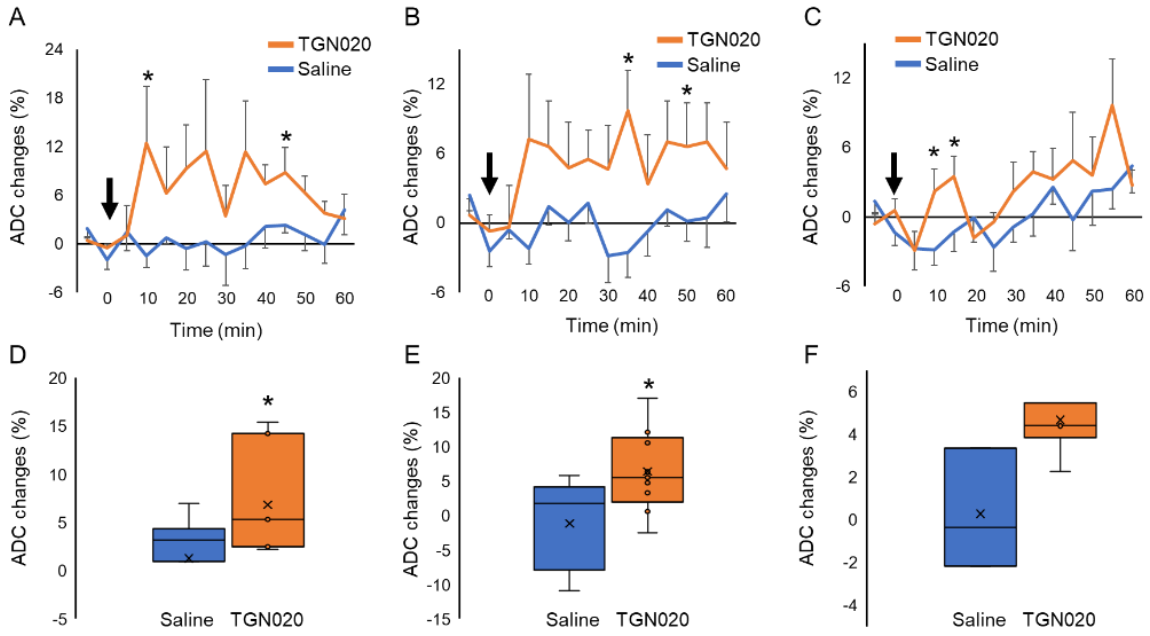

Figure 31: ADC mean values following saline or TGN-020 injection derived from diffusion MRI recordings. *Time-course of averaged ADC changes in (A) the cortex, (B) the striatum, and (C) the hippocampus. Arrowhead indicates the injection of saline or TGN020. Averaged ADC changes between 30 and 60 min after injection of saline or TGN020 in (D) the cortex, (E) the striatum, and (F) the hippocampus. *p<0.05 by paired t-test following ANOVA* ***(n****= 10 mice for saline injection, n= 9 mice for TGN-020 injection.)*

I.9 - Discussion

Brain flow transport is mediated by cerebrospinal fluid (CSF) circulation. This process plays important roles in the function, therefore the health of brain network. Disturbance in brain flow transport is being recognized as a severe factor exacerbating neurological pathologies like Alzheimer's disease.

As a major type of glial cells, astrocytes are distributed throughout the brain and strategically located between cerebral vasculature and brain parenchyma. The discovery of the critical involvement of astrocytes in brain fluid transport has led to the emergence of the concept of the glymphatic system (Rasmussen et al., 2022). It has been suggested that astrocyte volume

dynamics, via regulating the volume of the extracellular space, shapes the brain flow transport. Water flux underlies astrocyte volume regulation. Astrocytes express the bidirectional water channel Aquaporin 4 (AQP4) that has been suggested to modulate astrocyte volume change. However, the exact role of AQP4 in astrocyte volume regulation has been debated, causing an extended controversy on the mechanistic understanding of brain fluid transport and the glymphatic system.

The Chapter I study acutely discerns the role of AQP4 in astrocyte volume regulation in basal conditions and in response to environmental manipulations in brain parenchyma in mouse models. Interdisciplinary approaches have been developed or adopted, including in vivo chemical astrocyte targeting, ex vivo cellular fluorescence imaging in acute brain slices, in vivo fiberphotometry recording in freely moving animals and by diffusion-weighted magnetic resonance imaging (DW-MRI). The obtained results lead to the finding that AQP4 tonically sculpts astrocyte volume homeostasis in the brain parenchyma, perturbing of which significantly interferes with brain fluid transport. These results together shed light on the fundamental role of AQP4 in tuning astrocyte volume and therefore the extracellular route for brain flow, hence helping to reconcile the thus far debated aspects of glymphatic system and its implication in health and neurological disorders.

Regarding the physiological implications of the finding my data suggest that there is a constant net water efflux from astrocytes under the basal state of the brain. It implies that there is a constitutive water accumulation process in astrocytes. For instance, water is transported from perivascular space to brain parenchyma, which has been suggested to be a complementary mechanism for the production of the CSF in addition of the conventional sources from the choroid plexus (Drew, 2022). My finding also recalls the scenario in kidney where AQP4 abundantly expressed, directly underlining the constant efflux of water from local cells (Rasmussen et al., 2022). The observation of the AQP4 mediating basal water efflux in astrocyte might contribute to the maintenance of the convective flow in the parenchyma as claimed by the glymphatic concept (Plog and Nedergaard, 2018). This extends the early proposed mechanism supported by the arterial pulsation controlled with cardiovascular rhythms (Mestre et al., n.d.).

Taking into account of the polarized distribution of AQP4 in astrocytes, where it is enriched in the perivascular space and pial limitant (Nielsen et al., 1997). AQP4 at basal condition, tonically inhibits astrocyte swelling, suggesting it plays a more prominent role in mediating water efflux from astrocytes. Hence, AQP4 would be important for extruding water from astrocytes, into vascular circulation. It is plausible that a water efflux is critical for astrocytes to maintain their volume homeostasis (thereby the functional stability of the brain), by counterbalancing the constitutive water buildup in astrocytes. The constitutive water buildup in astrocytes could be induced by several mechanisms. In fact, a variety of co-transporters such as Na/K^+ co transporter (NKCC), bicarbonate cotransporter (NBC) and glutamate or GABA transporters (**Fig. 32**), together playing a role in bringing water into astrocytes accompanying the ion/transmitter influx (MacAulay and Zeuthen, 2010). In addition the internal water accumulation can be induced by the metabolic processes (references). Thus, it appears necessary for an efficient water efflux pathway to maintain astrocytes water homeostasis. The current observation of AQP4-mediated net water efflux would fulfill this demand. My observation shows that AQP4 is also involved in astrocyte water influx, which though, is inferior to its contribution to water efflux under basal state.

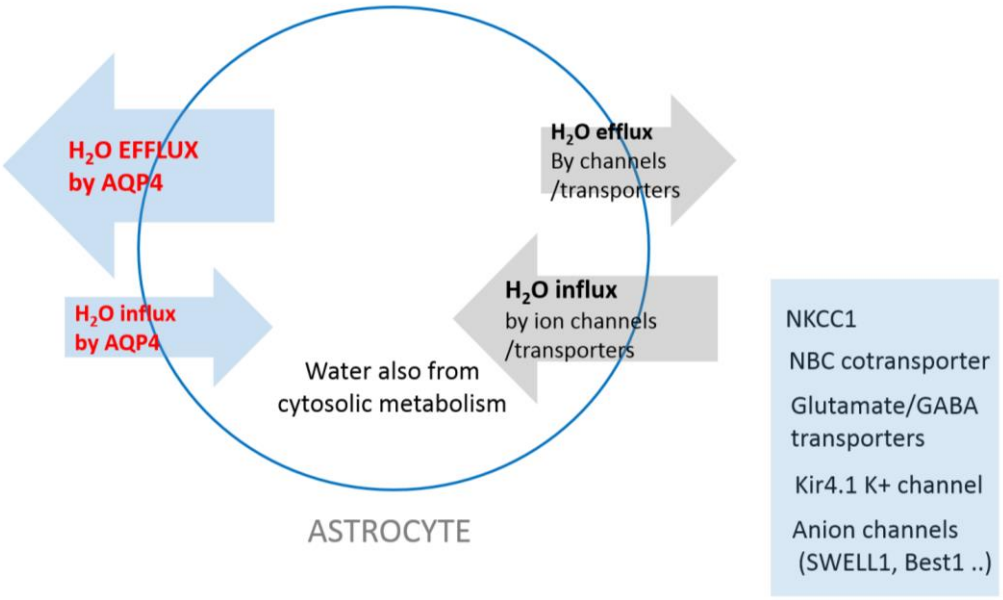

Figure 32: AQP4 mediates water efflux in astrocytes

The observation that AQP4 tonically inhibits the swelling of astrocytes lends support to the observation reported by Fiacco's group (Murphy et al., 2017) where knock-out of AQP4

facilitates astrocytes swelling induced by hypo-osmotic solution. However, as we here performed acute pharmacological inhibition of AQP4, the controversy between the results obtained with AQP4 KO animals needs be further investigated (Amiry-Moghaddam et al., 2004; Benfenati et al., 2011; Murphy et al., 2017).

The mechanism underlying the imbalanced engagement of AQP4 in astrocyte water influx and efflux could stem from at least two possibilities. One possibility is that the asymmetric role of AQP4 in water flux might be regulated at the channel level, namely AQP4 itself has an intrinsic property that facilitates more the water efflux from the cell while contributes less to the water influx. Another plausible scenario might be that AQP4 engagement in water flux is coordinated with other molecular machineries underlying water flux in astrocytes. As aforementioned, because diverse pathways could contribute to water buildup (**Fig. 32**), a net water efflux thus occurs via AQP4 at basal conditions to avoid water over accumulation in astrocytes.

Besides the physiological implications, the current results have several tiers of implications for brain pathology. In several pathologies like Alzheimer's disease, Parkinson disease, the polarization of AQP4 in astrocytic endfeet is lost and more accumulated in somatic regions (Ikeshima-Kataoka, 2016). Because intracellular metabolism is upregulated in reactive astrocytes in neurodegenerative disease and aging (Chen et al., 2022), one possibility might be that hyper-upregulated astrocytic metabolism occurs in somatic region, enriched with mitochondria (Jackson and Robinson, 2018), which would cause upregulated water production in the somatic region and thus requires more AQP4 to export water. This chronic adaptation could eventually shift the global distribution of AQP4 in astrocytes to pathological accumulation in the soma as an attempt to prevent the potential development of cytotoxic edema.

AQP4 is highly implicated in the formation and development of brain edema, but its role in the different phases of edema. In the brain, two types of edema have been documented: cytotoxic edema induced by over accumulation of water in astrocytes, and vasogenic edema caused by the massive water influx resulted from ruptured vascular system (Tait et al., 2008). Reducing AQP4 in astrocytes has been introduced as a putative strategy to slow down the formation of edema (Igarashi et al., 2011), however the specific type of edema concerned has not been discerned. My current data suggest that AQP4 mediates constant water efflux. Thus, in

conditions where cytotoxic edema firstly develops, keeping AQP4 in place, rather than simply blocking its function, would facilitate water efflux so slowing down the edema formation. However, in situations where vasogenic edema dominates, inhibiting AQP4 needs be considered at priority. Therefore, my current data suggest a mechanistic basis for condition-dependent intervention for cerebral edema amelioration.

Furthermore, my data provides a mechanistic hint for understanding the DW-MRI data. The DW-MRI data of my current study and that of (Debacker et al., 2020) both show that acutely blocking astrocyte AQP4 with TGN-020 increases water diffusion dynamics in mouse brain. My volume imaging data show that TGN-020 blocks AQP4-mediated net water efflux to cause astrocyte swelling, suggesting TGN-020 would decrease extracellular space while increasing intracellular space in astrocytes. Accordingly, the water diffusion rate would be increased inside astrocytes and reduced in extracellular space. DW-MRI provides a readout on the overall water diffusion in both intracellular and extracellular space (**Fig. 29**). Hence, a net increase in ADC in my observation reflects that TGN-020 causes an appreciable astrocyte swelling thereby an increase in the intracellular water diffusion, which surpasses the water diffusion reduction in extracellular space imposed by the swelling.

Alternatively but not exclusively, the glymphatic concept has proposed that the brain fluid in the extracellular space of parenchyma is not pure of Brownian motion, rather it represents a convective flow sustained by the arteriole pulsation and reaching the perivenous spaces (Mestre et al., 2020b). In this sense, a diminution in extracellular space as caused by TGN-020-induced astrocytes swelling would transiently increase the water diffusion rate along the glymphatic routes. Nevertheless, the current data MRI lacks sufficient spatial resolution to claim the convective flow occurring throughout the parenchyma. It is also possible that the convective flow mainly exists in perivascular space generated by local vascular pulsation as already acknowledged by conventional views on brain fluid transport (Smith and Verkman, 2019). Extending the volume imaging data, the DW-MRI results testify the important role of astrocyte AQP4 in regulating brain water diffusion. Furthermore to follow CSF/ISF diffusion in the extracellular space of brain parenchyma, specific MRI based neuroimaging techniques need to be applied. For example the diffusion weighted magnetic resonance spectroscopy (DW-MRS)

has been used to follow exogenously injected extracellular tracers like sucrose (Vincent et al, 2021).

In conclusion, my current study unveils a tonic role of AQP4 in regulating brain astrocyte volume dynamics, which helps to understand the cellular mechanism underlying astrocyte volume homeostasis, its pathological adaptation to neurological diseases and the interpretation of the MRI neuroimaging data. These data will thus contribute to the understanding of astrocyte water handling in neurophysiology and in brain disorders.

Chapter II: Probing disturbed astrocytes signals and volume regulation in amyloid pathologies

II.1 - Astrocytes and glymphatic system impairment in neuropathology

Astrocytes plays import role in brain physiology and the maintenance of body homeostasis through interactions with neurons and other glial cells. They display extensive adaptation to pathological environment, such as in neurodegenerative diseases like Alzheimer's disease, metabolic disorders, and brain injury (Buckman et al., 2013; Chiarini et al., 2017). Astrocytes show morphology remodeling, functional dysregulation, and molecular profile deviation by releasing or sensing of multiple types of cytokines and chemokines (Sofroniew and Vinters, 2010) (**Fig. 33**). Such pathological adaptation of astrocytes impairs their interaction with synaptic transmission and the regulation of neurovascular coupling. In addition, the communication between astrocytes and other glial cells including microglia, oligodendrocytes and NG2 cells can also be impaired. Such pathological changes have been proposed to either protect or to exacerbate disease development (Escartin et al., 2021).

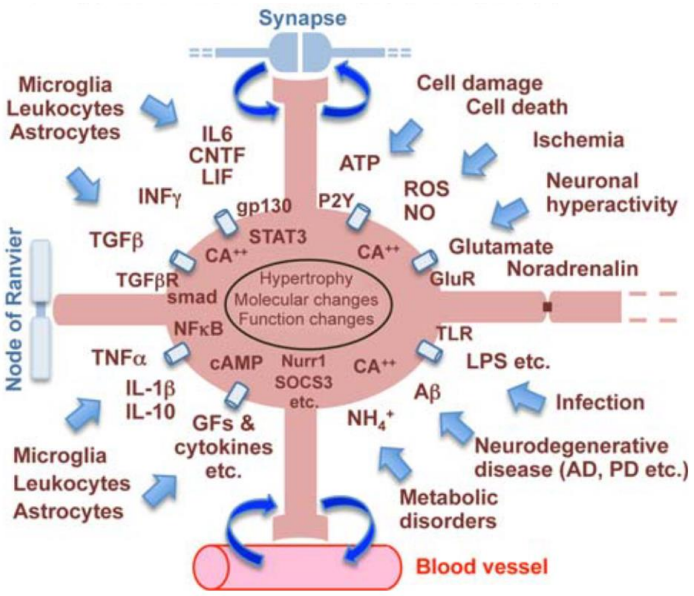

Figure 33: Astrocyte adaptations in pathologic brain (from Sofroniev et al 2010)

II.1.*1* - Astrocyte Ca^{2+} signal and neurodegenerative disease

Though electrically silent, astrocytes activity is encoded by dynamic intracellular Ca^{2+} signals. It was firstly discovered that glutamate triggers Ca^{2+} increase in astrocytes in vitro and in situ, followed by the discoveries of the expression in astrocytes of variable neurotransmitter sensitive G-protein coupled receptors (Bazargani and Attwell, 2016) (**Fig. 34**). Astrocytes Ca^{2+} signals can travel across population of cells in the CNS. It was later found that astrocyte Ca^{2+} can modulate synaptic transmission leading to the concept of the tripartite synapse (Verkhratsky and Nedergaard, 2018). In addition astrocyte Ca^{2+} was propose to trigger to release neuromodulatory signaling molecules, called the gliotransmitter (Harada et al., 2016).

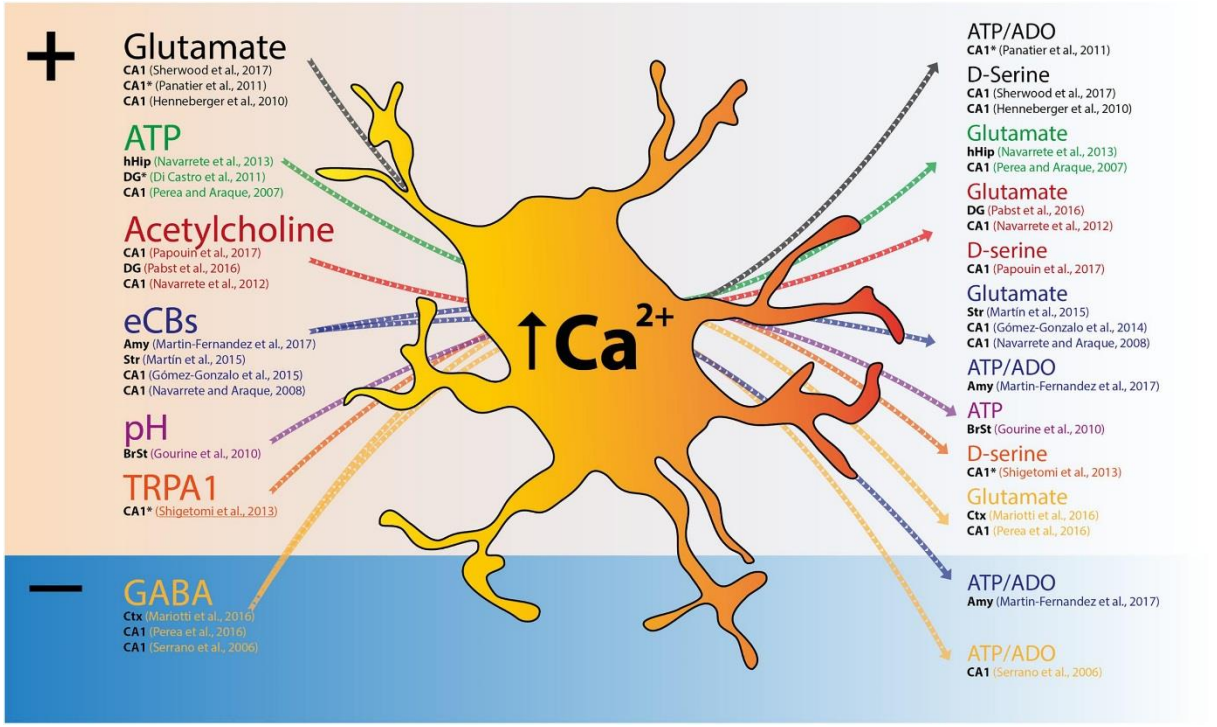

Figure 34: Excitatory and/or inhibitory signals trigger Ca^{2+} elevations in astrocytes and lead to gliotransmitter release. *Scheme depicting input signals that trigger astrocyte Ca^{2+} elevations and respective transmitter release. Both excitatory (+) and inhibitory (–) signals cause global or focal Ca^{2+} elevations in astrocytes (Left), and precede gliotransmitter release that might exert excitation or inhibition of neighboring synapses (Right). For each reference, the region studied is indicated in black (Amy, Amygdala; BrSt, brainstem; CA1, CA1 subfield of the hippocampus; Ctx, cortex; DG, dentate gyrus; hHip, human hippocampus; Str, Striatum). *Indicates the studies that described functional consequences to focal Ca^{2+}, rather than global Ca^{2+} responses. Figure and legends from (Bazargani and Attwell, 2016)*

Following the discovery that astrocytic Ca^{2+} signals are the key to understand astrocyte information procession, they are also importantly involved in the regulation of development of the CNS and neurophysiology (**Fig. 35**). For instance, in development astrocyte Ca^{2+} activity has been shown to help for synapses elimination (Yang et al 2016) and dendritic spine maturation (Sultan et al 2015; Hill et al 2019). At the cellular level astrocyte Ca^{2+} maintain extracellular K^+ homeostasis, neurotransmitter recycling and metabolism, neurovascular coupling, synaptic plasticity (Shigetomi et al., 2016). At the systemic level astrocyte $Ca^{2+}$is implicated in cognitive behavior such as memory consolidation, spatial learning, and memory retrieval (Denizot et al., 2019) Furthermore astrocytes Ca^{2+} signals are found to be important

for sensory processing, visual stimuli, somatosensory cortex plasticity, motor processing, motor coordination, and sleep (Nagai et al., 2021).

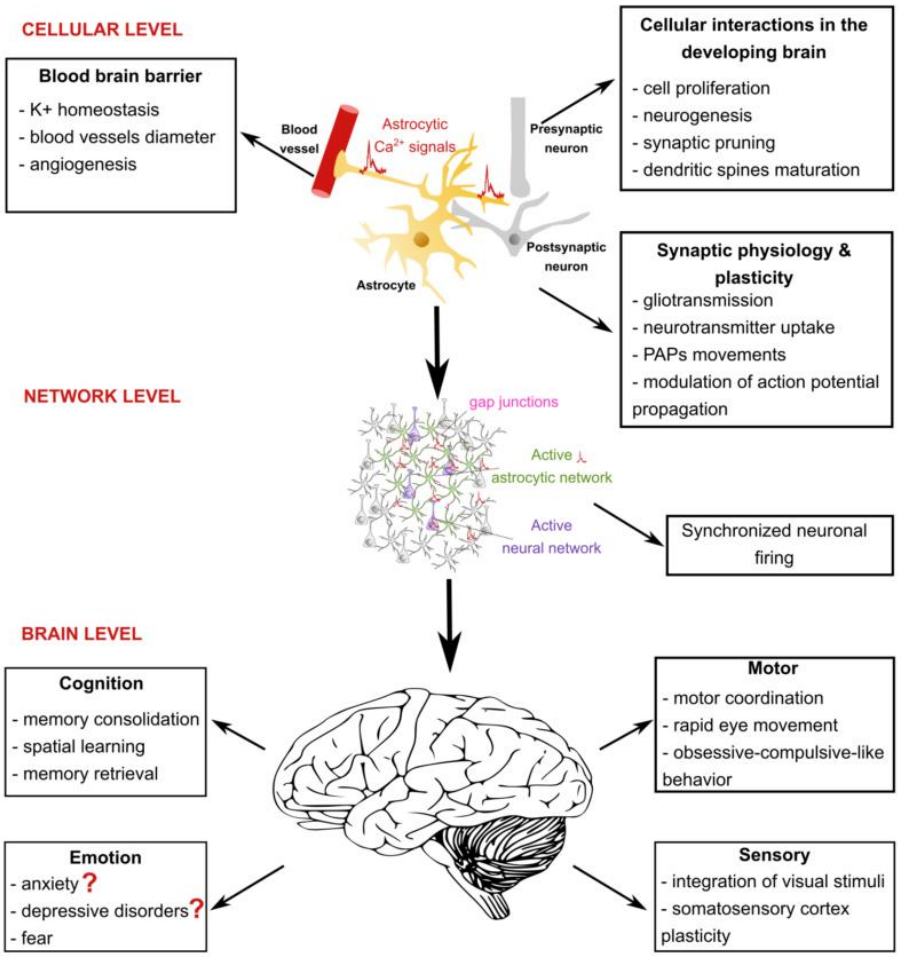

Figure 35: Functional role of astrocytic Ca^{2+}signals *(Denizot et al., 2019)*

Astrocyte Ca^{2+} is altered in brain pathologies

Glia was suggested as a contributor in brain pathologies, particularly astrocyte Ca^{2+} signals has been shown to be altered in neurological and psychiatric disorders (Denizot et al., 2019). Studies using Alzheimer's disease mouse models showed that astrocyte Ca^{2+} basal levels and transients were increased, near β-amyloid plaques (Verkhratsky, 2019). An increase of astrocyte Ca^{2+} signals was also observed in response to amyloid-β plaques (Abramov et al., 2004). In Hungtinton's disease, basal Ca^{2+} signals are reduced, however astrocytes still respond to cortical stimulation with Ca^{2+} signals (Jiang et al., 2016). In addition Ca^{2+} signaling of astrocyte has been shown to be up regulated in Parkinson's disease and epilepsy (Nedergaard

et al., 2010; Heuser and Enger, 2021). **These data raise the possibility that astrocyte Ca^{2+} signaling contributes in specific ways to brain disorders.**

II.1.*2* - Astrocyte Ca^{2+} signal modulates volume dynamics

Experimental investigations have indicated that astrocytes display Ca^{2+}-dependent cell volume dynamics. For instance using calcein based volume measurement in cultured astrocytes, Nedergaard's group has shown that ATP evocked Ca^{2+} rises in astrocytes increased their volume (**Fig. 36**; (Takano et al., 2005)).

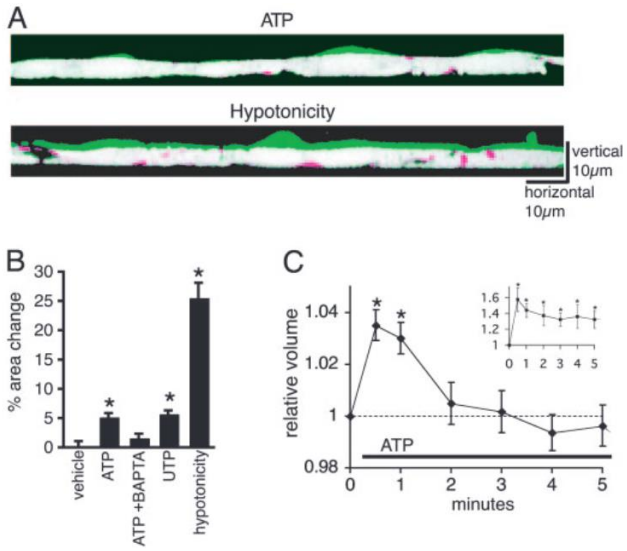

Figure 36: Astrocytic Ca^{2+} increases are associated with a transient increase in cell volume. *(A) Exposure to ATP (100µM) induces swelling of cultured astrocytes. Confocal vertical cross-sectional images of confluent astrocyte cultures with 3–5 cells in the field of view loaded with calcein AM (5M for30 min) were constructed from repetitive x-z line scans at 488 nm excitation. Two images of cross-sectional area before (red) and 1 min after the exposure to ATP (green) are overlapped to indicate the change in cell volume. Over-lapped areas (no change before and after ATP exposure) are displayed as white. Hypotonicity (214 mOsM) also induced cellular swelling. (B) Quantification of relative changes in cross-sectional areas 1 min after addition of vehicle (control,n12); ATP (100M,n23); ATP to cultures preloaded with BAPTA (20M for 30 min,n11); UTP (100M,n15) and hypotonicity (214mOsM,n6).*,P0.01 compared with control, Tukey-Kramer test. (C)Coulter counter analysis of relative changes in astrocytic cell volume evoked by ATP. ATP exposure of astrocytes in suspension triggered a transient increase in cell volume at 30 and 60 sec. (C Inset) Hypotonicity induced a large*

and sustained increase in astrocytic cell volume.n5;, P 0.05 compared with control, ttest. Mean ± SEM. (Figures and legends from (Takano et al., 2005))*

Also, the early study of our team has demonstrated that chelating basal Ca^{2+} in astrocytes using BAPTA-AM impaired the spontaneous remodeling of the plasma membrane (**Fig. 37A**). We also showed that Ca^{2+} increase in astrocytes could induce astrocytes volume change, using dual color imaging of calcein-based astrocyte volume change and glutamate-evoked Ca^{2+} dynamics in cultured astrocytes **(Fig. 37B**).

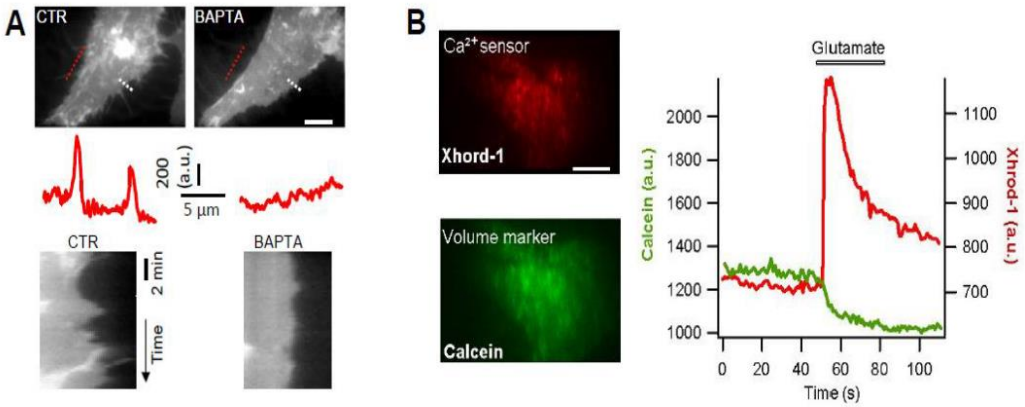

***Figure 37: Astrocytic Ca^{2+} signal modulates morphology and volume dynamics**. A, Astrocytic Ca2+ signaling is indispensable in maintaining cellular morphology and plasma membrane dynamics. The plasma membrane of primary cultured mouse cortical astrocytes was labeled by Lck-EGFP. In CTR condition, thin filaments attaching to the plasma membrane could be observed (red line scan), and the kymograph (left bottom) shows the dynamic changes of the local plasma membrane (positioned by the white dotted line) over time. In contrast, in astrocytes where intracellular Ca^{2+} signal was chelated by BAPTA-AM, near-membrane thin filaments were retracted and plasma membrane became static over time. B, Ca^{2+} rise in astrocytes alters cellular volume. The Ca^{2+} red chemical indicator Xrhod-1 and the membrane-impermeable volume marker calcein were coloaded into cultured astrocytes in their AM form. Local application of 100 µM glutamate triggered transient Ca^{2+} elevation accompanied by cell volume change reflected by the corresponding decrease in Calcein fluorescence. (Unpublished data of the host team).*

These results suggest that astrocyte Ca^{2+} plays a role in regulating the volume dynamics. In situ this phenomenon would likely regulate the extracellular space therefore the brain fluid transport in glymphatic system.

II.1.3 - Glymphatic system impairment in Alzheimer's disease

Glymphatic system, featured with the dynamic exchange between cerebrospinal fluid (CSF) and interstitial fluid (ISF), has emerged as a brain-wide clearance pathway for potentially toxic substances (Louveau et al., 2017) (**Fig. 38**). Glymphatic pathway is driven by the convective flow of the peri-arteriole CSF, through the parenchyma ISF, to the recirculation of CSF along the draining veins (Louveau et al., 2017). A functional link between the glymphatic system and the meningeal lymphatic vessels has been proposed for brain molecular clearance (Mesquita et al., 2018).

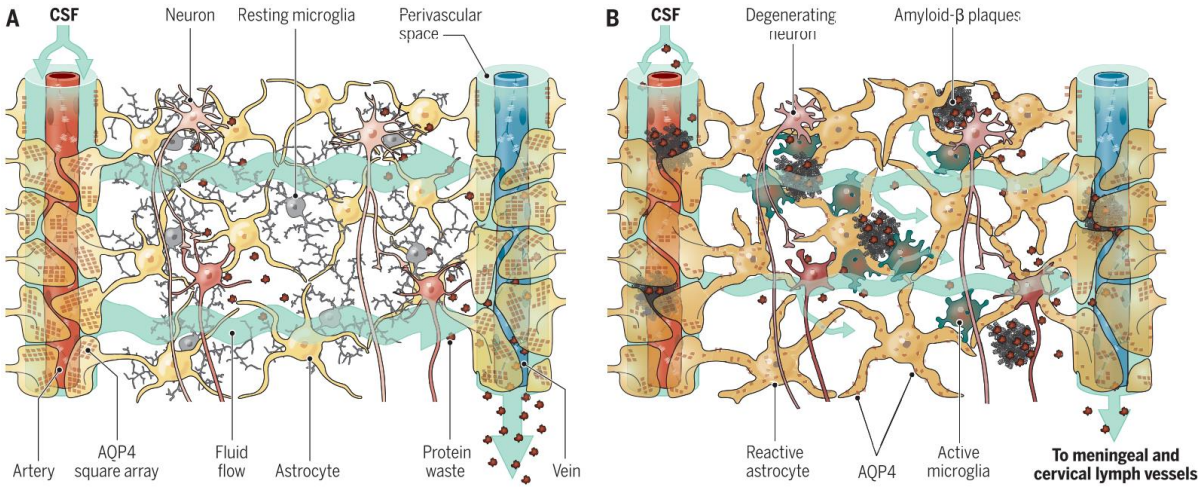

Figure 38: Impaired glymphatic system in Alzheimer's disease. *(A) Vascular endfeet of astrocytes create the perivascular spaces through which CSF enters the brain and pervades its interstitium. CSF enters these perivascular spaces from the subarachnoid space and is propelled by arterial pulsatility deep into the brain, from where CSF enters the neuropil, facilitated by the dense astrocytic expression of the water channel AQP4, which is arrayed in nanoclusters within the endfeet. CSF mixes with fluid in the extracellular space and leaves the brain via the perivenous spaces, as well as along cranial and spinal nerves. Interstitial solutes, including protein waste, are then carried through the glymphatic system and exported from the CNS via meningeal and cervical lymphatic vessels. (B)Amyloid-b plaque*

formation is associated with an inflammatory response, including reactive micro- and astrogliosis with dispersal of AQP4 nanoclusters. Age-related decline in CSF production, decrease in perivascular AQP4 polarization, gliosis, and plaque formation all impede directional glymphatic flow and thereby impair waste clearance. Notably, vascular amyloidosis might be initiated by several mechanisms. Amyloid-b might be taken up from the CSF by vascular smooth muscle cells expressing the low-density lipoprotein receptor-related protein 1 (LRP1). Alternatively, amyloid deposition might be initiated by the backflow of extracellular fluid containing amyloid-b into the periarterial space from the neuropil, rather than proceeding to the perivenous spaces, because of an increase in hydrostatic pressure on the venous side or an inflammation-associated loss of AQP4 localization to astrocytic endfeet. Figure and legends from (Nedergaard and Goldman, 2020)

Among the neurodegenerative disorders, Alzheimer's disease (AD) severely impacts the life quality of patients and imposes recurrent burden on the society (Scheltens et al., 2021). As a potential risk, the excessive brain accumulation of the amyloid β (Aβ) peptide is implicated in AD pathogenesis and the cognitive deficits(Scheltens et al., 2021). **Therapeutic strategies aiming at relieving cerebral Aβ depositions have provided promising results for further pre-clinical and clinical investigations** (Lobello et al., 2012)**.**

Efflux of Aβ across the brain vasculatures underlies its clearance (Roberts et al., 2014), hence highlighting the important involvement of glymphatic system. Glymphatic clearance has been suggested to rely on the water channel aquaporin 4 (AQP4), the most abundant water channel in the mammalian brain and predominantly expressed in astrocytes (Papadopoulos and Verkman, 2013). Despite the need for further validations (Smith et al., 2017b; Mestre et al., 2018), recent data in rodent models show that genetic or pharmacological inactivation of AQP4 impairs the glymphatic clearance of Aβ and tau (Harrison et al., 2020; Rosu et al., 2020). Manipulating astrocyte AQP4, therefore, might regulate the efficacy of glymphatic clearance so to ameliorate AD amyloidopathy. **However, it remains elusive how glymphatic clearance is impaired in brain pathology such as AD-associated amyloid deposition.**

II.2 - Hypothesis and initial explorations

Given the important implication of astrocytic volume change in shaping glymphatic system dynamics and the role of Ca^{2+} in volume regulation, I hypothesized that the pathologically altered astrocytic Ca^{2+} signaling may interfere with astrocyte volume regulation, thereby affecting extracellular diffusion route for fluid transport in the brain (e.g., the glymphatic system function).

In the Chapter II study, I (1) contributed to the exploration of pathologically altered Ca^{2+} responses of astrocytes to neurotoxic amyloid peptide (Pham et al., 2021); (2) initiated the in vivo exploration of modulating astrocyte volume dynamics in order to examine its ameliorative effect on amyloid deposition in an Alzheimer's mouse model.

II.3 - Results of experimental investigations

II.3.*1* - Astrocyte Ca^{2+} signal dysregulation by neurotoxic amyloid peptide

Excessive amounts of amyloid β (Aβ) peptide have been suggested to dysregulate synaptic transmission in Alzheimer's disease (AD). As a major type of glial cell in the mammalian brain, astrocytes regulate neuronal function and undergo activity alterations upon Aβ exposure. Yet the mechanistic steps underlying astrocytic responses to Aβ peptide remain to be elucidated. Here by fluorescence imaging of signaling pathways, we dissected astrocytic responses to Aβ25–35 peptide, a neurotoxic Aβ fragment present in AD patients. In native health astrocytes, Aβ25–35 evoked Ca^{2+} elevations via purinergic receptors, being also dependent on the opening of connexin (CX) hemichannels. Aβ25–35, however, induced a Ca^{2+} diminution in Aβ-preconditioned astrocytes as a result of the potentiation of the plasma membrane Ca^{2+} ATPase (PMCA). The PMCA and CX protein expression was observed with immunostaining in the brain tissue of hAPPJ20 AD mouse model. We also observed both Ca^{2+}-independent and Ca^{2+}-dependent glutamate release upon astrocytic Aβ exposure, with the former mediated by CX hemichannel and the latter by both anion channels and lysosome exocytosis. Our results suggest that Aβ peptide causes state-dependent responses in astrocytes, in association with a multiphasic release of signaling molecules. This study therefore helps to understand astrocyte engagement in AD-related amyloidopathy. This part of the study has been published (Pham et al., 2021).

Pham *et al. acta neuropathol commun* (2021) 9:44
https://doi.org/10.1186/s40478-021-01146-1

Acta Neuropathologica Communications

RESEARCH Open Access

Astrocytes respond to a neurotoxic Aβ fragment with state-dependent Ca^{2+} alteration and multiphasic transmitter release

Cuong Pham[1], Karine Hérault[2], Martin Oheim[3], Steeve Maldera[1], Vincent Vialou[1], Bruno Cauli[1] and Dongdong Li[1*]

Abstract

Excessive amounts of amyloid β (Aβ) peptide have been suggested to dysregulate synaptic transmission in Alzheimer's disease (AD). As a major type of glial cell in the mammalian brain, astrocytes regulate neuronal function and undergo activity alterations upon Aβ exposure. Yet the mechanistic steps underlying astrocytic responses to Aβ peptide remain to be elucidated. Here by fluorescence imaging of signaling pathways, we dissected astrocytic responses to Aβ25–35 peptide, a neurotoxic Aβ fragment present in AD patients. In native health astrocytes, Aβ25–35 evoked Ca^{2+} elevations via purinergic receptors, being also dependent on the opening of connexin (CX) hemichannels. Aβ25–35, however, induced a Ca^{2+} diminution in Aβ-preconditioned astrocytes as a result of the potentiation of the plasma membrane Ca^{2+} ATPase (PMCA). The PMCA and CX protein expression was observed with immunostaining in the brain tissue of hAPPJ20 AD mouse model. We also observed both Ca^{2+}-independent and Ca^{2+}-dependent glutamate release upon astrocytic Aβ exposure, with the former mediated by CX hemichannel and the latter by both anion channels and lysosome exocytosis. Our results suggest that Aβ peptide causes state-dependent responses in astrocytes, in association with a multiphasic release of signaling molecules. This study therefore helps to understand astrocyte engagement in AD-related amyloidopathy.

Keywords: ATP, Glutamate, Hemichannel, Lysosome, Alzheimer's disease

Introduction

Toxic Aβ peptides are implicated in the development of cognitive deficits of AD [10]. In the mammalian brain, information processing is sustained by dynamic interactions between neurons and glial cells [13]. Emerging evidence suggests that Aβ dysregulates neuron-glia communication thereby impairing synaptic transmission [33]. In the meanwhile, therapeutics targeting neuronal dysfunctions yield only limited effects [32], urging the need to examine Aβ-caused pathological adaptations in glial signaling.

Astrocytes are the major glial cell-type in the mammalian brain [34]. Albeit electrically non-excitable, their activity is encoded by intracellular Ca^{2+} signaling [43], which in turn modulates neuron activity, via for instance regulating ambient transmitter and ion recycling [19, 91], the delivery of energy fuels [76], the peri-synaptic structural remodeling [69] as well as the release of transmitter substances [5]. Astrocyte Ca^{2+} activity has been shown to be upregulated by Aβ peptides [2, 11, 85], and near amyloid plaques in AD mouse models [17, 47]. Aβ-caused Ca^{2+} hyperactivity was found to compromise neuronal survival [1]. Accordingly, inhibiting the Ca^{2+}-dependent protein phosphatase calcineurin in astrocytes ameliorates

*Correspondence: dongdong.li@inserm.fr
[1] Institute of Biology Paris Seine, Neuroscience Paris Seine, CNRS UMR8246, INSERM U1130, Sorbonne Université, 75005 Paris, France
Full list of author information is available at the end of the article

synaptic function in AD mouse model [27]. In addition, the cognitive deficit during AD progression has been attributed to synapse excitotoxicity, a process involving aberrated astrocytic handling of neurotransmitter recycling and signaling molecule release [63, 64, 90, 98]. While astrocytes are being recognized to participate in AD amyloidopathy, the dynamically weaved signaling cascades remain to be delineated.

Here, we imaged astrocytic signaling cascades in response to Aβ25–35, a neurotoxic Aβ fragment found in AD patients [4, 46, 57]. We observed that Aβ25–35 upregulated Ca^{2+} signals in primary astrocytes derived from mouse cortex, which involved the activation of metabotropic P2Y receptor and the opening of CX hemichannel. In contrast, Aβ25–35 caused a Ca^{2+} diminution in Aβ-preconditioned astrocytes that involved the potentiated Ca^{2+} extrusion via PMCA and the activation of cAMP signal. We further observed both Ca^{2+}-independent and -dependent glutamate release in astrocytes upon Aβ25–35 exposure, which relied respectively on CX hemichannel, anion channels and lysosome exocytosis. These results show a state-dependent adaptation in astrocyte responses to neurotoxic Aβ peptide, and suggest molecular targets to control astrocyte functions in AD amyloidopathy.

Materials and methods

Animals and preparation of primary cortical astrocytes

Our laboratory follows the European Union and institutional guidelines for the care and use of experimental animals (Council directive 86/609EEC). The care of experimental animals was also in conformity with the French National Charter on the ethics of animal experimentation. Primary astrocytes were cultured from the neocortex of P0-1 NMRI mice of either sex adapted from the published protocol [52, 56]. Astrocytes were plated in Petri dishes for 1 week prior to being transferred to cover slips (#1, BK-7, 25-mm, Menzel-Gläser) coated with poly-ornithine (Sigma). Cells were kept at 37 °C in a humidified 5% CO_2 atmosphere in Dulbecco's Modified Eagle Medium (DMEM, Invitrogen) supplemented with 5% fetal bovine serum (FBS, HyClone), penicillin (5 U/ml, Sigma), and streptomycin (5 µg/ml, Sigma). Recordings were made during the following week at room temperature (RT, 22–23 °C) in the standard extracellular saline containing (in mM): 140 NaCl, 5.5 KCl, 1.8 $CaCl_2$, 1 $MgCl_2$, 20 glucose, 10 HEPES (pH 7.3, adjusted with NaOH). The hAPPJ20 AD mouse model was obtained from The Jackson Lab (No: 34836-JAX), expressing mutated human amyloid precursor protein (hAPP) monogene comprising the Swedish (K670N/M671L) and the Indiana (V717F) mutations [44, 60]. The overexpression of the mutated hAPP was controlled under the human platelet-derived growth factor beta polypeptide promoter. This AD mouse model displays diffusive Aβ peptides at age ~ 5–7 months and plaques by age ~ 8–10 months [44, 60]. Breeding was made between hemizygote males and C57BL/6 females to obtain hAPPJ20 mice (~ 7 month old) for slice immunohistochemistry as stated below.

Fluorophores and drugs

The chemical Ca^{2+}-indicator dyes Oregon Green BAPTA-1 AM (OGB-1 AM) or Xrhod-1 AM (Invitrogen) were loaded into astrocytes by incubating them in dye-containing extracellular solutions (2 µM, 40 min for OGB-1; 200 nM, 10 min for Xrhod-1, respectively). To label lysosomes, astrocytes were incubated in 6.7 µM FM4-64 (Invitrogen) for 30 min. To fluorescently label ATP accumulation compartments in live cells, astrocytes were incubated in 50 µM MANT-ATP (Invitrogen) for 1 h. Prior to live cell imaging, cells were thoroughly washed during at least 30 min, and they were continuously perfused by dye-free solution (~ 0.5 ml/min) during imaging. BAPTA AM (Invitrogen; 100 µM for 50 min) was used to chelate astrocyte intracellular Ca^{2+}. Plasmids encoding fluorescent sensors were obtained from Addgene unless otherwise indicated. Lipofectamine 2000 (Invitrogen) was used for transfecting cDNA plasmids into astrocytes following the standard protocol provided by the supplier. Cells were used ~ 24 h after transfection. Suramin, MPEP, thapsigargin and Gap26 were purchased from Tocris, 2-APB from Ascent Scientific, forskolin from Abcam, Aβ25–35 from Bachem, and all other compounds from Sigma-Aldrich. Dual-channel local perfusion system was used to switch smoothly between control solution and specific pharmacological manipulations, and controlled by electric valves operated by a TTL trigger box commanded by MetaMorph (Molecular Devices). Immunostaining for mouse brain slices was performed following the standard protocol as previously described [70]. As for immunostaining of astrocyte primary cultures, cells were fixed with 1% paraformaldehyde (PFA, Sigma-Aldrich) for 10 min at RT, then washed three times with phosphate buffered saline (PBS, 5 min, at RT). After permeabilization and blockage of unspecific sites with PBS, 0.3% Triton X-100 and 2% bovine serum albumin (PBS-BT, 1 h at RT), astrocytes were probed with respective primary antibodies in the same solution overnight at 4 °C. After being washed with PBS three times at RT, cells were incubated with secondary antibodies in PBS-BT (2 h, RT). After three times of final washing (PBS, 5 min, RT) and rinsed afterwards with triple distilled water, cells were mounted with Mowiol (Millipore, Darmstadt, Germany) onto microscope

slides. Combinations of the primary and secondary antibodies used for fluorescence immunostaining are listed in Additional file 1: Table S1.

Fluorescence imaging and analysis

Total internal reflection fluorescence (TIRF) imaging was performed on a custom-made inverted microscope via the through-the-objective configuration (PlanApo TIRF × 60/NA1.45 oil objective, Olympus) [61]. The 488- and 568-nm excitation wavelengths were isolated from the beam of an Ar^+/Kr^+ multi-line laser (CVI Melles Griot) with an acousto-optical tunable filter (AA.Opto). Laser beam was directed onto the glass/water interface at a super-critical angle, thereby enabling the total reflection of the excitation beam and the generation of evanescent field on the side of astrocyte substrate. The penetration depth ($1/e^2$-intensity decay) of the evanescent field was estimated of the order of 200 nm [61], thereby allowing ultrathin optical sectioning in astrocyte subplasmalemmel region for dynamic signal recording. Emission fluorescence was further magnified (× 2) and acquired by an electron multiplying charge-coupled device (EMCCD, QuantEM 512, Princeton Instruments), and the effective pixel size in fluorescent images was 133 nm. The imaging hardwares were all controlled by MetaMorph software (Molecular Devices). For TIRF imaging, each field of view in general contains the footprint of a single astrocyte. In our recording, two to three separate astrocyte culture preparations were used and about three independent coverslips of each preparation for TIRF imaging per condition. Results were derived from signals of all recorded cells.

Background was estimated from the autofluorescence signal in non-labeled cells of the same preparation, and then subtracted from the fluorescent images. The contour of the footprint of single astrocytes was delineated with the ImageJ plugin Cell Outliner or with MetaMorph segmentation tool, from which the mean fluorescence was measured over time to generate the time courses of specific signals. The FRET ratio of the cAMP sensor GFP(nd)-EPAC1(dDEP)-mCherry and the donor/acceptor bleed-through control was obtained as previously reported [71]. During TIRF imaging, the 488-nm laser line was used to excite the cAMP sensor, while both GFP and mCherry fluorescence were simultaneously collected and projected by a custom image splitter side-by-side onto a single EMCCD camera. Details of the optical filter set are listed in Additional file 1: Table S2. Corrected by the amount of acceptor direct excitation and donor bleed-through [71], the FRET signal was calculated from the GFP/mCherry ratio and normalized to the pre-stimulation basal level as fractional changes.

Statistics

All data are expressed as mean ± standard deviation (SD), and the t-test was used for assessing the significance. Comparison of non-normally distributed data was also validated using their median ± absolute deviation and the non-parametric tests (Kolmogorov–Smirnov or Mann–Whitney U-test). All statistical operations were performed with Matlab (The MathWorks), with n.s., denoting non significant, $^*p < 0.05$, and $^{**}p < 0.01$.

Results

Astrocytic Ca^{2+} elevation induced by neurotoxic Aβ25–35

To study the acute response of astrocytes to Aβ, we used TIRF microscopy (TIRFM) to image near-membrane Ca^{2+} transients in primary astrocytes cultured from mouse cortex. With the cytosolic Ca^{2+} indicator OGB-1 AM, we observed an oscillatory Ca^{2+} increase upon the local application of submicromolar Aβ25–35 (0.5 μM, temporal integral = 17.6 ± 9.5 dF/F_0*s; Fig. 1a). Higher doses of Aβ evoked stronger (6 μM, integral = 119.5 ± 25.4 dF/F_0*s) and longer-lasting Ca^{2+} signals following a temporal delay (43.5 ± 21.6 s; Fig. 1b, c). This signal was absent in response to extracellular control solutions, either without Aβ peptide or containing the sequence-reversed peptide Aβ35–25 (6 μM, Additional file 1: Fig. S1a). To further confine Ca^{2+} detection in subplasmalemmal region, we also used the plasma membrane-targeted Ca^{2+} sensor Lck-GCaMP3 [80] (Fig. 1d, e). As before, Ca^{2+} elevations could be detected in response to submicromolar Aβ25–35 and gradually reached to a plateau level with increased doses (Fig. 1f). The similarity in Ca^{2+} profiles detected with the bulk indicator OGB-1 and the subplasmalemmal sensor Lck-GCaMP3, suggests that the neurotoxic Aβ25–35 causes Ca^{2+} elevations throughout astrocyte cytosol.

Purinergic activation contributes to Aβ-evoked astrocytic Ca^{2+} rise

Aβ peptides have been suggested to induce Ca^{2+} influx [1, 18], while other studies showed the contribution of intracellular Ca^{2+} release from the endoplasmic reticulum (ER) store [3, 31, 85]. We therefore examined in primary astrocytes the mechanism for Aβ25–35-evoked Ca^{2+} rise. Compared to control condition (temporal integral dF/F_0*s = 31.2 ± 11.9; Fig. 2a, j), removing Ca^{2+} from extracellular solution diminished the Aβ25–35-evoked Ca^{2+} signal (integral = 9.7 ± 10.1, $p < 0.01$; Fig. 2b, j). We then kept the extracellular Ca^{2+} at normal level while pre-depleting the internal ER Ca^{2+} store. To this end, the ER-resident Ca^{2+} ATPase was inhibited by thapsigargin (TG, 0.5 μM), which caused a prominent discharge of Ca^{2+} from ER store (Fig. 2c, top). This treatment

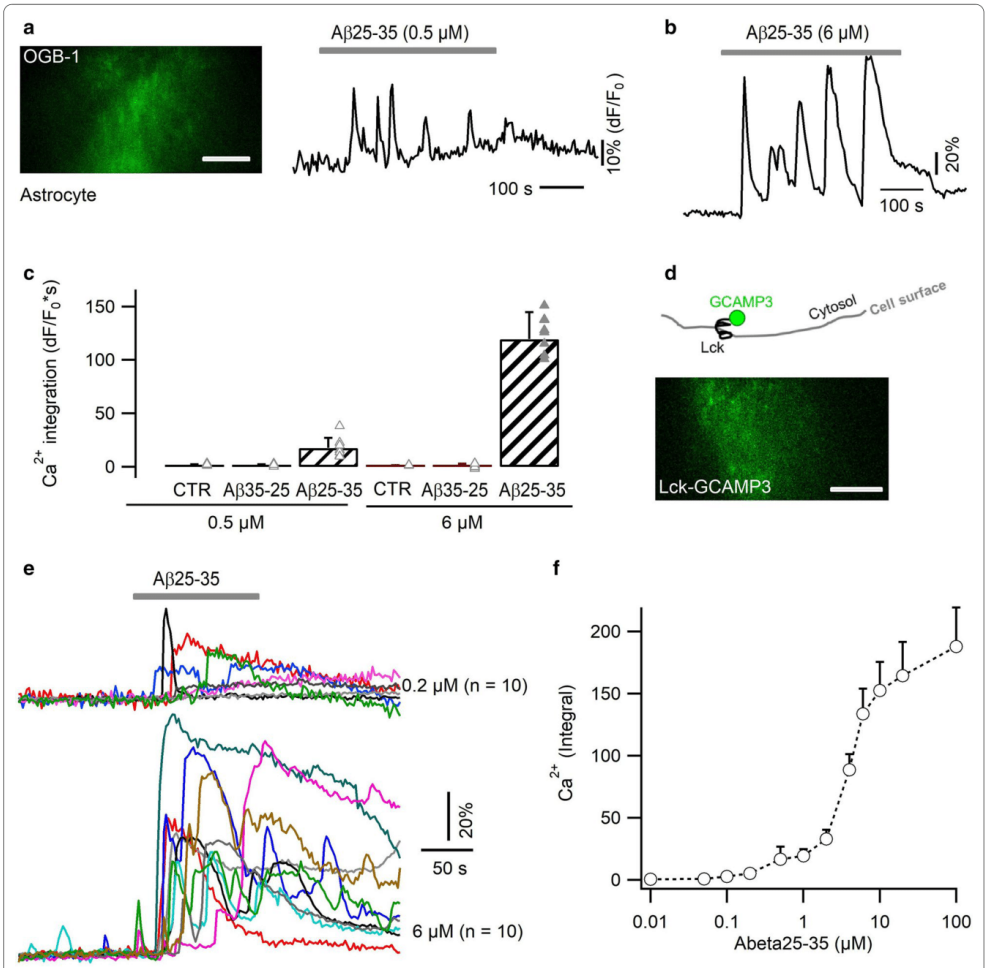

Fig. 1 Neurotoxic Aβ25–35 peptide triggered irregular Ca^{2+} rises in primary astrocytes. **a**, **b** Aβ-triggered Ca^{2+} transients in primary cultures of mouse cortical astrocytes, imaged with the chemical Ca^{2+} indicator OGB-1 AM. Subplasmalemmal Ca^{2+}-dependent fluorescence changes were selectively imaged by TIRFM. **c** Dose–response of the Aβ25–35 effect. The strength of Ca^{2+} signals was evaluated by their temporal integral over the same recording period (n = 8–13 astrocytes per condition). **d** Lck-GCaMP3 was expressed on the inner side of the astrocytic plasma membrane. Below, representative TIRFM image. **e** Astrocytic Ca^{2+} signals evoked by 0.2 μM and 6 μM Aβ25–35, respectively. Each trace denotes the response from a single cell. **f** Dose-responses curve of astrocyte Ca^{2+} response to Aβ peptide (n = 7–12 per condition). Scale bars, 10 μm

significantly decreased the subsequent responses to Aβ25–35 (integral = 18.5 ± 13.7%, $p < 0.05$; Fig. 2c, bottom; j). Since Ca^{2+} release from ER store is mediated by the inositol 1,4,5-trisphosphate (IP3) receptor, we examined the effect of its blocker 2-Aminoethoxydiphenyl borate (2-APB, 200 μM) and we also observed an inhibition impact (integral = 17.8 ± 9.6, $p < 0.05$; Fig. 2d, j). Thus, both Ca^{2+} influx and release from the ER store contribute to the Aβ-evoked astrocytic Ca^{2+} signal.

Ca^{2+} release from the internal store is recruited by the activation of metabotropic receptors. Astrocytes express a variety of receptors, among which

metabotropic glutamate receptor 5 (mGluR5) and purinergic P2 receptors respond with Ca^{2+} rises to glutamate and ATP, respectively [6]. While antagonizing mGluR5 with the group I mGluR antagonist MPEP showed no effect (50 µM, $p = 0.6$; Fig. 2e, j), Aβ-evoked Ca^{2+} signals were fully abolished by the combination of P2 receptor antagonists PPADS (100 µM) and suramin (50 µM, $p < 0.01$; Fig. 2f, j). This indicates that Aβ-induced Ca^{2+} increase requires the activation of astrocytic P2 receptors. Although both ionotropic P2X and metabotropic P2Y receptors were suggested to regulate astrocytic Ca^{2+} signal, we observed that the wide-spectrum P2X antagonist TNP-ATP [41] failed to inhibit Aβ-triggered Ca^{2+} rise (10 µM, $p = 0.53$, Fig. 2j). In contrast, the Aβ response was inhibited by antagonizing the P2Y1 receptor (5 µM MRS2179, integral $= 17.5 \pm 7.8$, $p < 0.01$; Fig. 2g, j), in line with its contribution to astrocyte Ca^{2+} hyperactivities in AD mouse model [17].

Metabotropic receptor activation triggers Ca^{2+} release from internal ER store, which then activates store-operated channels (SOCs) to induce Ca^{2+} influx [83]. Lipophilic molecules including Aβ peptide were suggested to facilitate Ca^{2+} influx through astrocytic SOCs [74, 88]. To image SOC-mediated Ca^{2+} upon, we used a standard protocol to image SOC-mediated Ca^{2+} influx [83]. ER store was first depleted by thapsigargin in Ca^{2+}-free solution, and then Ca^{2+} added back to generate SOC-mediated Ca^{2+} influx (Fig. 2h). Presence of Aβ25–35, indeed, facilitated SOC Ca^{2+} influx (peak amplitude, $dF/F_0 = 1.46 \pm 0.36$ vs. CTR 0.77 ± 0.27, $p < 0.05$; Fig. 2h), suggesting its contribution to the Ca^{2+} oscillations following P2Y1 receptor activation. These results corroborate the dual dependence of Aβ-evoked Ca^{2+} signal on both the internal store and Ca^{2+} influx (Fig. 2b, c, j).

One possible mechanism underlying P2Y1 activation by Aβ might be that it activated ATP-releasing pathways in astrocytes. In spinal cord and hippocampal astrocytes, ATP release was suggested to be mediated by the pore-forming P2X7 receptor [95], although its expression in astrocytes of specific regions was called into reconsideration [59]. We observed that P2X7 antagonist A740003 (20 µM) [35] failed to affect Aβ-triggered Ca^{2+} signal, echoing the absence of an effect of the wide-spectrum P2X blocker TNP-ATP (Fig. 2j). Alternatively, astrocytes express connexin (CX) hemichannels that mediate ATP release in physiological and pathological conditions [28, 98]. Immunostaining of CX43 protein was observed on the surface of cortical astrocytes in culture and in the cortex of hAPPJ20 AD mouse model [44, 60] (Additional file 1: Fig. S2). We found that blocking CX hemichannels with carbenoxlone (CBX, 50 µM) reduced Aβ-elicited Ca^{2+} oscillation (integral $= 13.2 \pm 15.5$ vs. CTR 37.5 ± 24.9, $p < 0.05$; Fig. 2i, j). Although astrocyte ATP was also shown to be released by pannexin hemichannel [36], its blocker probenecid (500 µM) failed to alter the Aβ25–35 effect (Fig. 2j). Hence, Aβ-caused Ca^{2+} oscillaitons depend on the opening of CX hemichannels, by which ATP might be released to activate the P2Y1 purinergic receptor.

Aβ diminishes Ca^{2+} level in preconditioned astrocytes

Astrocytes change status over chronic Aβ exposure [4, 64]. In AD patients and mouse models, astrocytes become reactive near Aβ plaques [55]. To examine potential response alterations in Aβ-conditioned astrocytes, we pre-incubated primary astrocyte cultures with submicromolar Aβ25–35 (0.5 µM) for different durations. Such preconditioning reduced the number of astrocytes displaying Ca^{2+} rises ('Rise' type response, Fig. 3a *left*) in response to the subsequent acute Aβ25–35 challenge, and over time started diminishing the basal Ca^{2+} level ('Mix' type resposne, Fig. 3a *middle*). After a 2-h preconditioning, most astrocytes responded to Aβ25–35 with a diminution in basal Ca^{2+} level ('Drop' type response, Fig. 3a *right*; Fig. 3b, versus control Additional file 1: Fig.

(See figure on next page.)

Fig. 2 A purinergic pathway underlies Aβ-evoked Ca^{2+} signal. Representative responses evoked by Aβ25–35 in astrocytes loaded with the chemical Ca^{2+} indicator OGB-1 AM, in control condition (**a**), in Ca^{2+}-free extracellular solution (**b**), following thapsigargin (TG, 0.5 µM) depletion of ER Ca^{2+} store (**c**, top trace reflecting the Ca^{2+} leak signal upon TG application), in the presence of the IP3 receptor antagonist 2-APB (**d**, 200 µM), and of the mGluR5 antagonist MPEP (**e**, 50 µM). Each trace represents the response of a single astrocyte. **f** Aβ-evoked Ca^{2+} responses were fully abolished by blocking purinergic P2 receptors with the combination of wide-spectrum antagonists PPADS (100 µM) and suramin (50 µM). **g** The P2Y1 antagonist MRS2179 (5 µM) attenuated Aβ-induced Ca^{2+} responses. **h** Aβ25–35 enhanced Ca^{2+} influx via store-operated channels (SOCs). SOCs were activated by fully depleting the ER store with TG in Ca^{2+}-free solution. SOC-mediated Ca^{2+} influx was induced by re-supplying Ca^{2+} in the extracellular solution. Ca^{2+} influx was significantly increased in the presence of Aβ25–35 (n = 11 cells per condition). **i** Effect of blocking connexin hemichannels with CBX (50 µM). **j** Aβ-evoked astrocyte Ca^{2+} responses in different conditions. Ca^{2+} signal strength was derived from the temporal integral of individual normalized traces (dF/F_0*s). Wide-spectrum P2X receptor antagonist TNP-ATP, P2X7 antagonist A740003 and pannexin blocker probenecid were applied at 10 µM, 20 µM and 500 µM, respectively. Control experiments were performed for a defined set of experiments as shown (n = 9–20 cells per condition)

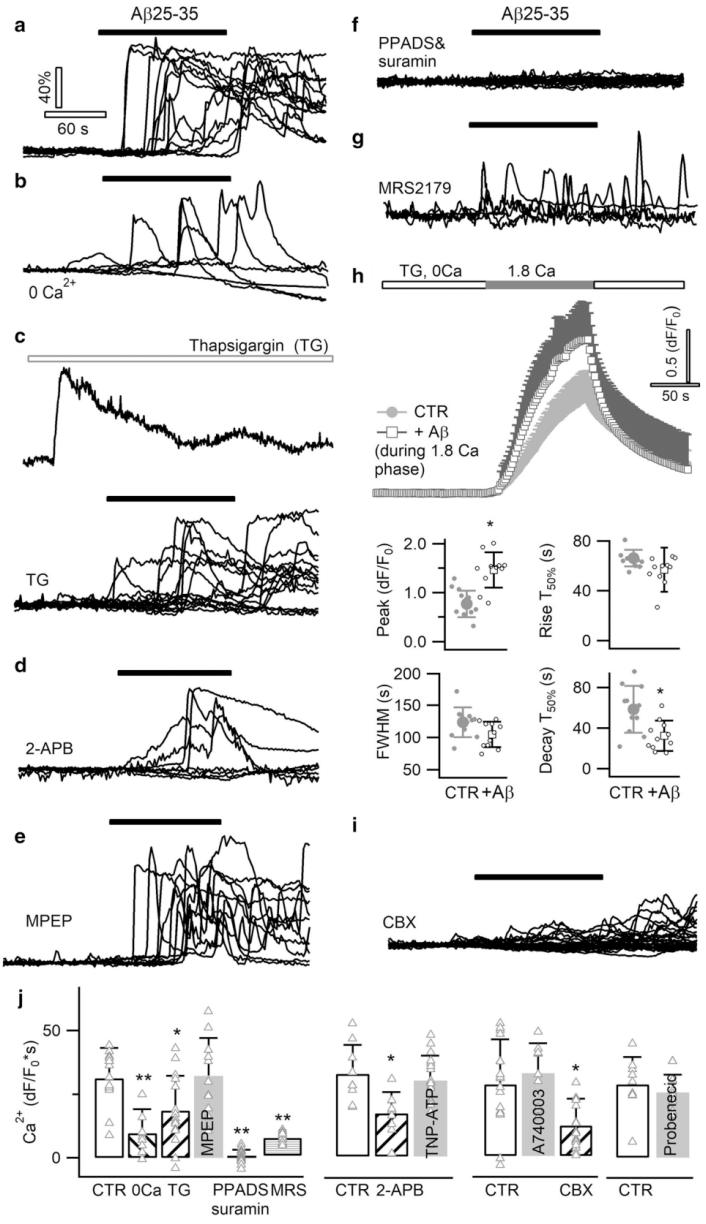
a
Aβ25-35
40%
60 s
b
0 Ca2+
c
Thapsigargin (TG)
TG
d
2-APB
e
MPEP
f
Aβ25-35
PPADS& suramin
g
MRS2179
h
TG, 0Ca
1.8 Ca
0.5 (dF/F0)
50 s
CTR
+ Aβ
(during 1.8 Ca phase)
Peak (dF/F0)
Rise T50% (s)
FWHM (s)
Decay T50% (s)
CTR +Aβ
i
CBX
j
Ca2+ (dF/F0*s)
CTR 0Ca TG
PPADS suramin
MRS
MPEP
CTR 2-APB
TNP-ATP
CTR
CBX
A740003
CTR
Probenecid

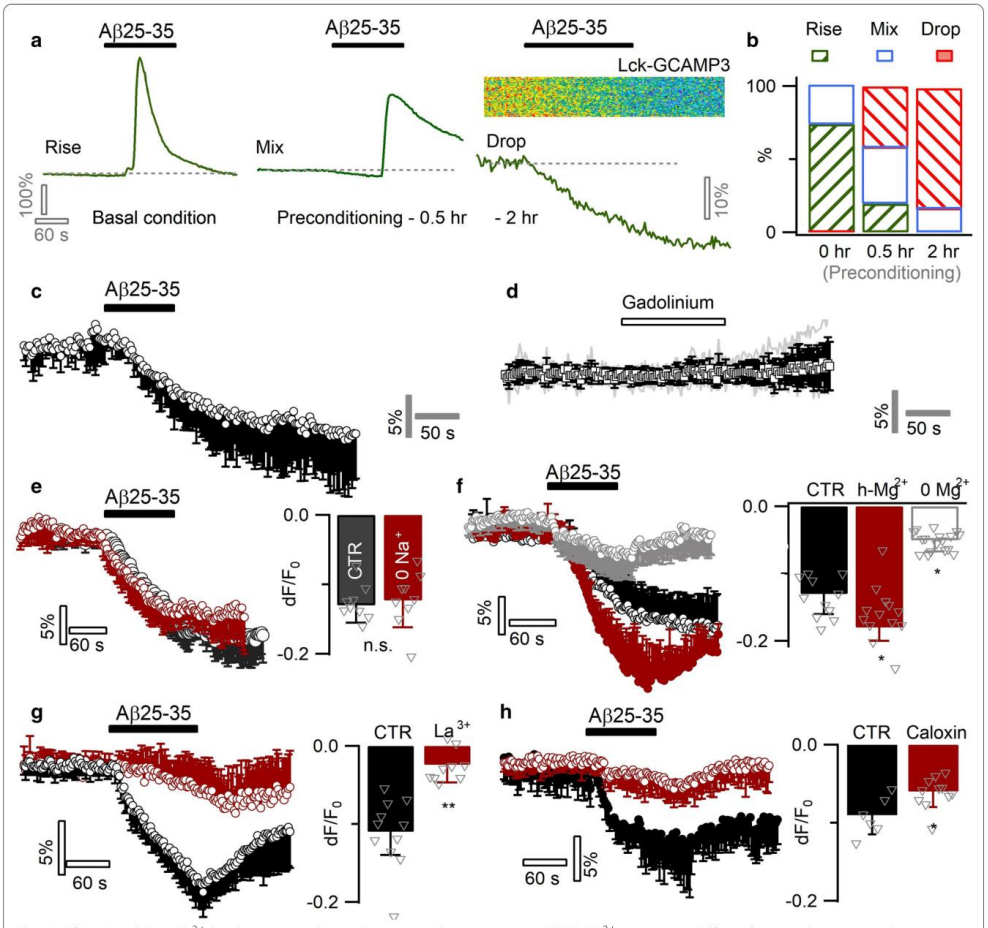

Fig. 3 Aβ25–35 inhibits Ca^{2+} levels in preconditioned astrocytes by potentiating PMCA Ca^{2+} extrusion. **a** Effect of preconditioning on the acute responses of Aβ25–35 (6 μM) in cultured mouse cortical astrocytes. Left, Ca^{2+} rise was triggered in intact astrocytes ('Rise' type response). Middle, after a short term incubation (i.e., preconditioning) of astrocytes with submicromolar Aβ25–35 (0.5 h, 0.5 μM), acute application of 6 μM Aβ25–35 caused a basal line drop mixed with Ca^{2+} rise ('Mix' type response). Right, following a ~ 2 h preconditioning in 0.5 μM Aβ25–35, astrocytes exhibited only a drop in the intracellular Ca^{2+} level ('Drop' type response). **b** The percentage of three types of astrocytes that either displayed a Ca^{2+} rise ('Rise'), an initial diminution followed by rise ('mix'), or only a drop in the basal Ca^{2+} levels (Drop'; n = 19–7 cells per condition). **c** Average of Aβ-induced Ca^{2+} diminution in Aβ25–35-preconditioned (2 h) astrocytes (n = 11). **d** Blocking spontaneous Ca^{2+} influx by gadolinium (100 μM) failed to mimic Aβ-evoked Ca^{2+} diminution (n = 8). **e** Inactivating NCX by Na^+-free solution showed no effect (n = 9 per condition). **f** Aβ-induced Ca^{2+} diminution affected by ambient Mg^{2+} concentration, implying the recruitment of an ATP-dependent pathway. Astrocytes were incubated in defined solutions 1 h prior to imaging (n = 11–17 per condition). **g**, **h** Inhibiting PMCA by La^{3+} (50 μM) or Caloxin 3A1 (500 μM) counterbalanced the Aβ-evoked astrocytic Ca^{2+} diminution (n = 6–11 per condition)

S1b). Spontaneous Ca^{2+} rises that occurred in a subpopulation of pre-conditioned astrocytes (16/117 cells), were also inhibited by an acute application of Aβ25–35 (Additional file 1: Fig. S1c, d).

We then probed potential mechanisms underlying the inhibition effect of Aβ. Spontaneous Ca^{2+} entry via SOC and the transient receptor potential cation channel A1 (TRPA1) channel regulates basal Ca^{2+} level in astrocytes [81, 83]. The inhibition effect of Aβ25–35 might be due to the blockade of this spontaneous Ca^{2+} entry. Yet blocking SOC and TRPA1 channels by the wide-spectrum blocker gadolinium (Gd^{3+}, 100 μM) [72, 81] failed to mimic the effect of Aβ25–35 (Fig. 3c, d). Alternatively, the Ca^{2+} diminution might be due to the potentiation of Ca^{2+} extrusion. We noted that chronic pre-conditioning of astrocytes with low Aβ25–35 gradually elevated intracellular Ca^{2+} level (Additional file 1: Fig. S1e). The overload of Ca^{2+} would likely facilitate its extrusion due to the increased efflux driving force. Potential extrusion pathways include Na^+/Ca^{2+} exchanger (NCX) that utilizes the Na^+ gradient to export intracellular Ca^{2+} and the plasma membrane Ca^{2+} ATPase (PMCA) driven by ATP hydrolysis [7, 26, 73]. Inhibiting NCX with Na^+-free external solution showed no effect on Aβ-caused Ca^{2+} diminution ($dF/F_0 = -12.6 \pm 6.7\%$ vs. CTR $dF/F_0 = -12.9 \pm 5.6\%$, $p = 0.7$; Fig. 3e). We then examined the role of PMCA ATPase. As ATP requires the binding to Mg^{2+} to become biologically active in the form Mg-ATP [30, 92], we sought to up- and down-regulate PMCA activity by bathing astrocytes, respectively, in high (20 mM) or zero concentration of extracellular Mg^{2+} (vs. CTR, 1 mM). This manipulation proportionally altered Aβ-induced Ca^{2+} decline (Fig. 3f). Further, the wide-spectrum PMCA blocker La^{3+} (50 μM) [7, 14, 82], largely antagonized the Ca^{2+} diminution induced by Aβ25–35 ($dF/F_0 = -2.4 \pm 3.7\%$ vs. CTR $dF/F_0 = -11.3 \pm 4.9\%$, $p < 0.01$; Fig. 3g). A similar effect was observed with the PMCA-blocking peptide caloxin 3A1 [22, 65] (500 μM, $dF/F_0 = -5.9 \pm 1.9\%$ vs. CTR $dF/F_0 = -9.1 \pm 2.3\%$, $p < 0.05$; Fig. 3h). As PMCA exports Ca^{2+} against its transmembrane gradient, we expected this process to be facilitated by the removal of extracellular Ca^{2+}. Indeed, Ca^{2+}-free external solution largely augmented the Aβ-potentiated Ca^{2+} efflux (Additional file 1: Fig. S1f). The expression of PMCA in astrocytes was observed by immunohistochemistry. Astrocytes characterized by GFAP immunostaining could be observed in the cortical region of a hAPPJ20 AD mouse model [44, 60] (Additional file 1: Fig. S3a). We observed PMCA immunostaining in GFAP-positive astrocytes in culture (Additional file 1: Fig. S3b). PMCA expression was also present in cortical astrocytes identified by a wide-spectrum marker S100β (Additional file 1: Fig. S3c), suggesting a general involvement of PMCA in astrocyte activity regulation. These results, together, suggest that Aβ25–35 potentiates PMCA-mediated Ca^{2+} extrusion in preconditioned astrocytes, thereby diminishing the intracellular Ca^{2+} level.

Aβ activates PMCA Ca^{2+}–H^+ exchange via cAMP signal

We next examined the signaling link between Aβ25–35 and PMCA potentiation. PMCA is activated upon intracellular rise of Ca^{2+} so as to prevent its overload [7, 62]. In preconditioned astrocytes, Aβ25–35 diminished basal Ca^{2+} level independent of its elevation, suggesting other signaling pathways than Ca^{2+} had been recruited. Another second messenger cAMP is also known to potentiate PMCA activity [16, 40]. Indeed, elevating cytosolic cAMP by forskolin (100 μM) induced a diminution in basal Ca^{2+} level (peak $dF/F_0 = -7.5 \pm 3.1\%$) in primary cultured astrocytes, which was counteracted by the PMCA blocker La^{3+} (50 μM, $dF/F_0 = -0.82 \pm 0.7\%$, $p < 0.01$; Fig. 4a). Forskolin also inhibited the spontaneous Ca^{2+} transients observed in a subpopulation of preconditioned astrocytes (Additional file 1: Fig. S1g), as seen with Aβ25–35 (Additional file 1: Fig. S1c, d). By a fluorescent FRET sensor GFP^{nd}-EPAC(dDEP)-mCherry [49, 87], astrocytic cAMP increase was detected upon Aβ25–35 application (Fig. 4b). These results suggest that cAMP signal is involved in Aβ potentiation of PMCA Ca^{2+} extrusion.

PMCA couples Ca^{2+} export with H^+ influx [7, 14]. In preconditioned astrocytes, we therefore performed dual-color imaging to simultaneously follow intracellular pH and Ca^{2+} dynamics during Aβ application. As the fluorescence of GFP protein can be quenched by H^+ [45], we used it here as a pH sensor. Meanwhile, we co-expressed a red-fluorescent Ca^{2+} sensor protein GECO-R [102] to image cytoplasmic Ca^{2+}. We observed a concomitant decrease in GFP fluorescence ($dF/F_0 = -4.0 \pm 3.7\%$) upon Aβ25–35-induced Ca^{2+} diminution ($dF/F_0 = -7.1 \pm 2.3\%$; Fig. 4c), indicating PMCA-mediated H^+ influx accompanying the Ca^{2+} extrusion. Consistently, such phenomenon was abolished by chelating cytosolic Ca^{2+} with 100 μM BAPTA AM (GFP, $dF/F_0 = 1.1 \pm 1.7\%$, $p < 0.01$; Fig. 4c). In preconditioned astrocytes that displayed mixed Ca^{2+} responses (i.e., *an initial Ca^{2+} diminution followed by elevation*) to Aβ25–35, we observed stepwise H^+ influx recorded by GFP quenching (Additional file 1: Fig. S1h) confirming the recruitment of PMCA by both Ca^{2+} phases. It is worth noting that H^+ is a potent inhibitor of astrocytic CX hemichannels [77]. In preconditioned astrocytes, Aβ25–35 pontentiates PMCA causing Ca^{2+} diminution and H^+ influx that would have inhibited CX hemichannels, an effect found to inhibit Ca^{2+} rises (Fig. 2i, j). Astrocytes hence display state-dependent Ca^{2+} responses to the neurotoxic Aβ25–35.

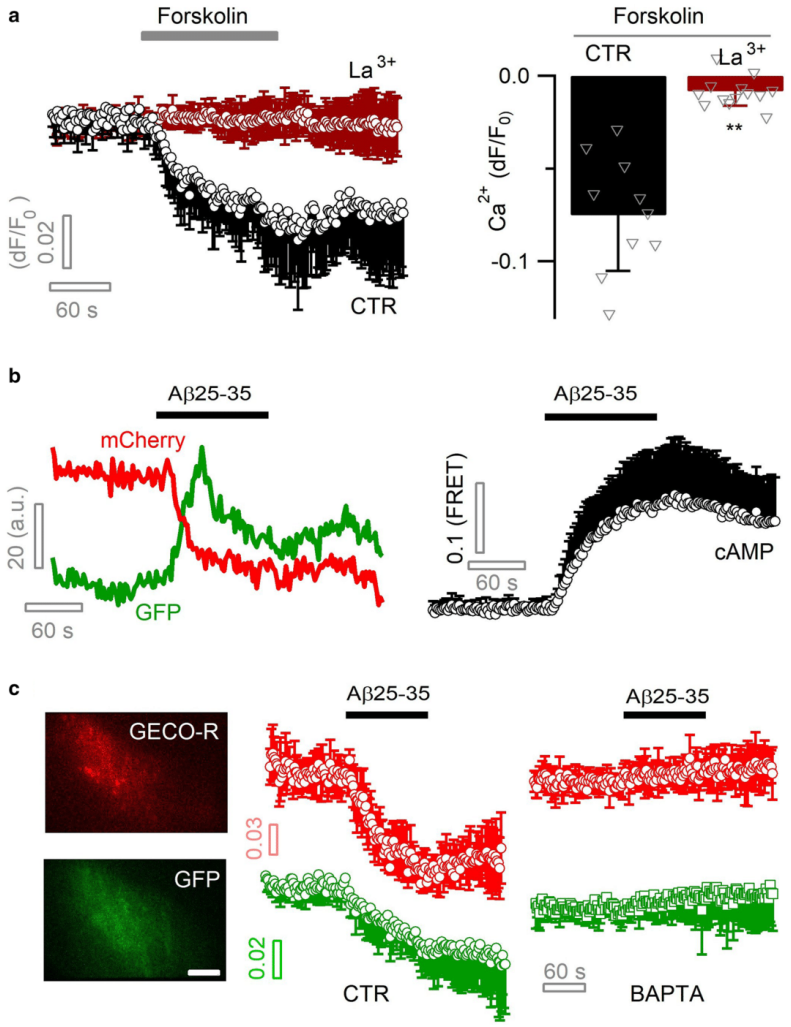

Fig. 4 Aβ potentiates astrocytic PMCA via cAMP signaling. **a** Elevation of astrocytic cAMP level increased PMCA-mediated Ca^{2+} extrusion. cAMP was elevated by forskolin (100 µM) and sub-cellular Ca^{2+} level imaged with Lck-GCaMP3 and TIRFM. Ca^{2+} diminution was blocked by the PMCA blocker La^{3+} (50 µM; n = 9–13 cells per condition). **b** Intracellular cAMP level was monitored with the FRET sensor GFP^{nd}-EPAC(dDEP)-mCherry and dual-color TIRFM. Left, representative dual-color recording of fluorescence change for EGFP and mCherry of the FRET sensor. Right, averaged astrocytic cAMP rise induced by Aβ25–35 (6 µM; n = 6). **c** PMCA-mediated astrocytic Ca^{2+} diminution was coupled with H^+ influx. Dual-color TIRFM recorded concomitant cytosolic Ca^{2+} and pH diminution, by expressing the red genetically encoded Ca^{2+} sensor GECO-R and the pH-sensitive GFP protein in same astrocytes. Both effects were abolished by chelating astrocyte cytoplasmic Ca^{2+} with BAPTA AM (100 µM; n = 7–9 cells per condition). Scale bar, 5 µm

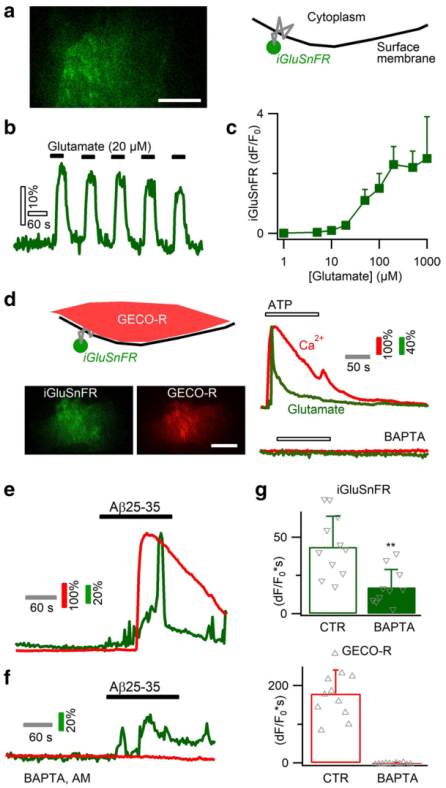

Fig. 5 Biphasic astrocytic glutamate release occurring in both a Ca^{2+}-dependent and -independent manner. **a** Imaging astrocytic glutamate release with green fluorescent sensor iGluSnFR expressed on the outer face of cell membrane. **b** CTR: repetitive fluorescence signals upon glutamate exposure. **c** Dose–response curve for astrocyte-expressed iGluSnR (n = 6–11 cells per concentration). **d** Dual-color imaging of astrocytic Ca^{2+} by the red sensor GECO-R and glutamate release by iGluSnFR. Right, ATP application evoked Ca^{2+} rise and glutamate release, which were both suppressed by BAPTA chelation of intracellular Ca^{2+}. **e** Aβ25–35 triggered a biphasic glutamate release, which started prior to Ca^{2+} rise and was further increased during Ca^{2+} elevation. **f**, **g** Chelating astrocytic Ca^{2+} with BAPTA partially reduced Aβ-induced glutamate release, confirming its occurrence in both Ca^{2+}-independent and -dependent manner (n = 10–11 cells per condition). Scale bars, 5 µm

Aβ25–35 evokes biphasic glutamate release from astrocytes

Astrocyte Ca^{2+} signals have been suggested to trigger the release of signaling molecules and affect neuronal activity [5]. During pathological Aβ accumulation, neurotoxicity has been attributed to excessive buildup of extracellular glutamate [37, 54, 63]. To examine how astrocytes contribute to such glutamate buildup, we imaged astrocyte glutamate release in response to Aβ25–35. We expressed the genetically encoded glutamate sensor iGluSnFR in primary cortical astrocytes [51], which showed repetitive fluorescence change upon glutamate puff (Fig. 5a, b). The dose–response curve reveals a dynamic range of ~ 10–200 µM glutamate (Fig. 5c). Triggering astrocyte Ca^{2+} elevation by ATP caused glutamate release, which was inhibited by the Ca^{2+} chelator BAPTA AM (100 µM, Fig. 5d). We then observed that Aβ25–35 application also induced glutamate release as reflected by the green fluorescence increase of iGluSnFR (Fig. 5e). We noted that during Aβ application, a fraction of glutamate was released before the onset of Ca^{2+} elevation and the Ca^{2+} signal then accelerated the release (Fig. 5e). We then performed similar experiments in astrocytes loaded with the Ca^{2+} chelator BAPTA AM. While intracellular Ca^{2+} signal was fully inhibited, a portion of glutamate was still released upon Aβ25–35 application, thereby validating the presence of a Ca^{2+}-independent release component (Fig. 5f, g). The presence of BAPTA, meanwhile, also reduced the total amount of glutamate release, showing the co-expression of Ca^{2+}-dependent release (integral dF/F_0*s = 17.2 ± 16.2 vs. CTR 43.6 ± 22.4; $p < 0.01$; Fig. 5g). Thus, Aβ25–35 induced astrocytic glutamate release via both Ca^{2+}-dependent and -independent mechanisms.

CX hemichannel affects Ca^{2+}-independent glutamate release

Glutamate is known to permeate through hemichannels [64, 97]. We confirmed this by artificially opening CX hemichannels in cultured astrocytes with Ca^{2+}-free solution [97], which indeed induced glutamate release (Additional file 1: Fig. S4). This occurred in the absence of intracellular Ca^{2+} increase, suggesting that CX hemichannels may contribute to the glutamate release preceding the Ca^{2+} rises.

We next imaged Aβ-evoked glutamate release in the absence and presence of the CX hemichannel blocker CBX (100 µM). As expected, this treatment reduced the glutamate release during the phase prior to Ca^{2+} increase ($dF/F_0 = 0.03 \pm 0.7$ vs. 0.31 ± 0.24 of CTR; $p < 0.01$; Fig. 6a). The overall Ca^{2+} signal and glutamate release throughout the recording period were also reduced (Fig. 6a), corroborating that hemichannel opening contributes to the Aβ-evoked Ca^{2+} signal. Applying during Aβ25–35 stimulation the mimetic peptide Gap26 (200 µM), a selective blocker of connexin43 hemichannel [20, 64], also inhibited the Ca^{2+} elevation and glutamate release as compared to control and to the inactive

scrambled peptide of Gap26 (Fig. 6b). Upon the washing of Gap26 and Aβ, glutamate release and Ca^{2+} signal reappeared (Fig. 6b), suggesting a post-inhibition rebound response. Applying Gap26 throughout recording (i.e., pre-, during- and post-Aβ application) inhibited the post-Aβ response (Fig. 6c). We then suppressed astrocyte Ca^{2+} signal with BAPTA and isolated the Aβ-induced Ca^{2+}-independent glutamate release that was found to be affected by Gap26 (temporal integral dF/F_0*s = 3.7 ± 3.4 vs. 19.7 ± 16.1 of CTR, $p < 0.01$; Fig. 6d). Hence, astrocyte CX hemichannel contributes to the Ca^{2+}-independent glutamate release induced by Aβ25–35.

Anion channel and lysosome exocytosis modulate Ca^{2+}-dependent glutamate release

Astrocyte CX hemichannel opening was suggested to be Ca^{2+}-sensitive [15], and may modulate Aβ-evoked Ca^{2+}-dependent glutamate release. One way to clarify this issue would be to block CX hemichannels, which however is known to interfere with Aβ-induced Ca^{2+} signal (Figs. 2, 6). To bypass this problem, we mimicked Aβ-evoked Ca^{2+} signals by ATP stimulation (30 μM, Fig. 7a) that partially recapitulated the purinergic receptor activation by Aβ25–35 (Fig. 2). ATP-triggered Ca^{2+} oscillations showed comparable patterns as the Aβ25–35-indcued signals (GECO-R, Fig. 7a) and triggered glutamate release (iGluSnFR, Fig. 7a). Yet contrary to our expectation, Ca^{2+}-activated glutamate release persisted in the presence of the CX hemichannel blocker CBX (100 μM, Fig. 7b, d), suggesting its dispensable involvement in this process. Alternatively, Ca^{2+}-sensitive anion channels represent another route for Ca^{2+}-activated glutamate release in astrocytes [29, 86, 93, 96]. Indeed, the anion channel blocker 5-nitro-2-(3-phenylpropylamino) benzoic acid (NPPB, 100 μM) reduced the Ca^{2+}-activated glutamate release (temporal integral dF/F_0*s = 1.3 ± 1.5 vs. 4.2 ± 1.9, $p < 0.05$; Fig. 7c, d). Also, during the response to Aβ25–35, astrocyte glutamate release over the phase of Ca^{2+} rise was reduced by another anion channel blocker DCPIB (50 μM, Fig. 7e), corroborating a role for anion channels in the Ca^{2+}-dependent glutamate release.

Another pathway for glutamate release could be Ca^{2+}-regulated vesicular exocytosis. In astrocytes, lysosomes are known vesicular compartments undergoing Ca^{2+}-activated exocytosis [38, 50, 101], though the involvement of small synaptic like vesicles is still debated [23, 75]. The vesicular glutamate transporter sialin [58] was observed on astrocyte lysosomes [50], suggesting their contribution to Ca^{2+}-dependent glutamate release. We therefore imaged with TIRFM lysosome exocytosis from primary astrocytes in response to Aβ25–35. Lysosomes were labeled with the red fluorescent dye FM4-64 [50, 101], and the concomitant Ca^{2+} signals monitored with the green fluorescent indicator OGB1 AM (Fig. 8a1). Following Aβ-evoked Ca^{2+} elevation, we observed an asynchronous lysosome exocytosis as reflected by FM dye destaining (Fig. 8a2, a3). We also used a pH-sensitive sensor to image exocytosis, where the GFP mutant pHluorin is conjugated to the intralumenal site of the lysosomal membrane protein CD63 [49] (Fig. 8b). CD63-pHluorin is quenched in the acidic lysosome lumen, and becomes fluorescent upon its exocytotic exposure to extracellular neutral solution. We observed that Aβ25–35 induced CD63-pHluorin brightening on astrocyte surface, thus corroborating the occurrence of lysosome exocytosis (Fig. 8b). A similar temporal distribution was found with the two exocytotic probes ($p = 0.6$; Fig. 8c), consistent with the co-localization of FM4-64 and CD63 in astrocyte lysosomes [50]. Next, to examine the potential glutamate storage in astrocyte lysosomes, we performed glutamate staining in cultured astrocytes that resulted in a punctuate labelling distributed across the cytoplasm (Additional file 1: Fig. S5a). Glutamate staining was diminished by the cathepsin C substrate glycyl-L-phenylalanine 2-naphthylamideto (GPN, 200 μM), a compound permeabilizing lysosomes by osmotic swelling [50, 101] (Additional file 1: Fig. S5a). On the other hand, the fluorescent nucleotide marker MANT-ATP showed little colocalization with FM4-64-labeled lysosomes (Additional file 1: Fig. S5b). It was also observed that permeabilization of lysosomes by GPN reduced the Aβ25–35-induced glutamate release (Fig. 8d), and the presence of anion channel blocker DCPIB (50 μM) showed no significant effect on astrocyte lysosome release (Fig. 8e). These data suggest the astrocyte lysosomes, in parallel with anion channels, contribute to Aβ-induced Ca^{2+}-dependent glutamate release.

(See figure on next page.)

Fig. 6 Involvement of CX hemichannels in Ca^{2+}-independent glutamate release. **a** Glutamate release prior to the Ca^{2+} elevation (top, CTR) was reduced by the CX hemichannel blocker CBX (100 μM; present throughout the recording; n = 8–13 cells per condition). **b** During the Aβ application phase, Ca^{2+}-independent glutamate release was blocked by another CX hemichannel blocker Gap26 peptide (200 μM). The inactive scramble peptide of Gap26 showed no effect (n = 8–10 cells per condition). **c** A more pronounced inhibition effect of Gap26 was observed when applying it throughout the entire imaging period (i.e., pre-, during- and post-Aβ; n = 12–14 per condition). **d** Chelating astrocytic Ca^{2+} with BAPTA AM isolated Ca^{2+}-independent astrocytic glutamate release, which was inhibited by CX hemichannel blocker Gap26 (n = 8–10 per condition)

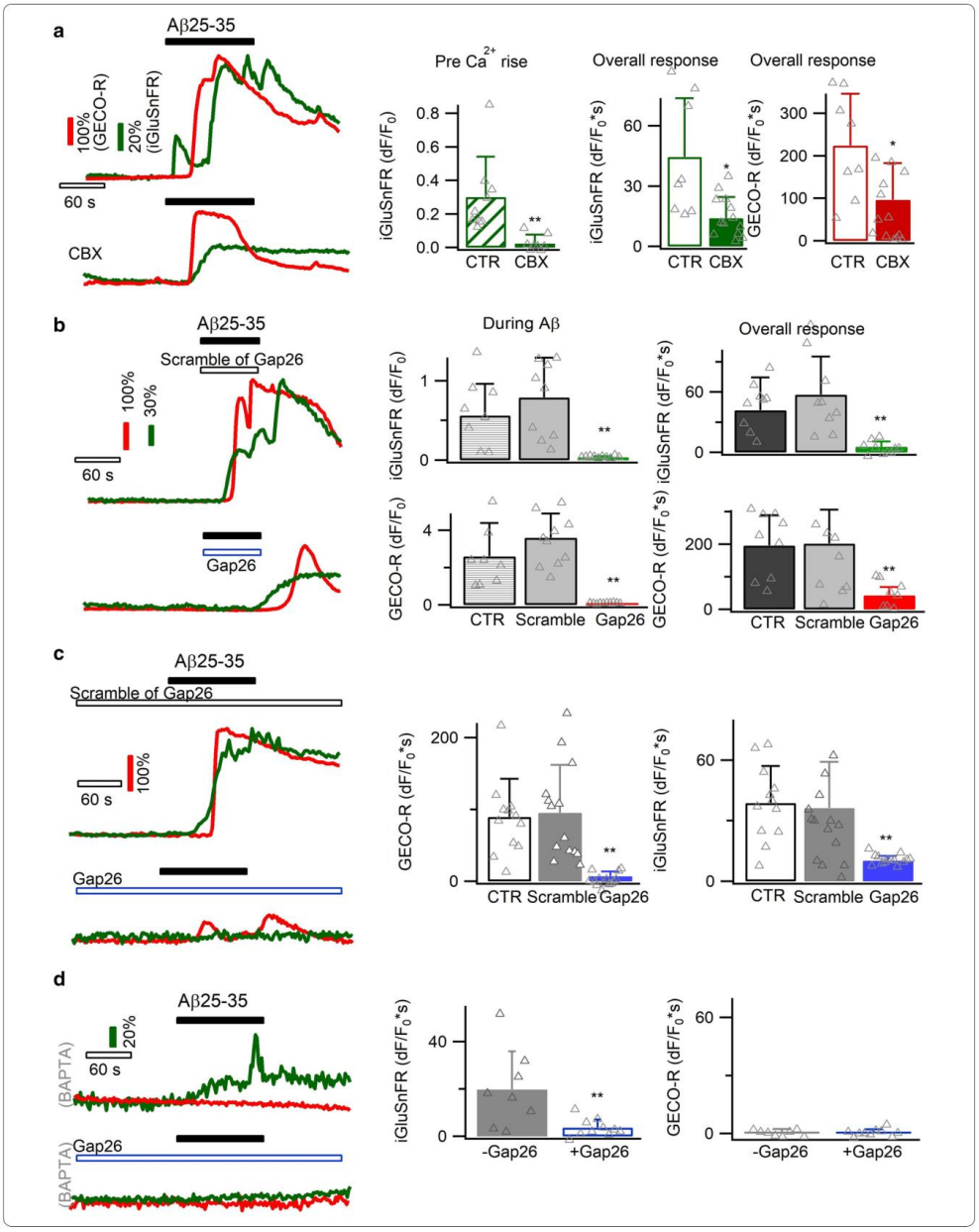
a
Aβ25-35
100% (GECO-R)
20% (iGluSnFR)
60 s
CBX
Pre Ca2+ rise
Overall response
Overall response
iGluSnFR (dF/F0)
iGluSnFR (dF/F0*s)
GECO-R (dF/F0*s)
CTR CBX
b
Aβ25-35
Scramble of Gap26
100%
30%
60 s
Gap26
During Aβ
Overall response
GECO-R (dF/F0)
CTR Scramble Gap26
c
Aβ25-35
Scramble of Gap26
100%
60 s
Gap26
d
Aβ25-35
20%
60 s
(BAPTA)
Gap26
-Gap26 +Gap26

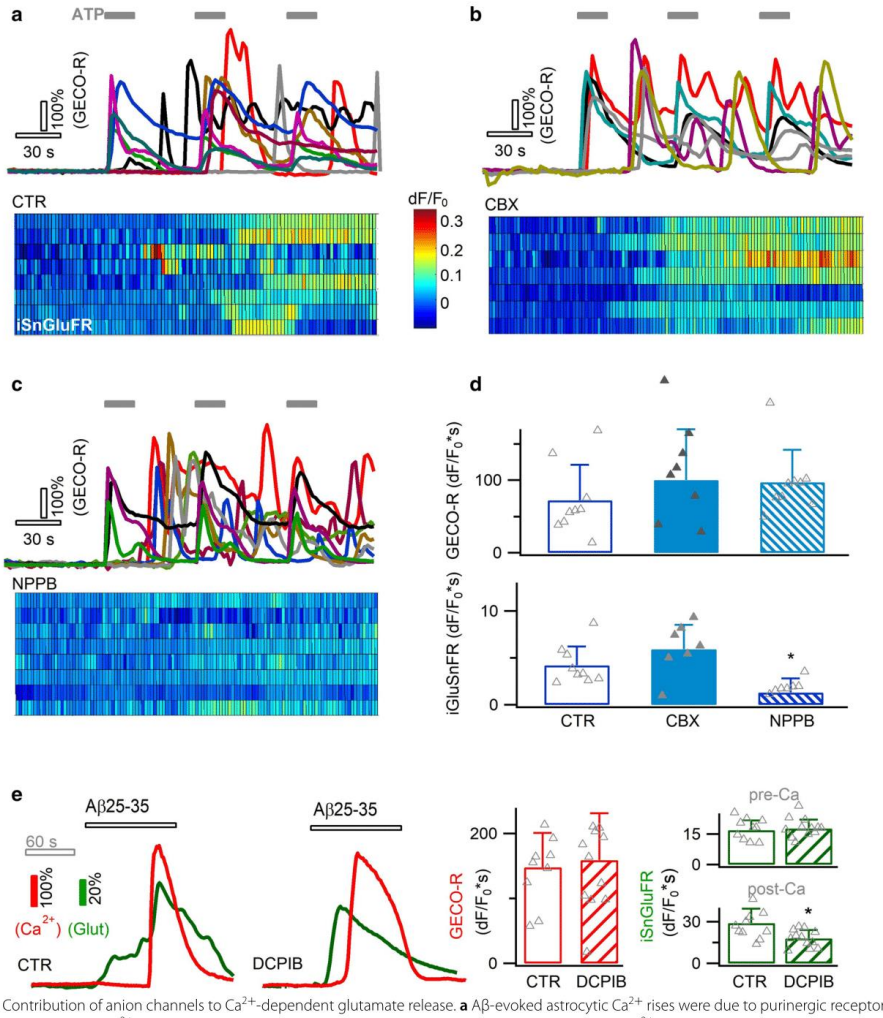

Fig. 7 Contribution of anion channels to Ca^{2+}-dependent glutamate release. **a** Aβ-evoked astrocytic Ca^{2+} rises were due to purinergic receptor activation. To examine Ca^{2+}-dependent glutamtae release, we applied ATP (30 μM) to trigger astrocytic Ca^{2+} and glutamate release. **b**–**d** Ca^{2+}-dependent glutamate release was unaffected by inhibition of CX hemichannel (CBX, 100 μM), but reduced by blocking anion channels with NPPB (100 μM) (n = 7–9 cells per condition). **e** During the response to Aβ25–35 (6 μM), inhibiting anion channels with DCPIB (50 μM) influenced the glutamate release during Ca^{2+} elevation phase (n = 10–12 cells per condition)

Discussion

In this study, we examined the sub-cellular mechanisms underlying the astrocytic response to the neurotoxic amyloid beta fragment. A state-dependent alteration of Ca^{2+} homeostasis in association with a multiphasic release of signaling transmitters have been observed in primary cortical astrocytes. As illustrated in Additional file 1: Fig. S6a, the free cytosolic Ca^{2+} concentration is maintained at physiological low level (~100 nM) in astrocyes in basal conditions [62], thereby restraining

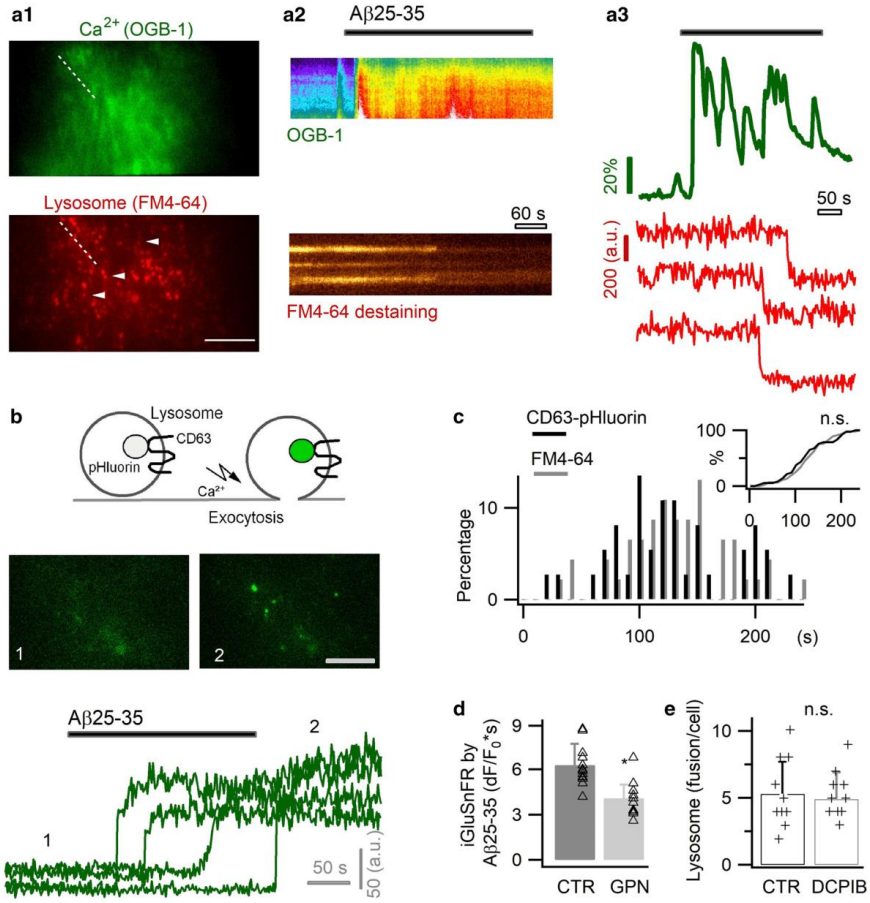

Fig. 8 Aβ25–35 triggered astrocytic lysosome exocytosis. **a** Astrocytes co-labeled with the green fluorescent Ca^{2+} indicator OGB-1 AM and the red-fluorescent lysosomal marker FM4-64 (**a1**). Application of Aβ25–35 (6 μM) evoked Ca^{2+} elevation followed by asynchronous exocytosis of lysosomes, as reflected by FM dye destaining (**a2**, **a3**). **b** Aβ-evoked lysosomal exocytosis imaged with CD63-pHluorin. **c** Temporal distribution of lysosomal exocytosis obtained with FM dye and CD63-pHluorin (n = 51–62 lysosomes from five cells per condition). *Inset*, cumulative histogram showing the temporal coincidence for the two lysosomal markers ($p = 0.7$). **d** Permeabilization of lysosomes by GPN affected the Aβ25–35-induced glutamate release (iGluSnFR, dF/F_0*s; n = 12 cells per condition; recording protocol is as Fig. 7e). **e** The presence of anion channel blocker DCPIB did not affect astrocyte lysosome release rate as measured by FM4-64 destaining (n = 10 cells per condition). Scale bars, 10 μm for **a**, 5 μm for **b**

the initial PMCA reaction to Aβ25–35 application. One possibility is that Aβ25–35 opens CX hemichannels leading to glutamate and ATP co-release, the latter triggering Ca^{2+} elevation to cause further glutamate release. In basal conditions, Aβ25–35 plays an excitatory role in upregulating astrocyte Ca^{2+} signals. In Aβ-preconditioned astrocytes (Additional file 1: Fig. S6b), the chronically overloaded intracellular Ca^{2+} sets a greater driving force for its efflux. Hence, PMCA Ca^{2+} export is readily activated by subsequent acute Aβ challenge, leading to an overshoot drop in the basal Ca^{2+} diminution and concomitant H^+ influx. H^+ then exerts an inhibitory effect on CX hemichannel opening, thereby blocking the hemichannel and the purinergic activaiton

of Ca^{2+} elevation. In this situation, Aβ tends to exert an inhibitory effect on astrocyte Ca^{2+} signal. Immunostaining of PMCA and CX43, a major hemichannel protein expressed in astrocyes, was observed in cultured astrocytes and in the cortex of hAPPJ20 AD mouse model.

Dysregulation of neuron-glia interaction emerges as an important aspect in Aβ pathology and the evolution of AD [33]. Aberrant Ca^{2+} signals have been noted as a hallmark of astrocyte functional remodeling in AD mouse models [17, 47]. Our current data support the potential contribution of astrocytes to the dysregulated neuroglial activities in amyloidopathy, for instance via the interference with purinergic and/or glutamatergic communications [54]. The primary culture of astrocytes is an in vitro model to study the sub-cellular mechanism involved in AD pathophysiology. Primary astrocytes were reported to display a portion of properties different from their in vivo counterparts, like the genes featuring the reactive state [9, 100]. In the current study, preconditioning primary astrocytes with submicromolar Aβ25-35 caused appreciable alteration in their subsequent response to high-dose Aβ, indicating a malleable adaptability in their functional status. This suggests that the cultured astrocytes used in this study were not fully reactivated, likely mirroring an early state during brain Aβ deposition.

We show that Aβ25–35 activates Ca^{2+} elevation via purinergic P2Y1 receptor activation that confirms the in vivo finding in AD mouse model [17]. The involvement of the Ca^{2+} release from the internal ER store is also in line with the previous in vitro study [85]. ER Ca^{2+} depletion is followed by Ca^{2+} influx via SOC channel [66], which was here observed to be facilitated by Aβ25-35, as previously reported with Aβ42 [74]. This therefore provides an additional mechanism for the upregulated astrocyte Ca^{2+} signal and explains in part its dependence on Ca^{2+} influx. We also show that Aβ25–35-caused Ca^{2+} signals depend on the opening of CX hemichannels, a major pathway for ATP release from astrocytes [28, 98]. It is possible that Aβ25–35 triggers ATP release from CX hemichannels that then activates astrocyte P2Y1 receptor to cause Ca^{2+} elevation. Interestingly, purinergic autocrine stimulation and subsequent glutamate release has also been observed following optogenetic activation of astrocytes with channelrhodopsin 2 [79]. Optical activation of astrocytes with light-gated GPCRs optoAR and melanopsin also triggered ATP release and autocrine activation of astrocytic purinergic receptors [25, 53]. Nevertheless, our current data could not fully exclude other possible mechanisms underlying Aβ25–35-induced Ca^{2+} signals. For instance, Aβ25–35 may directly activate astrocyte purinergic receptors, which could be mitigated by CX hemichannel blocking.

Besides the generally observed excitatory effect on astrocytic Ca^{2+} of Aβ peptides or plaques, we observed an inhibitory effect of Aβ25–35 in astrocytes preconditioned by submicromolar concentrations of Aβ. It was reported that Aβ25–35 not only triggered Ca^{2+} elevation, but also inhibited ATP-evoked Ca^{2+} elevation in primary cultures of rat astrocytes [85], implying a mixed status of the astrocytes used therein. We here attributed the mechanism of inhibition to the potentiation of PMCA-mediated Ca^{2+} extrusion from the cytoplasm, modulated by Aβ-triggered cAMP elevation. As ATP-driven pumps, PMCAs export cytosolic Ca^{2+} in a calmodulin-dependent manner to maintain its physiological low level [8, 62]. Overexpression of a human PMCA in striatal astrocytes was used to inhibit Ca^{2+} signals [99]. In our study, the ready activation of PMCA by Aβ in preconditioned astrocytes implies that their cytosolic Ca^{2+} concentration, due to the gradual overload upon the chronic Aβ exposure, has been hyper-shifted from the physiological level. As H^+ is a hemichannel inhibitor [77], the H^+ influx that was coupled with PMCA-mediated Ca^{2+} extrusion would have inhibited CX hemichannel, an effect that we found to attenuate Ca^{2+} elevations. This thus resulted in a dominant inhibitory effect in preconditioned astrocytes. Ca^{2+} export by PMCA likely represents a protective mechanism to counterbalance the early Ca^{2+} upregulation in astrocytes caused by Aβ. Nevertheless, PMCA activity is often impaired by recurrent activation and metabolic stresses [8], as it would be encountered as a consequence of long-term Aβ accumulation in AD [48]. Hence, Ca^{2+} hyperactivity could become eventually prevalent in astrocytes at the time when Aβ plaques are formed [17, 47].

In an AD mouse model, astrocytes Ca^{2+} hyperactivity occurs globally independent of their proximity to Aβ plaques, suggesting that the local Aβ pathology is transmitted by intercellular mechanisms [47]. We here observed Aβ25-35-caused multiphasic release of glutamate from astrocytes, which could activate adjacent astrocytes and neurons in situ. Our data also suggest that Aβ25-35 likely causes ATP release via CX hemichannels to activate astrocyte Ca^{2+} elevation (Additional file 1: Fig. S6a). CX hemichannels are known to release signaling molecules from astrocytes regulating neural activity in physiological and pathological conditions [28]. In AD mouse models, CX hemichannels have been implicated in the release of ATP and glutamate, which dysregulate synaptic transmission [98]. We here suggest the mechanistic steps underlying Aβ-induced glutamate and ATP release. CX hemichannels may initiate the ATP release that subsequently activated purinergic autoreceptor to elevate Ca^{2+} signal. Consistent with CX hemichannels being nonselective channel pores [28], they were here also observed to mediate Ca^{2+}-independent glutamate efflux. In addition, we noted that Aβ-evoked

Ca^{2+} signal further increased glutamate release. While Ca^{2+}-dependent glutamate release from astrocytes is being debated under physiological conditions [24, 78], it has been observed upon the hyper-regulated astrocyte Ca^{2+} signals in pathological conditions [89].

Our results suggest that Aβ-evoked Ca^{2+}-dependent glutamate release occurs via astrocytic anion channels and lysosome exocytosis. Astrocyte glutamate release was suggested to be mediated by mouse Bestrophin 1 channel in a Ca^{2+}-activated manner [67] (but see [94]). In APP/PS1 AD mouse model, excessive GABA release from astrocytic Bestrophin 1 channel was also observed to impair memory and learning [39]. In addition, SWELL-1 (i.e., LRRC8A) channel has been shown to constitute the anion channels that mediate glutamate release from astrocytes in association with cell swelling [96]. The relative roles of Bestrophin 1 and SWELL-1 in Aβ-evoked glutamate release needs be further evaluated. We also observed asynchronous lysosome exocytosis following Aβ-triggered Ca^{2+} signal, likely contributing to signaling molecule release. Lysosomes represent a population of vesicular compartments having a larger size than small secretory vesicles [49]. Although the physiological role of small secretory vesicles in astrocytes remains debated [75], lysosome exocytosis has been observed in response to pathological stimulations [21, 50, 84]. It is therefore plausible that lysosome exocytosis plays a role in modulating astrocytic signals in Aβ pathologies. Astrocytes could bidirectionally control synaptic transmission, for example via glutamatergic potentiation and purinergic/adenosinergic inhibition [12]. Hence, Aβ-evoked ATP and glutamate release would affect neuronal activities in situ during AD progression, with specific outputs depending on the receptor expression profiles of the local circuitry and their spatial correlation with astrocytic release sites. Aβ-induced glutamate release likely contributes to the glutamate neurotoxicity seen in AD context [90, 98]. Memantine, the uncompetitive antagonist with moderate affinity for the glutamate *N*-methyl-D-aspartate (NMDA) receptor, has been approved for the treatment of moderate to severe AD [68].

It has been noted that globally ablating pathologically altered astrocytes in AD mouse model worsens the disease [42]. Thus, understanding and hence being able to target dysregulations in specific signaling pathways in astrocytes holds the potential to ameliorate Aβ pathology. In this context, the current results provide testable targets to control astrocyte responses to neurotoxic Aβ peptide and will help to understand the astrocytic contributions.

Supplementary Information

The online version contains supplementary material available at https://doi.org/10.1186/s40478-021-01146-1.

Additional file 1. Figure S1–S6 and Table S1–S2.

Acknowledgements
We thank the animal facility and the imaging platform of the IBPS (Sorbonne Université, Paris, France). We thank Dr. Nicole Ropert for the discussion of experiments, Dr. Tao Xu for providing the CD63-pHluorin plasmid, Dr. Kees Jalink for GFP^{nd}-EPAC(dDEP)-mCherry plasmid and Dr. Lennart Mucke of the J. David Gladstone Institutes for hAPPJ20 mice. .

Authors' contributions
This work was initiated while DL, KH and MO were with the Neurophysiology and New Microscopies lab (INSERM U603) at Université Paris Descartes. CP, KH, SM, VV, BC and DL performed the experiments. CP and BC performed the experiments using the hAPPJ20 transgenic mice. CP and DL analyzed the data. DL supervised the study and wrote the manuscript with input from co-authors. All authors read and approved the manuscript.

Funding
This work was supported by the Agence Nationale de la Recherche, France (ANR-11-BSV4-0004; ANR-17-CE37-0010-03).

Availability of data and materials
The datasets used and analyzed during the current study are available from the corresponding author upon request.

Ethics approval and consent to participate
All animal care and experimental procedures are in conformity with the French National Charter on the ethics of animal experimentation.

Consent for publication
Not applicable.

Competing interests
The authors declare that they have no competing interests.

Author details
[1] Institute of Biology Paris Seine, Neuroscience Paris Seine, CNRS UMR8246, INSERM U1130, Sorbonne Université, 75005 Paris, France. [2] INSERM/UdA U1107 Neuro-Dol, Université Clermont Auvergne, 63100 Clermont-Ferrand, France. [3] Saints-Pères Paris Institute for the Neurosciences (SPPIN), CNRS UMR8003, Université de Paris, 75006 Paris, France.

Received: 11 January 2021 Accepted: 28 February 2021
Published online: 16 March 2021

References

1. Abramov AY, Canevari L, Duchen MR (2003) Changes in intracellular calcium and glutathione in astrocytes as the primary mechanism of amyloid neurotoxicity. J Neurosci 23:5088–5095
2. Abramov AY, Ionov M, Pavlov E, Duchen MR (2011) Membrane cholesterol content plays a key role in the neurotoxicity of beta-amyloid: implications for Alzheimer's disease. Aging Cell 10:595–603
3. Alberdi E, Wyssenbach A, Alberdi M, Sanchez-Gomez MV, Cavaliere F, Rodriguez JJ, Verkhratsky A, Matute C (2013) Ca(2+)-dependent endoplasmic reticulum stress correlates with astrogliosis in oligomeric amyloid beta-treated astrocytes and in a model of Alzheimer's disease. Aging Cell 12:292–302
4. Allaman I, Gavillet M, Belanger M, Laroche T, Viertl D, Lashuel HA, Magistretti PJ (2010) Amyloid-beta aggregates cause alterations of astrocytic metabolic phenotype: impact on neuronal viability. J Neurosci 30:3326–3338
5. Araque A, Carmignoto G, Haydon PG, Oliet SH, Robitaille R, Volterra A (2014) Gliotransmitters travel in time and space. Neuron 81:728–739
6. Bazargani N, Attwell D (2015) Astrocyte calcium signaling: the third wave. Nat Neurosci 19:182–189

7. Brini M, Carafoli E (2009) Calcium pumps in health and disease. Physiol Rev 89:1341–1378
8. Bruce JIE (2018) Metabolic regulation of the PMCA: role in cell death and survival. Cell Calcium 69:28–36. https://doi.org/10.1016/j.ceca.2017.06.001
9. Cahoy JD, Emery B, Kaushal A, Foo LC, Zamanian JL, Christopherson KS, Xing Y, Lubischer JL, Krieg PA, Krupenko SA et al (2008) A transcriptome database for astrocytes, neurons, and oligodendrocytes: a new resource for understanding brain development and function. J Neurosci 28:264–278
10. Camara H, De-Souza EA (2018) beta-amyloid accumulation slows earlier than expected in preclinical Alzheimer's disease patients. J Neurosci 38:9123–9125. https://doi.org/10.1523/JNEUROSCI.1592-18.2018
11. Chow S-K, Yu D, MacDonald CL, Buibas M, Silva GA (2009) Amyloid-beta directly induces spontaenous calcium transient, delayed intercellular calcium waves, and gliosis in rat cortical astrocytes. ASN Neuro. https://doi.org/10.1042/AN20090035
12. Covelo A, Araque A (2018) Neuronal activity determines distinct gliotransmitter release from a single astrocyte. Elife 7:e32237
13. Dallerac G, Zapata J, Rouach N (2018) Versatile control of synaptic circuits by astrocytes: where, when and how? Nat Rev Neurosci 19:729–743. https://doi.org/10.1038/s41583-018-0080-6
14. Daugirdas JT, Arrieta J, Ye M, Flores G, Battle DC (1995) Intracellular acidification associated with changes in free cytosolic calcium. Evidence for Ca^{2+}/H^{+} exchange via a plasma membrane $Ca^{(2+)}$-ATPase in vascular smooth muscle cells. J Clin Invest 95:1480–1489
15. De Vuyst E, Wang N, Decrock E, De Bock M, Vinken M, Van Moorhem M, Lai C, Culot M, Rogiers V, Cecchelli R et al (2009) Ca^{2+} regulation of connexin 43 hemichannels in C6 glioma and glial cells. Cell Calcium 46:176–187
16. Dean WL, Chen D, Brandt PC, Vanaman TC (1997) Regulation of platelet plasma membrane Ca2+-ATPase by cAMP-dependent and tyrosine phosphorylation. J Biol Chem 272:15113–15119
17. Delekate A, Fuchtemeier M, Schumacher T, Ulbrich C, Foddis M, Petzold GC (2014) Metabotropic P2Y1 receptor signalling mediates astrocytic hyperactivity in vivo in an Alzheimer's disease mouse model. Nat Commun 5:5422
18. Demuro A, Smith M, Parker I (2011) Single-channel Ca(2+) imaging implicates Abeta1-42 amyloid pores in Alzheimer's disease pathology. J Cell Biol 195:515–524
19. Devaraju P, Sun MY, Myers TL, Lauderdale K, Fiacco TA (2013) Astrocytic group I mGluR-dependent potentiation of astrocytic glutamate and potassium uptake. J Neurophysiol 109:2404–2414
20. Evans WH, Leybaert L (2007) Mimetic peptides as blockers of connexin channel-facilitated intercellular communication. Cell Commun Adhes 14:265–273
21. Fan Y, He JJ (2016) HIV-1 tat promotes lysosomal exocytosis in astrocytes and contributes to astrocyte-mediated tat neurotoxicity. J Biol Chem 291:22830–22840. https://doi.org/10.1074/jbc.M116.731836
22. Ferdek PE, Gerasimenko JV, Peng S, Tepikin AV, Petersen OH, Gerasimenko OV (2012) A novel role for Bcl-2 in regulation of cellular calcium extrusion. Curr Biol 22:1241–1246
23. Fiacco TA, Agulhon C, McCarthy KD (2009) Sorting out astrocyte physiology from pharmacology. Annu Rev Pharmacol Toxicol 49:151–174
24. Fiacco TA, McCarthy KD (2018) Multiple lines of evidence indicate that gliotransmission does not occur under physiological conditions. J Neurosci 38:3–13
25. Figueiredo M, Lane S, Stout RF Jr, Liu B, Parpura V, Teschemacher AG, Kasparov S (2014) Comparative analysis of optogenetic actuators in cultured astrocytes. Cell Calcium 56:208–214. https://doi.org/10.1016/j.ceca.2014.07.007
26. Fresu L, Dehpour A, Genazzani AA, Carafoli E, Guerini D (1999) Plasma membrane calcium ATPase isoforms in astrocytes. Glia 28:150–155
27. Furman JL, Sama DM, Gant JC, Beckett TL, Murphy MP, Bachstetter AD, Van Eldik LJ, Norris CM (2012) Targeting astrocytes ameliorates neurologic changes in a mouse model of Alzheimer's disease. J Neurosci 32:16129–16140
28. Giaume C, Leybaert L, Naus CC, Saez JC (2013) Connexin and pannexin hemichannels in brain glial cells: properties, pharmacology, and roles. Front Pharmacol 4:88
29. Gomez-Gonzalo M, Zehnder T, Requie LM, Bezzi P, Carmignoto G (2018) Insights into the release mechanism of astrocytic glutamate evoking in neurons NMDA receptor-mediated slow depolarizing inward currents. Glia 66:2188–2199. https://doi.org/10.1002/glia.23473
30. Gout E, Rebeille F, Douce R, Bligny R (2014) Interplay of Mg2+, ADP, and ATP in the cytosol and mitochondria: unravelling the role of Mg2+ in cell respiration. Proc Natl Acad Sci USA 111:E4560-4567. https://doi.org/10.1073/pnas.1406251111
31. Grolla AA, Fakhfouri G, Balzaretti G, Marcello E, Gardoni F, Canonico PL, Diluca M, Genazzani AA, Lim D (2012) Abeta leads to Ca(2+) signaling alterations and transcriptional changes in glial cells. Neurobiol Aging 34:511–522
32. Heneka MT, Carson MJ, El Khoury J, Landreth GE, Brosseron F, Feinstein DL, Jacobs AH, Wyss-Coray T, Vitorica J, Ransohoff RM et al (2015) Neuroinflammation in Alzheimer's disease. Lancet Neurol 14:388–405. https://doi.org/10.1016/S1474-4422(15)70016-5
33. Henstridge CM, Hyman BT, Spires-Jones TL (2019) Beyond the neuron-cellular interactions early in Alzheimer disease pathogenesis. Nat Rev Neurosci 20:94–108. https://doi.org/10.1038/s41583-018-0113-1
34. Herculano-Houzel S (2014) The glia/neuron ratio: how it varies uniformly across brain structures and species and what that means for brain physiology and evolution. Glia 62:1377–1391
35. Honore P, Donnelly-Roberts D, Namovic MT, Hsieh G, Zhu CZ, Mikusa JP, Hernandez G, Zhong C, Gauvin DM, Chandran P et al (2006) A-740003 [N-(1-{[(cyanoimino)(5-quinolinylamino) methyl]amino}-2,2-dimethylpropyl)-2-(3,4-dimethoxyphenyl)acetamide], a novel and selective P2X7 receptor antagonist, dose-dependently reduces neuropathic pain in the rat. J Pharmacol Exp Ther 319:1376–1385. https://doi.org/10.1124/jpet.106.111559
36. Iglesias R, Dahl G, Qiu F, Spray DC, Scemes E (2009) Pannexin 1: the molecular substrate of astrocyte "hemichannels." J Neurosci 29:7092–7097. https://doi.org/10.1523/JNEUROSCI.6062-08.2009
37. Jacob CP, Koutsilieri E, Bartl J, Neuen-Jacob E, Arzberger T, Zander N, Ravid R, Roggendorf W, Riederer P, Grunblatt E (2007) Alterations in expression of glutamatergic transporters and receptors in sporadic Alzheimer's disease. J Alzheimers Dis 11:97–116
38. Jaiswal JK, Fix M, Takano T, Nedergaard M, Simon SM (2007) Resolving vesicle fusion from lysis to monitor calcium-triggered lysosomal exocytosis in astrocytes. Proc Natl Acad Sci USA 104:14151–14156
39. Jo S, Yarishkin O, Hwang YJ, Chun YE, Park M, Woo DH, Bae JY, Kim T, Lee J, Chun H et al (2014) GABA from reactive astrocytes impairs memory in mouse models of Alzheimer's disease. Nat Med 20:886–896. https://doi.org/10.1038/nm.3639
40. Johansson JS, Nied LE, Haynes DH (1992) Cyclic AMP stimulates Ca(2+)-ATPase-mediated Ca2+ extrusion from human platelets. Biochim Biophys Acta 1105:19–28
41. Kasuya G, Yamaura T, Ma XB, Nakamura R, Takemoto M, Nagumo H, Tanaka E, Dohmae N, Nakane T, Yu Y et al (2017) Structural insights into the competitive inhibition of the ATP-gated P2X receptor channel. Nat Commun 8:876. https://doi.org/10.1038/s41467-017-00887-9
42. Katsouri L, Birch AM, Renziehausen AWJ, Zach C, Aman Y, Steeds H, Bonsu A, Palmer EOC, Mirzaei N, Ries M et al (2019) Ablation of reactive astrocytes exacerbates disease pathology in a model of Alzheimer's disease. Glia 68:1017–1030. https://doi.org/10.1002/glia.23759
43. Khakh BS, McCarthy KD (2015) Astrocyte calcium signaling: from observations to functions and the challenges therein. Cold Spring Harb Perspect Biol 7:a020404
44. Kimbrough IF, Robel S, Roberson ED, Sontheimer H (2015) Vascular amyloidosis impairs the gliovascular unit in a mouse model of Alzheimer's disease. Brain 138:3716–3733. https://doi.org/10.1093/brain/awv327
45. Kneen M, Farinas J, Li Y, Verkman AS (1998) Green fluorescent protein as a noninvasive intracellular pH indicator. Biophys J 74:1591–1599. https://doi.org/10.1016/S0006-3495(98)77870-1
46. Kubo T, Nishimura S, Kumagae Y, Kaneko I (2002) In vivo conversion of racemized beta-amyloid ([D-Ser 26]A beta 1–40) to truncated and toxic fragments ([D-Ser 26]A beta 25–35/40) and fragment presence in the brains of Alzheimer's patients. J Neurosci Res 70:474–483
47. Kuchibhotla KV, Lattarulo CR, Hyman BT, Bacskai BJ (2009) Synchronous hyperactivity and intercellular calcium waves in astrocytes in Alzheimer mice. Science 323:1211–1215

48. Le Douce J, Maugard M, Veran J, Matos M, Jégo P, Vigneron PA, Faivre E, Toussay X, Vandenberghe M, Balbastre Y et al (2020) Impairment of glycolysis-derived L-serine production in astrocytes contributes to cognitive deficits in Alzheimer's disease. Cell Metab 31:503-517 e508. https://doi.org/10.1016/j.cmet.2020.02.004
49. Li D, Hérault K, Zylbersztejn K, Lauterbach M, Guillon M, Oheim M, Ropert N (2015) Astrocyte VAMP3 vesicles undergo Ca^{2+}-independent cycling and modulate glutamate transporter trafficking. J Physiol 593:2807–2832
50. Li D, Ropert N, Koulakoff A, Giaume C, Oheim M (2008) Lysosomes are the major vesicular compartment undergoing Ca^{2+}-regulated exocytosis from cortical astrocytes. J Neurosci 28:7648–7658
51. Marvin JS, Borghuis BG, Tian L, Cichon J, Harnett MT, Akerboom J, Gordus A, Renninger SL, Chen TW, Bargmann CI et al (2013) An optimized fluorescent probe for visualizing glutamate neurotransmission. Nat Methods 10:162–170
52. McCarthy KD, de Vellis J (1980) Preparation of separate astroglial and oligodendroglial cell cultures from rat cerebral tissue. J Cell Biol 85:890–902
53. Mederos S, Hernandez-Vivanco A, Ramirez-Franco J, Martin-Fernandez M, Navarrete M, Yang A, Boyden ES, Perea G (2019) Melanopsin for precise optogenetic activation of astrocyte-neuron networks. Glia 67:915–934. https://doi.org/10.1002/glia.23580
54. Mehta A, Prabhakar M, Kumar P, Deshmukh R, Sharma PL (2013) Excitotoxicity: bridge to various triggers in neurodegenerative disorders. Eur J Pharmacol 698:6–18
55. Mei X, Ezan P, Giaume C, Koulakoff A (2010) Astroglial connexin immunoreactivity is specifically altered at beta-amyloid plaques in beta-amyloid precursor protein/presenilin1 mice. Neuroscience 171:92–105
56. Meme W, Ezan P, Venance L, Glowinski J, Giaume C (2004) ATP-induced inhibition of gap junctional communication is enhanced by interleukin-1 beta treatment in cultured astrocytes. Neuroscience 126:95–104
57. Millucci L, Ghezzi L, Bernardini G, Santucci A (2010) Conformations and biological activities of amyloid beta peptide 25–35. Curr Protein Pept Sci 11:54–67
58. Miyaji T, Echigo N, Hiasa M, Senoh S, Omote H, Moriyama Y (2008) Identification of a vesicular aspartate transporter. Proc Natl Acad Sci USA 105:11720–11724
59. Morgan J, Alves M, Conte G, Menéndez-Méndez A, de Diego-Garcia L, de Leo G, Beamer E, Smith J, Nicke A, Engel T (2020) Characterization of the expression of the ATP-gated P2X7 receptor following status epilepticus and during epilepsy using a P2X7-EGFP reporter mouse. Neurosci Bull. https://doi.org/10.1007/s12264-020-00573-9
60. Mucke L, Masliah E, Yu GQ, Mallory M, Rockenstein EM, Tatsuno G, Hu K, Kholodenko D, Johnson-Wood K, McConlogue L (2000) High-level neuronal expression of abeta 1–42 in wild-type human amyloid protein precursor transgenic mice: synaptotoxicity without plaque formation. J Neurosci 20:4050–4058
61. Nadrigny F, Li D, Kemnitz K, Ropert N, Koulakoff A, Rudolph S, Vitali M, Giaume C, Kirchhoff F, Oheim M (2007) Systematic colocalization errors between acridine orange and EGFP in astrocyte vesicular organelles. Biophys J 93:969–980
62. Nedergaard M, Rodriguez JJ, Verkhratsky A (2010) Glial calcium and diseases of the nervous system. Cell Calcium 47:140–149
63. Ong WY, Tanaka K, Dawe GS, Ittner LM, Farooqui AA (2013) Slow excitotoxicity in Alzheimer's disease. J Alzheimers Dis 35:643–668
64. Orellana JA, Shoji KF, Abudara V, Ezan P, Amigou E, Saez PJ, Jiang JX, Naus CC, Saez JC, Giaume C (2011) Amyloid beta-induced death in neurons involves glial and neuronal hemichannels. J Neurosci 31:4962–4977
65. Pande J, Szewczyk MM, Grover AK (2011) Allosteric inhibitors of plasma membrane Ca pumps: invention and applications of caloxins. World J Biol Chem 2:39–47
66. Parekh AB, Putney JW Jr (2005) Store-operated calcium channels. Physiol Rev 85:757–810. https://doi.org/10.1152/physrev.00057.2003
67. Park H, Oh SJ, Han KS, Woo DH, Mannaioni G, Traynelis SF, Lee CJ (2009) Bestrophin-1 encodes for the Ca2+-activated anion channel in hippocampal astrocytes. J Neurosci 29:13063–13073
68. Parsons CG, Stöffler A, Danysz W (2007) Memantine: a NMDA receptor antagonist that improves memory by restoration of homeostasis in the glutamatergic system—too little activation is bad, too much is even worse. Neuropharmacology 53:699–723
69. Perez-Alvarez A, Navarrete M, Covelo A, Martin ED, Araque A (2014) Structural and functional plasticity of astrocyte processes and dendritic spine interactions. J Neurosci 34:12738–12744
70. Pham C, Moro DH, Mouffle C, Didienne S, Hepp R, Pfrieger FW, Mangin JM, Legendre P, Martin C, Luquet S et al (2020) Mapping astrocyte activity domains by light sheet imaging and spatio-temporal correlation screening. Neuroimage 220:117069. https://doi.org/10.1016/j.neuroimage.2020.117069
71. Ponsioen B, Zhao J, Riedl J, Zwartkruis F, van der Krogt G, Zaccolo M, Moolenaar WH, Bos JL, Jalink K (2004) Detecting cAMP-induced Epac activation by fluorescence resonance energy transfer: Epac as a novel cAMP indicator. EMBO Rep 5:1176–1180
72. Putney JW (2010) Pharmacology of store-operated calcium channels. Mol Interv 10:209–218. https://doi.org/10.1124/mi.10.4.4
73. Reyes RC, Verkhratsky A, Parpura V (2012) Plasmalemmal Na+/Ca2+ exchanger modulates Ca2+-dependent exocytotic release of glutamate from rat cortical astrocytes. ASN Neuro 4:AN20110059
74. Ronco V, Grolla AA, Glasnov TN, Canonico PL, Verkhratsky A, Genazzani AA, Lim D (2014) Differential deregulation of astrocytic calcium signalling by amyloid-β, TNFα, IL-1β and LPS. Cell Calcium 55:219–229. https://doi.org/10.1016/j.ceca.2014.02.016
75. Ropert N, Jalil A, Li D (2016) Expression and cellular function of vSNARE proteins in brain astrocytes. Neuroscience 323:76–83
76. Rouach N, Koulakoff A, Abudara V, Willecke K, Giaume C (2008) Astroglial metabolic networks sustain hippocampal synaptic transmission. Science 322:1551–1555
77. Saez JC, Contreras JE, Bukauskas FF, Retamal MA, Bennett MV (2003) Gap junction hemichannels in astrocytes of the CNS. Acta Physiol Scand 179:9–22. https://doi.org/10.1046/j.1365-201X.2003.01196.x
78. Savtchouk I, Volterra A (2018) Gliotransmission: beyond Black-and-White. J Neurosci 38:14–25
79. Shen W, Nikolic L, Meunier C, Pfrieger F, Audinat E (2017) An autocrine purinergic signaling controls astrocyte-induced neuronal excitation. Sci Rep 7:11280. https://doi.org/10.1038/s41598-017-11793-x
80. Shigetomi E, Kracun S, Sofroniew MV, Khakh BS (2010) A genetically targeted optical sensor to monitor calcium signals in astrocyte processes. Nat Neurosci 13:759–766
81. Shigetomi E, Tong X, Kwan KY, Corey DP, Khakh BS (2011) TRPA1 channels regulate astrocyte resting calcium and inhibitory synapse efficacy through GAT-3. Nat Neurosci 15:70–80
82. Shimizu H, Borin ML, Blaustein MP (1997) Use of La3+ to distinguish activity of the plasmalemmal Ca2+ pump from Na+/Ca2+ exchange in arterial myocytes. Cell Calcium 21:31–41
83. Singaravelu K, Lohr C, Deitmer JW (2006) Regulation of store-operated calcium entry by calcium-independent phospholipase A2 in rat cerebellar astrocytes. J Neurosci 26:9579–9592. https://doi.org/10.1523/JNEUROSCI.2604-06.2006
84. Sreetama SC, Takano T, Nedergaard M, Simon SM, Jaiswal JK (2016) Injured astrocytes are repaired by Synaptotagmin XI-regulated lysosome exocytosis. Cell Death Differ 23:596–607. https://doi.org/10.1038/cdd.2015.124
85. Stix B, Reiser G (1998) Beta-amyloid peptide 25–35 regulates basal and hormone-stimulated Ca2+ levels in cultured rat astrocytes. Neurosci Lett 243:121–124
86. Takano T, Kang J, Jaiswal JK, Simon SM, Lin JH, Yu Y, Li Y, Yang J, Dienel G, Zielke HR et al (2005) Receptor-mediated glutamate release from volume sensitive channels in astrocytes. Proc Natl Acad Sci USA 102:16466–16471
87. van der Krogt GN, Ogink J, Ponsioen B, Jalink K (2008) A comparison of donor-acceptor pairs for genetically encoded FRET sensors: application to the Epac cAMP sensor as an example. PLoS ONE 3:e1916
88. Verdier Y, Zarandi M, Penke B (2004) Amyloid beta-peptide interactions with neuronal and glial cell plasma membrane: binding sites and implications for Alzheimer's disease. J Pept Sci 10:229–248
89. Verkhratsky A, Sofroniew MV, Messing A, deLanerolle NC, Rempe D, Rodriguez JJ, Nedergaard M (2012) Neurological diseases as primary gliopathies: a reassessment of neurocentrism. ASN Neuro 4:e00082. https://doi.org/10.1042/AN20120010

90. Walton HS, Dodd PR (2007) Glutamate-glutamine cycling in Alzheimer's disease. Neurochem Int 50:1052–1066
91. Wang F, Smith NA, Xu Q, Fujita T, Baba A, Matsuda T, Takano T, Bekar L, Nedergaard M (2012) Astrocytes modulate neural network activity by Ca(2)+-dependent uptake of extracellular K+. Sci Signal 5:ra26
92. Wilson JE, Chin A (1991) Chelation of divalent cations by ATP, studied by titration calorimetry. Anal Biochem 193:16–19. https://doi.org/10.1016/0003-2697(91)90036-s
93. Woo D, Han K-S, Shim J, Yoon B-E, Kim E, Bae J, Oh S, Hwang E, Marmorstein A, Bae Y et al (2012) TREK-1 and Best1 channels mediate fast and slow glutamate release in astrocytes upon GPCR activation. Cell 151:25–40
94. Xiao Q, Hartzell HC, Yu K (2010) Bestrophins and retinopathies. Pflugers Arch 460:559–569
95. Xiong Y, Teng S, Zheng L, Sun S, Li J, Guo N, Li M, Wang L, Zhu F, Wang C et al (2018) Stretch-induced Ca(2+) independent ATP release in hippocampal astrocytes. J Physiol 596:1931–1947. https://doi.org/10.1113/JP275805
96. Yang J, Vitery MDC, Chen J, Osei-Owusu J, Chu J, Qiu Z (2019) Glutamate-releasing SWELL1 channel in astrocytes modulates synaptic transmission and promotes brain damage in stroke. Neuron. https://doi.org/10.1016/j.neuron.2019.03.029
97. Ye ZC, Wyeth MS, Baltan-Tekkok S, Ransom BR (2003) Functional hemichannels in astrocytes: a novel mechanism of glutamate release. J Neurosci 23:3588–3596
98. Yi C, Mei X, Ezan P, Mato S, Matias I, Giaume C, Koulakoff A (2016) Astroglial connexin43 contributes to neuronal suffering in a mouse model of Alzheimer's disease. Cell Death Differ 23:1691–1701. https://doi.org/10.1038/cdd.2016.63
99. Yu X, Taylor AMW, Nagai J, Golshani P, Evans CJ, Coppola G, Khakh BS (2018) Reducing astrocyte calcium signaling in vivo alters striatal microcircuits and causes repetitive behavior. Neuron 99(1170–1187):e1179. https://doi.org/10.1016/j.neuron.2018.08.015
100. Zamanian JL, Xu L, Foo LC, Nouri N, Zhou L, Giffard RG, Barres BA (2012) Genomic analysis of reactive astrogliosis. J Neurosci 32:6391–6410
101. Zhang Z, Chen G, Zhou W, Song A, Xu T, Luo Q, Wang W, Gu XS, Duan S (2007) Regulated ATP release from astrocytes through lysosome exocytosis. Nat Cell Biol 9:945–953
102. Zhao Y, Araki S, Wu J, Teramoto T, Chang YF, Nakano M, Abdelfattah AS, Fujiwara M, Ishihara T, Nagai T et al (2011) An expanded palette of genetically encoded Ca(2)(+) indicators. Science 333:1888–1891

Publisher's Note

Supplementary material

Astrocytes respond to a neurotoxic Aβ fragment with state-dependent Ca^{2+} alteration and multiphasic transmitter release

Abbreviation list:

2-APB – 2-Aminoethoxydiphenyl borate

Aβ – amyloid β

AD – Alzheimer's disease

cAMP – cyclic adenosine monophosphate

CBX - carbenoxolone

CX – connexin

DCPIB –

4-[(2-butyl-6,7-dichloro-2-cyclopentyl-2,3-dihydro-1-oxo-1*H*-inden-5-yl)oxy]butanoic acid

EPAC – exchange protein directly activated by cAMP

ER – endoplasmic reticulum

FRET – fluorescence resonance energy transfer

GLT-1 – glutamate transporter 1

GLAST – glutamate aspartate transporter

GPN – glycyl-L-phenylalanine 2-naphthylamide

mGluR – metabotropic glutamate receptor

MPEP – 2-Methyl-6-(phenylethynyl)pyridine

NCX – sodium calcium exchanger

NPPB – 5-nitro-2-(3-phenylpropylamino) benzoic acid

OGB-1 – Oregon green bapta 1

PMCA – plasma membrane Ca^{2+} ATPase

PPADS – pyridoxalphosphate-6-azophenyl-2',4'-disulfonic acid

SOC – store-operated channel

SD – standard deviation

TIRFM – total internal reflection fluorescence microscopy

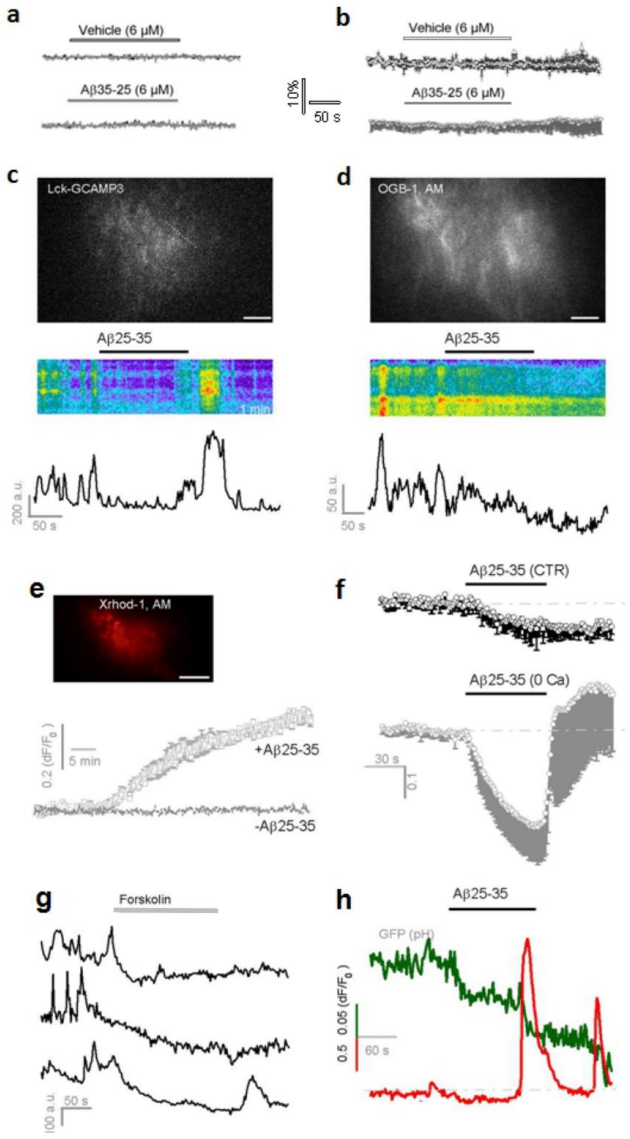

Fig. S1 Effects of Aβ25-35 on astrocyte Ca^{2+} signaling. Cultured astrocytes in basal condition (**a**) and after Aβ preconditioning (**b;** Aβ25-35, 0.5 μM, 2 hr) in response to either vehicle (i.e., equal molar H_2O) or the reversed peptide Aβ35-25 (n = 7 per condition). (**c-d**) Inhibitory effect of Aβ (6 μM) on spontaneous astrocytic Ca^{2+} oscillation. (**e**) Preconditioning with Aβ25-35 (0.5 μM) caused gradual Ca^{2+} overload in astrocytes. The chemical Ca^{2+} dye

Xrhod-1, AM was used for long-term Ca^{2+} imaging (n = 8 cells for each). (**f**) Removing extracellular Ca^{2+} facilitated Aβ25-35-caused Ca^{2+} diminution (n = 9 for CTR, n = 7 for zero external Ca^{2+} condition). (**g**) Inhibition of spontaneous astrocyte Ca^{2+} oscillations by forskolin (100 μM). (**h**) Stepwise decreases in intracellular pH observed in the 'mix' type astrocyte Ca^{2+} response, which was evoked by Aβ25-35 (6 μM) in astrocytes after short-term preconditioning (Aβ25-35 0.5 μM, 0.5 hr). The red Ca^{2+} sensor GECO-R and the pH-sensitive GFP fluorescent protein were co-expressed in cultured astrocytes. During Aβ25-35 application, the initial small diminution in basal Ca^{2+} was likely due to the direct potentiation of PMCA that meanwhile caused H^+ influx thereby decreasing the GFP fluorescence. The delayed Ca^{2+} rise would have also activated PMCA to confine the Ca^{2+} elevation, inducing more H^+ influx to further quench the GFP fluorescence. During the elevation phase, cytosolic Ca^{2+} could also be buffered into ER via the sacro/endoplasmic reticulum Ca^{2+} ATPase. Scale bars, 5 μm.

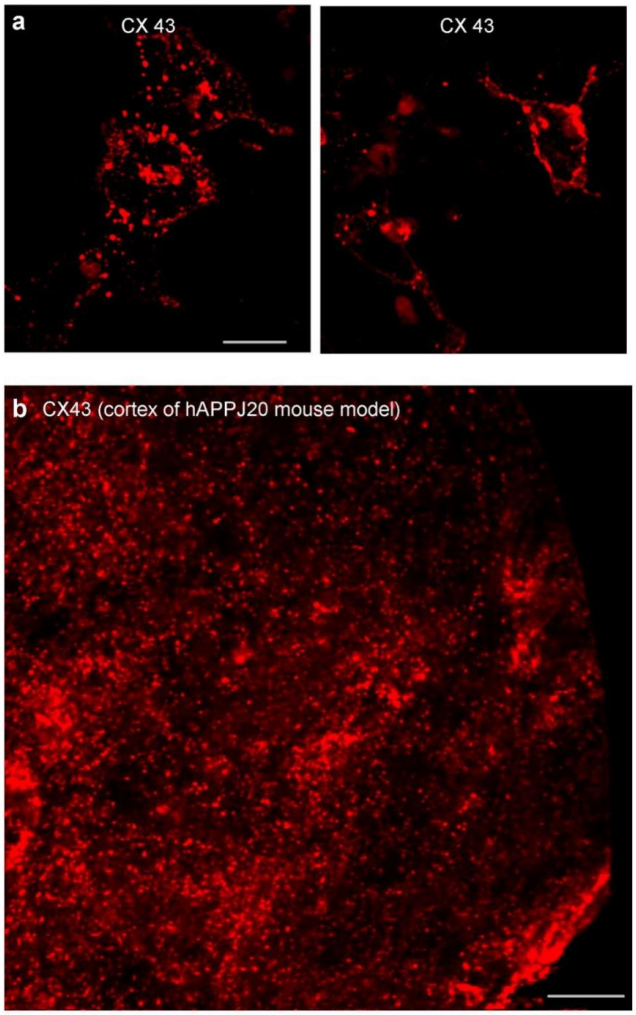

Fig. S2 Immunostaining of connexin 43 in cultured cortical astrocytes (**a**) and in somatosensory cortex of hAPPJ20 AD mouse (~7 month age; **b**). Scale bars, 20 µm.

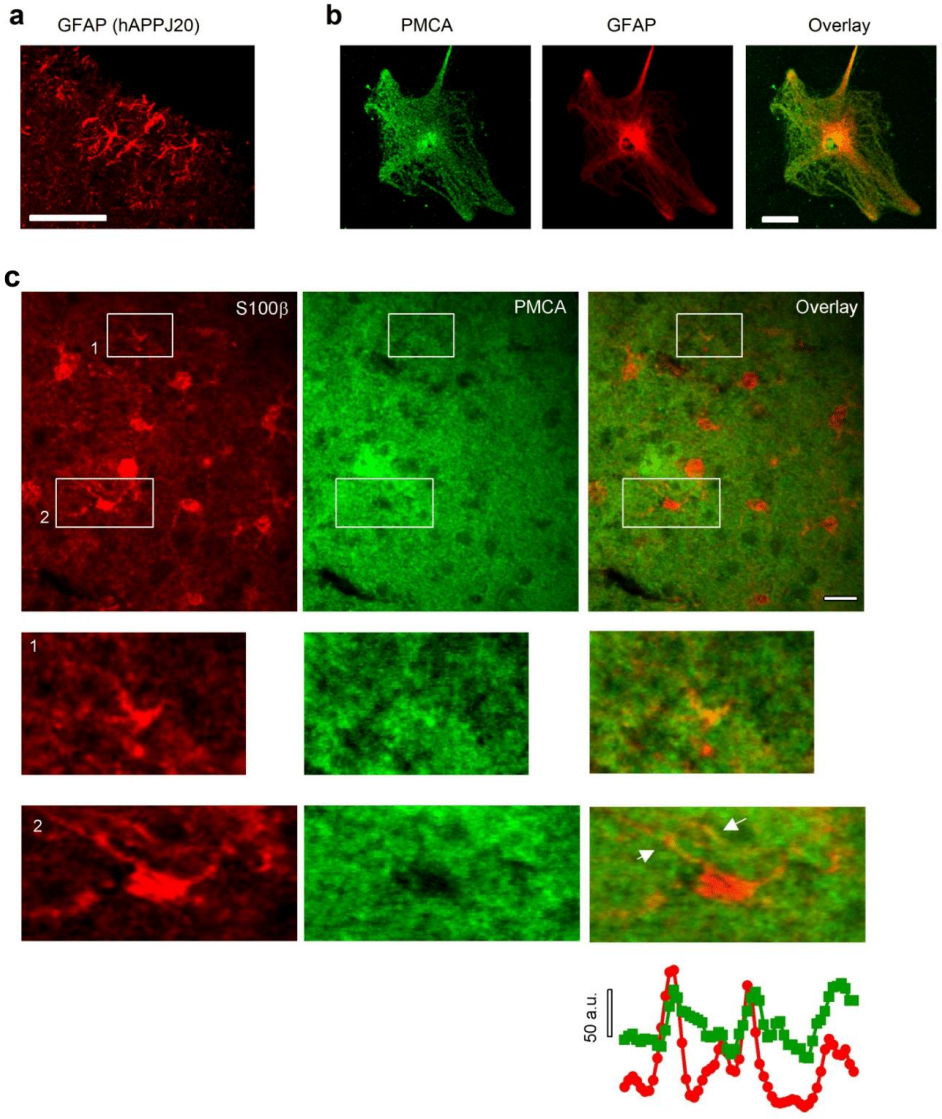

Fig. S3 Immunostaining of PMCA in astrocytes. (**a**) GFAP-positive astrocytes observed by immunostaining in the somatosensory cortex of J20 AD mouse model (~7 month old). Scale bar, 50 µm. (**b**) Immunostaining of a pan PMCA antibody against the astrocyte marker GFAP in cultured cortical astrocytes of wild-type mice. Scale bar, 10 µm. (**c**) PMCA

immunostaining in astrocytes in somatosensory cortex of hAPPJ20 AD mouse model. The diffuse staining pattern is consistent with the membranous expression of PMCA. A subpopulation of PMCA labeling was observed to surround S100β-positive astrocytic somata, and present in S100β-identified processes. Mouse age is ~7 month. Scale bar, 20 µm.

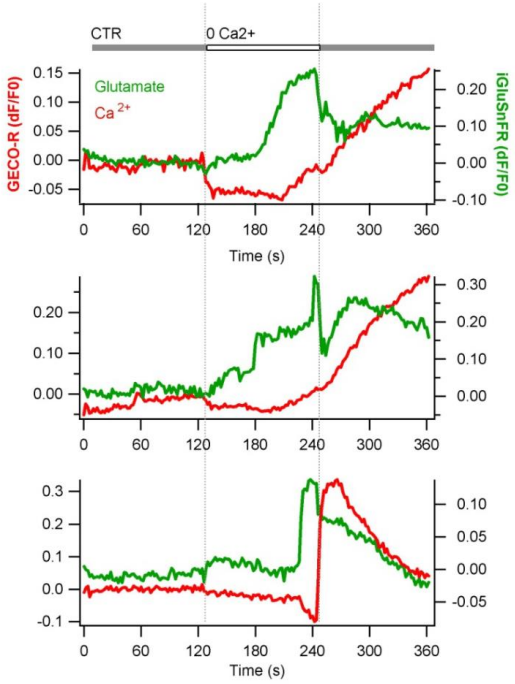

Fig. S4 Astrocyte glutamate release via opened CX hemichannels. CX hemichannels were opened by Ca^{2+}-free solution (open bar). Cytosolic Ca^{2+} and glutamate release were simultaneously imaged with TRIFM, in astrocytes co-expressing the red GECO-R and green iGluSnFR sensor. Glutamate release was observed in the absence of Ca^{2+} elevation. A diminution in cytosolic Ca^{2+} was observed in the phase of 0 Ca^{2+}, indicating the gradual Ca^{2+} efflux due to the reversed ion gradient. Switching back to control solution (1.8 mM Ca^{2+}) re-closed CX hemichannels, causing a transient inhibition for the glutamate release; meanwhile, re-supplying Ca^{2+} elevated Ca^{2+} levels in the cytosol that then sustained another

phase of glutamate release. This result is in line with the co-existence of Ca^{2+}-independent and -dependent glutamate release from astrocytes.

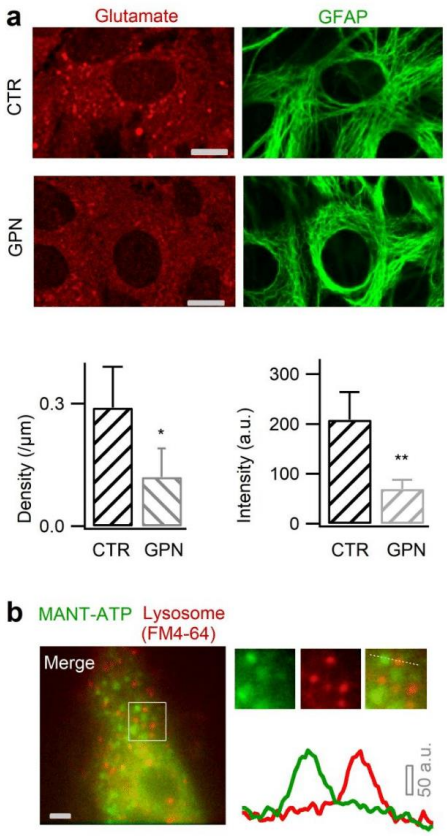

Fig. S5 Astrocyte lysosomes versus glutamate staining and ATP indicator. (**a**) Glutamate immunostaining in cultured astrocytes concentrated in perinuclear vesicular compartments. Punctate staining was reduced by cathepsin C substrate GPN (200 µM), a lysosome-disrupting compound (n = 9 - 11 cells per condition). Scale bar, 5 µm. (**b**) Representative spatial distribution of the fluorescent ATP marker MANT-ATP (50 µM, 1 hr) and the lysosomal marker FM4-64 (6.7 µM, 30 min). Scale bar, 10 µm.

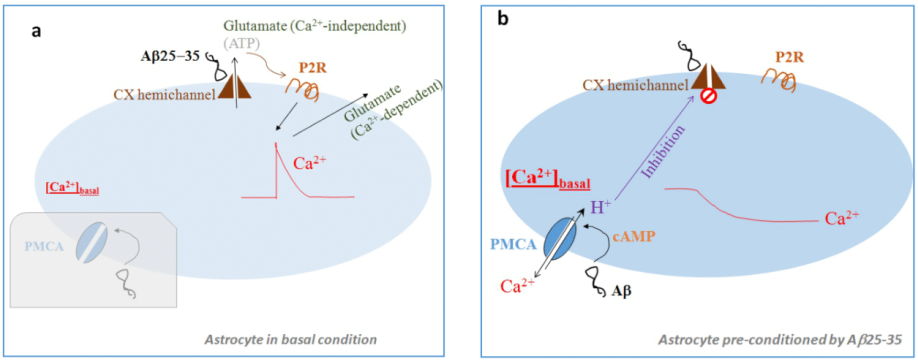

Fig. S6 Astrocyte response to Aβ25-35. (**a**) In astrocyes of basal conditions, cytosolic Ca^{2+} is maintainted at physiological low level (~100 nM) and PMCA shows no strong reaction to Aβ25-35. Meanwhile, Aβ25-35 acts on CX hemichannels leading to the release of glutamate, and likely ATP, in a Ca^{2+}-independent manner. Activation of purinergic P2 receptors then contributes to the intracellular Ca^{2+} elevation that triggers the Ca^{2+}-dependent release of glutamate. Aβ25-35 therefore plays an excitatory role in astrocytes in basal conditions. (**b**) Preconditioning of astrocytes with submicromolar Aβ25-35 peptide leads to gradual intracellular Ca^{2+} overload thereby setting a greater driving tendency for Ca^{2+} efflux. In this situation, PMCA actively reacts to subsequent Aβ25-35 stimulation, extruding cytosolic Ca^{2+} to the extracellular space therefore lowering the intracellular Ca^{2+} level. The coupled H^+ influx then inhibits the opening of CX hemichannels and the intracellular Ca^{2+} elevation. Aβ25-35 hence exerts an inhibitory effect on the inracellular Ca^{2+} level in preconditioned astrocytes.

Table S1 Antibodies used for fluorescence immunostaining

Experiments	Primary antibodies	Secondary antibodies
Single staining		
GFAP in brain slices of hAPPJ20 AD mouse model (Figure 3i)	Rb GFAP, Agilent/DAKO, Cat N° Z0334, 1/1000	Alexa 594 Goat (G) anti-Rb, Invitrogen, Cat N° A11012, 1/1000
Connexin 43 staining in brain slices of hAPPJ20 AD mouse model and in cultured astrocytes (Figure S2)	Rb Connexin 43, Sigma, Cat N° C6219, 1/1500	Alexa 594 G anti-Rb, Invitrogen, Cat N° A11012, 1/1000
Double staining		
GFAP and PMCA in cultured astrocytes (Figure 3j)	Rb GFAP, Agilent/DAKO, Cat N° Z0334, 1/1000 Mouse (M) pan PMCA ATPase Monoclonal Antibody, ThermoFisher Scientific, Cat N° MA3-914, 1/500	Alexa 594 Goat (G) anti-Rb, Invitrogen, Cat N° A11012, 1/1000 Alexa 488 G anti M IgG2A, Invitrogen, Cat N° A-21131, 1/1000
S100β and PMCA co-staining in the cortex of J20 AD mouse (Figure S3)	Rb monoclonal S100β , Abcam, Cat N° ab52642, 1/500 Mouse (M) pan PMCA ATPase Monoclonal Antibody, ThermoFisher Scientific, Cat N° MA3-914, 1/500	Alexa 594 G anti-Rb, Invitrogen, Cat N° A11012, 1/1000 Alexa 488 G anti M IgG2A, Invitrogen, cat N°A-21131, 1/1000

Table S2 Combinations of excitation wavelengths and filters for TIRFM imaging

Fluorophore	Excitation laser line (nm)	Dichroic filter (nm)	Emission filter (nm)
EGFP, pHluorin	488	500LP or PolyX[§]	535(50)BP
GECO-R	568	PolyX[§]	600LP
GFP(nd)-EPAC1(dDEP)-mCherry	488	PolyX[§]	535(50)&600LP[$]
OGB-1	488	PolyX[§]	535(50)BP
OGB-1 and FM4-64	488	PolyX[§]	535(50)&675(50)BP[$]
Xrhod-1	568	PolyX[§]	600LP or 615(45)BP

[§]PolyX – custom dual dichroic mirror with 488/568/NIR reflection bands and low ripple high-transmission elsewhere (AHF Analysentechnik).
[$]*denotes filters for simultaneous view with a custom dual-view device*.

II.3.2 - Initial in vivo experiment to modulate glymphatic diffusion in an Alzheimer's mouse model

In **Chapter I** study, combining the multimodal imaging approaches and the selective AQP4 blocker TGN-020, I have examined the acute influence of AQP4 on astrocyte volume regulation. The results suggest that acutely blocking AQP4 activity with TGN-020 induces astrocyte swelling, indicating AQP4 tonically constrains astrocyte swelling, and accordingly, acute inhibition of AQP4 facilitates hypotonically evoked astrocyte swelling and impedes hypertonically induced astrocyte shrinking. **These results suggest that pharmacologically targeting AQP4 will shape astrocyte volume dynamics, and thereby the extracellular route, which might be used to modulate glymphatic clearance of amyloid β peptide in AD brain.**

To probe this hypothesis, I have started to employ the hAPPJ20 AD mouse model, used in my recent study (Pham et al., 2021), to design experiments to examine the potential effect of modulating astrocytic AQP4 on brain to Aβ1-42 peptide deposition.

As the hAPPJ20 AD mouse model start forming Aβ1-42 fibrils/plaques after 4-5 month of age (**Fig. 39**). I have decided to manipulate AQP4 function in vivo in pre-plaque phase, thereby enabling the evaluation of astrocyte impact on the formation of Aβ fibrils, and the inference on the clearance of diffusible Aβ peptides. I therefore started using 4-month old mice to pharmacologically manipulate AQP4 functions in vivo for 1 week, so as to determine the effect on the subsequent Aβ1-42 deposition. In addition to the AQP4 blocker TGN-020, I also used the AQP4 facilitator, TGN-073 (N-(3-benzyloxypyridin- 2-yl)-benzene-sulfonamide) (Huber et al., 2018), thus allowing the paired comparison between the loss- and gain-of-function interventions.

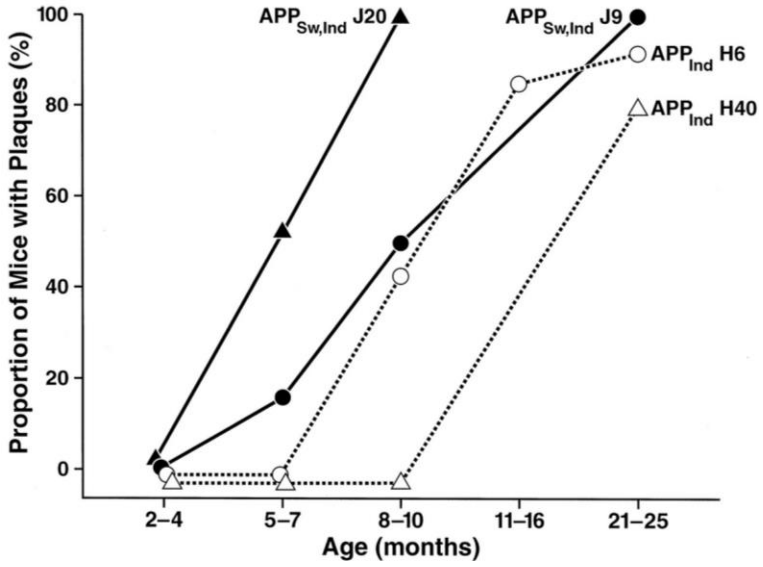

Figure 39: Aβ plaque formation time course in hAPP J20 mice (Mucke et al., 2000)

Three groups of mice (n = 5 each) have been planned for: 1) receiving vehicle IP injection; 2) receiving AQP4 inhibitor TGN-020 injection (250 mg/kg body weight); 3) receiving AQP4 facilitator TGN-73 (250 mg/kg body weight). Injection are to be performed once a day for one week. The amount of Aβ peptides be imaged in brain slices, following vital labeling with Thioflavin T (20 µM). This molecular probe displays high fluorescence upon binding to Aβ fibrils and the fluorescence signal correlates linearly with the concentration of Aβ peptides Aβ1-40 and Aβ1-42, the major forms associated with AD development (Xue et al., 2017). The extent of Aβ1-42 deposition can thus be estimated by the level of Thioflavin fluorescence intensity. This set of experiments helps to pinpoint the efficacy of manipulating AQP4 on the glymphatic clearance of Aβ1-42 from the hAPPJ20 AD mouse model, providing clues on controlling Aβ deposition during the early stage of amyloidopathy.

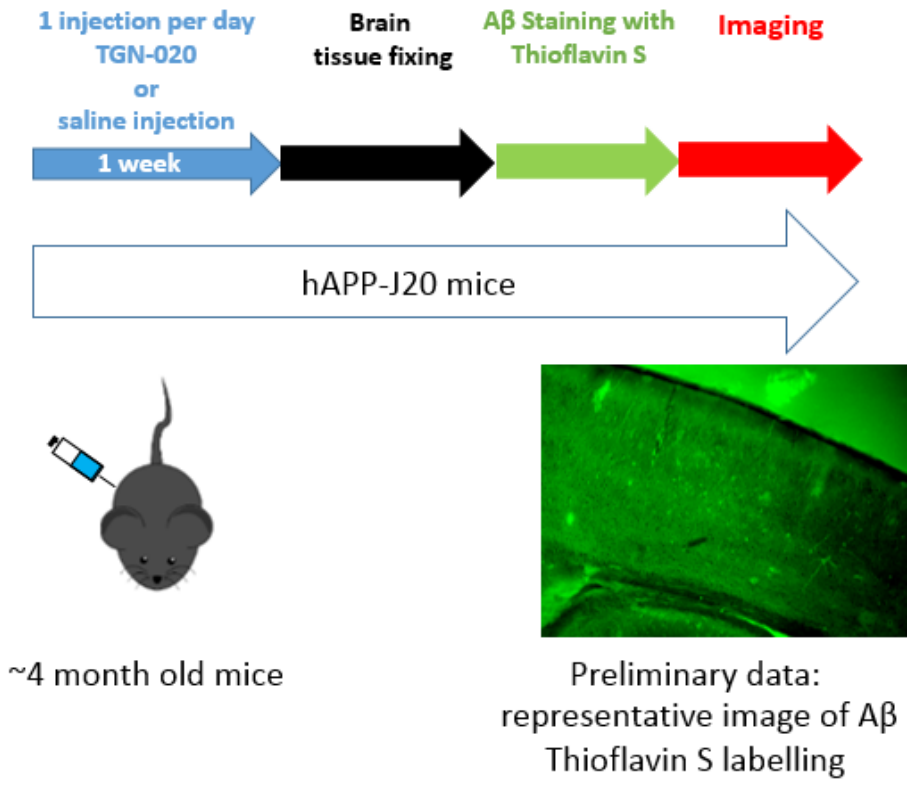

Figure 40: Experiments for exanimating the effect of AQP4 on Aβ clearance in AD mouse model (on going).

These experiments are in collaboration with Dr. Bruno Cauli in our laboratory; the experimental protocol is illustrated in **Fig. 40**. I have tested the planned experimental protocols in 4 mice, and obtained fluorescence staining of Aβ1-42 in mouse brain using the full brain scope microscope. The initial results show wide spread Aβ distribution, with an appreciable amount deposited along vascular-like structures, implying the presence of Aβ in the perivascular spaces along the glymphatic diffusion pathways. Because i) the requirement of the age-matched AD mice, and the adjustment of the feasible in vivo pharmacological treatment protocols took me an unexpected amount of time, ii) the taking place of the full cleaning processes in the mice-handling animal houses in our laboratory, interrupted the in vivo AQP4 experiments during my last year of PhD study, these experiments are still on-going. Nevertheless, I have already finished the sampling of two groups of mice (control vs. TGN-020), which will be imaged in short time. It is expected that facilitating the water flux by potentiating the AQP4 with TGN-073 would help to clear Aβ, thereby reducing its deposition. TGN-020, via blocking AQP4,

would cause astrocyte swelling, reduce extracellular space and exacerbate Aβ accumulation. The expected results will hence provide clues on the therapeutic potential of targeting astrocyte AQP4. Pharmacological strategy holds the advantage that it could be readily tested in vivo over flexible time windows and by different doses.

II.4 - Perspectives

The proposed experiments in this chapter possess multiple perspectives. First, the results suggest a mechanism link between astrocyte Ca^{2+} dynamics and volume control. Early studies mainly investigated the phenomena using cultured astrocytes (Takano et al., 2005; Mola et al., 2016). Because astrocytes in culture show different features from their in vivo states (Zamanian et al., 2012), so it is necessary to explore astrocyte Ca^{2+} regulation of volume dynamics in situ. The experimental strategies I explored so far enabled the study of this important scientific question at multiscale level, from brain slices to all brain scale in vivo in mouse model. Secondly, thus far the effect of regulating astrocyte AQP4 on the clearance of amyloid β or other waste molecules remains to be clarified. My current results so far suggest that AQP4 plays an important role in maintaining the volume homeostasis of astrocytes in situ, making it possible to target astrocyte AQP4 to regulate extracellular space, and the brain fluid transport. Further experiments to establish the efficacy of this treatment on amelioration of cognitive behavior will pave the way for preclinical tests. There is a change in the polarization AQP4 distribution at the astrocytic endfeet in several neuropathologies including Alzheimer's disease (Ikeshima-Kataoka, 2016) So alternatively to understands the mechanism of the disruption in AQP4 localisation under neuropathology will help to rescue the functional distribution thereby preventing disease development. A recent report suggest that the clinical drug trifluoperazine can modulate the trafficking of AQP4 in vivo (Kitchen et al., 2020) which ameliorates the recovery from brain edema. Therefore this strategy could be also used to control AQP4 dysfunction in neurodegenerative disease. Thirdly, my Ph.D study also shows that diffusion MRI is noninvasive method and sensitive for brain fluid transport detection. This technique could be used for early diagnostics of brain fluid transport disruption linked pathologies. It can further extended to follow the development of other neurological disease, and metabolism disorders in the brain.

Chapter III: Collaborative works

The scientific knowledge from my PhD study has also fostered collaborative works for understanding:

I) Brain astrocyte activity remodeling in obesity-associated metabolic syndromes. The results of this part contribute to the discovery that the calcium signaling of hypothalamic astrocytes undergoes heterogeneous remodeling in anatomically defined nuclei implicated in systemic metabolism regulation. This work has helped to delineate the important participation of astrocytes in energy balance control. This part of the study has been published (Herrera Moro Chao et al, 2022).

II) The molecular mechanisms underlying the trafficking of calcium-permeable transient potential receptor ion channels. This work suggests testable molecular targets for interrogating the calcium signaling mechanisms in nervous cells including astrocytes (Tian et al, 2019).

III.1 - Contribution to the understanding of brain astrocytes adaptation to systemic metabolic disorders.

Article

Cell Metabolism

Hypothalamic astrocytes control systemic glucose metabolism and energy balance

Graphical abstract

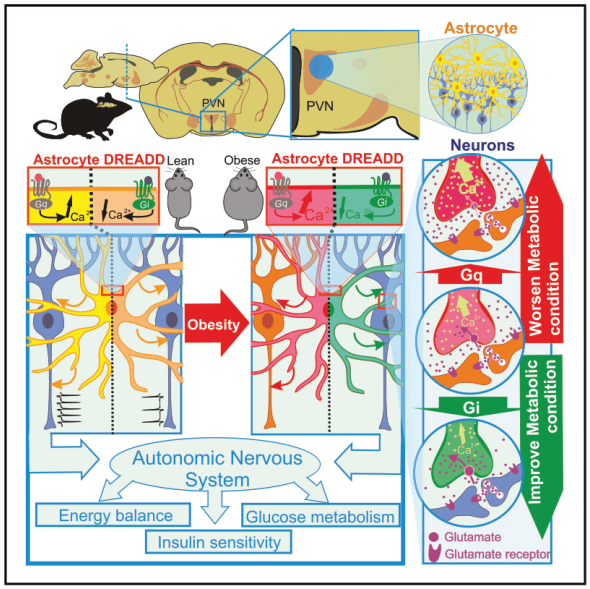

Highlights

- Diet-induced obesity induces astrocytic Ca^{2+} signal remodeling in the hypothalamus
- PVN astrocytes can control PVN parvocellular neuronal firing
- PVN astrocytes bidirectionally affect systemic metabolism in obese mice
- Astrocytic control of extracellular glutamate is impaired in obesity

Authors

Daniela Herrera Moro Chao, Matthew K. Kirchner, Cuong Pham, ..., Claire Martin, Javier E. Stern, Serge H. Luquet

Correspondence

herrerad@umn.edu (D.H.M.C.), serge.luquet@u-paris.fr (S.H.L.)

In brief

Herrera Moro Chao et al. show that obesity promotes anatomically restricted remodeling of hypothalamic astrocyte activity. In the paraventricular nucleus of the hypothalamus (PVN), chemogenetic manipulation of astrocytes results in bidirectional control of neighboring neuron activity, autonomic outflow, glucose metabolism, and energy balance through the control of ambient glutamate levels.

Herrera Moro Chao et al., 2022, Cell Metabolism *34*, 1532–1547
October 4, 2022
https://doi.org/10.1016/j.cmet.2022.09.002

CellPress

CellPress

Cell Metabolism

Article

Hypothalamic astrocytes control systemic glucose metabolism and energy balance

Daniela Herrera Moro Chao,[1,8,*] Matthew K. Kirchner,[3,4,8] Cuong Pham,[5] Ewout Foppen,[1] Raphael G.P. Denis,[1,2] Julien Castel,[1] Chloe Morel,[1] Enrica Montalban,[1] Rim Hassouna,[1] Linh-Chi Bui,[1] Justine Renault,[1] Christine Mouffle,[5] Cristina García-Cáceres,[6,7] Matthias H. Tschöp,[6] Dongdong Li,[5,9] Claire Martin,[1,9] Javier E. Stern,[3,4,9] and Serge H. Luquet[1,9,10,*]

[1]Université Paris Cité, CNRS, Unité de Biologie Fonctionnelle et Adaptative, Paris, France
[2]Institut Cochin, Université Paris Cité, INSERM U1016, CNRS UMR 8104, 75014 Paris, France
[3]Neuroscience Institute, Georgia State University, Atlanta, GA 30303, USA
[4]Center for Neuroinflammation and Cardiometabolic Diseases, Georgia State University, Atlanta, GA 30302, USA
[5]Institute of Biology Paris Seine, Neuroscience Paris Seine, CNRS UMR8246, INSERM U1130, Sorbonne Universite, Paris 75005, France
[6]Helmholtz Diabetes Center (HDC) & German Center for Diabetes Research (DZD), Helmholtz Zentrum München, Neuherberg, 85764, Germany; Division of Metabolic Diseases, Technische Universität München, Munich, 80333, Germany
[7]Medizinische Klinik and Poliklinik IV, Klinikum der Universität, Ludwig-Maximilians-Universität München, Munich, Germany
[8]These authors contributed equally
[9]Senior author
[10]Lead contact
*Correspondence: herrerad@umn.edu (D.H.M.C.), serge.luquet@u-paris.fr (S.H.L.)
https://doi.org/10.1016/j.cmet.2022.09.002

SUMMARY

The hypothalamus is key in the control of energy balance. However, strategies targeting hypothalamic neurons have failed to provide viable options to treat most metabolic diseases. Conversely, the role of astrocytes in systemic metabolic control has remained largely unexplored. Here, we show that obesity promotes anatomically restricted remodeling of hypothalamic astrocyte activity. In the paraventricular nucleus (PVN) of the hypothalamus, chemogenetic manipulation of astrocytes results in bidirectional control of neighboring neuron activity, autonomic outflow, glucose metabolism, and energy balance. This process recruits a mechanism involving the astrocytic control of ambient glutamate levels, which becomes defective in obesity. Positive or negative chemogenetic manipulation of PVN astrocyte Ca^{2+} signals, respectively, worsens or improves metabolic status of diet-induced obese mice. Collectively, these findings highlight a yet unappreciated role for astrocytes in the direct control of systemic metabolism and suggest potential targets for anti-obesity strategy.

INTRODUCTION

Obesity is a public health concern associated with a higher incidence of type 2 diabetes, cardiovascular disease, and other life-threatening comorbidities (Morton et al., 2014; Saklayen, 2018). Understanding the mechanisms underlying the onset and progression of the disease is essential to identify potential targets for therapeutic intervention. In mammals, energy homeostasis results from the balance between energy expenditure and nutrient intake. Nervous inputs and circulating factors are integrated by discrete neural circuits in the brain, which, in turn, provide an adaptive behavioral, neuroendocrine, and metabolic response (Morton et al., 2014). In the hypothalamus, specialized neuronal populations maintain a strict monitoring of the peripheral metabolic state and regulate food intake and body metabolism by modulating the autonomic nervous system (ANS) (Dietrich and Horvath, 2013; Roh et al., 2016; Timper and Brüning, 2017; Yi et al., 2010). In particular, pre-autonomic neurons located in the paraventricular nucleus (PVN) have emerged as important hypothalamic autonomic/neuroendocrine regulators of the physiology of energy balance. (Licht et al., 2013; Thayer et al., 2010). They modulate feeding, energy expenditure, neurohormonal response, and cardiovascular function through autonomic efferents projecting to the brainstem and spinal autonomic outputs (Betley et al., 2013; Dampney et al., 2018; Li et al., 2019; Münzberg et al., 2016). The activity of hypothalamic neurons is tightly dependent on adequate delivery of energy substrates provided by astrocytes, the major type of glial cells in the brain (García-Cáceres et al., 2019; Verkhratsky, 2018). In physiological and pathological conditions, astrocytes exert a wide spectrum of adaptive functions that can promote and preserve neuronal health, such as synaptogenesis, synaptic efficacy, and plasticity within neuronal networks (Freire-Regatillo et al., 2017; Verkhratsky, 2018). By occupying a strategic position in brain circuits, at the interface between blood vessels and neurons, they participate in the transport and sensing of nutrients

CellPress

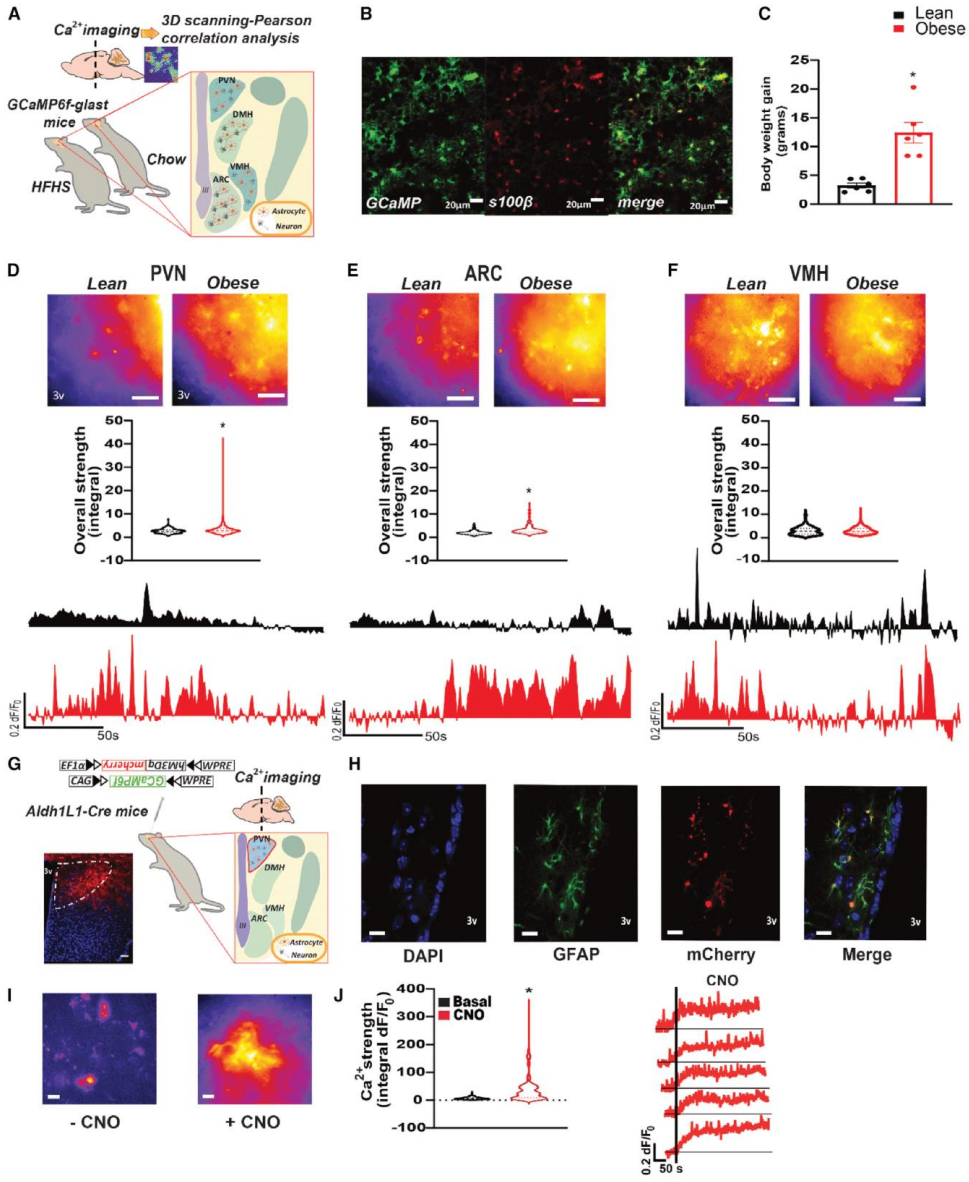

Figure 1. Hypothalamic astrocytes display Ca^{2+} hyperactivity in a heterogeneous manner during diet-induced obesity

(A) Experimental setting.

(B) Representative confocal photomicrograph for GCaMP (green) and s100β (red) immunoreactivity in the PVN of GCaMP6f-Glast-CreER^{T2} mice.

(C) Body weight gain of GCaMP6f-Glast-CreER^{T2} mice after 4-month chow (lean, n = 6) or HFHS (obese, n = 6) diet consumption.

(legend continued on next page)

and metabolic factors across the blood brain barrier (Allen and Eroglu, 2017).

Hypothalamic astrocytes are being recognized as important players in the control of systemic energy metabolism (Caruso et al., 2013; García-Cáceres et al., 2013, 2016; Kim et al., 2014), and obesity leads to central low-grade inflammation triggers inflammatory-like response in hypothalamic astrocytes and reactive gliosis in several hypothalamic areas (Horvath et al., 2010), including the PVN (Buckman et al., 2013; Dalvi et al., 2017; De Souza et al., 2005; Milanski et al., 2009; Robb et al., 2020; Thaler et al., 2012). However, the direct contribution of astrocytes as gate keeper of PVN output, as well as their involvement in the control of bodily energy and glucose metabolism remain an open question.

In the current study, we took advantage of gain-loss-function and loss-of-function approaches allowing for the direct and selective imaging and manipulation of astrocytes to explore the causal role of astrocytes in metabolic response. We first show that although obesity indeed promotes astrocyte calcium (Ca^{2+}) activity remodeling that are anatomically defined to hypothalamic sub-nuclei. Astrocytic response could be mimicked by chemogenetic activation of astrocyte by Gq-coupled designer receptors exclusively activated by designer drugs (DREADDs). *in vivo* chemogenetic activation or inhibition of PVN astrocyte Ca^{2+} signaling exerted bidirectional control over neighboring PVN neuron firing, autonomic outflow, glucose metabolism, and energy balance. Finally, we found that the underlying mechanism by which astrocytes gate neural activity in the PVN relies on excitatory amino acid transporters (EAATs)-dependent control of ambient glutamate. In obese mice, this mechanism was selectively impaired and the chemogenetic increase (Gq) or decrease (Gi) of astrocytic Ca^{2+} led to metabolic aggravation or amelioration, respectively.

In summary, we show that PVN astrocytes exert direct control over systemic glucose metabolism and energy balance and support a concept in which obesity-associated diseases might be partially mediated through molecular and signaling modifications in hypothalamic astrocyte-neuron communication.

RESULTS

Diet-induced obesity induces astrocytic Ca^{2+} signal remodeling in the hypothalamus

We first assessed how diet-induced obesity (DIO) alters astrocytic Ca^{2+} signaling as a proxy for astrocyte activity (Figure 1A). The genetically encoded Ca^{2+} sensor GCaMP6f was expressed in astrocytes by crossing the tamoxifen-inducible Glast-CreER^{T2} line and the Cre-dependent GCaMP6f line (Pham et al., 2020). Astrocyte-specific expression of GCaMP6f after tamoxifen treatment was evidenced by co-localization of the astrocyte marker s100β and GCaMP6f in stellated cells characteristic of astrocytes (Figure 1B). GCaMP6f-expressing mice were fed either regular diet or high-fat high-sugar (HFHS, 45% fat and 35% sugar) diet for 2–3 months. Exposure to HFHS diet led to metabolic alteration characterized by increased body weight (Figure 1C), decreased glucose tolerance, and increased glucose-induced plasma insulin (Figures S1A and S1B). Using wide-field fluorescence imaging that enabled the integration of global Ca^{2+} signals, we imaged intrinsic Ca^{2+} activity in hypothalamic astrocytes in acute brain slices. Active regions were identified using the spatio-temporal correlation screening method (Pham et al., 2020) (Figures S1C and S1D). We observed that basal astrocyte Ca^{2+} signals in obese mice showed an overall increase in the PVN (Figures 1D, S1C, and S1D), the arcuate nucleus (ARC) (Figure 1E), and the dorsomedial nucleus of the hypothalamus (DMH) (Figure S1H). Interestingly, in the ventromedial nucleus of the hypothalamus (VMH), astrocytes remained relatively protected from diet-induced hyperactivity (Figure 1F). In the PVN, we quantitatively analyzed the Ca^{2+} imaging data in PVN, the region of focus in the current study and quantified the kinetic parameters between lean and obese animals. The result shows that the duration of Ca^{2+} signaling was reduced in obese animals (Figure S1E), whereas the frequency and amplitude were significantly enhanced in obese animals (Figure S1G). Taken together, these results indicate that DIO causes heterogeneous and anatomically restricted remodeling of astrocytic Ca^{2+} activity in metabolically relevant hypothalamic structures. These results are in perfect line with previous observation depicting increased hypothalamic astrocyte reactivity in obese mice (Horvath et al., 2010).

PVN astrocytes control systemic glucose metabolism

Given the prominent role of PVN neural substrate in the control of metabolism (Li et al., 2019; Sutton et al., 2016), we explored how direct manipulation of PVN astrocyte activity affects energy homeostasis through cell-specific DREADDs engineering. Mice expressing the Cre enzyme under the astrocyte-specific promoter Aldehyde dehydrogenase family 1, member L1 (Cahoy et al., 2008) (Aldh1L1-Cre mice), received an intra-PVN injection of a mixture of Cre-dependent viruses allowing for the expression of (1) mCherry alone (AAV 2/5.EF1α.DIO.mCherry, control) or Gq-coupled hM3Dq DREADD fused with mCherry (AAV 2/5.EF1α.DIO.hM3Dq.mCherry, Gq DREADD) together with (2) Cre-dependent expression of the Ca^{2+} sensor (pAAV5.CAG.-Flex.GCaMP6f.WPRE) (Figure 1G). Astrocyte-specific expression of hM3Dq was confirmed by the co-localization of mCherry

(D–F) Pseudo-images (top), overall Ca^{2+} strength (middle), and time course Ca^{2+} signal traces of spontaneous astrocyte activity with under-curve area shaded (bottom) in (D) PVN (lean n = 195, obese n = 1619), (E) ARC (lean n = 295, obese n = 220), or (F) VMH (lean n = 216, obese n = 1,428) of lean or obese GCaMP6f-Glast-CreER^{T2} mice. Scale bar, 20 μm.

(G) Experimental setting for viral-mediated approaches in the PVN and representative confocal image of corresponding DREADD-mCherry signal (red). Cell nuclei are shown in DAPI (blue), scale bar, 50 μm.

(H) Representative confocal photomicrograph of double immunofluorescence of GFAP (green) and mCherry (red) in the PVN of DREADD injected mice. Cell nuclei are labeled with DAPI (blue). Scale bar, 20 μm.

(I and J) (I) Pseudo-images and (J) overall Ca^{2+} strength (left) and representative Ca^{2+} signal traces (right) before (n = 263) and after (n = 422) CNO bath application in PVN astrocytes. Scale bar, 20 μm. Histogram data are expressed as mean +/− SEM.

* $p < 0.05$ by Student's t test (C)–(F), (J).

See also Figure S1, for statistical details, see Data S1.

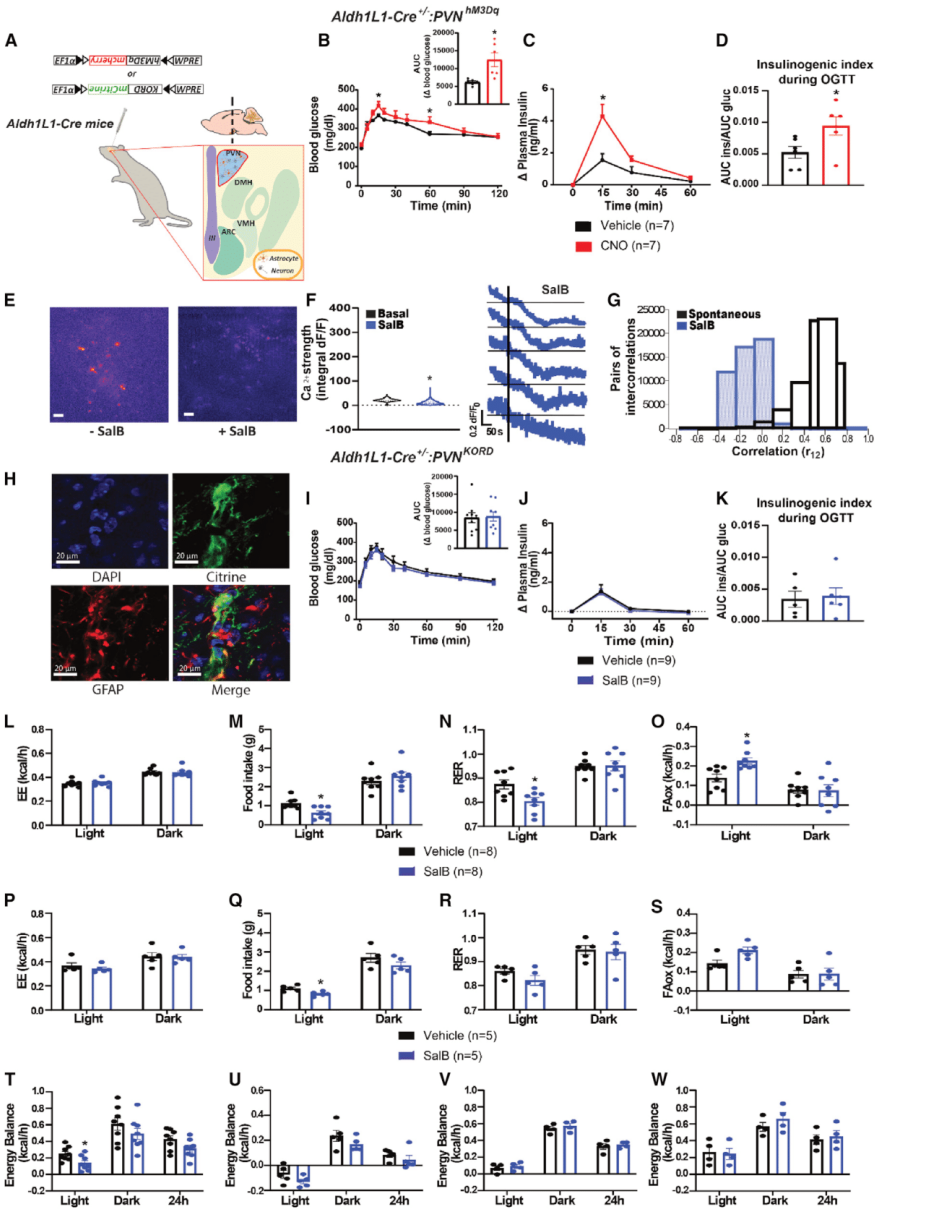

(legend on next page)

fluorescent signal with glial fibrillary acidic protein (GFAP) reactivity (Figure 1H). This combined viral approach allowed us to monitor how selective activation of astrocytic Gq-coupled hM3Dq by clozapine-N-oxide (CNO) would affect PVN astrocytic intrinsic Ca^{2+} activity in acute brain slices. Compared with the minor effect in mCherry expressing control mice (Figures S1I and S1J), CNO bath application significantly increased astrocytic Ca^{2+} strength in the PVN as a result of hM3Dq activation (Figures 1I and 1J). Using temporal correlation between Ca^{2+} signals as an evaluation of their synchronization, we observed that in contrast to control mice (Figure S1K), CNO activation of astrocytic hM3Dq drastically increased Ca^{2+} signal synchronization compared with spontaneous signals (Figure S1L). This result demonstrates that Gq signaling modulation enables selective activation and synchronization of Ca^{2+} signals in PVN astrocytes.

We next explored how direct manipulation of PVN astrocytes could affect systemic metabolism. Aldh1L1-$Cre^{+/-}$ mice received bilateral PVN injections of viruses expressing either mCherry (AAV5-EF1a-DIO-mCherry; Aldh1L1-$Cre^{+/-}$:$PVN^{mCherry}$) or hM3Dq (AAV5-EF1a-DIO-hM3Dq-mCherry; Aldh1L1-$Cre^{+/-}$:PVN^{hM3Dq}) (Figure 2A). To evaluate potential unspecific metabolic consequences of peripheral CNO injections (Gomez et al., 2017), we also injected AAV5-EF1a-DIO-hM3Dq-mCherry in Aldh1L1-$Cre^{-/-}$ mice (Aldh1L1-$Cre^{-/-}$:PVN^{hM3Dq}). CNO-mediated activation of PVN astrocytes had no consequence on overall whole body energy expenditure (EE), food intake, or energy balance in control mice (Aldh1L1-$Cre^{+/-}$:$PVN^{mCherry}$ and Aldh1L1-$Cre^{-/-}$:PVN^{hM3Dq}) nor in hM3Dq expressing mice (Aldh1L1-$Cre^{+/-}$:PVN^{hM3Dq}; Figures S2A–S2I). However, chemogenetic stimulation of PVN astrocytes by peripheral CNO administration decreased glucose clearance (Figure 2B), increased plasma insulin levels (Figure 2C), and corresponding insulinogenic index (Figure 2D), revealing increased insulin release after an oral glucose tolerance test in Aldh1L1-$Cre^{+/-}$:PVN^{hM3Dq}. No significant effect was found in control animals (Figures S2J–S2Q).

Given this striking result, we sought to reproduce this phenomenon in an alternative genetic background. To this aim, C57BL/6 mice received bilateral intra-PVN injection of AAV5-GFAP-hM3Dq-mCherry (C57Bl6j:PVN^{hM3Dq}) or control vector AAV5-GFAP-mCherry (C57Bl6j:$PVN^{mCherry}$). Although ineffective in control C57Bl6j:$PVN^{mCherry}$ (Figures S3A–S3D), CNO-mediated activation of PVN astrocytes in C57Bl6j:PVN^{hM3Dq} resulted in higher glucose-induced insulin release (Figure S3F), leading to a trend of altered insulin sensitivity as assessed by insulinogenic index (Figure S3G). These results suggest that chemogenetic manipulation of Gq GPCR pathway in PVN astrocytes readily impairs peripheral glucose metabolism and insulin release, both being common outcomes preceding insulin-resistance states.

We next probed the reciprocal phenomenon by specifically triggering Gi GPCR pathway in PVN astrocytes. Aldh1L1-$Cre^{+/-}$ mice received bilateral injection of AAV5 virus with a modified backbone (pAAV5-EF1a-DIO-HA-KORD-Citrine) to achieve astrocyte, Cre-dependent expression of kappa-opiod receptor (KORD), a recently developed chemogenetic GPCR that can be activated by the pharmacologically inert ligand salvinorin B (SalB) (Vardy et al., 2015) (Figure 2A). After PVN injection of a mixture of virus allowing the co-expression of KORD and GCaMP6f, we could assess astrocyte Ca^{2+} signals before and after KORD activation in acute hypothalamic slices. Bath application of SalB led to a decrease in Ca^{2+} signal strength (Figures 2E and 2F) and global synchronization (Figure 2G) in KORD expressing mice, whereas these effects appeared marginal in control mCherry expressing mice (Figures S4A–S4C). Accordingly, the decrease in intracellular Ca^{2+} release was more pronounced after KORD activation compared with mCherry expressing mice (Figure S4D). Astrocyte-specific KORD expression was corroborated by the co-localization of mCitrine and GFAP reactivity in PVN astrocytes (Figure 2H).

We further assessed *in vivo* the metabolic output arising from decreasing Ca^{2+} activity *in vivo* in PVN astrocytes. Aldh1L1-$Cre^{+/-}$ or control Aldh1L1-$Cre^{-/-}$ mice received bilateral injections of AAV5-EF1a-DIO-HA.KORD-mCitrine in the PVN. Peripheral SalB administration did not affect glucose clearance, plasma insulin, or insulinogenic index after an oral glucose load in both Aldh1L1-$Cre^{-/-}$:PVN^{KORD} (Figures S4E–S4L) and Aldh1L1-$Cre^{-/+}$:PVN^{KORD} mice (Figures 2I–2K).

This result was similar when GFAP-driven expression of hM4Di was achieved in C57Bl6J mice (C57Bl6j:PVN^{hM4Di}) (Figures S5A–S5D). However, given the potency difference between hM4Di and KORD-mediated Gi intracellular signaling (Vardy et al., 2015) and the potential discrepancy between Aldh1l1-CRE and C57Bl6J genetic background, we further explored the metabolic consequence of KORD-mediated Gi signaling in GFAP-positive astrocytes. C57Bl6j mice received intra-PVN injection of a mixture of AAV5-GFAP-Cre virus and

Figure 2. PVN astrocytes regulate glucose metabolism and energy balance

(A) Experimental design for chemogenetic approaches.

(B–D) (B) Blood glucose (Vehicle = 6, CNO = 6) and corresponding area under the curve (AUC, top right), (C) plasma insulin change (Vehicle = 7, CNO = 7), and (D) insulinogenic index (Vehicle = 6, CNO = 6) after Vehicle or CNO i.p. administration followed by an OGTT in Aldh1L1-$Cre^{+/-}$:PVN^{hM3Dq} mice.

(E–G) (E) Pseudo-images, (F) overall Ca^{2+} strength (left, basal = 723, SalB = 1,446) and time course Ca^{2+} signal traces (right) of GCaMP signals, and (G) distribution of temporal correlations of Ca^{2+} responses of all paired active domains (as an estimation of global synchronization) before (n = 22,530) and after (n = 49,352) SalB bath application to PVN slices of Aldh1L1-Cre mice expressing KORD receptor. Scale bar, 20 μm. Overall Ca^{2+} strength data are expressed as mean +/− SEM.

(H) Representative confocal photomicrograph of double immunofluorescence of GFAP (red) and mCitrine (green) in the PVN of Aldh1L1-$Cre^{+/-}$:PVN^{KORD} mice. Cell nuclei are labeled with DAPI (blue).

(I–K) (I) Blood glucose (Vehicle = 9, SalB = 9) and corresponding AUC (top right), (J) plasma insulin change (Vehicle = 5, SalB = 6), and (K) insulinogenic index (Vehicle = 5, SalB = 6) after Vehicle or SalB i.p. administration followed by an OGTT in Aldh1L1-$Cre^{+/-}$:PVN^{KORD} mice.

(L–W) Energy expenditure (EE), food intake, respiratory exchange ratio (RER), and fatty acid oxidation (FAox) after Vehicle or SalB i.p. injection to (L)–(O) Aldh1L1-$Cre^{+/-}$:PVN^{KORD} (Vehicle n = 8, SalB n = 8) and (P)–(S) C57Bl6j:PVN^{KORD} (Vehicle n = 5, SalB n = 5) mice. (T)–(W) Energy balance after Vehicle or SalB i.p. administration in (T) Aldh1L1-$Cre^{+/-}$:PVN^{KORD} (Vehicle n = 8, SalB n = 8), (U) C57Bl6j:PVN^{KORD} (Vehicle n = 5, SalB n = 5), (V) Aldh1L1-$Cre^{-/-}$:PVN^{KORD} (Vehicle n = 4, SalB n = 4), and the control mice (W) Aldh1L1-$Cre^{+/-}$:$PVN^{mCherry}$ (Vehicle n = 4, SalB n = 4) mice. Data are expressed as mean +/− SEM.

*$p < 0.05$ by two-way ANOVA (B)–(C), (I)–(W) and Student's t test (B), (D), (F), (I), and (K).

See also Figures S2, S3, and S4, for statistical details, see Data S1.

AAV5-EF1a-DIO-HA.KORD-mCitrine allowing for KORD expression in GFAP-expressing cells upon Cre-mediated recombination (Figure S3I). KORD expression was visualized by human influenza hemagglutinin (HA) tag presence in GFAP-positive astrocytes (Figure S3J). Here, again, Gi signaling initiation through SalB-mediated KORD activation in C57Bl6j:PVN^{KORD} mice did not affect any of the aforementioned parameters (Figures S3K–S3N), in line with our observations in Aldh1L1-Cre$^{+/-}$ mice.

Similarly, metabolic efficiency analysis revealed that although peripheral injection of SalB had no effect the control groups (Aldh1L1-Cre$^{-/-}$:PVN^{KORD}; Aldh1L1-Cre$^{+/-}$:PVN^{mcherry} Figures S4M–S4T), KORD/Gi-mediated modulation of PVN astrocytes did not modify EE (Figure 2L) but induced a decrease in food intake (Figure 2M) and RER (Figure 2N) while increasing FA oxidation (Figure 2O) during the light period. A similar output was observed in C57Bl6j:PVN^{KORD} mice (Figures 2P–2S). Accordingly, SalB administration to Aldh1L1-Cre$^{+/-}$:PVN^{KORD} affected energy balance during the light period (Figure 2T), with a trends for a decrease in C57Bl6j:PVN^{KORD} mice (Figure 2U). No effect of SalB administration was observed in control mice Aldh1L1-Cre$^{-/-}$:PVN^{KORD} and Aldh1L1-Cre$^{+/-}$:PVN^{mCherry} (Figures 2V and 2W). These results suggest that although Gq-coupled hM3Dq DREADD modify glucose metabolism and insulin release, activation of astrocytic Gi-KORD receptor in both Aldh1L1 and GFAP-expressing astrocytes in the PVN of lean mice promotes only subtle changes in energy utilization.

PVN astrocytes modulate sympathetic output and thermogenesis

Given the prominent role played by pre-autonomic PVN neurons in autonomic control of energy balance and glucose metabolism (Geerling et al., 2014; Stanley et al., 2019; Stern et al., 2016), we hypothesized that chemogenetic activation of PVN astrocytes could exert control over PVN-mediated sympathetic output. As a proxy of autonomic outflow, we first measured change in urine mono-aminergic content as a consequence of chemogenetic activation (Gq) or inhibition (Gi) of PVN astrocytes. ANOVA main effect probability indicated that although no change was observed following CNO or SalB administration in control Aldh1L1-Cre$^{+/-}$:PVN^{mCherry} mice (Figures 3A and 3C), activation of Gq signaling in PVN astrocytes in Aldh1L1-Cre$^{+/-}$:PVN^{hM3Dq} mice significantly increased urine monoamine concentrations (Figure 3B). In contrast, KORD-mediated Gi activation showed the opposite effect, with a decrease in urine norepinephrine (NA), as well as a tendency to decrease dopamine (DA) and Serotonin (5HT) in Aldh1L1-Cre$^{+/-}$:PVN^{KORD} mice (Figure 3D). We further explored if astrocytes in the PVN participate in the regulation of brown adipose tissue (BAT) activity. We monitored *in vivo* BAT metabolic activity by ultrasound and spectral photoacoustic imaging (Clemmensen et al., 2018; Karlas et al., 2019). We observed that PVN astrocyte activation increased local oxygen saturation in BAT blood supply in Aldh1L1-Cre$^{+/-}$PVN^{hM3Dq} mice (Figures 3E and 3F). We next assessed the functional connection between PVN astrocyte activation and thermogenic output. Mice were administered the agonist of cold receptor transient receptor potential cation channel subfamily M member 8 (TRPM8) icilin in order to pharmacologically trigger an adaptive autonomic response similar to the one triggered by cold exposure (Clemmensen et al., 2018). We used BAT monoamine content as a readout of sympathetic outflow (Virtue and Vidal-Puig, 2013). Although CNO intraperitoneal (i.p.) injection in control mice had no significant effect on BAT monoamine content (Figure 3G), astrocyte Gq activation in the PVN promoted an increase in adrenaline (AD) and 5HT BAT content in Aldh1L1-Cre$^{+/-}$:PVN^{hM3Dq} mice (Figure 3H). Using telemetric core body temperature measurements, we next demonstrated that PVN astrocyte activation through chemogenetic Gq activation was coupled to increased whole body temperature in Aldh1L1-Cre$^{+/-}$:PVN^{hM3Dq} mice (Figure 3I). Finally, we confirmed that Gq signaling activation of PVN GFAP-positive astrocytes in C57Bl6 mice (C57Bl6j:PVN^{hM3Dq}; Figure 3J) recapitulated the increase in monoamine content and in BAT (Figure 3K), which were not observed in control C57Bl6j:PVN^{mCherry} mice (Figure 3L). Altogether, these results suggest that PVN astrocytes exert efficient control over ANS output, thermogenesis, and possibly peripheral glucose metabolism.

PVN astrocytes exert bidirectional control over systemic glucose metabolism and energy balance in obese mice

Control C57Bl6j:PVN^{mCherry} mice and C57Bl6j:PVN^{hM3Dq} mice were submitted to 8 weeks of HFHS and assessed for glucose control and metabolic efficiency change induced by PVN astrocyte Gq activation. CNO injection had no effects in obese control mice (Figures S6A–S6H); however, in obese C57Bl6j:PVN^{hM3Dq} mice, it led to an acute and drastic deterioration of glucose tolerance (Figures 4A and 4B) associated with large increases in glucose-induced insulin release (Figure 4C), insulinogenic index (Figure 4D), and c-peptide release (Figure 4E), indicative of acute state of insulin resistance. PVN astrocyte control of glucose metabolism seemed to operate independently from changes in metabolic efficiency, since neither food intake (Figure 4F), RER (Figure S6I), nor FA oxidation (Figure S6J) were affected by CNO i.p. injection of obese C57Bl6j:PVN^{hM3Dq} mice. Whole body energy expenditure was reduced during the dark period (Figure 4G) and, accordingly, showed higher positive energy balance (Figure 4H). These results suggest that activation of PVN astrocytes promotes disturbances in systemic glucose metabolism and thereby potentially exacerbate energy storage and metabolic syndrome during obesity.

We next probed whether Gi-coupled receptor activation in PVN astrocytes has the opposite effect on metabolism. Gi activation had no impact on glucose tolerance in obese C57Bl6j:PVN^{hM4Di} mice (Figure S5E), whereas KORD activation promoted a beneficial effect in obese C57Bl6j:PVN^{KORD} mice (Figures 4I and 4J). In both obese C57Bl6j:PVN^{hM4Di} and C57Bl6j:PVN^{KORD} mice, PVN astrocyte Gi-coupled activation of hM4Di or KORD reduced the level of glucose-induced insulin release during the OGTT (Figures S5F and S4K) or insulinogenic index (Figures S5G and S4L). However, consistently, plasma c-peptide release was reduced following activation of both receptors (Figures S5H and S4M). Given the prominent role of the PVN in the control of hypothalamic-pituitary-adrenal axis, we probed whether chemogenetic manipulation of PVN astrocytes would modulate corticosterone level (Figures S5I–S5L). In lean mice, chemogenetic activation of Gq or Gi signaling in PVN astrocyte had marginal effect on circulating corticosterone (Figures S5I and S5J). However, CNO-mediated Gq but not Gi activation in PVN astrocytes led to a

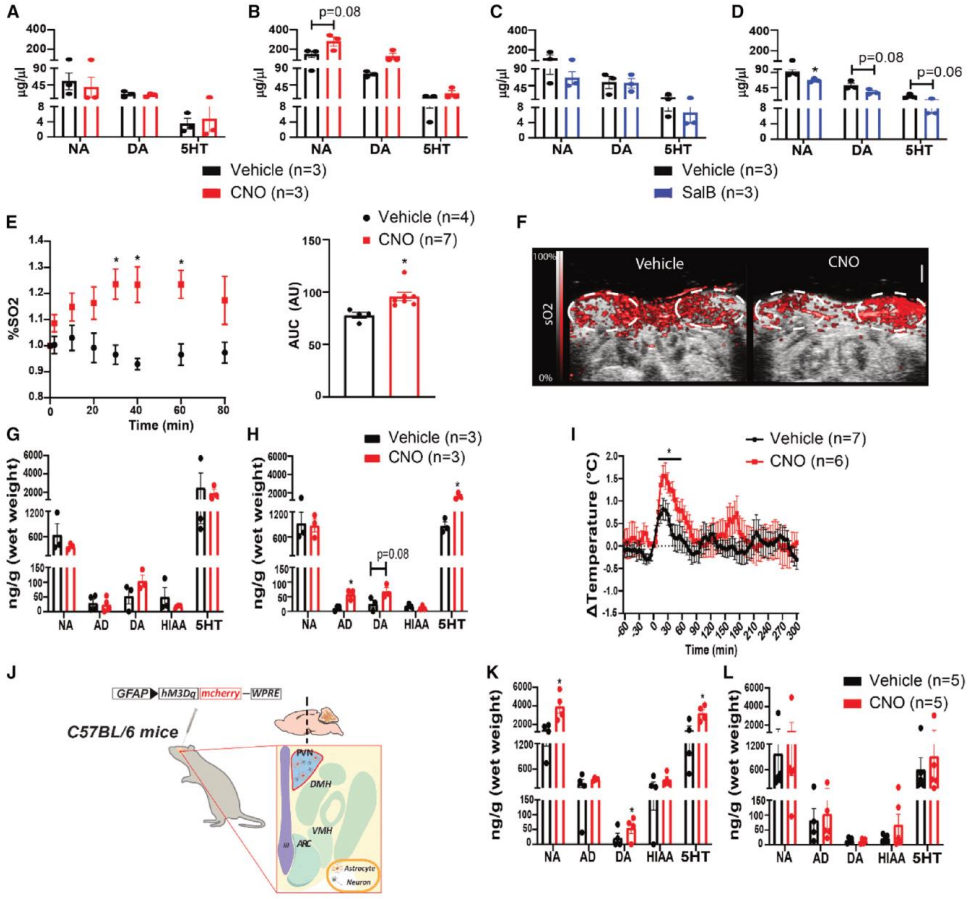

Figure 3. PVN astrocytes regulate sympathetic output and thermogenesis

(A–D) Urine mono-aminergic noradrenaline (NA), dopamine (DA), and serotonin (5HT) concentrations in (A) Aldh1L1-Cre$^{+/-}$:PVN^{mCherry} (Vehicle n = 3, CNO n = 3) and (B) Aldh1L1-Cre$^{+/-}$:PVN^{hM3Dq} (Vehicle n = 3, CNO n = 3) mice after Vehicle or CNO i.p. injection, or in (C) Aldh1L1-Cre$^{+/-}$:PVN^{mCherry} (Vehicle n = 3, SalB n = 3) and (D) Aldh1L1-Cre$^{+/-}$:PVN^{KORD} (Vehicle n = 3, SalB n = 3) mice after Vehicle or SalB i.p. administration.

(E) Time course local oxygen consumption (as percentage of blood saturated oxygen [sO_2]) in BAT (left) and as AUC (right) after Vehicle (n = 4) or CNO (n = 7) i.p. injection to Aldh1L1-Cre$^{+/-}$:PVN^{hM3Dq} mice.

(F) Representative images of photoacoustic recording of BAT 40 min after Vehicle (left) or CNO (right) i.p. administration in Aldh1L1-Cre$^{+/-}$:PVN^{hM3Dq} mice.

(G and H) BAT mono-aminergic NA, adrenaline (AD), DA, 5-hydroxyindolacetic acid (HIAA) and 5HT content in (G) Aldh1L1-Cre$^{+/-}$:PVN^{mCherry} (Vehicle n = 3, CNO n = 3), and (H) Aldh1L1-Cre$^{+/-}$:PVN^{hM3Dq} (Vehicle n = 3, CNO n = 3) mice after Vehicle or CNO i.p. administration.

(I) Time course change in core body temperature of Aldh1L1-Cre$^{+/-}$:PVN^{hM3Dq} mice after Vehicle (n = 7) or CNO (n = 6) i.p. injection.

(J) Representative image of viral delivery of GFAP-hM3Dq in the PVN of C57BL/6 mice.

(K–L) BAT mono-aminergic (NA, AD, DA, HIAA, and 5HT) content in (K) C57Bl6j:PVN^{hM3Dq} (Vehicle n = 4, CNO n = 4) and (L) C57Bl6j:PVN^{mCherry} (Vehicle n = 5, CNO n = 5) mice after Vehicle or CNO i.p. administration. AU refers to arbitrary units. Data are expressed as mean +/− SEM. * $p < 0.05$ by two-way ANOVA (A)–(E), (G)–(L) and Student's t test (E).

For statistical details, see Data S1.

significant decrease in corticosterone level in obese mice (Figures S5K and S5L). Moreover, SalB injection in C57Bl6j:PVN^{KORD} promoted a decrease in food intake (Figure 4N) and RER (Figure S6K) and an increase in FA oxidation (Figure S6L), with no changes in energy expenditure (Figure 4O). Finally, contrary to astrocyte Gq receptor activation,

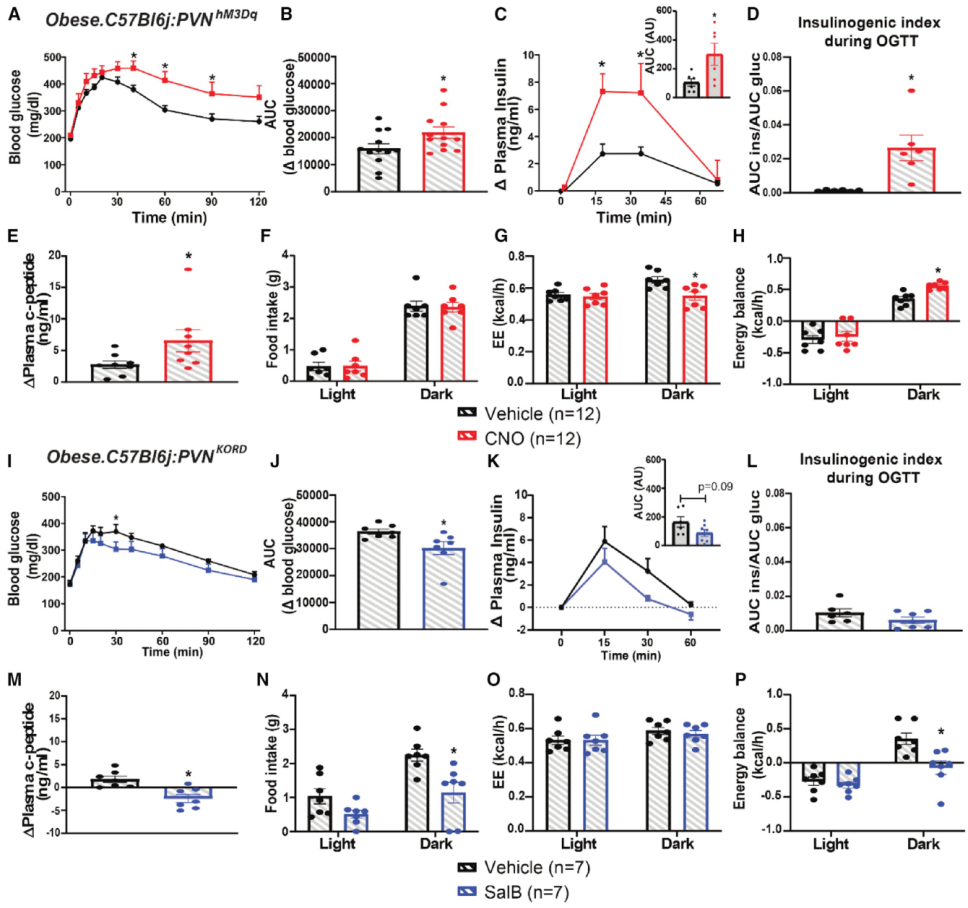

Figure 4. Astrocytes in the PVN exert bidirectional control over systemic glucose metabolism and energy balance in obese mice

(A–E) (A) Blood glucose (Vehicle = 12, CNO = 12), (B) glucose AUC, (C) plasma insulin change (Vehicle = 6, CNO = 6) and corresponding AUC (top right), (D) insulinogenic index (Vehicle = 6, CNO = 6), and (E) plasma c-peptide (Vehicle = 8, CNO = 8) change after Vehicle or CNO i.p. administration followed by an OGTT in obese C57Bl6j:PVN^{hM3Dq} mice.

(F–H) (F) Food intake, (G) EE, and (H) energy balance after Vehicle or CNO i.p. injection to obese C57Bl6j:PVN^{hM3Dq} (Vehicle = 7, CNO = 7) mice.

(I–M) (I) Blood glucose (Vehicle = 7, SalB = 8), (J) corresponding AUC, (K) plasma insulin change (Vehicle = 6, SalB = 7) and corresponding AUC (top right), (L) insulinogenic index (Vehicle = 6, SalB = 7), and (M) plasma c-peptide change (Vehicle = 7, SalB = 7) after Vehicle or SalB i.p. administration followed by an OGTT in obese C57Bl6j:PVN^{KORD} mice.

(N–P) (N) Food intake, (O) EE, and (P) energy balance after Vehicle or SalB i.p. injection to obese C57Bl6j:PVN^{KORD} (Vehicle = 7, SalB = 7) mice. AU refers to arbitrary units. Data are expressed as mean +/− SEM. * $p < 0.05$ by two-way ANOVA (A), (C), (F)–(I), (K), and (N)–(P) and Student's t test (B)–(E) and (J)–(M). See also Figures S5 and S6, for statistical details, see Data S1.

KORD-mediated Gi stimulation in PVN astrocytes promoted negative energy balance during the dark period in obese C57Bl6j:PVN^{KORD} mice (Figure 4P). These results indicate that PVN astrocytes exert bidirectional control over systemic glucose metabolism and energy balance.

Chemogenetic modulation of astrocyte activity controls PVN parvocellular neuronal firing

We then set out to probe the cellular and molecular mechanism by which PVN astrocytes exert dynamic control of whole body metabolic outputs. Parvocellular pre-autonomic neurons in the

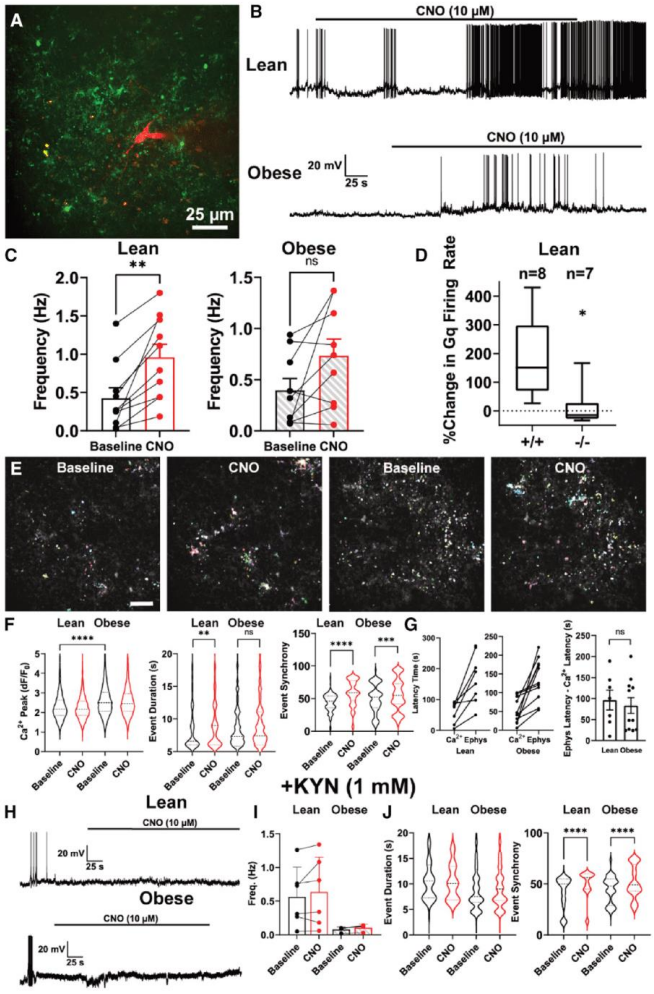

Figure 5. Chemogenetic activation of Gq-coupled receptor in PVN astrocytes enhances parvocellular neuronal firing in lean mice

(A) Representative image of a patched parvocellular neuron labeled with Alexa 555 (red) in the PVN of C57Bl6j:PVN^{hM3Dq} mice expressing GCaMP6 (green).

(B) Firing activity traces in parvocellular PVN neurons in response to CNO in lean (top) and obese (bottom) C57Bl6j:PVN^{hM3Dq} mice.

(C) Parvocellular PVN neuron spike frequency in response to CNO in lean (left, n = 10) and obese (right, n = 9) C57Bl6j:PVN^{hM3Dq} mice.

(D) %Change in the parvocellular PVN neuron action potential firing frequency after CNO bath application in lean C57Bl6j:PVN^{hM3Dq} (Gq$^{+/+}$, n = 8) or C57Bl6j:PVN^{mCherry} (Gq$^{-/-}$, n = 7) mice.

(E) Photomicrograph of Ca^{2+} event analysis overlay in PVN slices of C57Bl6j:PVN^{hM3Dq} mice, in the presence of CNO in both lean (left) and obese (right) animals. Scale bar, 25 μm.

(F) Summary data of astrocyte Ca^{2+} activity. Ca^{2+} strength (left, Lean/Baseline n = 3,036; Lean/CNO n = 3,009; Obese/Baseline n = 5,132; Obese/CNO n = 5,016); event duration (middle, Lean/Baseline n = 3,036; Lean/CNO n = 3,009; Obese/Baseline n = 5,132; Obese/CNO n = 5,016), and event synchrony (right, Lean/Baseline n = 618, Lean/CNO n = 543, Obese/Baseline n = 815, Obese/CNO n = 541) of GCaMP signals in PVN of lean or obese C57Bl6j:PVN^{hM3Dq} mice.

(G) (Left) Latency of astrocytic Ca^{2+} activity response to CNO application and the upregulation of PVN neuronal spiking activity in lean (n = 7) and obese (n = 11) C57Bl6j:PVN^{hM3Dq} mice. (Right) Difference between the chemogenetic Gq-induced upregulation of Ca^{2+} activity in astrocytes and parvocellular neuronal firing (Lean n = 7, Obese n = 11).

(H) PVN parvocellular firing activity traces recorded from lean (top) and obese (bottom) C57Bl6j:PVN^{hM3Dq} mice, combining bath application of CNO and glutamate channel blocker kynurenic acid (KYN, 1 mM).

(I) Parvocellular PVN neuron spike frequency in the presence of KYN and CNO, in both lean (solid, n = 6) and obese (striped, n = 4) C57Bl6j:PVN^{hM3Dq} mice.

(J) Summary data of AQuA astrocyte Ca^{2+} activity analysis. Ca^{2+} event duration (left, Lean/Baseline n = 128, Lean/CNO n = 124, Obese/Baseline n = 2,158; Obese/CNO n = 1,885) or event synchrony (right, Lean/Baseline n = 429, Lean/CNO n = 282, Obese/Baseline n = 429, Obese/CNO n = 257) in the presence of CNO/KYN. Data are expressed as mean +/− SEM. * $p < 0.05$, ** $p < 0.01$, *** $p < 0.001$, **** $p < 0.0001$ by two-way ANOVA (C) and (I), Student's t test (D) and (G), and Brown-Forsythe ANOVA (F) and (J). For statistical details, see Data S1.

PVN send efferent projections to autonomic centers in the brainstem and spinal cord to generate essential adaptive metabolic responses for proper systemic glucose metabolism and energy balance regulation (Geerling et al., 2014; Stanley et al., 2010; Stern et al., 2016). We investigated astrocyte-neuron communication by patching parvocellular neurons and recording their activity (Figure 5A) before and after chemogenetic manipulation of astrocyte Gq or Gi receptor in lean or obese mice. The recorded neurons displayed membrane properties characteristic of parvocellular pre-sympathetic neurons, namely the presence of a low-threshold spike and absence of a transient outward rectification (Luther and Tasker, 2000; Stern, 2001). We combined this approach with simultaneous confocal imaging of astrocyte Ca^{2+} signals after expression of GCaMP6f in either GFAP or Aldh1L1 expressing astrocytes. Activation of Gq-coupled hM3Dq expressing PVN astrocytes by CNO significantly increased neuronal firing frequency from lean C57Bl6j:PVN^{hM3Dq} mice (Figures 5B and 5C). Conversely,

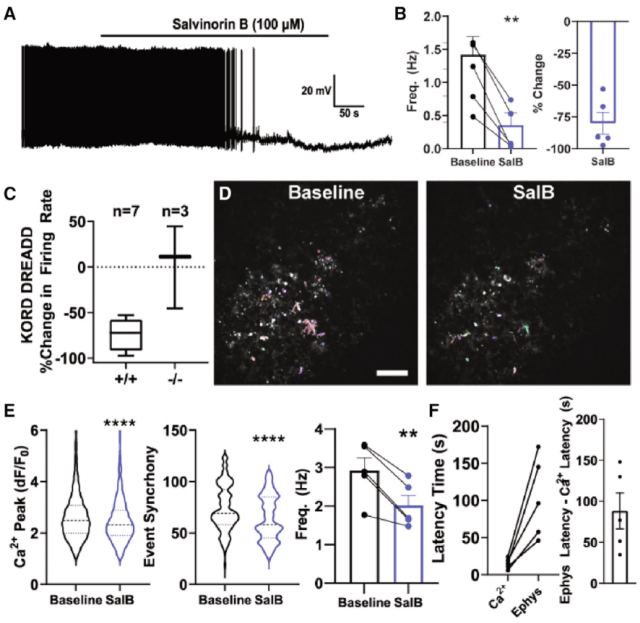

Figure 6. Astrocyte KORD-Gi receptor chemogenetic activation inhibits PVN parvocellular neuronal firing

(A) Firing activity traces in parvocellular PVN neurons in response to SalB in Aldh1L1-Cre$^{+/-}$:PVN^{KORD} mice.

(B) Parvocellular PVN neuron spike frequency (left) and percentage of decrease in firing frequency (right) in the presence of SalB in Aldh1L1-Cre$^{+/-}$:PVN^{KORD} mice (n = 5).

(C) %Change in the parvocellular PVN neuron action potential firing frequency after SalB bath application in Aldh1L1-Cre$^{+/-}$:PVN^{KORD} (KORD$^{+/+}$, n = 7) or Aldh1L1-Cre$^{+/-}$:PVN^{mCherry} (KORD$^{-/-}$, n = 3) mice.

(D) Photomicrograph of Ca^{2+} event analysis overlay in PVN slices of Aldh1L1-Cre$^{+/-}$:PVN^{KORD} mice, in the presence of SalB. Scale bar, 25 μm.

(E) Summary data of astrocyte Ca^{2+} activity. Ca^{2+} strength (left, Control n = 3,646, SalB n = 2,620), event synchrony (middle, Control n = 3,646, SalB n = 2,620), and event frequency (right, n = 5) of GCaMP signals in PVN of Aldh1L1-Cre$^{+/-}$:PVN^{KORD} mice.

(F) (Left) Latency of astrocytic Ca^{2+} activity response to SalB application and the upregulation of PVN neuronal spiking activity in Aldh1L1-Cre$^{+/-}$:PVN^{KORD} mice. (Right) Difference between the Gi-induced downregulation of Ca^{2+} activity in astrocytes and parvocellular neuronal firing. Data are expressed as mean +/− SEM. * $p < 0.05$, ** $p < 0.01$, *** $p < 0.0001$ by paired Student's t test (B), (E_{right}); unpaired Student's t test (C), and Welch's t test ($E_{left, middle}$).

See also Figure S7, for statistical details, see Data S1.

a blunted effect was observed in obese mice (Figures 5B and 5C). CNO failed to affect firing frequency in the control group of C57Bl6j:PVN^{mcherry} mice (Figure 5D). We also quantified astrocytic Ca^{2+} activity in an event-based manner using AQuA method (Wang et al., 2019) for both lean and obese C57Bl6j:PVN^{hM3Dq} mice. CNO failed to significantly increase the mean Ca^{2+} event peak in lean or obese C57Bl6j:PVN^{hM3Dq} mice. However, the basal Ca^{2+} peaks in obese mice were significantly higher than lean mice (Figures 5E and 5F). On the other hand, CNO significantly prolonged Ca^{2+} event duration and increased Ca^{2+} event synchrony both in lean and in obese C57Bl6j:PVN^{hM3Dq} mice (Figures 5E and 5F). These results are in line with data obtained from wide-field fluorescent imaging (Figure 1). We then evaluated the latency between astrocytic Ca^{2+} upregulation and the increase in neuronal spike frequency. We found that CNO-induced Ca^{2+} response appeared first in astrocytes followed by neurons, suggesting that changes in astrocyte Ca^{2+} activity significantly preceded those in neuronal firing discharge. These results confirm a sequence of events in which astrocyte Gq activation promotes changes in neural activity (Figure 5G). The latency between activation of astrocytes and upregulation of neuronal spike activity did not differ significantly between lean and obese mice (Figure 5G, *right*).

Astrocytes maintain a constant bidirectional communication with neurons, and glutamate is recognized as a key signaling molecule underlying neuro-glial interactions (Durkee and Araque, 2019). Therefore, we investigated if glutamatergic communication is involved in the excitation of parvocellular neurons following astrocyte chemogenetic activation. Blockade of ionotropic glutamate receptors (KYN, 1 mM) prevented the CNO-induced increase in neuronal activity both in lean and in obese C57Bl6j:PVN^{hM3Dq} mice (Figures 5H and 5I). Interestingly, although CNO effects on astrocyte Ca^{2+} event synchrony persisted in the presence of KYN (Figure 5J, *right*), CNO effects on Ca^{2+} event duration were partially blunted (Figure 5J, *left*).

We next assessed the effect of astrocyte KORD-Gi-mediated activation on parvocellular neuronal firing. SalB application significantly lowered neuronal activity in acute brain PVN slices of lean Aldh1L1-Cre$^{+/-}$:PVN^{KORD} mice (Figures 6A and 6B) but had no effect in control Aldh1L1-Cre$^{+/-}$:PVN^{mcherry} mice (Figure 6C). Importantly, KORD-Gi activation also decreased astrocyte intracellular Ca^{2+} activity, which manifested as a reduction in event amplitude, event synchrony, and event frequency (Figures 6D and 6E), whereas event duration remained unchanged (data not shown). As we observed with chemogenetic activation of Gq in astrocytes, KORD-Gi-mediated inhibition of astrocyte Ca^{2+} activity preceded the evoked inhibition of neuronal spike activity (Figure 6F). Similar to CNO, we found that KYN prevented the SalB-evoked decrease in neuronal activity in Aldh1L1-Cre$^{+/-}$:PVN^{KORD} mice (Figures S7A and S7B), although the decrease in astrocyte Ca^{2+} activities persisted (Figure S7C). Taken together, our results indicate that PVN astrocytes exert bidirectional control over parvocellular firing activity and that both effects involve a glutamate-dependent mechanism.

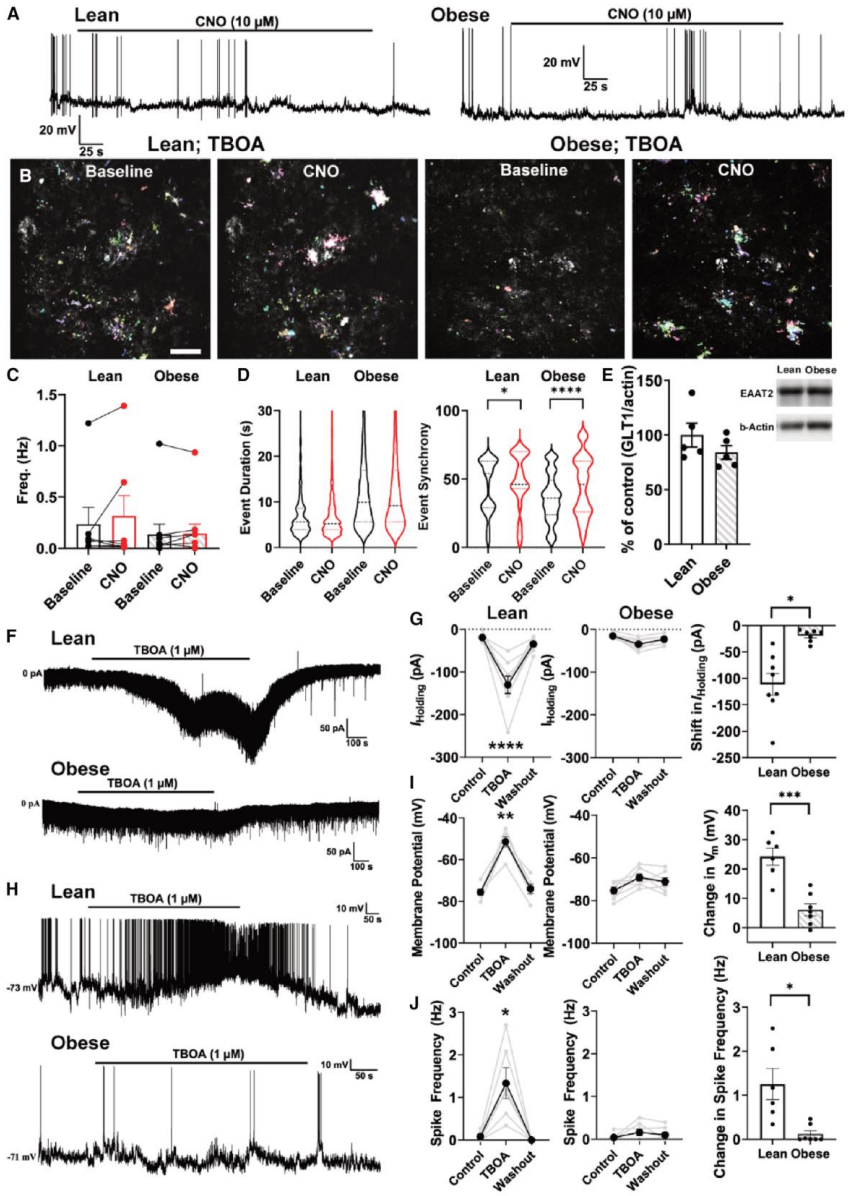

(legend on next page)

Astrocytic control of extracellular glutamate is impaired in obesity and instrumental to the control of PVN neuron firing

Astrocyte-mediated glutamate signaling to neurons could involve glutamate release and/or modulation of ambient glutamate levels via changes in the activity of astrocyte-selective excitatory amino-acid transporters (EAATs) (Rose et al., 2017). Thus, to determine whether the glutamate-dependent communication between astrocytes and neurons reported above involve modulation of EAAT activity, we repeated experiments in the presence of the glutamate transport blocker DL-*threo*-β-Benzyloxyaspartic acid (TBOA). In this condition, activation of astrocytes by CNO failed to upregulate neuronal activity both in lean and in obese C57Bl6j:PVN^{hM3Dq} mice (Figures 7A and 7C), whereas CNO effects on astrocyte Ca^{2+} event synchrony persisted (Figure 7D). Similarly, TBOA also prevented the KORD-mediated inhibition of neuronal firing (Figures S7D and S7E), without impacting KORD-induced astrocyte Ca^{2+} inhibition (Figure S7F). Together, these results suggest that the glutamate-dependent increase and decrease of PVN neuronal activity following astrocyte Gq and Gi receptor activation, respectively, is mediated via a bidirectional control of glutamate transporter activity.

Finally, we explore if the function and/or expression of astrocyte EEATs is altered in obese mice. Western blot analysis of PVN samples showed no significant difference in EAAT2 protein expression levels between lean and obese mice (Figure 7E). We then tested and compared the effects of TBOA per se on membrane excitability and firing activity of PVN parvocellular neurons. In the voltage clamp mode, we found that bath-applied TBOA produced a significant inward shift in $I_{Holding}$ in lean mice (Figures 7F and 7G), which we previously showed to be due to the slow buildup of glutamate in the extracellular space leading to activation of neuronal extrasynaptic NMDARs (Fleming et al., 2011; Stern et al., 2016; Zhang and Stern, 2017). Surprisingly, TBOA application failed to significantly affect $I_{Holding}$ in PVN neurons in obese mice (Figures 7F and 7G), resulting in a significantly smaller inward shift in $I_{Holding}$ in obese compared with lean mice (Figure 7G, *right*). Similarly, we found that although TBOA produced a significant membrane depolarization (Figures 7H and 7I) and increase in spike frequency (Figure 7J, *left*) in neurons in lean mice, these effects were absent in obese mice (Figures 7H–7J). Taken together, our results show a blunted effect of TBOA on membrane excitability and firing activity in obese mice, supporting the notion that in this condition, astrocyte glutamate uptake activity is severely blunted.

DISCUSSION

In the present study, we show that PVN astrocytes exert a direct and reversible control on neuron firing, energy balance, systemic glucose metabolism, and insulin sensitivity and that specific targeting of astrocyte activity in the PVN exerts beneficial effects on metabolic disturbances during obesity.

Astrocytes, the most prevalent glial cells in the CNS, express a wide arrange of neuropeptide and hormonal and nutrient receptors and exhibit a specific type of excitability mediated by ionic signaling and fluctuations of intracellular Ca^{2+} concentration (Nedergaard et al., 2010). Using Ca^{2+} signals as a proxy of cellular activity, we show that obesity is associated with hyperactivity in hypothalamic astrocytes, recalling the previous association described between high fat feeding and astrocyte reactivity (Horvath et al., 2010). In that regard, hypothalamic inflammation and gliosis have been suggested to underlie hypothalamic circuit dysfunction, which can lead to hyperphagia, insulin, and leptin resistance and consequent obesity (De Souza et al., 2005; Douglass et al., 2017; Reis et al., 2015; Thaler et al., 2012). In addition, abnormal Ca^{2+} glial signaling has been associated with the pathophysiological function of astrocytes and regulation of reactive astrogliosis during brain injury and neuropathology (Denisov et al., 2021; Kanemaru et al., 2013; Nedergaard et al., 2010). We show here that obesity affected hypothalamic astrocyte activity in a heterogenous manner, characterized by increased activity in the ARC, DMH, and PVN but sparing the VMH. This supports the idea that astrocytes are not a functionally homogeneous cellular population

Figure 7. Astrocyte glutamatergic transport signaling contributes to PVN astrocyte-neuron interaction

(A) PVN parvocellular firing activity traces recorded from lean (left) and obese (right) C57Bl6j:PVN^{hM3Dq} mice, combining bath application of CNO and glutamate transporter blocker DL-*threo*-β-Benzyloxyaspartic acid (TBOA, 1 μM).

(B) Representative images of AQuA Ca^{2+} event analysis overlay of GCaMP signals in PVN slices of lean (left) or obese (right) C57Bl6j:PVN^{hM3Dq} mice, demonstrating the strength of Ca^{2+} signals at baseline activity and in the presence of SalB and TBOA. Each image is an average of 10 frames. Scale bar, 25 μm.

(C) PVN parvocellular neuron spike frequency at baseline activity and in the presence of CNO and TBOA in both lean (solid, n = 6) and obese (striped, n = 4) C57Bl6j:PVN^{hM3Dq} mice.

(D) Summary data of astrocyte Ca^{2+} activity in the presence of CNO/TBOA. Ca^{2+} event duration (left, Lean/Baseline n = 352, Lean/CNO n = 339, Obese/Baseline n = 4,903; Obese/CNO n = 4,332) and event synchrony (right, Lean/Baseline n = 457, Lean/CNO n = 312, Obese/Baseline n = 1,338; Obese/CNO n = 818) of GCaMP signals in PVN of lean or obese C57Bl6j:PVN^{hM3Dq} mice.

(E) Protein quantification and representative western blot (inset) of glutamate transporter GLT1 (EAAT2) in lean (solid, n = 5 biological replicants, 1 technical replicant each) and obese (striped, n = 5 biological replicants, 1 technical replicant each) C57BL/6 mice.

(F) Membrane and firing properties of parvocellular neurons during voltage clamp, after TBOA (1 μM) bath application to PVN slices of lean (top) and obese (bottom) C57BL/6 mice. Holding current ($I_{Holding}$).

(G) Summary graphs representing the shifts in $I_{Holding}$ in lean (left, n = 8), obese (middle, n = 7), and their difference (right).

(H) Parvocellular neuron membrane potential (mV) and spike frequency (Hz) in current clamp, during TBOA bath application to PVN slices of lean (top) and obese (bottom) C57BL/6 mice.

(I) Summary graphs representing the shifts in membrane potential in lean (left, n = 6), obese (middle, n = 6), and their difference (right).

(J) Summary graphs representing the shifts in spike frequency in lean (left, n = 6), obese (middle, n = 6), and their difference (right). Data are expressed as mean +/− SEM. * $p < 0.05$, ** $p < 0.01$, *** $p < 0.0001$ by two-way ANOVA (C), Brown-Forsythe ANOVA (D), unpaired Student's t test (E,G_{right}, I_{right}, J_{right}), and repeated measures ANOVA ($G_{left, middle}$), ($I_{left, middle}$), and ($J_{left, middle}$).

For statistical details, see Data S1.

throughout the brain but rather exhibit inter- and intra-regional differences in molecular and cellular profiles (Haim and Rowitch, 2017; Hill et al., 1996; Khakh and Sofroniew, 2015).

In this study, we focused our interest on the PVN, which contains key neuroendocrine neurons controlling systemic metabolism. Strikingly, manipulating PVN astrocytic intracellular signaling cascade and Ca^{2+} waves through chemogenetic Gq/Gi engineering, respectively, aggravated (Gq) or improved (KORD-Gi) the metabolic condition in obese mice. In the same line, we found that activation of astrocytic Gq, but not Gi signaling led to change in stress-induced corticosterone level in obese mice (Figures S5K and S5L), indicating that both intracellular cascade (Gq/Gi) and nutritional condition (lean/obese) affect astrocyte-neuron coupling in PVN neural network.

Correspondingly, previous evidence supports beneficial consequences of astrocyte Gi receptor activation, as it corrects astrocyte atrophy and behavioral outputs observed during neurodegenerative diseases (Douglass et al., 2017; Yu et al., 2020). We here reveal that PVN astrocytes exert a direct and reversible control of energy balance, systemic glucose metabolism, and insulin sensitivity. Astrocyte-mediated control of PVN neuron activity might even be an essential component of a recently described functional PVN-pancreas transneuronal circuits directly connecting the PVN to autonomic control beta cell function and glucose metabolism (Papazoglou et al., 2022).

Our data show that chemogenetic control and nutritional modulation of astrocyte networks within the PVN control neighboring parvocellular neuron firing activity. In all cases, changes in astrocytic Ca^{2+} events preceded the one observed in neuronal firing, further establishing that changes in PVN neuron firing were a consequence of DREADD-mediated activation of astrocytic Ca^{2+} events.

At the mechanistic level, astrocyte-evoked effects on PVN firing activity were prevented by glutamate receptor blockade, supporting the notion that glutamate signaling is a core component of astrocytic control of PVN neuronal activity. Glutamate-mediated astrocyte-neuron crosstalk could involve active vesicular and non-vesicular glutamate release (Araque et al., 1998; Bezzi et al., 1998; Fellin et al., 2004; Innocenti et al., 2000) as well as the control of ambient glutamate levels of via the activity of potent glutamate transporters, particularly GLT1.

In our hands, selective blockade of glutamate transporters prevented the change in neuron firing initiated by either Gq or Gi chemogenetic manipulation of PVN astrocytes.

Moreover, the delayed firing response of PVN neurons following astrocytic manipulations is consistent with a slow buildup of glutamate in the extracellular space. These results align with previous studies pointing at astrocyte GLT1 as a key regulator of astrocyte-neuronal communication in the PVN and supraoptic nucleus (SON) (Fleming et al., 2011; Gordon et al., 2009; Zhang et al., 2017).

Similarly, angiotensin II activation of Gq AT1 receptors on astrocytes inhibited GLT1 transporter activity, leading to an elevation of extracellular glutamate levels, activation of extrasynaptic N-methyl-D-aspartate receptor (NMDARs), and increased firing of PVN neurons (Stern et al., 2016). Hence, it is possible that Gq DREADD-mediated increase of astrocyte Ca^{2+} activity firing recruits the similar pathways to increase parvocellular neuron activity (Fleming et al., 2011; Zhang et al., 2017) and could mediate the bimodal regulation of PVN neurons by local astrocytes.

Given that 80% of glutamate released undergo active reuptake by astrocyte GLT-1 and EAAT1 transporters, a critical role for astrocyte glutamate transport in PVN region would have been expected. Our study provides a shift in paradigm by furnishing experimental evidence that beyond the buffering of glutamate at the multipartite synapse, astrocytes act as gatekeepers of neuronal activity. Targeting astrocyte activity, therefore, may offer upstream control of PVN output, thereby coping with obesity-associated metabolic defects.

We found indeed that obesity leads to a disruption in astrocyte-neuronal communication in the PVN. Principally, CNO failed to upregulate neuronal firing in obese mice, despite the fact that DREADDs-induced modulation of astrocytic Ca^{2+} activity persisted. Thus, we propose that the blunted CNO effect on PVN firing activity is a consequence of a steady-state inhibition of GLT1 activity by basally enhanced astrocyte Ca^{2+} activity in obese mice. This is supported by our results showing an almost completely blunted/occluded effect of TBOA per se on the extrasynaptic glutamate tonic current and firing activity of PVN neurons in obese mice. The fact that no changes in GLT1 protein levels were observed further corroborates a blunted activity of GLT1 in astrocytes in this condition. The mechanisms underlying the exacerbated basal astrocyte Ca^{2+} activity and blunted GLT1 activity in obese mice remain unknown at present. We also acknowledge that the Ca^{2+}-related events we recorded might parallel other unknown important intracellular adaptive mechanisms.

Given the pivotal role of the ANS in the control of virtually every metabolically active tissue, a profound mal-adaptation of astrocyte-dependent control of these neurons will inevitably result in a chronic perturbation of peripheral organ activity, a feature that has been proposed as a possible central cause of the metabolic syndrome (Buijs et al., 2006; Marina et al., 2016; Zhang and Stern, 2017). One would indeed expect that in the complex, neuron-glia interplay within PVN astrocyte-neurons share a high degree of intricacy as it has been very recently demonstrated in feeding-related neurons of the ARC nucleus (Varela et al., 2021a, 2021b). Unfortunately, the tools currently available to finely dissect astrocyte function *in vivo* with respect to their diversity are still scarce.

In sum, our study demonstrates that PVN astrocytes exert a direct and reversible control of systemic glucose metabolism, insulin sensitivity, and energy balance suggesting that future anti-obesity strategies leverage astrocyte function. Further studies are however warranted to identify the genetic and metabolic signatures that specify sub-populations of astrocytes in discrete hypothalamic nuclei. The latter being a requisite to harness the full benefit of astrocyte-directed approaches to cope with metabolic diseases.

Limitations of the study

Due to the lack of current investigating tools allowing to finely dissect sub-categories of astrocyte, our study does not provide a complete readout of which subset(s) of astrocytes are involved in the described mechanism. Also, although change in intracellular Ca^{2+} waves are indicative of astrocytic response, they might not recapitulate to the full extent the complex response of astrocytes to change in nutrient availability and obesogenic

environment. Finally, we used *ex-vivo* electrophysiology to identify extrasynaptic glutamate signaling as a key component of adaptive astrocytic response; however, our study does not provide *in vivo* confirmation for this observation. Further studies are needed to fully flush out how controlling ambient glutamate allows astrocyte to operate control over energy homeostasis.

STAR★METHODS

Detailed methods are provided in the online version of this paper and include the following:

- KEY RESOURCES TABLE
- RESOURCE AVAILABILITY
  - Lead contact
  - Materials availability
  - Data and code availability
- EXPERIMENTAL MODELS AND SUBJECT DETAILS
  - Animals
- METHOD DETAILS
  - Viral constructs
  - Surgical procedures
  - Photoacoustic BAT imaging
  - Indirect calorimetry analysis
  - Oral glucose tolerance test
  - Corticosterone level measurement
  - *Ex-vivo* epifluorescence calcium imaging
  - Simultaneous *ex-vivo* whole-cell patch clamp electrophysiology and confocal Ca^{2+} imaging
  - Brain tissue Immunofluorescence
  - Western Blotting
  - Mono-aminergic content determination
- QUANTIFICATION AND STATISTICAL ANALYSIS
  - Statistical analysis

SUPPLEMENTAL INFORMATION

Supplemental information can be found online at https://doi.org/10.1016/j.cmet.2022.09.002.

ACKNOWLEDGMENTS

This work was funded by the French National Research Agency/Agence Nationale de la Recherche (ANR) grant # ANR-15-CE14-0030-01, ANR-15-CE14-0030-02, and ANR-15-CE14-0030-03 "Nutripathos" and the ANR-20-CE14-0025-01 "AstrObesity." We acknowledge funding supports from the Centre National de la Recherche Scientifique(CNRS), The Université Paris Cité, and the Foundation pour la Recherche Médicale (FRM). J.E.S. was supported from National Heart, Lung, and Blood Institute Grant NIH HL090948, National Institute of Neurological Disorders and Stroke Grant NIH NS094640, and funding provided by the Center for Neuroinflammation and Cardiometabolic Diseases(CNCD) at Georgia State University. M.K.K. was supported from National Heart, Lung, and Blood Institute grant F32 HL158172-01. E.M. was supported by the FRM. C.G.-C. was supported from the European Research Council (ERC) (STG grant AstroNeuroCrosstalk # 757393), the German Research Foundation (DFG) under Germany's Excellence Strategy within the framework of the Munich Cluster for Systems Neurology (EXC 2145 SyNergy—ID 390857198), and Helmholtz Excellence Network. M.H.T. was supported from ERC AdG HypoFlam, 695054, European Research Council Executive Agency (ERCEA), DFG Excellence Cluster SyNergy EXC 2145 SyNergy – ID 390857198, German Research Foundation(DFG), and ExNet-0041-Phase2-3, Initiative and Networking Fund of the Helmholtz Association. We thank Giuseppe Gangarossa for scientific and technical expertise. We thank Olja Kacanski for administrative support, Isabelle Le Parco, Ludovic Maingault, Angélique Dauvin, Aurélie Djemat, Magguy Boa, and Daniel Quintas for animals' care and Florianne Michel for genotyping. Telemetry experiments were supported by "The Continuous Glucose Telemetry Award 2018" obtained by Raphaël G.P. Denis and sponsored by Data Sciences International. We acknowledge the technical platforms Functional and Physiological Exploration (FPE) and Bioprofiler of the Université Paris Cité, CNRS, Unité de Biologie Fonctionnelle et Adaptative, F-75013 Paris, France, the viral production facility of the UMR Inserm 1089 and the animal core facility "Buffon" of the Université Paris Cité/Institut Jacques Monod. We thank the animal facility of IBPS of Sorbonne Université, Paris. Finally, we would like to thank Xuelong Mi at Virginia Tech for his critical technical support using the AQuA astrocytic calcium analysis.

AUTHOR CONTRIBUTIONS

D.H.M.C. initiated and developed the project and critically participated in the overall project design. D.H.M.C. performed and M.K.K. contributed to designing research, performing experiments, analyzing data, interpreting results of experiments, preparing figures, and writing of the manuscript. C.P., E.F., R.G.P.D., J.C., C.Morel., E.M., R.H., L.-C.B., J.R., and C.Mouffle contributed to performing experiments and data analysis. C.G.-C. and M.H.T. contributed to funding and critical analysis of experimental plan and conception. D.H.M.C., D.L., C.Martin., and J.E.S. contributed to conception of the research project, writing of the manuscript, and approving the final version of the manuscript. S.H.L. supervised the whole project, secured funding, provided guidance, designed the initial experimental plan, and finalized the manuscript with the help of the co-authors.

DECLARATION OF INTERESTS

The authors declare no competing interests.

Received: February 23, 2022
Revised: June 23, 2022
Accepted: September 2, 2022
Published: October 4, 2022

REFERENCES

Allen, N.J., and Eroglu, C. (2017). Cell biology of astrocyte-synapse interactions. Neuron *96*, 697–708.

Araque, A., Sanzgiri, R.P., Parpura, V., and Haydon, P.G. (1998). Calcium elevation in astrocytes causes an NMDA receptor-dependent increase in the frequency of miniature synaptic currents in cultured hippocampal neurons. J. Neurosci. *18*, 6822–6829.

Arch, J.R., Hislop, D., Wang, S.J., and Speakman, J.R. (2006). Some mathematical and technical issues in the measurement and interpretation of open-circuit indirect calorimetry in small animals. Int. J. Obes. (Lond) *30*, 1322–1331.

Ben Haim, L., and Rowitch, D.H. (2017). Functional diversity of astrocytes in neural circuit regulation. Nat. Rev. Neurosci. *18*, 31–41.

Berland, C., Montalban, E., Perrin, E., Di Miceli, M., Nakamura, Y., Martinat, M., Sullivan, M., Davis, X.S., Shenasa, M.A., Martin, C., et al. (2020). Circulating triglycerides gate dopamine-associated behaviors through DRD2-expressing neurons. Cell Metab. *31*, 773–790.e11.

Betley, J.N., Cao, Z.F., Ritola, K.D., and Sternson, S.M. (2013). Parallel, redundant circuit organization for homeostatic control of feeding behavior. Cell *155*, 1337–1350.

Bezzi, P., Carmignoto, G., Pasti, L., Vesce, S., Rossi, D., Rizzini, B.L., Pozzan, T., and Volterra, A. (1998). Prostaglandins stimulate calcium-dependent glutamate release in astrocytes. Nature *391*, 281–285.

Buckman, L.B., Thompson, M.M., Moreno, H.N., and Ellacott, K.L. (2013). Regional astrogliosis in the mouse hypothalamus in response to obesity. J. Comp. Neurol. *521*, 1322–1333.

Buijs, R.M., Scheer, F.A., Kreier, F., Yi, C., Bos, N., Goncharuk, V.D., and Kalsbeek, A. (2006). Organization of circadian functions: interaction with the body. Prog Brain Res *153*, 341–360. https://doi.org/10.1016/S0079-6123(06)53020-1.

Cahoy, J.D., Emery, B., Kaushal, A., Foo, L.C., Zamanian, J.L., Christopherson, K.S., Xing, Y., Lubischer, J.L., Krieg, P.A., Krupenko, S.A., et al. (2008). A transcriptome database for astrocytes, neurons, and oligodendrocytes: a new resource for understanding brain development and function. J. Neurosci. *28*, 264–278.

Caruso, C., Carniglia, L., Durand, D., Scimonelli, T.N., and Lasaga, M. (2013). Astrocytes: new targets of melanocortin 4 receptor actions. J. Mol. Endocrinol. *51*, R33–R50.

Clemmensen, C., Jall, S., Kleinert, M., Quarta, C., Gruber, T., Reber, J., Sachs, S., Fischer, K., Feuchtinger, A., Karlas, A., et al. (2018). Coordinated targeting of cold and nicotinic receptors synergistically improves obesity and type 2 diabetes. Nat. Commun. *9*, 4304.

Dalvi, P.S., Chalmers, J.A., Luo, V., Han, D.Y., Wellhauser, L., Liu, Y., Tran, D.Q., Castel, J., Luquet, S., Wheeler, M.B., and Belsham, D.D. (2017). High fat induces acute and chronic inflammation in the hypothalamus: effect of high-fat diet, palmitate and TNF-alpha on appetite-regulating NPY neurons. Int. J. Obes. (Lond) *41*, 149–158.

Dampney, R.A., Michelini, L.C., Li, D.P., and Pan, H.L. (2018). Regulation of sympathetic vasomotor activity by the hypothalamic paraventricular nucleus in normotensive and hypertensive states. Am. J. Physiol. Heart Circ. Physiol. *315*, H1200–H1214.

De Souza, C.T., Araujo, E.P., Bordin, S., Ashimine, R., Zollner, R.L., Boschero, A.C., Saad, M.J., and Velloso, L.A. (2005). Consumption of a fat-rich diet activates a proinflammatory response and induces insulin resistance in the hypothalamus. Endocrinology *146*, 4192–4199.

Denisov, P., Popov, A., Brazhe, A., Lazareva, N., Verkhratsky, A., and Semyanov, A. (2021). Caloric restriction modifies spatiotemporal calcium dynamics in mouse hippocampal astrocytes. Biochim. Biophys. Acta Mol. Cell Res. *1868*, 119034.

Dietrich, M.O., and Horvath, T.L. (2013). Hypothalamic control of energy balance: insights into the role of synaptic plasticity. Trends Neurosci. *36*, 65–73.

Douglass, J.D., Dorfman, M.D., Fasnacht, R., Shaffer, L.D., and Thaler, J.P. (2017). Astrocyte IKKβ/NF-κB signaling is required for diet-induced obesity and hypothalamic inflammation. Mol. Metab. *6*, 366–373.

Durkee, C.A., and Araque, A. (2019). Diversity and specificity of astrocyte-neuron communication. Neuroscience *396*, 73–78.

Even, P.C., and Nadkarni, N.A. (2012). Indirect calorimetry in laboratory mice and rats: principles, practical considerations, interpretation and perspectives. Am. J. Physiol. Regul. Integr. Comp. Physiol. *303*, R459–R476.

Fellin, T., Pascual, O., Gobbo, S., Pozzan, T., Haydon, P.G., and Carmignoto, G. (2004). Neuronal synchrony mediated by astrocytic glutamate through activation of extrasynaptic NMDA receptors. Neuron *43*, 729–743.

Fleming, T.M., Scott, V., Naskar, K., Joe, N., Brown, C.H., and Stern, J.E. (2011). State-dependent changes in astrocyte regulation of extrasynaptic NMDA receptor signalling in neurosecretory neurons. J. Physiol. *589*, 3929–3941.

Frayn, K.N. (1983). Calculation of substrate oxidation rates in vivo from gaseous exchange. J. Appl. Physiol. Respir. Environ. Exerc. Physiol. *55*, 628–634.

Freire-Regatillo, A., Argente-Arizón, P., Argente, J., García-Segura, L.M., and Chowen, J.A. (2017). Non-neuronal cells in the hypothalamic adaptation to metabolic signals. Front. Endocrinol. (Lausanne) *8*, 51.

García-Cáceres, C., Balland, E., Prevot, V., Luquet, S., Woods, S.C., Koch, M., Horvath, T.L., Yi, C.X., Chowen, J.A., Verkhratsky, A., et al. (2019). Role of astrocytes, microglia, and tanycytes in brain control of systemic metabolism. Nat. Neurosci. *22*, 7–14.

García-Cáceres, C., Quarta, C., Varela, L., Gao, Y., Gruber, T., Legutko, B., Jastroch, M., Johansson, P., Ninkovic, J., Yi, C.X., et al. (2016). Astrocytic insulin signaling couples brain glucose uptake with nutrient availability. Cell *166*, 867–880.

García-Cáceres, C., Yi, C.X., and Tschöp, M.H. (2013). Hypothalamic astrocytes in obesity. Endocrinol. Metab. Clin. North Am. *42*, 57–66.

Geerling, J.J., Boon, M.R., Kooijman, S., Parlevliet, E.T., Havekes, L.M., Romijn, J.A., Meurs, I.M., and Rensen, P.C. (2014). Sympathetic nervous system control of triglyceride metabolism: novel concepts derived from recent studies. J. Lipid Res. *55*, 180–189.

Gomez, J.L., Bonaventura, J., Lesniak, W., Mathews, W.B., Sysa-Shah, P., Rodriguez, L.A., Ellis, R.J., Richie, C.T., Harvey, B.K., Dannals, R.F., et al. (2017). Chemogenetics revealed: DREADD occupancy and activation via converted clozapine. Science *357*, 503–507.

Gordon, G.R., Iremonger, K.J., Kantevari, S., Ellis-Davies, G.C., MacVicar, B.A., and Bains, J.S. (2009). Astrocyte-mediated distributed plasticity at hypothalamic glutamate synapses. Neuron *64*, 391–403.

Hall, K.D., Heymsfield, S.B., Kemnitz, J.W., Klein, S., Schoeller, D.A., and Speakman, J.R. (2012). Energy balance and its components: implications for body weight regulation. Am. J. Clin. Nutr. *95*, 989–994.

Herrera Moro Chao, D., Wang, Y., Foppen, E., Ottenhoff, R., van Roomen, C., Parlevliet, E.T., van Eijk, M., Verhoek, M., Boot, R., Marques, A.R., et al. (2019). The iminosugar AMP-DNM improves satiety and activates brown adipose tissue Through GLP1. Diabetes *68*, 2223–2234.

Hill, S.J., Barbarese, E., and McIntosh, T.K. (1996). Regional heterogeneity in the response of astrocytes following traumatic brain injury in the adult rat. J. Neuropathol. Exp. Neurol. *55*, 1221–1229.

Horvath, T.L., Sarman, B., García-Cáceres, C., Enriori, P.J., Sotonyi, P., Shanabrough, M., Borok, E., Argente, J., Chowen, J.A., Perez-Tilve, D., et al. (2010). Synaptic input organization of the melanocortin system predicts diet-induced hypothalamic reactive gliosis and obesity. Proc. Natl. Acad. Sci. USA *107*, 14875–14880.

Innocenti, B., Parpura, V., and Haydon, P.G. (2000). Imaging extracellular waves of glutamate during calcium signaling in cultured astrocytes. J. Neurosci. *20*, 1800–1808.

Kanemaru, K., Kubota, J., Sekiya, H., Hirose, K., Okubo, Y., and Iino, M. (2013). Calcium-dependent N-cadherin up-regulation mediates reactive astrogliosis and neuroprotection after brain injury. Proc. Natl. Acad. Sci. USA *110*, 11612–11617.

Karlas, A., Reber, J., Liapis, E., Paul-Yuan, K., and Ntziachristos, V. (2019). Multispectral optoacoustic tomography of brown adipose tissue. Handb. Exp. Pharmacol. *251*, 325–336.

Khakh, B.S., and Sofroniew, M.V. (2015). Diversity of astrocyte functions and phenotypes in neural circuits. Nat. Neurosci. *18*, 942–952.

Kim, J.G., Suyama, S., Koch, M., Jin, S., Argente-Arizon, P., Argente, J., Liu, Z.W., Zimmer, M.R., Jeong, J.K., Szigeti-Buck, K., et al. (2014). Leptin signaling in astrocytes regulates hypothalamic neuronal circuits and feeding. Nat. Neurosci. *17*, 908–910.

Li, C., Navarrete, J., Liang-Guallpa, J., Lu, C., Funderburk, S.C., Chang, R.B., Liberles, S.D., Olson, D.P., and Krashes, M.J. (2019). Defined paraventricular hypothalamic populations exhibit differential responses to food contingent on caloric state. Cell Metab. *29*, 681–694.e5.

Licht, C.M., de Geus, E.J., and Penninx, B.W. (2013). Dysregulation of the autonomic nervous system predicts the development of the metabolic syndrome. J. Clin. Endocrinol. Metab. *98*, 2484–2493.

Luther, J.A., and Tasker, J.G. (2000). Voltage-gated currents distinguish parvocellular from magnocellular neurones in the rat hypothalamic paraventricular nucleus. J. Physiol. *523*, 193–209.

Marina, N., Teschemacher, A.G., Kasparov, S., and Gourine, A.V. (2016). Glia, sympathetic activity and cardiovascular disease. Exp Physiol *101*, 565–576. https://doi.org/10.1113/EP085713.

Milanski, M., Degasperi, G., Coope, A., Morari, J., Denis, R., Cintra, D.E., Tsukumo, D.M., Anhe, G., Amaral, M.E., Takahashi, H.K., et al. (2009). Saturated fatty acids produce an inflammatory response predominantly through the activation of TLR4 signaling in hypothalamus: implications for the pathogenesis of obesity. J. Neurosci. *29*, 359–370.

Morton, G.J., Meek, T.H., and Schwartz, M.W. (2014). Neurobiology of food intake in health and disease. Nat. Rev. Neurosci. *15*, 367–378.

Münzberg, H., Qualls-Creekmore, E., Berthoud, H.R., Morrison, C.D., and Yu, S. (2016). Neural control of energy expenditure. Handb. Exp. Pharmacol. *233*, 173–194.

Nedergaard, M., Rodríguez, J.J., and Verkhratsky, A. (2010). Glial calcium and diseases of the nervous system. Cell Calcium *47*, 140–149.

Papazoglou, I., Lee, J.H., Cui, Z., Li, C., Fulgenzi, G., Bahn, Y.J., Staniszewska-Goraczniak, H.M., Piñol, R.A., Hogue, I.B., Enquist, L.W., et al. (2022). A distinct hypothalamus-to-beta cell circuit modulates insulin secretion. Cell Metab. *34*, 285–298.e7.

Pham, C., Moro, D.H., Mouffle, C., Didienne, S., Hepp, R., Pfrieger, F.W., Mangin, J.M., Legendre, P., Martin, C., Luquet, S., et al. (2020). Mapping astrocyte activity domains by light sheet imaging and spatio-temporal correlation screening. Neuroimage *220*, 117069.

Reis, W.L., Yi, C.X., Gao, Y., Tschöp, M.H., and Stern, J.E. (2015). Brain innate immunity regulates hypothalamic arcuate neuronal activity and feeding behavior. Endocrinology *156*, 1303–1315.

Robb, J.L., Morrissey, N.A., Weightman Potter, P.G., Smithers, H.E., Beall, C., and Ellacott, K.L.J. (2020). Immunometabolic changes in glia - A potential role in the pathophysiology of obesity and diabetes. Neuroscience *447*, 167–181.

Roh, E., Song, D.K., and Kim, M.S. (2016). Emerging role of the brain in the homeostatic regulation of energy and glucose metabolism. Exp. Mol. Med. *48*, e216.

Rose, C.R., Felix, L., Zeug, A., Dietrich, D., Reiner, A., and Henneberger, C. (2017). Astroglial glutamate signaling and uptake in the hippocampus. Front. Mol. Neurosci. *10*, 451.

Saklayen, M.G. (2018). The global epidemic of the metabolic syndrome. Curr. Hypertens. Rep. *20*, 12.

Singh, B., and Saxena, A. (2010). Surrogate markers of insulin resistance: a review. World J. Diabetes *1*, 36–47.

Stanley, S., Moheet, A., and Seaquist, E.R. (2019). Central mechanisms of glucose sensing and counterregulation in defense of hypoglycemia. Endocr. Rev. *40*, 768–788.

Stanley, S., Pinto, S., Segal, J., Pérez, C.A., Viale, A., DeFalco, J., Cai, X., Heisler, L.K., and Friedman, J.M. (2010). Identification of neuronal subpopulations that project from hypothalamus to both liver and adipose tissue polysynaptically. Proc. Natl. Acad. Sci. USA *107*, 7024–7029.

Stern, J.E. (2001). Electrophysiological and morphological properties of pre-autonomic neurones in the rat hypothalamic paraventricular nucleus. J. Physiol. *537*, 161–177.

Stern, J.E., Son, S., Biancardi, V.C., Zheng, H., Sharma, N., and Patel, K.P. (2016). Astrocytes contribute to angiotensin II stimulation of hypothalamic neuronal activity and sympathetic outflow. Hypertension *68*, 1483–1493.

Sutton, A.K., Myers, M.G., Jr., and Olson, D.P. (2016). The role of PVH circuits in leptin action and energy balance. Annu. Rev. Physiol. *78*, 207–221.

Tasker, J.G., and Dudek, F.E. (1991). Electrophysiological properties of neurones in the region of the paraventricular nucleus in slices of rat hypothalamus. J. Physiol. *434*, 271–293.

Thaler, J.P., Yi, C.X., Schur, E.A., Guyenet, S.J., Hwang, B.H., Dietrich, M.O., Zhao, X., Sarruf, D.A., Izgur, V., Maravilla, K.R., et al. (2012). Obesity is associated with hypothalamic injury in rodents and humans. J. Clin. Invest. *122*, 153–162.

Thayer, J.F., Yamamoto, S.S., and Brosschot, J.F. (2010). The relationship of autonomic imbalance, heart rate variability and cardiovascular disease risk factors. Int. J. Cardiol. *141*, 122–131.

Timper, K., and Brüning, J.C. (2017). Hypothalamic circuits regulating appetite and energy homeostasis: pathways to obesity. Dis. Model. Mech. *10*, 679–689.

Vardy, E., Robinson, J.E., Li, C., Olsen, R.H.J., DiBerto, J.F., Giguere, P.M., Sassano, F.M., Huang, X.P., Zhu, H., Urban, D.J., et al. (2015). A new DREADD facilitates the multiplexed chemogenetic interrogation of behavior. Neuron *86*, 936–946.

Varela, L., Kim, J.G., Fernández-Tussy, P., Aryal, B., Liu, Z.W., Fernández-Hernando, C., and Horvath, T.L. (2021a). Astrocytic lipid metabolism determines susceptibility to diet-induced obesity. Sci. Adv. *7*, eabj2814.

Varela, L., Stutz, B., Song, J.E., Kim, J.G., Liu, Z.W., Gao, X.B., and Horvath, T.L. (2021b). Hunger-promoting AgRP neurons trigger an astrocyte-mediated feed-forward autoactivation loop in mice. J. Clin. Invest. *131*.

Verkhratsky, A., and Nedergaard, M. (2018). Physiology of Astroglia. Physiol. Rev. *98*, 239–389.

Virtue, S., and Vidal-Puig, A. (2013). Assessment of brown adipose tissue function. Front. Physiol. *4*, 128.

Wang, Y., DelRosso, N.V., Vaidyanathan, T.V., Cahill, M.K., Reitman, M.E., Pittolo, S., Mi, X., Yu, G., and Poskanzer, K.E. (2019). Accurate quantification of astrocyte and neurotransmitter fluorescence dynamics for single-cell and population-level physiology. Nat. Neurosci. *22*, 1936–1944.

Yi, C.X., la Fleur, S.E., Fliers, E., and Kalsbeek, A. (2010). The role of the autonomic nervous liver innervation in the control of energy metabolism. Biochim. Biophys. Acta *1802*, 416–431.

Yu, X., Nagai, J., Marti-Solano, M., Soto, J.S., Coppola, G., Babu, M.M., and Khakh, B.S. (2020). Context-specific striatal astrocyte molecular responses are phenotypically exploitable. Neuron *108*, 1146–1162.e10.

Zhang, M., and Stern, J.E. (2017). Altered NMDA receptor-evoked intracellular Ca2+ dynamics in magnocellular neurosecretory neurons of hypertensive rats. J. Physiol. *595*, 7399–7411.

Zhang, Y., Reichel, J.M., Han, C., Zuniga-Hertz, J.P., and Cai, D. (2017). Astrocytic process plasticity and IKKβ/NF-κB in central control of blood glucose, blood pressure, and body weight. Cell Metab. *25*, 1091–1102.e4.

STAR★METHODS

KEY RESOURCES TABLE

REAGENT or RESOURCE	SOURCE	IDENTIFIER
Antibodies		
chicken anti-Green fluorescent protein	Aves Labs	#GFP-1010
rabbit anti-s100β	Abcam	#41548
rabbit anti-Ds Red	Living Colors	#632496
mouse anti-GFAP	Sigma-Aldrich	#G3893
rabbit anti-HA epitope tag	Rockland	#600-401-384
rabbit anti-EEAT2	Novus Biologicals	#NBP1-59632
anti-chicken Alexa 488	Thermo fisher Scientific	#A32931
anti-rabbit Alexa 594	Thermo fisher Scientific	#A32754
anti-mouse Alexa 488	Thermo fisher Scientific	# A32766
anti-rabbit Alexa 647	Thermo fisher Scientific	# A32795
HRP anti-rabbit	Cell Signaling Technology	#7074
Bacterial and virus strains		
AAV 2/5.EF1α.DIO.hM3Dq.mCherry	gift from Brian Roth.	Addgene viral prep #50460-AAV5
AAV 2/5.EF1α.DIO.hM4Di.mCherry	gift from Brian Roth.	Addgene viral prep #50461-AAV5
AAV 2/5.EF1α.DIO.mCherry	gift from Brian Roth.	Addgene viral prep #50462-AAV5
AAV 2/5.GFAP.hM3Dq.mCherry	gift from Brian Roth.	Addgene viral prep #50478-AAV5
AAV 2/5.GFAP.hM4Di.mCherry	gift from Brian Roth.	Addgene viral prep #50479-AAV5
AAV 2/5.GFAP104.mCherry	gift from Edward Boyden.	Addgene viral prep #58909-AAV5
AAV 2/5.GFAP.Cre.WPRE	gift from James M. Wilson.	Addgene viral prep #105550-AAV5
pAAV.CAG.Flex.GCaMP6f.WPRE	was a gift from Douglas Kim and GENIE project.	Addgene viral prep #100835-AAV5
AAV5.GfaABC1D.Lck.GCaMP6f.SV40	gift from Baljit Khak.	Addgene viral prep #52925-AAV5
AAV 2/5.EF1α.DIO.KORD.mCitrine	viral production facility of the UMR INSERM 1089 (Nantes, France)	N/A
Deposited data		
Data S1	This paper	Unprocessed source data underlying all blots and graphs and corresponding statistical details.
Chemicals, peptides and recombinant proteins		
Clozapine N-oxide dihydrochloride	Tocris	#6329
Salvinorin B	Hello Bio	#HB4887
Kynurenic Acid	Abcam	#ab120256
TFB-TBOA	Tocris	#2532
DAPI	Vectashield	#H-1200
Alexa 555	Invitrogen	A20501MP
Phosphatase inhibitor cocktail	Sigma-Aldrich	#P5726
Protease inhibitor cocktail	Roche	#11836153001
Icilin	Tocris	#1531
Experimental models: Organisms/strains		
C57Bl/6J mice	Janvier	N/A
B6.FVB-Tg (Tg(Aldh1l1-cre) JD1884Htz)	Jackson Labs	https://www.jax.org/strain/023748
Glast-Cre (Tg(Slc1a3-cre/ERT2) 45-72Fwp) (to generate GCaMP6f/ Glast-CreER^{T2})	Gensat	http://www.informatics.jax.org/allele/MGI:4420274

(*Continued on next page*)

Continued

REAGENT or RESOURCE	SOURCE	IDENTIFIER
B6.129S-Gt (*ROSA*)*26Sor*$^{tm95.1(CAG-GCaMP6f)Hze}$/J) (to generate GCaMP6f/Glast-CreER^{T2})	Jackson Labs	https://www.jax.org/strain/024105
Software and algorithms		
Phenomaster TSE Systems GmbH	TSE Systems GmbH	N/A
Ponemah software	DSI	RRID:SCR_017107
Vevo Lab software	Visualsonics	RRID:SCR_015816
ImageJ	NIH	RRID:SCR_003070
MATLAB v2019b	The MathWorks, Inc.	RRID:SCR_001622
IGOR Pro (v8)	Wavemetrics Inc.	RRID:SCR_000325
pCLAMP Software Suite	Molecular Devices LLC	RRID:SCR_011323
Andor FUSION	Andor Technology Ltd.	N/A
AQuA Script for MatLab	https://github.com/yu-lab-vt/AQuA	N/A
GraphPad Prism 8	GraphPad Software	RRID:SCR_002798
LabSolution software	Shimadzu	N/A
MetaMorph	Molecular Devices LLC	RRID:SCR_002368
Other		
Telemetric devices (HD-XG)	DSI	https://www.datasci.com/products/implantable-telemetry/small-animal-telemetry/hd-xg
Mouse ultrasensitive insulin ELISA kit	ALPCO	#80-INSMSU-E01
Mouse C-peptide ELISA kit	Crystal Chem	#90050
BC Assay protein assay Kit	Interchim Uptima	#UP40840B
C18 5μM Beckman Ultrasphere column	Hichrom	#235330
Chow Diet	Safe diets	#A03
High-Fat high-Sucrose Diet	Brogaarden	#D12451 Research Diet

RESOURCE AVAILABILITY

Lead contact

Further information and requests for resources and reagents should be directed to and will be fulfilled by the lead contact, Serge Luquet (serge.luquet@u-paris.fr).

Materials availability

This study did not generate new unique reagents.

Data and code availability

- Data reported in this paper will be shared by the lead contact upon request.
- Original data for creating all graphs in the paper and the corresponding statistical details are provided in Data S1.
- This study did not report original code.
- Any additional information required to reanalyze the data reported in this study is available from the lead contact upon request.

EXPERIMENTAL MODELS AND SUBJECT DETAILS

Animals

Unless noted otherwise, littermates of the same sex were randomly assigned to experimental groups. All animal protocols were approved by the Animal Care Committee of the University of Paris (APAFIS # 2015062611174320), Institut Biologie Paris Seine of Sorbonne University (C75-05-24) or the Georgia State University IAUCUC protocols. Twelve to fifteen-week-old male Aldh1-L1-Cre (Tg(Aldh1l1-cre)) JD1884Htz, Jackson laboratory, Bar Harbor, USA), male C57BL/6J (Janvier, Le Genest St-Isle, France) or male GCaMP6f/Glast-CreER^{T2} (Pham et al., 2020) mice were individually housed at constant temperature (23± 2°C) and submitted to a 12/12h light/dark cycle. All mice had access to regular chow diet (Safe, Augy, France) and water ad libitum, unless stated otherwise. Additionally, age matched C57BL/6J or GCaMP6f/Glast-CreER^{T2} mice groups were fed with either chow diet or high-fat high-sugar diet (HFHS, cat n. D12451, Research Diets, New Brunswick, USA) for twelve to sixteen weeks. Body weight

was measured every week. Body weight gain was calculated as the difference between week one, twelve-sixteen weeks of HFHS diet exposure.

METHOD DETAILS

Viral constructs

Designer receptor exclusively activated by designer drugs (DREADD) and GCaMP6f viruses were purchased from http://www.addgene.org/, unless stated otherwise. pAAV-EF1α-DIO-hM3Dq-mCherry ($2.4x10^{12}$ vg/ml, working dilution 1:6, Addgene plasmid #50460-AAV5; http://www.addgene.org/50460/; RRID:Addgene_50460), pAAV-EF1α-DIO-hM4Di-mCherry ($2.4x10^{12}$ vg/ml, working dilution 1:6, Addgene plasmid #50461-AAV5; http://www.addgene.org/50461/; RRID:Addgene_50461), pAAV-EF1α-DIO-mCherry ($3.6x10^{12}$ vg/ml, working dilution 1:4, Addgene plasmid #50462-AAV5; http://www.addgene.org/50462/; RRID:Addgene_50462), pAAV-GFAP-hM3Dq-mCherry ($9.1x10^{12}$ vg/ml, working dilution 1:2, Addgene plasmid #50478-AAV5; http://www.addgene.org/50478/; RRID:Addgene_50478) and pAAV-GFAP-hM4Di-mCherry ($3.2x10^{11}$ vg/ml, working dilution 1:1.5, Addgene plasmid #50479-AAV5; http://www.addgene.org/50479/; RRID:Addgene_50479) were a gift of Bryan Roth. pAAV-GFAP104-mCherry ($6.4x10^{12}$ vg/ml, working dilution 1:1.5, Addgene plasmid #50479-AAV5; http://www.addgene.org/50479/; RRID:Addgene_50479) was a gift of Edward Boyden. pAAV-GFAP-Cre.WPRE ($2.2x10^{12}$ vg/ml, working dilution 1:10, Addgene plasmid #105550-AAV5; http://www.addgene.org/105550/; RRID:Addgene_105550) was a gift from James M Wilson. pAAV-CAG-Flex.GCaMP6f.WPRE ($3.15x10^{13}$ vg/ml, working dilution 1:10, Addgene plasmid #100835-AAV5; http://www.addgene.org/100835/; RRID:Addgene_100835) was a gift of Douglas Kim and GENIE Project. pAAV-GfaACC1D.Lck-GCaMP6f.SV40 ($1.53x10^{13}$ vg/ml, working dilution 1:5, Addgene plasmid #52925-AAV5; http://www.addgene.org/52295/; RRID:Addgene_52925) was a gift of Baljit Khak. In order to produce the pAAV-EF1α-DIO-KORD-mCitrine, the NheI/AscI fragment containing the HA-KORD-Citrine cassette from addgene#65417 was subcloned in Nhe1/AscI backbone pAAV-EF1a-DIO-hM3D(Gq)-mCherry (addgene#50460) to produce pAAV-EF1a-DIO-HA-KORD-Citrine and subsequent adeno-associated virus 5HType 2/5 ($2.4x10^{12}$ vg/ml, working dilution 1:6) were produced by the viral production facility of the UMR INSERM 1089 (Nantes, France).

Surgical procedures

For all surgical procedures, mice were rapidly anesthetized with isoflurane (3%), followed by intraperitoneal (ip) injection of analgesic Buprenorphine (Buprecare, 0.3 mg/kg, Recipharm, Lancashire, UK) and Ketoprofen (Ketofen, 10 mg/kg, France) and maintained under 1.5% isoflurane anesthesia throughout the surgery.

Stereotaxic surgery

Male Aldh1-L1-Cre$^{+/-}$, Aldh1-L1-Cre$^{-/-}$ and male C57BL/6J mice received bilateral viral injections (0.3 μl) in the PVN (stereotaxic coordinates: AP -0.8mm, L +0.3mm, V -4.9mm) at a rate of 0.1 μl/min. The injection needle was carefully removed after 5 minutes waiting at the injection site and 2 minutes waiting half way to the top (Berland et al., 2020). Mice recovered for at least 3 weeks after the surgery before being involved in experimental procedures.

Continuous body temperature telemetry implantation

Two-weeks after stereotaxic delivery of viral vectors, additional groups of male C57BL/6J mice were implanted with telemetric devices (HD-XG, Data Sciences International (DSI), Minnesota, USA) in the abdominal cavity. After a seven-day period recovery time, the implanted mice were then installed on the DSI receiver. Data were collected using a Ponemah acquisition system (DSI).

Photoacoustic BAT imaging

Male Aldh1L1-Cre$^{+/-}$ mice previously injected in the PVN with DREADD viruses were anesthetized under isoflurane and placed on a heated platform. Respiration and cardiac rhythm were constantly monitored. Hair was removed above the interscapular BAT and optic gel was applied before positioning the transducer to ensure a good transmission of the signal. Image acquisition, before and after vehicle (0.9% Sterile sodium chloride solution (Fisher Scientific, Illkrich, France) or Clozapine-N-oxide dihydrocloride (CNO, 0.6mg/kg, Tocris, Bristol, UK) ip injection, was performed using a Vevo LAZR system (FujiFilm VisualSonics, Toronto, ON, Canada) which combine ultrasound and photoacoustic imaging. Light generated from a tunable laser (680–970 nm) is delivered to the tissue through fiber optic bundles integrated into linear-arrays mounted on the ultrasonic transducer (LZ400, fc = 30 MHz). Spectral unmixing analyses were performed with Vevo®Lab software.

Indirect calorimetry analysis

After stereotaxic surgery and viral delivery, male Aldh1-L1-Cre$^{+/-}$, Aldh1-L1-Cre$^{-/-}$ and C57BL/6J mice were monitored for metabolic efficiency (Labmaster, TSE Systems GmbH, Bad Homburg, Germany). After an initial period of acclimation in the calorimetry cages, Vehicle (Vehicle matched with CNO injected group: 0.9% Sterile sodium chloride solution (Fisher Scientific, Illkrich, France) or Vehicle matched with SalB injected group: 0.6% DMSO (Sigma-Aldrich, Saint-Louis, USA) in 0.9% sterile sodium chloride solution (Fisher Scientific, Illkrich, France)), CNO (0.6mg/kg dissolved in 0.9% Sterile sodium chloride solution, Tocris, Bristol, UK) or Salvinorin B (SalB, 10mg/kg, dissolved in DMSO and injected in a 0.6% DMSO final solution, Hellobio, Dunshaughlin, Republic of Ireland) were ip injected with a two-day interval between injections depending on the corresponding DREADD expressing group.

Metabolic efficiency was assessed as previously described (Berland et al., 2020). Additionally, fatty acid oxidation (Frayn, 1983; Herrera Moro Chao et al., 2019) and energy balance (Hall et al., 2012) were calculated as previously reported. Briefly, whole energy

expenditure (EE), O_2 consumption and CO_2 production, respiratory exchange rate (RER=VCO_2/VO_2,), fatty acid oxidation (FAO), and locomotor activity using calorimetric cages with bedding, food and water (Labmaster, TSE Systems GmbH, Bad Homburg, Germany) were recorded as previously reported (Berland et al., 2020; Frayn, 1983; Hall et al., 2012; Herrera Moro Chao et al., 2019). Ratio of gases was determined through an indirect open circuit calorimeter (Arch et al., 2006; Even and Nadkarni, 2012). This system monitors O_2 and CO_2 concentration by volume at the inlet ports of a tide cage through which a known flow of air is being ventilated (0.4 L/min) and compared regularly to a reference empty cage. For optimal analysis, the flow rate was adjusted according to the animal body weights to set the differential in the composition of the expired gases between 0.4-0.9% (Labmaster, TSE Systems GmbH, Bad Homburg, Germany). The flow was previously calibrated with O_2 and CO_2 mixture of known concentrations (Air Liquide, S.A. France). O_2 consumption and CO_2 production were recorded every 15 min for each animal during the entire experiment. Whole energy expenditure (EE) was calculated using the Weir equation for respiratory gas exchange measurements. Food consumption was measured as the instrument combines a set of highly sensitive feeding sensors for automated online measurements. Mice had access to food and water *ad libitum*. To allow measurement of every ambulatory movement, each cage was embedded in a frame with an infrared light beam-based activity monitoring system with online measurement at 100 Hz. The sensors for gases and detection of movements operated efficiently in both light and dark phases, allowing continuous recording.

Body mass composition was analyzed using an Echo Medical systems' EchoMRI (Whole Body Composition Analyzers, EchoMRI, Houston, USA), according to manufacturer's instructions. Readings of body composition were given within 1 min. Data analysis was performed on Excel XP using extracted raw values of VO_2 consumed (expressed in ml/h), VCO_2 production (expressed in ml/h), and energy expenditure (kcal/h).

Oral glucose tolerance test

Viral injected male Aldh1-L1-Cre$^{+/-}$, Aldh1-L1-Cre$^{-/-}$ and C57BL/6J mice and non-injected GCaMP6f/Glast-CreER^{T2} mice were fasted for four hours. A small tail cut incision was performed to take blood samples and measure glycemia with a glucometer (A. Menarini Diagnostics, France). The mice were ip injected firstly with Vehicle, CNO (0.6 mg/kg) or SalB (10 mg/kg) and fifteen minutes after received a glucose oral gavage (2 g/kg). Blood glucose levels were measured after 0, 5, 10, 15, 20, 30, 45, 60, 90 and 120 minutes and blood samples were only taken at 0, 15, 30, and 90 minutes after receiving the glucose oral gavage. Plasma samples were further processed for insulin (mouse ultrasensitive insulin ELISA kit, ALPCO, Salem, USA) and c-peptide (mouse C-peptide ELISA kit, Crystal Chem, IL, USA) measurements. Insulinogenic index was calculated as the area under the curve (AUC) of plasma insulin change during OGTT (in pmol/l) divided AUC of glycaemia during OGTT (in mmol/l) as described (Singh and Saxena, 2010).

Corticosterone level measurement

Circulating corticosterone was measured in blood draw using the DtetctX® corticosterone chemiluminescent ELISA kits from #K014 ArborAssays™ (source Clinisciences S.A.S Nanterre, France).

Ex-vivo epifluorescence calcium imaging

Male Aldh1-L1-Cre$^{+/-}$ mice previously injected with GCamP6f and DREADDs viral constructs and GCaMP6f/Glast-CreER^{T2} mice were terminally anaesthetized using isoflurane. Brains were removed and placed in ice-cold oxygenated slicing artificial cerebrospinal solution (aCSF, 30mM NaCl, 4.5mM KCl, 1.2mM NaH_2PO_4, 1mM $MgCl_2$, 26mM $NaHCO_3$, and 10mM D-Glucose and 194mM Sucrose) and subsequently cut into 300-μm thick PVN coronal slices using a vibratome (Leica VT1200S, Nussloch, Germany). Next, brain slices were recovered in aCSF (124mM NaCl, 4.5mM KCl, 1.2mM NaH_2PO_4, 1mM $MgCl_2$, 2mM $CaCl_2$, 26mM $NaHCO_3$, and 10mM D-Glucose) at 37 °C for 60 minutes. Imaging was carried out at room temperature under constant perfusion (~3 ml/min) of oxygenated aCSF. The overall cellular fluorescence of astrocytes expressing GCaMP6f was collected by epifluorescence illumination. A narrow-band monochromator light source (Polychrome II, TILL Photonics, Germany) was directly coupled to the imaging objective via an optical fiber. Fluorescence signal was collected with a 40x 0.8NA or a 63x 1.0NA water immersion objective (Zeiss, Germany) and digital electron-multiplying charge-coupled device (EMCCD Cascade 512B, Photometrics, Birmingham, UK). The imaging system was hosted in an upright microscope (Zeiss Axioskop 50, Germany) and coordinated by MetaMorph software (Molecular Devices, USA) (Pham, 2020). A double-band dichroic/filter set was used to reflect the excitation wavelength (470 nm) to slices and filter the emitted GCaMP6 green fluorescence (Di03-R488/561-t3; FF01-523/610, Semrock). The same filter was used for slices expressing both GCaMP6 and DREADD-mCherry. PVN slices were transferred to the imaging chamber, where 3-minute astrocyte spontaneous activity recordings were performed in slices of GCaMP6f/Glast-CreER^{T2} mice. In the case of PVN slices of Aldh1-L1-Cre$^{+/-}$ mice, we performed a basal epifluorescence recording (60 seconds), followed by a 120 second bath application of CNO (10μM) or SalB (100μM) and 240 seconds recording over the washing of the compounds.

The responsive regions displaying Ca^{2+} signals were scrutinized by the three-dimensional spatio-temporal correlation screening method (Pham et al., 2020). Background signal was subtracted from the raw images by using the minimal intensity projection of the entire stack. Ca^{2+} signals of individual responsive regions were normalized as dF/F_0, with F_0 representing the baseline intensity and quantified using Matlab (The MathWorks, France) and Igor Pro (Wavemetrics, USA). We gauged signal strength of Ca^{2+} traces of single responsive regions by calculating their temporal integration and normalizing per minute. The global temporal synchronization of detected Ca^{2+} signals was determined by the temporal Pearson's correlation coefficients of all combinations between single Ca^{2+} regions (Pham et al., 2020).

Simultaneous *ex-vivo* whole-cell patch clamp electrophysiology and confocal Ca^{2+} imaging

Viral injected male Aldh1-L1-Cre$^{+/-}$ and C57BL/6J mice were anesthetized with pentobarbital (50 mg kg^{-1} ip) and subsequently perfused through the heart with 30 mL of ice cold aCSF sucrose solution with NaCl replaced by equal-osmol sucrose (in mM: 200 sucrose, 2.5 KCl, 1 $MgSO_4$, 26 $NaHCO_3$, 1,25 NaH_2PO_4, 20 D-Glucose, 0.4 ascorbic acid, and 2.0 $CaCl_2$; pH 7.2; 300-305 mosmol l^{-1}). The brain was subsequently removed, mounted in the chamber of a vibratome (Leica VT1200s, Leica Microsystems, Buffalo Grove, IL, USA) using superglue and the ventral surface pressed firmly against a block of 3% KCl agar. The brain was submerged in sucrose solution and bubbled constantly with 95% O_2/5% CO_2. Coronal slices (240 μm thickness) containing the PVN were cut and placed in a holding chamber filled with aCSF and bubbled with 95% O_2/5% CO_2. The aCSF is identical in composition to the sucrose solution, but with 200 mM sucrose replaced by 119 mM NaCl. The slice chamber was warmed using a water bath at 32°C for 20 minutes before placement at room temperature for a total minimum of 60 minutes rest before proceeding with the experiment.

Slices were placed into a chamber on the stage of a microscope and perfused constantly (~3 ml/min) with aCSF bubbled continuously with 95% O_2/5% CO_2 and warmed to 32°C. Parvocellular neurons were targeted for patch clamp using morphological properties such small soma size relative to their magnocellular counterparts, as well as their proximity to as many GCaMP-expressing astrocytes as possible. Whole cell current clamp recordings were obtained from PVN parvocellular neurons using pipettes (2.5-4 MΩ) pulled from borosilicate glass (o.d. 1.5 mm) using a P-97 flaming/brown horizontal micropipette puller (Sutter Instruments, Novato, CA). The pipette internal solution consisted of (in mM): 135 $KMeSO_4$, 8 NaCl, 10 HEPES, 2 Mg-ATP, 0.3 Na-GTP, 6 phosphocreatine, 0.2 EGTA with pH 7.2-7.3 and 285-295 mOsmol (kg H_2O)$^{-1}$. The liquid junction potential for the $KMeSO_4$ internal was approximately -10 mV and was not corrected. Occasionally, Alexa 555 (50 μM, Invitrogen, MA, USA) was included to visualize the neuron. For current clamp recordings, traces were obtained with an Axopatch 200B amplifier (Axon Instruments, Foster City, CA) and digitized using an Axon 1440B Digitizer (Axon Instruments, Foster City, CA) at 10 kHz on a desktop computer running Clampex 10 software (Molecular Devices). In the experiments where DL-threo-beta-Benzyloxyaspartate (TBOA, 1 μM, Tocris, Bristol, UK) alone was bath applied, cells were recorded in voltage clamp, held at -70 mV, and filtered at 2 kHz. Data were discarded if series resistance exceeded a 20% change over the course of the recording. To positively confirm a patched cell was indeed a parvocellular neuron, a series of increasingly negative current injections was applied to the cell from a resting membrane potential of -60mV. The activation of a low threshold depolarization in response to the cessation of current injection confirms parvocellular identity (Tasker and Dudek, 1991). Basal recordings of parvocellular and astrocytic Ca^{2+} activity were firstly performed for a minimum of 250 seconds before bath application of either CNO (10 μM) or SalB (100 μM) for 250 seconds. Additional recordings adding CNO or SalB combined with kynurenic Acid (KYN, 1 mM, Abcam, Cambridge, UK) or TBOA (1 μM, Tocris, Bristol, UK), were performed after washout for a minimum of 5 minutes after initial application of CNO/SalB. Data were analyzed using either Clampfit or Igor Pro 8 (Wavemetrics Inc.).

Simultaneously, GCaMP6f expression in astrocytes was visualized using the Dragonfly 200 laser spinning disk confocal imaging system and an iXon 888 EMCCD camera (Andor Technology, Belfast, UK). Using Andor's FUSION software, we captured time series images with z-stacking to maximize acquisition of astrocytic Ca^{2+} events near the patched neuron. To quantify network-wide Ca^{2+}signals within the confocal plane, we employed the Astrocyte Quantification and Analysis (AQuA) method that extracts event-based information from optical sectioning image series (Wang et al., 2019). Image background was subtracted, and images were converted from FUSION's native file format to TIFFs in ImageJ (NIH). Imaging videos of astrocytic GCaMP were then processed using the AQuA script run through Matlab (v2019b) (MathWorks, Natick, MA, USA). Full details of the script functionality and code can be found at: https://github.com/yu-lab-vt/AQuA. The parameters used for the analysis are as follows: intensity threshold scaling factor 1, smoothing (sigma) 1.5, minimum Size (pixels) 24, temporal cut threshold 2, growing z threshold 1, rising time uncertainty 2, slowest delay in propagation 2, propagation smoothness 1, z score threshold 2, maximum distance 0, minimum correlation 0, maximum time difference 2, temporally extended events disabled, ignore delay tau enabled. We filtered out events lasting longer than 60 seconds and whose amplitude exceeded a 10 dF/F_0 change in amplitude to minimize inclusion of artifacts in the analysis. Event data were imported into Prism 8 for analysis (GraphPad, San Diego, CA, USA). Some waveform data and figures were generated in Igor Pro (Wavemetrics, Portland OR, USA).

Brain tissue Immunofluorescence

Viral injected male Aldh1-L1-Cre$^{+/-}$ and C57BL/6J mice received Vehicle, CNO or SalB ip injection. Sixty minutes later, the mice were euthanized with pentobarbital (500 mg/kg, Dolethal, Vetoquinol, France). An additional group of GCaMP6f/Glast-CreER^{T2} mice was also euthanized. Mice were transcardially perfused with 0.1 M sodium phosphate buffer (PBS, pH 7.5) followed by 4% paraformaldehyde in phosphate buffer (0.1 M, pH 7.2). Brains were removed and post-fixed overnight in 4% paraformaldehyde. Afterwards, the brains were transferred to 30% sucrose in PBS for 2 days for cryoprotection. Next, 25 μm brain sections were cut in a freezing cryostat (Leica, Wetzlar, Germany) and further processed for immunofluorescence following the procedure previously described (Berland et al., 2020). Sections were processed as free-floating and incubated at 4°C overnight with chicken anti-Green fluorescent protein (GFP, 1:500, Aves Labs, Davis, California, USA), rabbit anti-s100β (1:500, Abcam, Cambridge, UK), rabbit Ds Red (1:1000, Living colors, Takara Bio, St-Germain-en-Laye, France), mouse anti-Glial fibrillary acidic protein (GFAP, 1:1000, Sigma-Aldrich, Saint-Louis, USA) or rabbit anti-HA epitope tag (1:2000, Rockland, Limerick, USA) primary antibodies. The next day, sections were rinsed in Tris-buffered saline (TBS, 0.25M Tris and 0.5M NaCl, pH 7.5) and incubated for 2 hours with secondary antibodies (1:1000, Thermo fisher Scientific, MA, USA) conjugated with fluorescent dyes: goat anti-chicken Alexa 488, donkey anti-rabbit Alexa 594, donkey anti-mouse Alexa 488 and donkey anti-rabbit Alexa 647. After rinsing, the sections were mounted and coverslipped with

DAPI (Vectashield, Burlingade, California, USA) and examined with a confocal laser scanning microscope (Zeiss LSM 510, Oberkochen, Germany) with a color digital camera and AxioVision 3.0 imaging software.

Western Blotting

C57BL/6J mice were euthanized with pentobarbital (500 mg/kg, Dolethal, Vetoquinol, France) and shortly after decapitated. The mouse head was then immediately immersed in liquid nitrogen for 4 seconds. After removal of the brain, the anterior hypothalamus was dissected on ice-cold surface and brain lysates were prepared in a solution containing 1% Sodium dodecyl sulfate (SDS, Sigma-Aldrich, Saint-Louis, USA), 0.2% phosphatase inhibitors (phosphatase inhibitor cocktail, Sigma-Aldrich, Saint-Louis, USA) and 0.1% protease inhibitors (protease inhibitor cocktail, Roche, Boulogne-Billancourt, France). Protein content in the hypothalamic lysates was measured with a BC Assay protein quantification Kit (Interchim Uptima, Montlucon, France). Western blotting was performed as previously described (Berland et al., 2020). Equal amounts of proteins (15 μg) for each sample were loaded onto 10-12% polyacrylamide gels. Proteins were separated by SDS-PAGE and transferred to PVDF membranes (Millipore). Membranes were immunoblotted with rabbit anti-EEAT2 (1:500, Novus Biologicals, Abingdon, UK). HRP-coupled secondary antibody anti-rabbit (1:10000, Cell Signaling Technology, Charles Renard, France) was matched with an ECL detection system. Quantification was performed using Image J software (NIH).

Mono-aminergic content determination

Viral injected male Aldh1-L1-Cre$^{+/-}$ and C57BL/6J mice were injected ip with Vehicle or CNO, followed by icilin ip (5 mg/kg, Tocris, Bristol, UK) and sacrificed with pentobarbital (500 mg/kg, Dolethal, Vetoquinol, France) after sixty minutes. Interscapular brown adipose tissue (BAT) was dissected and immediately snap frozen in liquid nitrogen. Additional viral injected male Aldh1-L1-Cre$^{+/-}$ and C57BL/6J mice received Vehicle, CNO or SalB ip injection and were euthanized sixty minutes later. Urine (removed from the bladder) was collected and immediately stored at -80°C. Monoamine analyses were performed at the Bioprofiler platform of the Unit "Biologie Fonctionnelle et Adaptative", University of Paris, BFA, UMR 8251 CNRS, F75205, Paris, France. Catecholamines and metabolites were analyzed by reversed phase-High-performance Liquid Chromatography using a Shimadzu system connected to a Waters 2465 electrochemical detector (HPLC-ED, Waters, USA) with a glassy carbon working electrode (0.7V, 10nA). BAT was homogenized in an ice-cold solution, containing 0.4% ethylenediaminetetraacetic acid and 0.1M perchloric acid, while urine samples were processed using MonoSpin PBA columns (Interchim, Montlucon, France). After centrifugation, the supernatant was further analyzed with HLPC-ED. Mobile phase (58,5 mM Sodium Acetate (Sigma, St Louis, USA), 0.7mM Octane Sulfonic Acid (Sigma O 0133, St Louis, USA), pH 3,8 for mobile phase A and 100% MeOH for mobile phase B) was pumped at a flow rate of 1ml/min and monoamines and metabolite concentrations were detected at an oxidation potential of 750mV compared to the reference electrode. Compounds were separated by an isocratic flow (90% A / 10% B) using a Kromasil® AIT column (length 250mm; internal diameter 4.6mm; particle size 5μm) at 30°C. Catecholamines and metabolites were quantified using LabSolution software (Shimadzu, Kyoto, Japan) by integration of the peak absorbance area, employing a calibration curve established with known catecholamine concentrations.

QUANTIFICATION AND STATISTICAL ANALYSIS

Statistical analysis

Results are expressed as the mean ± SEM. All statistical analysis was performed using GraphPad Prism 8 (La Jolla, CA, USA). Data were analyzed by T-test, two-way or one-way ANOVA depending on each experimental design. Pairwise comparisons were evaluated with a Tukey post-hoc test. Blood glucose, plasma insulin, $\%SO_2$ and body temperature values were analyzed by ANOVA of repeated measures with 2 between subject factors: *Time* and *Substance*. An adjustment of Bonferroni was performed with significant values set as $p<0.05$. All details related to statistical analyses are summarized in Data S1.

Cell Metabolism, Volume *34*

Supplemental information

Hypothalamic astrocytes control systemic glucose metabolism and energy balance

Daniela Herrera Moro Chao, Matthew K. Kirchner, Cuong Pham, Ewout Foppen, Raphael G.P. Denis, Julien Castel, Chloe Morel, Enrica Montalban, Rim Hassouna, Linh-Chi Bui, Justine Renault, Christine Mouffle, Cristina García-Cáceres, Matthias H. Tschöp, Dongdong Li, Claire Martin, Javier E. Stern, and Serge H. Luquet

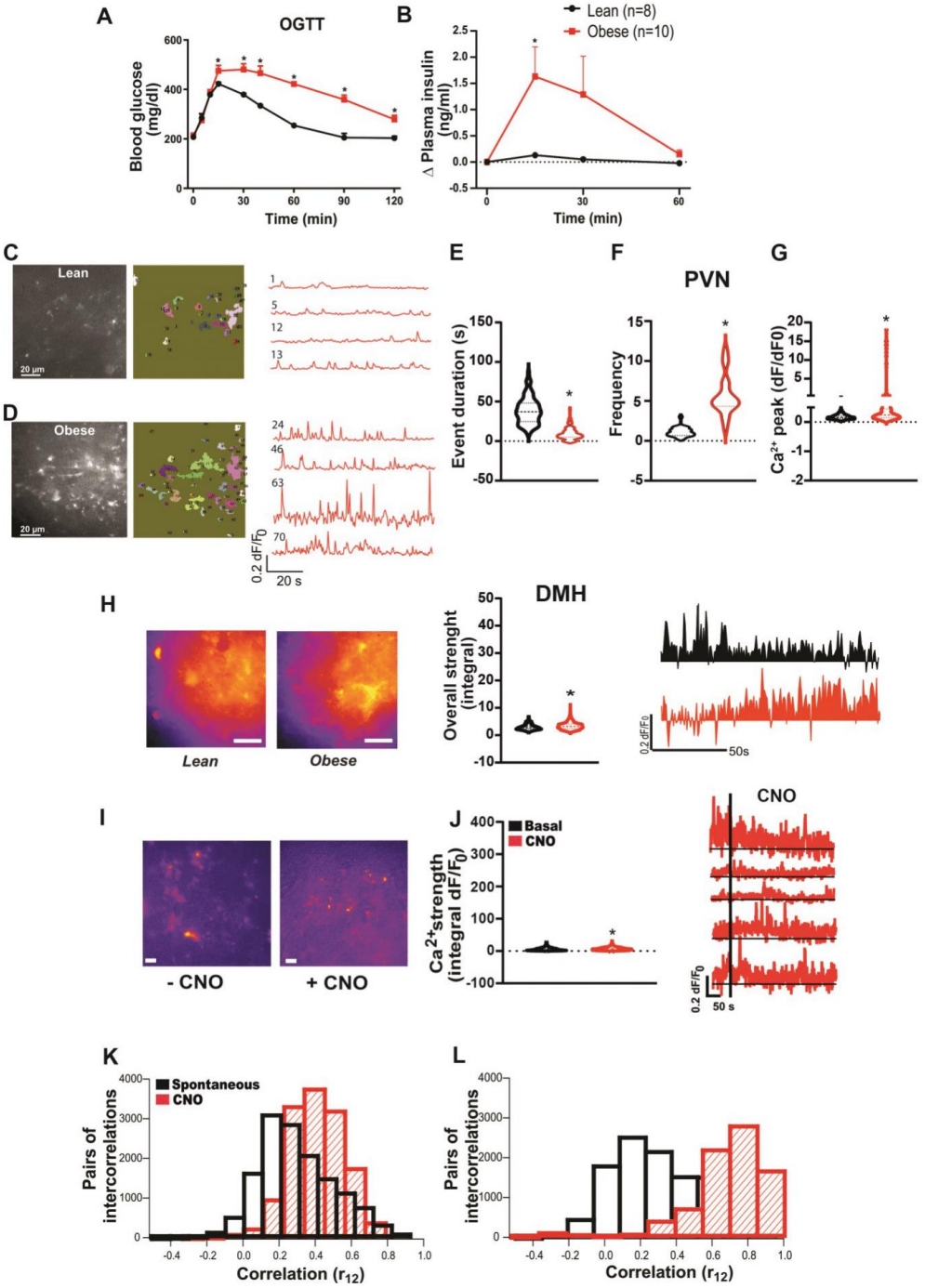
A
OGTT
Blood glucose (mg/dl)
Time (min)
B
Lean (n=8)
Obese (n=10)
Δ Plasma insulin (ng/ml)
Time (min)
C
Lean
20 µm
D
Obese
20 µm
0.2 dF/F0
20 s
E
PVN
Event duration (s)
F
Frequency
G
Ca2+ peak (dF/dF0)
H
Lean
Obese
DMH
Overall strenght (integral)
0.2 dF/F0
50s
I
- CNO
+ CNO
J
Basal
CNO
Ca2+strength (integral dF/F0)
CNO
0.2 dF/F0
50 s
K
Spontaneous
CNO
Pairs of intercorrelations
Correlation (r12)
L
Pairs of intercorrelations
Correlation (r12)

Supplementary Figure 1. Nutritional and chemogenetic-induced change in astrocytic calcium events in hypothalamic nuclei. Related to figure 1. (A) Blood glucose (lean n=8, obese n=7) and **(B)** plasma insulin change (lean n=8, obese n=10) during an OGTT in GCaMP6f-Glast-CreER^{T2} mice after 4-month chow or HFHS diet consumption. **(C-D)** Average projection of time-lapse GCaMP epifluorescence images (left), detected Ca^{2+} active domains (middle) and representative signal traces (right) of spontaneous Ca^{2+} activity in the PVN of **(C)** lean or **(D)** obese mice. (**E**) Comparison of Ca^{2+} event duration, (**F**) Ca^{2+} event frequency, (**G**) Ca^{2+} event peaks between astrocytes in lean (n= 147) and obese (n=167). **(H)** Fluorescence projection of global GCaMP6 signals from time-lapse images of DMH of lean or obese GCaMP6f-Glast-CreER^{T2} mice (left), comparison of overall Ca^{2+} signal strength (middle, lean n=140, obese n=1185) and representative spontaneous Ca^{2+} signal with under-curve area being shadowed. Scale bar: 20μm. **(I)** Fluorescence projection (left), **(J)** overall Ca^{2+} strength (middle, lean n=500, obese n=1492) and time-course Ca^{2+} signal traces (right) of GCaMP signals in the PVN of Aldh1L1-Cre mice expressing mCherry control viral construct before and after CNO bath application. Scale bar: 20μm. Histogram data are expressed as mean +/- SEM. **(K,L)** Distribution of temporal correlations between Ca^{2+} responses of all paired active domains (as an estimation of global synchronization) before and after CNO bath application to PVN slices of Aldh1L1-Cre mice expressing **(K)** mCherry control (Spontaneous n=500, CNO n=15857) or **(L)** hM3Dq receptor (Spontaneous n=12629, CNO n=9137) viral construct. * $P<0.05$ by 2-way ANOVA (A-B) and Student's t-test (E-G,H-I). For statistical details, see table S1.

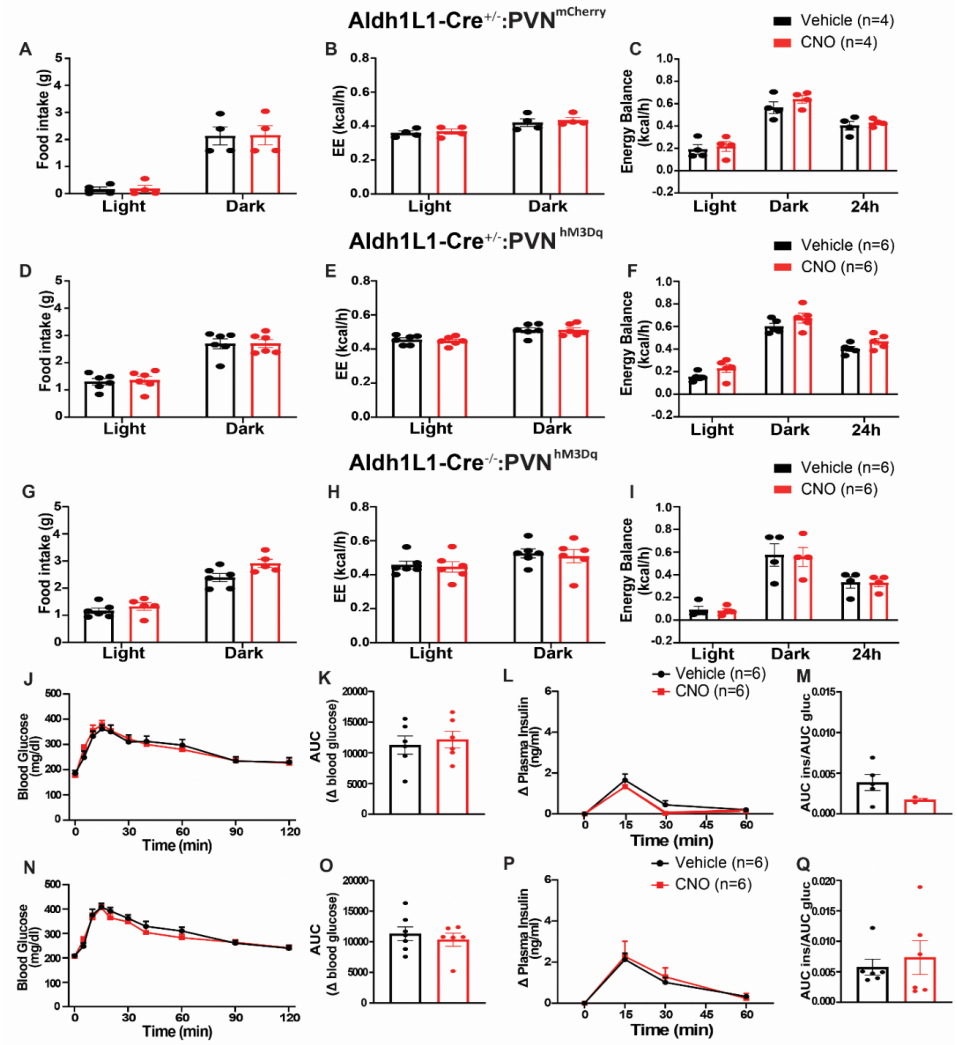

Supplementary Figure 2. Astrocyte Gq receptor chemogenetic activation in the PVN does not modulate food intake and energy balance in lean mice. Related to figure 2. (A-I) Food intake, energy expenditure (EE) and energy balance after Vehicle or CNO ip administration in **(A-C)** Aldh1L1-Cre$^{+/-}$:PVN^{mCherry} (Vehicle n=4, CNO n=4), **(D-F)** Aldh1L1-Cre$^{+/-}$:PVN^{hM3Dq} (Vehicle n=6, CNO n=6) and **(G-I)** Aldh1L1-Cre$^{-/-}$:PVN^{hM3Dq} (Vehicle n=6, CNO n=6) mice. **(J-Q)** Blood glucose (Aldh1L1-Cre$^{+/-}$:PVN^{mCherry}, Vehicle n=6, CNO n=6; Aldh1L1-Cre$^{-/-}$:PVN^{hM3Dq}, Vehicle n=6, CNO

n=6), corresponding area under the curve (AUC), plasma insulin change (Aldh1L1-Cre$^{+/-}$:PVN^{mCherry}, Vehicle n=5, CNO n=3; Aldh1L1-Cre$^{-/-}$:PVN^{hM3Dq}, Vehicle n=6, CNO n=6) and insulinogenic index (Aldh1L1-Cre$^{+/-}$:PVN^{mCherry}, Vehicle n=5, CNO n=3; Aldh1L1-Cre$^{-/-}$:PVN^{hM3Dq}, Vehicle n=6, CNO n=6) after Vehicle or CNO ip administration followed by an OGTT in **(J-M)** Aldh1L1-Cre$^{+/-}$:PVN^{mCherry} and **(N-Q)** Aldh1L1-Cre$^{-/-}$:PVN^{hM3Dq} mice. AU refers to arbitrary units. Data are expressed as mean +/- SEM.* P<0.05 by 2-way ANOVA (A-J,L,N,P) and Student's t-test (K,M,O,Q). For statistical details, see table S1.

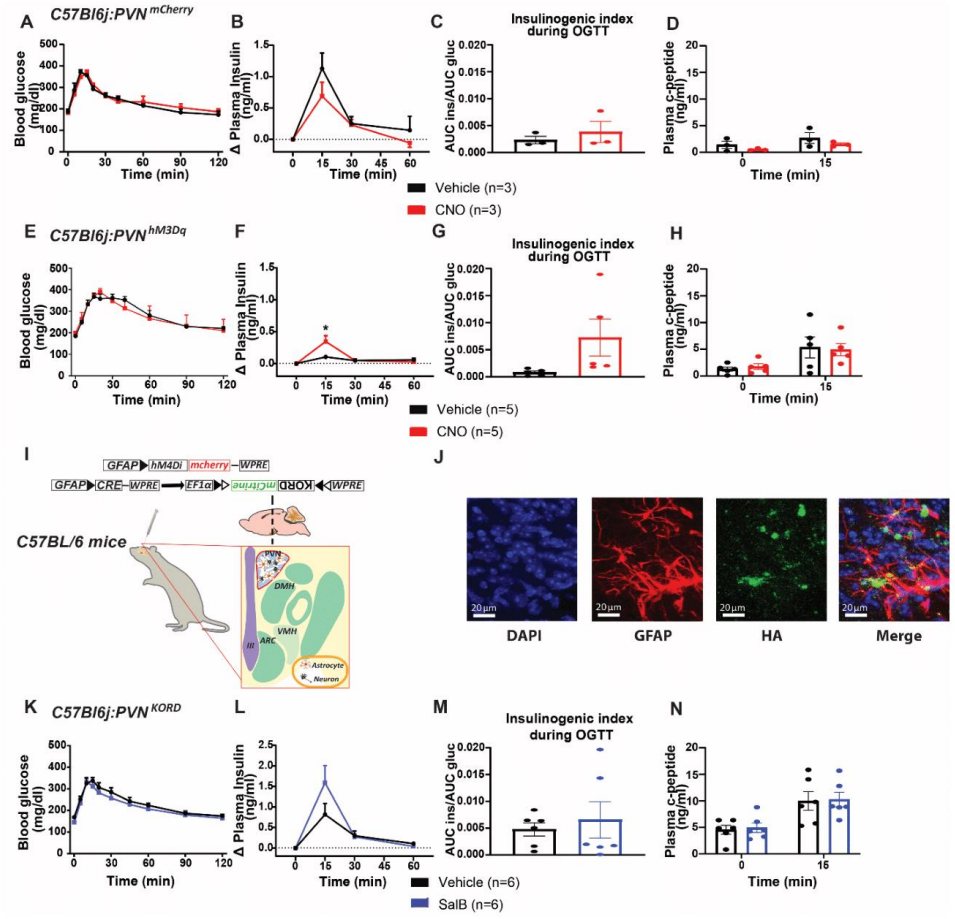

Supplementary Figure 3. Gq receptor chemogenetic activation in GFAP-positive astrocytes in the PVN modulates glucose metabolism in lean mice. Related to figure 2. (A-H) Blood glucose, plasma insulin change, insulinogenic index and plasma c-peptide after Vehicle or CNO ip administration followed by an OGTT in **(A-D)** C57Bl6j:PVN^{mCherry} (Vehicle n=3, CNO=3) and **(E-H)** C57Bl6j:PVN^{hM3Dq} (Vehicle n=5, CNO=5) mice. **(I)** Representative image of viral mix delivery of GFAP-Cre and Cre-KORD, to express SalB-sensitive KORD Gi receptor, or CNO-sensitive GFAP-Gi DREADD in the PVN of C57BL/6 mice. **(J)** Confocal images of double immunofluorescence of GFAP (red) and human influenza hemaglutinin (HA) tag (green) in the PVN of C57Bl6j:PVN^{KORD} mice. Cell nuclei are shown in DAPI (blue). **(K)** Blood glucose, **(L)** plasma insulin change, **(M)**

insulinogenic index and **(N)** plasma c-peptide after Vehicle or SalB ip administration followed by an OGTT in C57Bl6j:PVN^{KORD} (Vehicle n=6, SalB n=6) mice. Data are expressed as mean +/- SEM.* P<0.05 by 2-way ANOVA (A-B,D,E-F,H,K-L,N) and Student's t-test (C,G,M). For statistical details, see table S1.

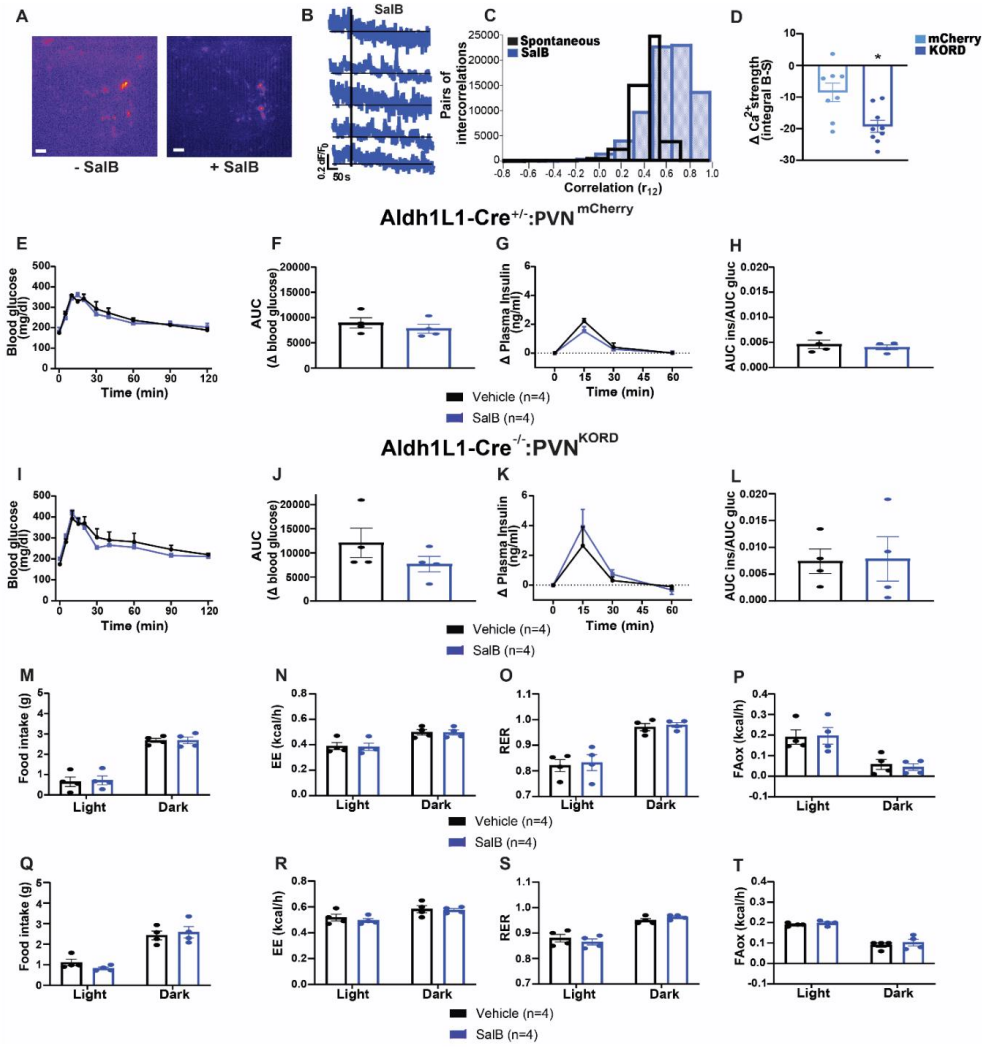

Supplementary Figure 4. Chemogenetic-specific ligand Salvinorin B has marginal effect in control animal. Related to figure 2. (A) Pseudo-images, **(B)** time-course Ca^{2+} signal traces of GCaMP signals, **(C)** distribution of temporal correlations (Spontaneous n=35622, SalB n=164623) between Ca^{2+} responses of all paired active domains before and after SalB bath application to PVN slices of Aldh1L1-Cre mice expressing mCherry control viral construct. **(D)** Change in overall Ca^{2+} strength (mCherry n=8, KORD n=9) after SalB bath application (integral basal-stimulation: integral B-S) to PVN slices of Aldh1L1-Cre mice expressing KORD receptor or mCherry control

viral construct. Overall Ca^{2+} strength data are expressed as mean +/- SEM. Scale bar: 20µm. **(E-L)** Blood glucose, corresponding AUC, plasma insulin change and insulinogenic index after Vehicle or SalB ip administration followed by an OGTT in **(E-H)** Aldh1L1-$Cre^{+/-}$:$PVN^{mCherry}$ (Vehicle n=4, SalB n=4) and **(I-L)** Aldh1L1-$Cre^{-/-}$:PVN^{KORD} (Vehicle n=4, SalB n=4) mice. **(M-T)** Food intake, EE, respiratory exchange ratio and fatty acid oxidation FAox after Vehicle or SalB ip injection to **(M-P)** Aldh1L1-$Cre^{-/-}$:PVN^{KORD} (Vehicle n=4, SalB n=4) and **(Q-T)** Aldh1L1-$Cre^{+/-}$:$PVN^{mCherry}$ (Vehicle n=4, SalB n=4) mice. AU refers to arbitrary units. Data are expressed as mean +/- SEM.* $P<0.05$ by Student's t-test (D,F,H,J,L) and 2-way ANOVA (E,G,I,K,M-T). For statistical details, see table S1.

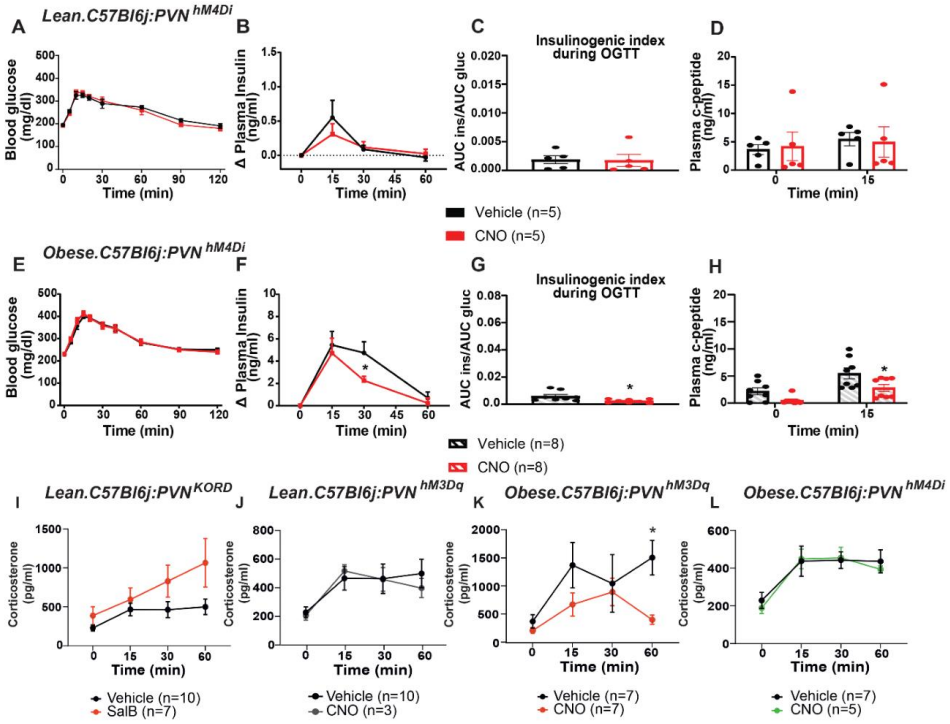

Supplementary Figure 5. Astrocyte Gi receptor chemogenetic activation in the PVN improves glucose metabolism in obese mice. Related to figure 2 and 4. (A-H) Blood glucose (lean, Vehicle n=5, CNO n=5; obese, Vehicle n=10, CNO n=10), plasma insulin change (lean, Vehicle n=5, CNO n=5; obese, Vehicle n=8, CNO n=8), insulinogenic index (lean, Vehicle n=5, CNO n=5; obese, Vehicle n=8, CNO n=8) and plasma c-peptide (lean, Vehicle n=5, CNO n=5; obese, Vehicle n=8, CNO n=8) after Vehicle or CNO ip administration followed by an OGTT in **(A-D)** lean or **(E-H)** obese C57Bl6j:PVN^{hM4Di} mice. **(I-L)** Corticosterone level in **(I)** lean C57Bl6j:PVN^{KORD} (Vehicle n=10, SalB n=7), **(J)** lean C57Bl6j:PVN^{hM3Dq} (Vehicle n=10, CNO n=3), **(K)** Obese C57Bl6j:PVN^{hM3Dq} (Vehicle n=7, CNO n=7) and **(L)** Obese C57Bl6j:PVN^{hM4Di} (Vehicle n=7, CNO n=5) after Vehicle, SalB or CNO ip administration. Data are expressed as mean +/- SEM.* P<0.05 by 2-way ANOVA (A-B,D,E-F,H,I-L) and Student's t-test (C,G). For statistical details, see table S1.

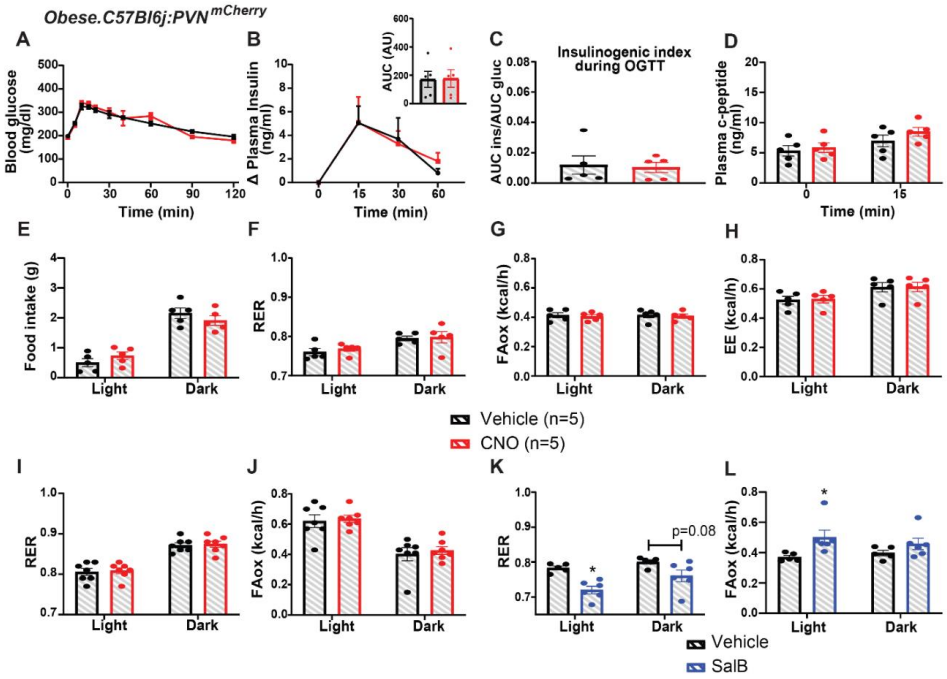

Supplementary Figure 6. Chemogenetic manipulations of PVN astrocytes in obese mice. Related to figure 4. (A) Blood glucose, **(B)** plasma insulin change and corresponding AUC (top right), **(C)** insulinogenic index and **(D)** plasma c-peptide after Vehicle or CNO ip administration followed by an OGTT in obese C57Bl6j:PVN^{mCherry} (Vehicle n=5, CNO n=5) control mice. **(E)** Food intake, **(F)** RER, **(G)** FAox and **(H)** EE after Vehicle or CNO ip injection to obese C57Bl6j:PVN^{mCherry} (Vehicle n=5, CNO n=5) control mice. **(I-L)** RER and FAox of obese **(I-J)** C57Bl6j:PVN^{hM3Dq} (Vehicle n=7, CNO n=7) mice after Vehicle or CNO ip injection, or of obese **(K-L)** C57Bl6j:PVN^{KORD} (Vehicle n=5, SalB n=6) mice after Vehicle or SalB ip administration. AU refers to arbitrary units. Data are expressed as mean +/- SEM.* P<0.05 by 2-way ANOVA (A-B,D-L) and Student's t-test (B-C). For statistical details, see table S1.

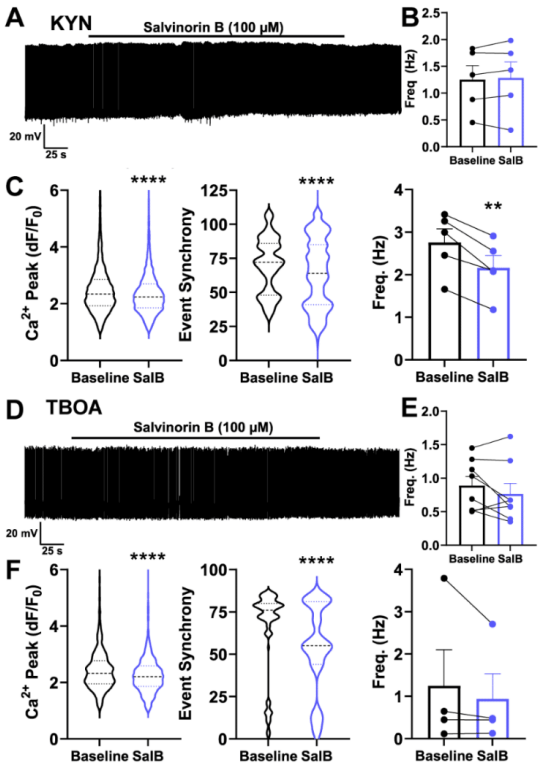

Supplementary Figure 7. Astrocyte glutamatergic transport signaling mediates astrocyte KORD receptor-driven modulation of parvocellular neuron activity. Related to figure 6. (A) Example trace recorded from Aldh1L1-Cre$^{+/-}$:PVN^{KORD} mice, demonstrating the SalB effect in the presence of Kynurenic Acid (KYN, 1 mM) on parvocellular spike activity. **(B)** Parvocellular PVN neuron firing frequency in the presence of SalB and KYN in Aldh1L1-Cre$^{+/-}$:PVN^{KORD} mice (n=5). **(C)** Summary data of astrocyte Ca^{2+} activity. Ca^{2+} strength (left, Control n= 3446, SalB n=2701), event synchrony (middle, Control n= 3446, SalB n=2701) and event frequency (right, n=5) of GCaMP signals in PVN of Aldh1L1-Cre$^{+/-}$:PVN^{KORD} mice in the presence of SalB/KYN. **(D)** Example trace recorded from Aldh1L1-Cre$^{+/-}$:PVN^{KORD} mice, demonstrating the SalB effect in the presence of DL-*threo*-β-Benzyloxyaspartic acid (TBOA, 1 μM) on parvocellular spike activity. **(E)** Parvocellular neuron spike frequency in the presence of TBOA and SalB in PVN slices of Aldh1L1-

$Cre^{+/-}$:PVN^{KORD} mice. **(F)** Summary data of AQuA astrocyte Ca^{2+} activity analysis. Ca^{2+} strength (left, Control n=1147, SalB n=837), event synchrony (middle, Control n=1147, SalB n=837) and event frequency (right, n=4) in the presence of TBOA/SalB. Data are expressed as mean +/- SEM. * P<0.05, ** P<0.01, *** P<0.0001 by paired t-test (B, C_{right},E, F_{right}) and Welch's t-test ($C_{left,\ middle}$, $F_{left,\ middle}$). For statistical details, see table S1.

III.2 - Contribution to the mechanistic study on the cellular trafficking of the Ca^{2+} ion channel TRPV

Recovery from tachyphylaxis of TRPV1 coincides with recycling to the surface membrane

Quan Tian[a,1], Juan Hu[a,1], Chang Xie[a,1], Kaidi Mei[a], Cuong Pham[b], Xiaoyi Mo[a], Régine Hepp[b], Sylvia Soares[b], Fatiha Nothias[b], Yuanyuan Wang[a], Qiang Liu[a], Fen Cai[a], Bo Zhong[a], Dongdong Li[b,2], and Jing Yao[a,2]

[a]Hubei Key Laboratory of Cell Homeostasis, College of Life Sciences, Wuhan University, Wuhan, 430072 Hubei, China; and [b]Sorbonne Université, Institut de Biologie de Paris-Seine, Neuroscience Paris Seine, CNRS UMR8246, INSERM U1130, 75005 Paris, France

Edited by Francisco Bezanilla, The University of Chicago, Chicago, IL, and approved January 31, 2019 (received for review November 20, 2018)

The transient receptor potential vanilloid-1 (TRPV1) ion channel is essential for sensation of thermal and chemical pain. TRPV1 activation is accompanied by Ca^{2+}-dependent desensitization; acute desensitization reflects rapid reduction in channel activity during stimulation, whereas tachyphylaxis denotes the diminution in TRPV1 responses to repetitive stimulation. Acute desensitization has been attributed to conformational changes of the TRPV1 channel; however, the mechanisms underlying the establishment of tachyphylaxis remain to be defined. Here, we report that the degree of whole-cell TRPV1 tachyphylaxis is regulated by the strength of inducing stimulation. Using light-sheet microscopy and pH-sensitive sensor pHluorin to follow TRPV1 endocytosis and exocytosis trafficking, we provide real-time information that tachyphylaxis of different degrees concurs with TRPV1 recycling to the plasma membrane in a proportional manner. This process controls TRPV1 surface expression level thereby the whole-cell nociceptive response. We further show that activity-gated TRPV1 trafficking associates with intracellular Ca^{2+} signals of distinct kinetics, and recruits recycling routes mediated by synaptotagmin 1 and 7, respectively. These results suggest that activity-dependent TRPV1 recycling contributes to the establishment of tachyphylaxis.

desensitization | calcium | synaptotagmin | pain | TRP channel

Transient receptor potential vanilloid-1 (TRPV1) is a Ca^{2+}-permeable cation channel expressed in sensory nerves specialized for pain detection (1, 2). Ca^{2+} influx upon TRPV1 activation induces channel desensitization, with acute desensitization referring to the rapid reduction in the evoked inward current, and tachyphylaxis denoting current diminutions over repetitive stimulation (1, 3, 4). Desensitization can be leveraged to treat clinical pain. For instance, the TRPV1 agonist capsaicin has been used as a therapeutic analgesic (5, 6).

The mechanism underlying TRPV1 acute desensitization has been widely explored and converged on agonist-induced conformational changes at the channel level (1, 2). In this regard, TRPV1 interacts in a Ca^{2+}-dependent manner with either or both calcinerin (7), calmodulin (8), and phosphatidylinositol 4,5-bisphosphate (9), to regulate channel gating and inactivate response. Relatively, much remains to be understood on the mechanisms underlying the establishment of tachyphylaxis. Early studies show that phosphorylation of TRPV1 by protein kinase A and mutation at the corresponding phosphorylation site affect the induction of tachyphylaxis, which yet display little effect on acute desensitization (1, 7, 10). Likely, the establishment of tachyphylaxis recruits other mechanisms besides those assigned for acute desensitization.

Here, we observed by whole-cell patch clamp that the extent of tachyphylaxis is regulated by the strength of inducing stimulation. Imaging TRPV1 exocytosis and endocytosis trafficking in real time by light-sheet microscopy and a pH-sensitive sensor, we show that TRPV1 channels undergo activity-dependent recycling to control their surface expression thereby the strength of whole-cell desensitization. We also show that stimulation of different strengths elicits intracellular Ca^{2+} signals of different kinetics and regulates TRPV1 recycling via distinct routes mediated by synaptotagmin 1 and 7, respectively. These results suggest the contribution of TRPV1 trafficking to the establishment of tachyphylaxis.

Results

Whole-Cell Tachyphylaxis Is Stimulation Strength Dependent. TRPV1 tachyphylaxis is a Ca^{2+}-dependent process and has been induced by saturated doses of capsaicin (1, 4, 9). We applied different doses of capsaicin to induce desensitization in TRPV1-expressing HEK 293 cells. A reference current was evoked by 1 μM capsaicin in the absence of Ca^{2+} at the beginning. Then in the presence of external Ca^{2+} (Fig. 1 *A–D*, *color bar*), capsaicin stimulation led whole-cell responses to a tachyphylaxis state. Subsequent stimulation by similar doses only elicited a much reduced response (Fig. 1 *A–D*). Tachyphylaxis is known to reduce the agonist affinity of TRPV1, rather than its loss of function (1). Indeed, following low (0.3 or 1 μM) capsaicin-induced tachyphylaxis, increasing subsequent stimulation to supramaximal range (5–100 μM capsaicin) evoked whole-cell currents approaching the pretachyphylaxis level (Fig. 1 *A*, *B*, and *E*, *blue and green* vs. *black*).

However, as for the tachyphylaxis induced by relatively high doses of capsaicin (3–10 μM), the supramaximal stimulations

Significance

TRPV1 ion channel plays an important role in the transmission and modulation of pain. Desensitization of TRPV1 in nociceptors is adaptable for analgesic therapy. One type of desensitization is tachyphylaxis that reflects reduced TRPV1 responses to repetitive stimuli. To understand the mechanism underlying the whole-cell tachyphylaxis, here we used an orthogonal electro-optical approach integrating electrophysiology and light-sheet microscopy. We show that the intensity of tachyphylaxis is regulated by the strength of inducing stimulation, and that TRPV1 channels undergo activity-gated recycling to regulate their surface expression level thereby the degree of tachyphylaxis. This study provides real-time insights into the establishment of tachyphylaxis and helps to understand desensitization-based analgesics.

Author contributions: D.L. and J.Y. designed research; Q.T., J.H., C.X., K.M., C.P., X.M., Y.W., Q.L., F.C., D.L., and J.Y. performed research; R.H., S.S., F.N., and B.Z. contributed new reagents/analytic tools; Q.T., J.H., C.X., K.M., X.M., Y.W., Q.L., F.C., D.L., and J.Y. analyzed data; and D.L. and J.Y. wrote the paper.

The authors declare no conflict of interest.

This article is a PNAS Direct Submission.

[1]Q.T., J.H., and C.X. contributed equally to this work.

[2]To whom correspondence may be addressed. Email: dongdong.li@inserm.fr or jyao@whu.edu.cn.

This article contains supporting information online at www.pnas.org/lookup/suppl/doi:10.1073/pnas.1819635116/-/DCSupplemental.

Published online February 25, 2019.

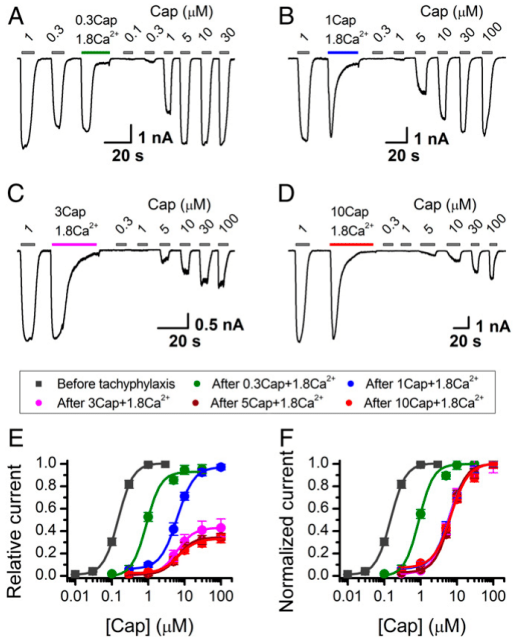

Fig. 1. Tachyphylaxis is regulated by the strength of preimposed stimulation. (*A–D*) Representative traces showing repetitive activation of TRPV1 channels after desensitization induced by 0.3 μM, 1 μM, 3 μM, and 10 μM capsaicin in the presence of Ca^{2+} (1.8 mM), as indicated by the color bars. Responses shown under gray bars were recorded in the absence of external Ca^{2+} to prevent further desensitization and gain whole-cell responses. A small current appeared upon the washing out of Ca^{2+}, reflecting its inhibitory effect on TRPV1 activity as reported (42). The pipette solution contained no adenosine triphosphate (ATP). (*E*) Dose–response curves for whole-cell TRPV1 currents obtained before and after tachyphylaxis induction. Data are shown as relative values to the reference current evoked by 1 μM capsaicin at the beginning of each recording. Solid lines are fits to Hill equation (n = 7–18 cells for each condition). (*F*) Dose–response curves normalized to their intrinsic maximum. Recordings were from transiently transfected HEK 293 cells held at −60 mV. Cap, capsaicin. Error bars, SEM.

could not trigger currents close to the pretachyphylaxis level (Fig. 1 *C* and *D*). The derived dose–response curves ended at a much lower level than that observed for low capsaicin-induced tachyphylaxis (Fig. 1*E*). Hence, the degree of tachyphylaxis, namely the inhibitory effect on whole-cell TRPV1 current, is dependent on the strength of the inducing stimulation.

Notably, though 1 μM and 3–10 μM capsaicin all lie in the saturation range in evoking TRPV1 whole-cell current under control condition (Fig. 1*E*, *gray square*), they induced tachyphylaxis to different extents (Fig. 1*E*, *blue* vs. *reddish*). Apart from the subsaturation dose (Fig. 1*F*, *green*), all saturated doses of capsaicin (1–10 μM) caused an almost identical right-shift in normalized dose–response curves (Fig. 1*F*, *blue and reddish*), indicating a similar reduction in the agonist affinity of TRPV1. Thus, tachyphylaxis of varied degrees induced by distinct saturated doses of capsaicin, could not be explained by the reduction in TRPV1 agonist affinity and would have recruited other mechanistic pathways.

Light-Sheet Imaging of TRPV1 Trafficking. TRPV1 expression level at the plasma membrane is another factor in shaping whole-cell nociceptive responses (11, 12) and has been suggested to be regulated by TRPV1 exocytosis and endocytosis (13, 14). To explore TRPV1 trafficking in real time, we engineered a TRPV1 fusion protein comprising the pH-dependent green fluorescent protein (GFP) mutant pHluorin that is green fluorescent in a neutral condition and dim in an acidic environment (15). The electrophysiological property of TRPV1 was unaffected by the insertion of pHluorin (*SI Appendix*, Fig. S1). In our configuration, TRPV1-pHluorin is dim when trapped into acidic trafficking vesicles and of high fluorescence upon exocytic insertion into the plasma membrane (*SI Appendix*, Fig. S2*A*). We could then follow TRPV1 surface expression and subcellular trafficking by dynamic imaging of pHluorin fluorescence.

To gain high-quality imaging, and avoid potential phototoxicity of laser scanning microscopy, we have used light-sheet microscopy that enables scanless optical sectioning and wide-field image acquisition by digital camera (16). Light sheet of μm-scale thickness and perpendicular to the optical axis of imaging objective, was generated via an orthogonally placed excitation objective (*SI Appendix*, Fig. S2*B*). The thin light sheet evidently improved the image quality of TRPV1-pHluorin-expressing HEK cells relative to conventional epifluorescence (*SI Appendix*, Fig. S2*B*, *Right*). A supramaximal dose of capsaicin caused a pronounced diminution in TRPV1-pHluorin fluorescence followed by a gradual recovery (*SI Appendix*, Fig. S2*C*), reflecting the retrieval of TRPV1 channels by endocytosis and their reinsertion by subsequent exocytosis. Inhibiting general endocytosis pathways by hypertonic solution (17) largely blocked the capsaicin-evoked fluorescence diminution (*SI Appendix*, Fig. S2 *D* and *F*), with a transient increase unmasked that implies the co-occurrence of exocytosis. Further, omission of external Ca^{2+} inhibited both the exocytosis and endocytosis of TRPV1-pHluorin (*SI Appendix*, Fig. S2 *E* and *F*), confirming the Ca^{2+}-dependence of TRPV1 recycling (1, 18, 19). Together, light-sheet imaging of TRPV1-pHluorin enables real-time mapping of TRPV1 trafficking and surface expression.

Stimulation Strength Regulates TRPV1 Recycling. To examine TRPV1 surface expression during strength-gated tachyphylaxis, we imaged TRPV1-pHluorin in HEK 293 cells upon 1 and 10 μM capsaicin stimulation in the presence of external Ca^{2+}. While both stimuli evoked an initial loss in TRPV1 surface expression followed by a subsequent recovery, the high-dose capsaicin induced a significantly greater reduction in TRPV1 expression (-0.68 ± 0.04, vs. -0.43 ± 0.03, $P < 0.01$) followed by a much delayed recovery (Fig. 2 *A–C*). At 5 min after 1 μM capsaicin stimulation, TRPV1 surface expression recovered to about 95% of the control level, while with 10 μM capsaicin stimulation, TRPV1 expression only recovered to 48% of the initial level at the same time point (Fig. 2*D*, $P < 0.01$). Thus, stimulation of distinct strengths evoked TRPV1 recycling in a different manner and resulted in proportional loss in TRPV1 surface expression. The delayed recovery in TRPV1 surface expression level induced by high capsaicin renders the post-tachyphylaxis currents persistently inferior to those obtained after low capsaicin stimulation (Fig. 1*E*, *red* vs. *blue*).

The dependence of TRPV1 trafficking on stimulation strength was further confirmed by using varied doses of capsaicin (Fig. 2*E*). A small overshoot was noted in recovery phase of 1 μM capsaicin stimulation (Fig. 2*A*), which in fact gradually went back to the initial level as revealed by a longer period of imaging (Fig. 2*F*, 20 min). The transient overshoot, therefore, reflects a transitory step for TRPV1 expression recovery. In contrast, the loss in TRPV1 expression caused by 10 μM capsaicin persisted even over a long imaging period (Fig. 2*F*). Juxtaposing the time course of patch-clamp current and the TRPV1-pHluorin fluorescence validated the correlation between the loss in surface TRPV1 expression and the reduction in whole-cell response (*SI Appendix*, Fig. S3).

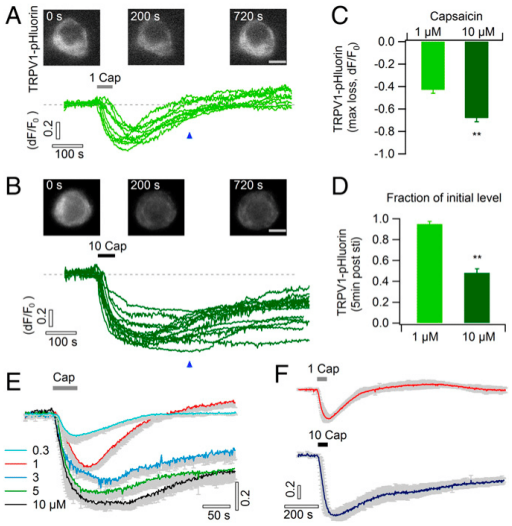

Fig. 2. TRPV1 channels undergo activity-dependent endocytosis and exocytosis recycling. (*A*) HEK cells expressing TRPV1-pHluorin and stimulated by 1 μM capsaicin. Each single trace was derived from an individual cell, with a ring-shape region of interest (ROI) traced along the cell surface while excluding nucleus hole. Fluorescence change is expressed as dF/F_0 with F_0 as the mean intensity of prestimulation baseline. (*B*) HEK cells expressing TRPV1-pHluorin and stimulated by 10 μM capsaicin. (*C*) The peak loss in TRPV1-pHluorin fluorescence for 1 μM ($n = 10$ cells) and 10 μM capsaicin (13 cells) stimulation. (*D*) Recovery in TRPV1-pHluorin level quantified as the fraction to the prestimulation control level. The timing when the values were measured is indicated by blue arrowheads in *A* and *B*. (*E*) TRPV1-pHluorin recycling triggered by varied doses of capsaicin (0.3–10 μM, $n = 7$–13 cells for each condition). (*F*) Imaging of TRPV1-pHluorin trafficking for a long period (20 min; $n = 10$ for 1 μM, and 8 for 10 μM capsaicin). (Scale bars, 10 μm.)

Collectively, we show that TRPV1 recycling is stimulation strength dependent, which shapes the channel expression level and whole-cell tachyphylaxis.

In parallel, we confirmed this phenomenon in primary dorsal root ganglia (DRG) neurons that express endogenous TRPV1 channels. Similar to the above results, low-dose capsaicin (1 μM) induced tachyphylaxis with whole-cell currents fully recovered by supramaximal doses of capsaicin (*SI Appendix*, Fig. S4 *A* and *C*), a process to counteract agonist affinity reduction that was facilitated by additive acidification (H^+) (20). The same manipulation, however, failed to recover the whole-cell current following high capsaicin-induced tachyphylaxis (10 μM, *SI Appendix*, Fig. S4 *B* and *D*), echoing the additional contribution of the reduction in TRPV1 surface expression. As observed with light-sheet imaging, low capsaicin induced a transient reduction in TRPV1 expression that was followed by a quick recovery, whereas high capsaicin evoked a more pronounced and persistent loss in TRPV1 expression level (*SI Appendix*, Fig. S4 *E* and *F*).

TRPV1 Exocytosis Assists Whole-Cell Current Recovery. During tachyphylaxis induction, capsaicin elicited endocytosis retrieval of surface TRPV1 followed by exocytosis-mediated recovery. This process is regulated by the stimulation strength as determined by both stimulation dose (Figs. 1 and 2) and duration (Fig. 3 *A* and *B*). We further pondered that suspending recording for a brief period right after tachyphylaxis induction could facilitate the exocytic reinsertion of TRPV1 and the whole-cell currents. As expected, a 5-min pause augmented the whole-cell response after 1 μM capsaicin-induced desensitization, compared with the condition without interim pause (Fig. 3 *C* and *F*, *blue* vs. *open circle*). This observation is consistent with the almost full recovery of TRPV1 surface expression at ∼5 min after stimulation of low capsaicin (1 μM, Fig. 2*D*). A 5-min pause also enhanced the whole-cell current over high capsaicin-induced tachyphylaxis (Fig. 3 *D* and *F*, *red* vs. *open square*). Mirroring the partial recovery in TRPV1 expression upon high capsaicin stimulation (10 μM, Fig. 2*D*), the 5-min interim pause was still unable to rescue whole-cell response to pretachyphylaxis level (Fig. 3*F*, *red* vs. *gray*). As corroboration, adding another 5-min pause (10 min, in total) further increased whole-cell current following high capsaicin stimulation (Fig. 3 *E* and *F*, *orange* vs. *red*). Together, these results consolidate that facilitating the recovery in TRPV1 surface expression helps to rescue the whole-cell nociceptive response.

Ca^{2+} Signals During TRPV1 Recycling. As Ca^{2+} signal regulates TRPV1 desensitization (1, 4) and subcellular trafficking (21), we probed the Ca^{2+} kinetics over low and high capsaicin stimulation. Dual-color light-sheet imaging was performed in HEK cells expressing TRPV1-pHluorin and also loaded with a red-fluorescent Ca^{2+} indicator Rhod-2, AM (Fig. 4*A*). The absence of their cross-talk was ensured by using spectrally excluded excitation light and band-pass filters (*SI Appendix*, Fig. S5*A*), and also validated by imaging cells only harboring a single fluorophore (*SI Appendix*, Fig. S5*B*). We observed over TRPV1 recycling robust Ca^{2+} rises in response to both low and high capsaicin stimulation (Fig. 4*B*). Notably, though the peak amplitude was similar for both stimuli, Ca^{2+} rises evoked by high-dose capsaicin appeared longer-lasting and remained high at 5 min after stimulation (Fig. 4*C*), corresponding to sustained loss in TRPV1 surface expression (Fig. 4*D*). Hence, high-dose capsaicin triggers long-lasting Ca^{2+} signal along with delayed recovery of TRPV1 expression.

We also observed that reducing external Ca^{2+} concentration prevented the loss in TRPV1 surface expression in response to high capsaicin (Fig. 4*E*), suggesting the amount of Ca^{2+} influx influences channel recycling. To evaluate directly the amount of Ca^{2+} influx triggered by low- and high-dose capsaicin, we blocked the internal Ca^{2+} buffering process by inhibiting endoplasmic reticulum Ca^{2+} ATPase with thapsigargin (22). In this condition, high-dose capsaicin was found to evoke a higher amount of Ca^{2+} influx than low-dose capsaicin (Fig. 4*F*; $dF/F_0 = 0.86 \pm 0.06$ for 10 Cap vs. 0.69 ± 0.05 for 1 Cap, $n = 8$ cells for each condition, $P < 0.05$). The slow recovery in high capsaicin-induced Ca^{2+} signal could also be a reduction in the efflux of Ca^{2+} from the cell. We therefore examined the activity of Na^+/Ca^{2+} exchanger (NCX), a principal pathway for activity-gated Ca^{2+} export powered by Na^+ gradient across the plasma membrane (23). Inhibiting NCX upon capsaicin stimulation would unmask its operating activity as reflected by the slowing down in Ca^{2+} recovery rate. Inactivating NCX by omitting external Na^+ [replaced by *N*-methyl-D-glucamine$^+$ ($NMDG^+$)] delayed Ca^{2+} recovery in response to both low and high capsaicin stimulation, yet in the latter condition the recovery phase was less affected (Fig. 4*G*; reduction in declining rate, 0.008 ± 0.002 dF/F_0/min for 10 Cap, vs. 0.013 ± 0.003 dF/F_0/min for 1 Cap vs.; $n = 7$ cells for each condition, $P < 0.05$). This observation suggests that the operating activity of NCX is compromised upon high capsaicin challenge, which together with the greater amount of Ca^{2+} influx, contributes to the delayed recovery in evoked Ca^{2+} signals.

Synaptotagmin Regulation of TRPV1 Recycling. To understand the mechanism underlying Ca^{2+}-regulated TRPV1 recycling over tachyphylaxis induction, we studied the role of synaptotagmin

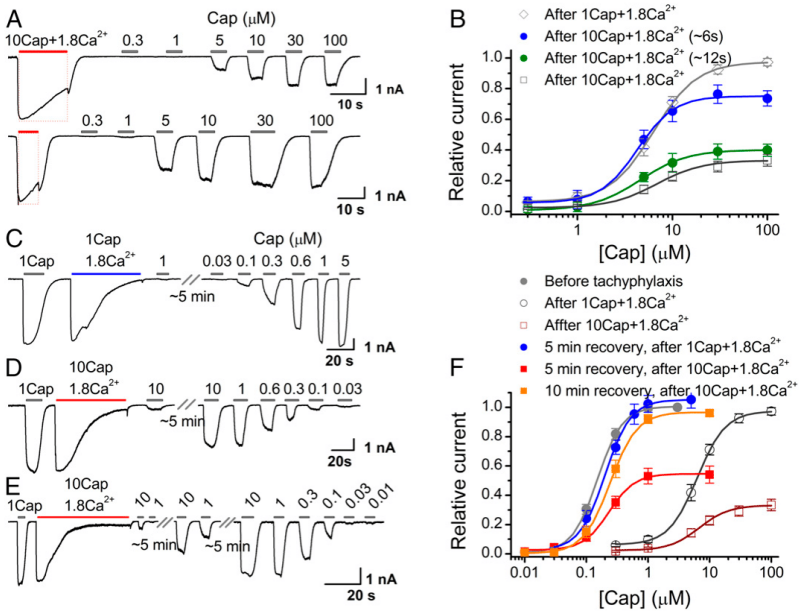

Fig. 3. Interim pause facilitates the restoration of whole-cell TRPV1 currents. (*A*) Whole-cell recording of a TRPV1-expressing HEK 293 cell. Desensitization was induced by 10 μM capsaicin (1.8 mM Ca^{2+}) over shorter periods (12 s, *Top*; 6 s, *Bottom*). (*B*) Dose–response curves of whole-cell currents during tachyphylaxis period. Data from briefer stimulation are compared with those obtained after normal stimulation durations (~60 s, gray traces). (*C*) After tachyphylaxis induced by 1 μM capsaicin, current was hardly triggered by similar stimulation. A 5-min pause helped the recovery of whole-cell current to the pretachyphylaxis level. (*D*) Facilitating effect of interim pause seen for 10 μM capsaicin-evoked desensitization. The facilitation was further enhanced by a longer pause period (5 min + 5 min; *E*). (*F*) Dose–response curves of whole-cell TRPV1 currents of different conditions, normalized to their initial reference current. Solid lines are fits to the Hill equation (n = 6–10 cells for each condition). The pipette solution contained 3 mM Na_2ATP and 3 mM Mg ATP. Error bars, SEM.

(Syt) proteins that serve as Ca^{2+} sensors in subcellular trafficking (24). Syt1 and Syt9 have been shown to interact with TRPV1 at the protein level by coimmunoprecipitation (co-IP) (18). We confirmed this result (Fig. 5*A*), and further found that Syt9 showed little effect on whole-cell TRPV1 responses during tachyphylaxis (*SI Appendix*, Fig. S6 *A* and *B*). Expression of Syt1 together with TRPV1 in HEK cells, albeit still leaving unchanged tachyphylaxis responses induced by high capsaicin (10 μM), facilitated the current recovery for low capsaicin-induced tachyphylaxis (1 μM, Fig. 5 *B* and *C*, *light blue* vs. *gray circle*). This effect was prevented when mutating Syt1 to inactivate its Ca^{2+}-binding site [Syt1(4D/N)] (25) (Fig. 5*C*). Moreover, light-sheet imaging revealed a facilitating effect of Syt1 on TRPV1 expression recovery following 1 μM, but not 10 μM capsaicin stimulation (Fig. 5 *D* and *H*). These results suggest that Syt1 regulates fast TRPV1 recycling as triggered by low-dose capsaicin, while playing a marginal role in the slow recycling process following high capsaicin stimulation. This resembles the established role of Syt1 in regulating fast exocytosis near the plasma membrane (24). We also noted that Syt1 was preferentially expressed on cell surface (*SI Appendix*, Fig. S7), suggesting the subplasmalemmal occurrence of fast TRPV1 recycling.

Strong stimulation has been found to trap TRPV1 channels in intracellular endosomal and lysosomal networks (19). We observed a delayed recycling of TRPV1 upon high-dose capsaicin stimulation, which possibly involves the traveling through cytosolic compartments. Among Syt proteins, Syt7 orchestrates the trafficking and fusion of endosomal and lysosomal compartments (26, 27). We found that though not directly interacting with TRPV1 (Fig. 5*E*), Syt7 expression inhibited the recovery of whole-cell TRPV1 current during high capsaicin-induced tachyphylaxis (Fig. 5 *F* and *G*, *light red* vs. *gray triangle*). This effect was abolished by inactivating the Ca^{2+}-binding site [Syt7 (4D/N)] (Fig. 5*G*), and not seen with the Ca^{2+}-insensitive Syt4 (28) (Fig. 5*E* and *SI Appendix*, Fig. S6 *C* and *D*). In contrast, Syt7 showed a marginal effect on the desensitization responses evoked by low-dose capsaicin (Fig. 5*G*). Light-sheet imaging showed that Syt7 selectively inhibited TRPV1 recycling upon high (10 μM), but not low (1 μM) capsaicin stimulation (Fig. 5*H* vs. Fig. 5*D*). Given the role of Syt7 in endosomal and lysosomal trafficking, our results likely reflect that Syt7 via enhancing interorganelle fusion hindered the targeted redelivery of TRPV1 to the plasma membrane. Also distinct from Syt1, Syt7 was expressed throughout cell cytoplasm, compatible with its role in intracellular trafficking (*SI Appendix*, Fig. S7). Together, these results suggest that Syt7 regulates slow TRPV1 recycling during high capsaicin-induced tachyphylaxis.

Discussion

Tachyphylaxis is therapeutically relevant for pain treatment, in conditions barely tractable by conventional analgesics (3, 29). We show here that stimulation strength shapes the extent of whole-cell tachyphylaxis, as modulated by TRPV1 recycling (*SI Appendix*, Fig. S8). The observation that a persistent reduction in TRPV1 responses requires high-intensity stimuli provides a mechanistic basis for the need of large-dose capsaicin in tackling neuropathic pains (29). Exocytic insertion of TRPV1 has been suggested to tune channel expression levels in a Ca^{2+}- and SNARE-dependent manner (1, 11, 13, 18, 30–32). Relatively,

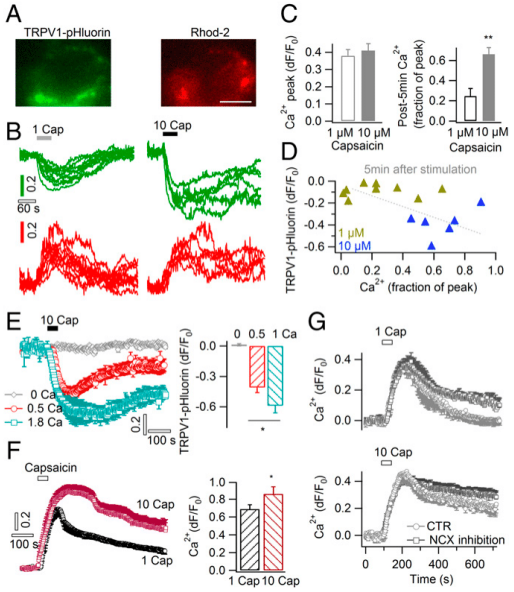

Fig. 4. Ca^{2+} signals during stimulation strength-gated TRPV1 recycling. (*A*) Representative images of HEK 293 cells expressing TRPV1-pHluorin and loaded with the red Ca^{2+} dye Rhod-2, AM. (*B*) Fluorescence time courses of TRPV1-pHluorin and Rhod-2 in response to 1 μM and 10 μM capsaicin, respectively. A single trace denotes an individual cell, and fluorescence change is expressed as dF/F_0. (*C*) Peak amplitude of Ca^{2+} signals and the Ca^{2+} levels at 5 min after the stimulation onset (n = 9 for 1 μM, 6 for 10 μM capsaicin). (*D*) Scatter plot showing the apparent loss in TRPV1 surface expression against the corresponding Ca^{2+} levels, both measured at 5min post the stimulation. (*E*) TRPV1-pHluorin recycling triggered by 10 μM capsaicin in different concentrations of Ca^{2+} (n = 6–8 cells for each condition). (*F*) Ca^{2+} signals evoked by 1 μM and 10 μM capsaicin in cells with ER Ca^{2+} ATPase inhibited by thapsigargin (0.5 μM, pretreatment 10 min, n = 8 cells for each condition). (*G*) Differential alteration in the declining phase of low and high capsaicin-evoked Ca^{2+} signals upon NCX inhibition (n = 6–10 cells for each condition). (Scale bar, 10 μm.)

little is known on TRPV1 endocytic retrieval, though steady-state examination a few minutes apart showed intracellular TRPV1 accumulation over capsaicin stimulation (19). Also, previous results were mostly obtained from antibody-based assays in fixed cells or extracted tissues. By light-sheet microscopy and TRPV1-pHluorin, we achieved real-time imaging of TRPV1 recycling at layers away from the cell-coverslip adhesion site. This helps to avoid potential interference of certain adhesive substrates (e.g., polylysine) to TRPV1 activity (12).

We revealed a tunable coupling between TRPV1 endocytosis and exocytosis over strength-memorizing tachyphylaxis. The time scale of TRPV1 endocytosis is comparable to that found for clathrin-mediated endocytosis, in the order of tens to one hundred seconds (33). Activity-gated recycling imposes a net effect on TRPV1 surface expression, whereby whole-cell responses over tachyphylaxis. Recent study by total internal reflection fluorescence microscopy reveals that mobile TRPV1 in the plasma membrane becomes abruptly static upon activation (34), implying a preceding step to confine TRPV1 on endocytic sites for intracellular translocation. Fluorescence resonance energy transfer unveiled TRPV1 in subplasmalemmal caveolar structures (35), suggesting their implication in channel endocytosis.

The present TRPV1-pHluorin labeling does not appear as an idea ring on the cell surface, likely because the light sheet has a thickness in the order of several microns and still collects certain amount of out-of-focus fluorescence. Also, pHluorin could be weakly fluorescent in organelles with moderate acidic levels (e.g.,

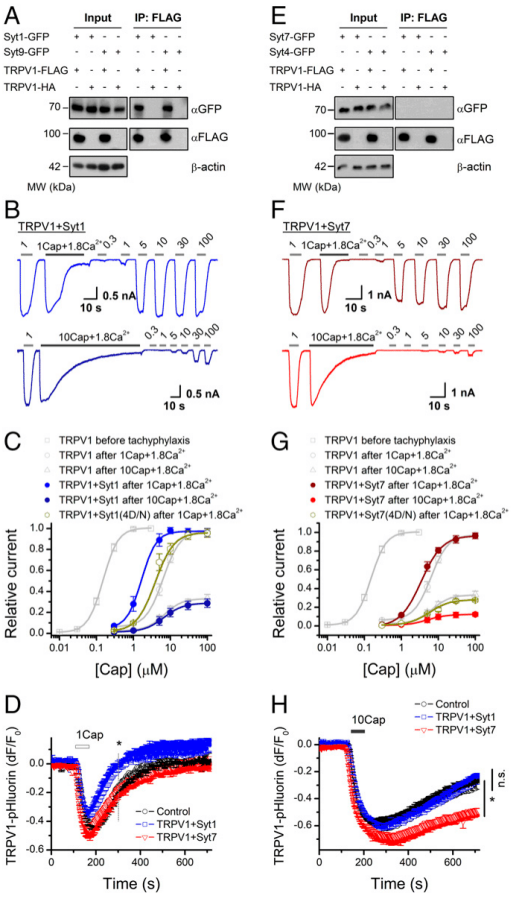

Fig. 5. Synaptotagmin regulation of TRPV1 recycling. (*A*) Interaction of Syt1 and Syt9 with TRPV1. Immunoprecipitation (IP, with anti-FLAG) and immunoblot analysis (with anti-FLAG and anti-GFP) of HEK 293 cells transfected with plasmids as indicated. Molecular weight standards (MW, in kDa) are shown on the left. (*B*) Whole-cell currents in HEK cells coexpressing TRPV1 and Syt1 in response to 1 μM and 10 μM capsaicin, respectively. (*C*) Pooled dose–response curves showing Syt1 facilitation of current recovery during 1 μM capsaicin-induced tachyphylaxis (*blue* vs. *gray open circle*, n = 6–7 cells for each condition; solid lines are fitting by Hill equation). Gray traces are without Syt1. (*D*) Low capsaicin-evoked TRPV1 recycling was facilitated by Syt1, but not by Syt7 (n = 8–10 cells for each condition). TRPV1-pHluorin and red fluorescent Syt1-tdTomato were coexpressed in HEK cells, with the absence of cross-talk verified (*SI Appendix*, Figs. S5 and S7). (*E–G*) Parallel experiments to examine the interaction of TRPV1 with Syt7 and Syt4, and record their impact on whole-cell TRPV1 currents (n = 6–8 cells for the pooled dose–response curves). (*H*) Light-sheet imaging of TRPV1 recycling upon 10 μM capsaicin stimulation, which was retarded by Syt7 expression (Syt7-tdTomato; n = 9–12 cells for each condition).

~6.3 in endosomes) (36, 37), thereby adding background signals to TRPV1-pHluorin imaging. We detected barely the recovery in TRPV1-pHluorin fluorescence upon high capsaicin stimulation in DRG neurons. It is possible that transfection of TRPV1-pHluorin in neurons may not fully substitute endogenous TRPV1 channels. Their interaction with regulatory proteins for subcellular trafficking (e.g., SNAREs and synaptotagmins) might also be tighter than TRPV1-pHluorin, which to some extent compromises the recycling rate of TRPV1-pHluorin.

Distinct Ca^{2+} signals were found during tachyphylaxis induction and TRPV1 recycling. High-dose capsaicin triggered relatively greater Ca^{2+} influx, reminiscent of TRPV1 pore dilation that is suggested to augment channel conductance and alter ion selectivity upon strong stimulation (38) (but see ref. 39). The effect of high-dose capsaicin on NCX Ca^{2+} export could be due to the possible disturbance of capsaicin, as a lipophilic molecule (2), to the local lipid environment of NCX, a factor known to alter its activity (40). In relaying Ca^{2+} signals to subcellular trafficking, members of Syt protein family behave as Ca^{2+} sensors (24). We show intriguingly that Syt1 and Syt7 regulate the fast and slow TRPV1 recycling, respectively, in a condition-specific manner. Thus, different trafficking routes are recruited by stimuli of varied strengths to regulate whole-cell TRPV1 tachyphylaxis (*SI Appendix*, Fig. S8). This finding also suggests the influence of Ca^{2+} on TRPV1 trafficking going beyond the subplasmalemmal zone.

Materials and Methods

The wild-type rat TRPV1 cDNA was generously provided by Dr. Feng Qin (State University of New York at Buffalo). TRPV1-615-pHluorin GFP (Insertion of pHluorin GFP gene after No. 614 residue of TRPV1) was made using the overlap-extension PCR method as previously described (41). Patch-clamp recordings were made in whole-cell configuration using an EPC10 amplifier (HEKA). Light-sheet imaging was performed using a wide-field upright microscope (Zeiss Axioskop 50) and an independent optical module (Alpha3 light sheet add-on, Zeiss EC EPIPlan ×10, 0.25NA) (*SI Appendix*, Fig. S2*A*). Detailed methods are provided in *SI Appendix*.

ACKNOWLEDGMENTS. We thank Steve Didienne for fabricating imaging accessories, and Dr. Luna Gao, Mr. Yifu Han, and our colleagues for comments and discussions. We also sincerely thank Dr. Sheela Vyas for her critical reading of the manuscript. This work was supported by the National Natural Science Foundation of China (Grants 31628005, 31830031, 31671209, 31871174, 31601864, and 31728014), National Basic Research Program of China (Grant 2014CB910304), Natural Science Foundation of Hubei Province (Grants 2017CFA063 and 2018CFA016), Fundamental Research Funds for the Central Universities (Grants 2042017KF0242 and 2042017KF0199), and CAS Key Laboratory of Receptor Research (Grant SIMM1804YKF-02). The work was also supported in part by Agence Nationale de la Recherche (Grant NUTRIPATHOS, ANR-15-CE14-0030, France).

1. Planells-Cases R, Valente P, Ferrer-Montiel A, Qin F, Szallasi A (2011) Complex regulation of TRPV1 and related thermo-TRPs: Implications for therapeutic intervention. *Adv Exp Med Biol* 704:491–515.
2. Morales-Lázaro SL, Simon SA, Rosenbaum T (2013) The role of endogenous molecules in modulating pain through transient receptor potential vanilloid 1 (TRPV1). *J Physiol* 591:3109–3121.
3. Touska F, Marsakova L, Teisinger J, Vlachova V (2011) A "cute" desensitization of TRPV1. *Curr Pharm Biotechnol* 12:122–129.
4. Vyklický L, et al. (2008) Calcium-dependent desensitization of vanilloid receptor TRPV1: A mechanism possibly involved in analgesia induced by topical application of capsaicin. *Physiol Res* 57:S59–S68.
5. Knotkova H, Pappagallo M, Szallasi A (2008) Capsaicin (TRPV1 agonist) therapy for pain relief: Farewell or revival? *Clin J Pain* 24:142–154.
6. Szolcsányi J (2014) Capsaicin and sensory neurones: A historical perspective. *Prog Drug Res* 68:1–37.
7. Mohapatra DP, Nau C (2005) Regulation of Ca2+-dependent desensitization in the vanilloid receptor TRPV1 by calcineurin and cAMP-dependent protein kinase. *J Biol Chem* 280:13424–13432.
8. Lishko PV, Procko E, Jin X, Phelps CB, Gaudet R (2007) The ankyrin repeats of TRPV1 bind multiple ligands and modulate channel sensitivity. *Neuron* 54:905–918.
9. Yao J, Qin F (2009) Interaction with phosphoinositides confers adaptation onto the TRPV1 pain receptor. *PLoS Biol* 7:e46.
10. Bhave G, et al. (2002) cAMP-dependent protein kinase regulates desensitization of the capsaicin receptor (VR1) by direct phosphorylation. *Neuron* 35:721–731.
11. Camprubí-Robles M, Planells-Cases R, Ferrer-Montiel A (2009) Differential contribution of SNARE-dependent exocytosis to inflammatory potentiation of TRPV1 in nociceptors. *FASEB J* 23:3722–3733.
12. Stein AT, Ufret-Vincenty CA, Hua L, Santana LF, Gordon SE (2006) Phosphoinositide 3-kinase binds to TRPV1 and mediates NGF-stimulated TRPV1 trafficking to the plasma membrane. *J Gen Physiol* 128:509–522.
13. Devesa I, et al. (2014) αCGRP is essential for algesic exocytotic mobilization of TRPV1 channels in peptidergic nociceptors. *Proc Natl Acad Sci USA* 111:18345–18350.
14. Ferrandiz-Huertas C, Mathivanan S, Wolf CJ, Devesa I, Ferrer-Montiel A (2014) Trafficking of thermoTRP channels. *Membranes (Basel)* 4:525–564.
15. Burrone J, Li Z, Murthy VN (2006) Studying vesicle cycling in presynaptic terminals using the genetically encoded probe synaptopHluorin. *Nat Protoc* 1:2970–2978.
16. Power RM, Huisken J (2017) A guide to light-sheet fluorescence microscopy for multiscale imaging. *Nat Methods* 14:360–373.
17. Heuser JE, Anderson RG (1989) Hypertonic media inhibit receptor-mediated endocytosis by blocking clathrin-coated pit formation. *J Cell Biol* 108:389–400.
18. Morenilla-Palao C, Planells-Cases R, García-Sanz N, Ferrer-Montiel A (2004) Regulated exocytosis contributes to protein kinase C potentiation of vanilloid receptor activity. *J Biol Chem* 279:25665–25672.
19. Sanz-Salvador L, Andrés-Borderia A, Ferrer-Montiel A, Planells-Cases R (2012) Agonist- and Ca2+-dependent desensitization of TRPV1 channel targets the receptor to lysosomes for degradation. *J Biol Chem* 287:19462–19471.
20. Jordt SE, Tominaga M, Julius D (2000) Acid potentiation of the capsaicin receptor determined by a key extracellular site. *Proc Natl Acad Sci USA* 97:8134–8139.
21. Vogel SS (2009) Channeling calcium: A shared mechanism for exocytosis-endocytosis coupling. *Sci Signal* 2:pe80.
22. Brini M, Carafoli E (2009) Calcium pumps in health and disease. *Physiol Rev* 89:1341–1378.
23. Blaustein MP, Lederer WJ (1999) Sodium/calcium exchange: Its physiological implications. *Physiol Rev* 79:763–854.
24. Südhof TC (2002) Synaptotagmins: Why so many? *J Biol Chem* 277:7629–7632.
25. Lee J, Guan Z, Akbergenova Y, Littleton JT (2013) Genetic analysis of synaptotagmin C2 domain specificity in regulating spontaneous and evoked neurotransmitter release. *J Neurosci* 33:187–200.
26. Trajkovic K, Jeong H, Krainc D (2017) Mutant huntingtin is secreted via a late endosomal/lysosomal unconventional secretory pathway. *J Neurosci* 37:9000–9012.
27. Volynski KE, Krishnakumar SS (2018) Synergistic control of neurotransmitter release by different members of the synaptotagmin family. *Curr Opin Neurobiol* 51:154–162.
28. Dai H, et al. (2004) Structural basis for the evolutionary inactivation of Ca^{2+} binding to synaptotagmin 4. *Nat Struct Mol Biol* 11:844–849.
29. Robbins WR, et al. (1998) Treatment of intractable pain with topical large-dose capsaicin: Preliminary report. *Anesth Analg* 86:579–583.
30. Chuang HH, et al. (2001) Bradykinin and nerve growth factor release the capsaicin receptor from PtdIns(4,5)P2-mediated inhibition. *Nature* 411:957–962.
31. Zhang X, Huang J, McNaughton PA (2005) NGF rapidly increases membrane expression of TRPV1 heat-gated ion channels. *EMBO J* 24:4211–4223.
32. Meng J, Wang J, Steinhoff M, Dolly JO (2016) TNFα induces co-trafficking of TRPV1/TRPA1 in VAMP1-containing vesicles to the plasmalemma via Munc18-1/syntaxin1/SNAP-25 mediated fusion. *Sci Rep* 6:21226.
33. He K, et al. (2017) Dynamics of phosphoinositide conversion in clathrin-mediated endocytic traffic. *Nature* 552:410–414.
34. Senning EN, Gordon SE (2015) Activity and Ca^{2+} regulate the mobility of TRPV1 channels in the plasma membrane of sensory neurons. *eLife* 4:e03819.
35. Storti B, Di Rienzo C, Cardarelli F, Bizzarri R, Beltram F (2015) Unveiling TRPV1 spatiotemporal organization in live cell membranes. *PLoS One* 10:e0116900.
36. Sankaranarayanan S, De Angelis D, Rothman JE, Ryan TA (2000) The use of pHluorins for optical measurements of presynaptic activity. *Biophys J* 79:2199–2208.
37. Casey JR, Grinstein S, Orlowski J (2010) Sensors and regulators of intracellular pH. *Nat Rev Mol Cell Biol* 11:50–61.
38. Chung MK, Güler AD, Caterina MJ (2008) TRPV1 shows dynamic ionic selectivity during agonist stimulation. *Nat Neurosci* 11:555–564.
39. Li M, Toombes GE, Silberberg SD, Swartz KJ (2015) Physical basis of apparent pore dilation of ATP-activated P2X receptor channels. *Nat Neurosci* 18:1577–1583.
40. Philipson KD, Ward R (1985) Effects of fatty acids on Na+-Ca2+ exchange and Ca2+ permeability of cardiac sarcolemmal vesicles. *J Biol Chem* 260:9666–9671.
41. Yao J, Liu B, Qin F (2011) Modular thermal sensors in temperature-gated transient receptor potential (TRP) channels. *Proc Natl Acad Sci USA* 108:11109–11114.
42. Samways DS, Egan TM (2011) Calcium-dependent decrease in the single-channel conductance of TRPV1. *Pflugers Arch* 462:681–691.

Supporting Information

Recovery from tachyphylaxis of TRPV1 coincides with recycling to the surface membrane

Quan Tian, Juan Hu, Chang Xie, Kaidi Mei, Cuong Pham, Xiaoyi Mo, Régine Hepp, Sylvia Soares, Fatiha Nothias, Yuanyuan Wang, Qiang Liu, Fen Cai, Bo Zhong, Dongdong Li, Jing Yao

SI Materials and Methods

Expression constructs and transfection in HEK 293 cells. The wild-type rat TRPV1 cDNA was generously provided by Dr. Feng Qin (State University of New York at Buffalo, Buffalo). Enhanced green fluorescent protein (EGFP)-TRPV1 and TRPV1-615-pHluorin GFP (Insertion of pHluorin gene after No. 614 residue of TRPV1) were made using the overlap-extension polymerase chain reaction (PCR) method as previously described (1). Synaptotagmin 1 (Syt1) and Syt9 were kindly provided by Dr. Zhengxing Wu (Huazhong University of Science and Technology), and Syt4 and Syt7 by Dr. Liangyi Chen (Peking University). DNAs encoding Syt1 (D230N, D232N, D363N, and D365N) and Syt7 (D225N, D227N, D357N, and D359N), represented by Syt1(4D/N) and Syt7(4D/N) respectively, were made by standard overlap-extension PCR. All recombinant constructs were verified by DNA sequencing. HEK 293 cells were grown in Dulbecco's modified Eagle's medium (DMEM, Thermo Fisher Scientific, MA, USA) containing 4.5 mg/ml glucose, 10% heat-inactivated fetal bovine serum (FBS), 50 units/ml penicillin, and 50 μg/ml streptomycin, and were incubated at 37 °C in a humidified incubator gassed with 5% CO_2. Cells at a confluence of ~80% were transfected with the desired DNA constructs using calcium phosphate precipitation method as described previously (1). Transfected HEK 293 cells were reseeded on 12 mm round glass coverslips coated by poly-L-lysine. Experiments took place ~12-24 h after transfection.

Isolation of dorsal root ganglion (DRG) neurons. The animal protocol used in this study was approved by the Institutional Animal Care and Use Committee of Wuhan University, and in accordance with European Community guiding principles on the care and use of animals (86/609/CEE). Primary culture of DRG neurons were prepared as previously described with minor modification for imaging (2), and for electrophysiology (3). Taking the latter as an example, briefly, six to eight-week-old adult C57 male mice were deeply anaesthetized and decapitated. DRGs, together with dorsal-ventral roots and attached spinal nerves were taken out from the spinal column. After removing the attached nerves and surrounding connective tissues, about 10-14 DRGs from thoracic and lumbar segments of spinal cords were rapidly dissected and cleaned in Ca^{2+}/Mg^{2+}-free Hank's balanced salt solution (HBSS). Ganglia were dissociated by enzymatic treatment with collagenase type IA (1 mg/ml), trypsin (0.4 mg/ml) and DNase I (0.1 mg/ml) and incubated at 37 ˚C for 40 min. Gentle mechanical trituration were performed every 10 min through fire-polished glass pipettes until solution became cloudy. The resulting suspension of single cells was

www.pnas.org/cgi/doi/10.1073/pnas.1819635116

collected by centrifuge. Then cells were seeded onto poly-L-lysine–coated coverslips, maintained in DMEM (Gibco, Thermo Fisher Scientific, MA, USA) containing 10% heat-inactivated fetal bovine serum (FBS, Gibco, Thermo Fisher Scientific) and 1% penicillin/streptomycin, and cultured at 37 °C in a humidified incubator with 5% CO_2. Patch-clamp recordings were carried out ~12–24 hrs after plating. TRPV1-pHluorin was transfected into DRG neurons with Lipofectamine 2000 (Invitrogen) following the protocol provided by the manufacturer.

Electrophysiology. Patch-clamp recordings were made in whole-cell configuration. For the recombinant expressing system, green fluorescent EGFP was used as a marker for gene expression. Recording pipettes were pulled from borosilicate glass capillaries (World Precision Instruments), and fire-polished to a resistance between 2–4 MΩ when filled with internal solution containing (in mM) 140 CsCl, 2.0 $MgCl_2$, 5 EGTA, 10 HEPES, pH 7.4 (adjusted with CsOH). The zero Ca^{2+} bath solution for whole-cell recording from HEK 293 cells contained (in mM): 140 NaCl, 5 KCl, 3 EGTA, and 10 HEPES, pH 7.4 adjusted with NaOH. The control solution containing physiological 1.8 mM Ca^{2+} contained (mM): 140 NaCl, 5 KCl, 1.8 $CaCl_2$, and 10 HEPES, pH 7.4 (adjusted with NaOH). For recording in DRG neurons, the bath solution contained the following (in mM): 140 NaCl, 5 KCl, 2 $MgCl_2$, 2 $CaCl_2$, 10 glucose, 10 HEPES, pH 7.4 adjusted with NaOH and the pipette solution contained (in mM): 140 CsCl, 5 EGTA, and 10 HEPES, pH 7.3 adjusted with CsOH. Na^+/Ca^{2+} exchanger was inhibited by the bath solution of zero Na^+, in which Na^+ was replaced by an equal molar amount of N-methyl-D-glucamine (NMDG), with osmolarity and pH controlled to match the control bath solution. Isolated cells were voltage clamped in the whole-cell mode using an EPC10 amplifier (HEKA, Lambrecht, Germany). Voltage commands were made from the Patchmaster program. For a subset of recordings, currents were amplified using an Axopatch 200B amplifier (Molecular Devices, Sunnyvale, CA) and recorded through a BNC-2090/MIO acquisition system (National Instruments, Austin, TX) using a homemade program, QStudio developed by Dr. Feng Qin at State University of New York at Buffalo. Whole-cell recordings were typically sampled at 5 kHz and filtered at 1 kHz. Exchange of external solutions was performed using a gravity-driven local perfusion system. As determined by the conductance tests, the solution around a patch under study was fully controlled by the application of a solution with a flow rate of 100 µl/min or greater. Capsaicin or capsazepine were dissolved in pure ethanol to make a stock solution. All the stocks were diluted in the bath solution to the desired concentrations right before the experiment. The final concentrations of ethanol did not exceed 0.3%, which had no effect on the currents. Unless otherwise noted, all chemicals were purchased from Sigma (Millipore Sigma, St. Louis, MO). All patch-clamp recordings were made at room temperature (22-24 °C).

Imaging and fluorophores. Light-sheet imaging was performed based on a wide-field upright microscope (Zeiss Axioskop 50, Germany) equipped with water-immersion objectives. Epifluorescence excitation from a monochromator light source (Polychrome II, TILL Photonics, Germany) was coupled to the imaging objective via an optical fiber. The fluorescence signal was collected using a digital electron-multiplying charge-coupled device (EMCCD Cascade 512B, Photometrics).

The in-focus light-sheet was generated from a 473-nm or a 561-nm DPSS laser

(CNI, China), coupled via a wavelength combiner (Thorlabs) to an independent optical module (Alpha3 light sheet add-on, Phaseview, France), that was orthogonally positioned and equipped with an air objective (Zeiss EC EPIPlan ×10, 0.25NA) (Fig. S2*B*). The center thickness of the light sheet was estimated in the order of 1-2 μm (4):

$$\omega = \frac{2\lambda}{\pi NA^2} \qquad (1)$$

where λ is the wavelength of the excitation light, and NA the numerical aperture of the excitation objective. A chamber for light-sheet excitation was designed using 3D modeling program (Trimble SketchUP; Fig. S2*B*), with a dimension (mm): 20 wide × 30 high × 46 long. It was constructed by a Mojo 3D printer (STRATASYS, USA) using acrylonitrile butadiene styrene material and the fused deposition modeling procedure at 100-μm *z*-step. Two 22×22 mm glass coverslips (#1, Erie Science Company, USA) were glued (Dow Corning GmbH, Germany) to each side of the chamber thereby enabling the lateral illumination of the cells by light sheet. The chamber was mounted on a motorized PI translation stage (Physik Instrumente GmbH, Germany) driven by computer. Laser excitation and image acquisition were controlled by MetaMorph (Molecular Devices, USA).

The red-fluorescent Ca^{2+} indicator Rhod-2, AM (FluoProbes) was dissolved in Pluronic F-127 (20%) DMSO solution to prepare the stock solution. To load the Ca^{2+} indicator into HEK 293 cells and DRG neurons, they were incubated in the extracellular solution containing a final concentration of 1 μM Rhod-2, AM, for 10 min. Then, cells were continuously washed with dye-free solution for at least 30 min prior to imaging. To simultaneously image TRPV1-pHluorin trafficking and cytosolic Ca^{2+} signals, we used dual-excitation (473-nm and 561-nm laser lines) and dual-emission protocol, with a double-band dichroic (Semrock Di03-R488/561) and emission filter combination (Semrock FF01-523/610) being used (Fig. S5A). The calcium and pHluorin signals were analyzed within the same ring-shape region of interest (ROI), traced along the near-membrane region while excluding the nucleus hole by Image J software (NIH).

Co-immunoprecipitation and immunoblot. Denaturing immunoprecipitations were performed as previously described (5). In brief, cells transfected with the desired plasmids were washed with ice-cold PBS and lysed in Nonidet P-40 lysis buffer containing 150 mM NaCl, 1mM EDTA, 1% Noidet P-40, 1% proteinase and phosphatase inhibitor cocktail (Bimake), and boiled at 95 °C for 15 min. Cell lysates were subjected to SDS-PAGE (sodium dodecyl sulfate-polyacrylamide gel elecgtrophoresis) and immunoblot analysis were performed with corresponding antibodies. For immunoprecipitation assays, the lysates were precipitated with the appropriate antibodies, and the precipitants were washed three times with lysis buffer containing 50 mM Tris–HCl, 150 mM NaCl, 1% TritonX-100, and 500 mM NaCl, followed by immunoblot analysis. Anti-DYKDDDDK tag antibody (mouse, B23102) for testing the expression of FLAG tagged proteins was got from Bimake, anti-GFP antibody (rabbit, HT801), anti-HA antibody (rabbit, E022180) and anti-FLAG antibody (rabbit, RG001060) were purchased from TransGen Biotech, EarthOx Life Sciences and Solarbio, respectively.

Statistics. Electrophysiological data were analyzed offline with Clampfit (Molecular

Devices), IGOR (Wavemetrics, Lake Oswego, OR, USA), SigmaPlot (SPSS Science, Chicago, IL, USA) and OriginPro (OriginLab Corporation, MA, USA). For dose-response analysis, the modified Hill equation was used: Y = A1 + (A2 - A1) / [1 + 10^(logEC_{50} – X)*n_H], in which EC_{50} is the half maximal effective concentration, and n_H is the Hill coefficient. Unless stated otherwise, the data are expressed as mean ± standard error (SEM), from a population of cells (*n*), and *t*-test used for testing the significance of *p* values. Significant difference is indicated by a *p* value less than 0.05 (*$p < 0.05$, **$p < 0.01$).

References

1. Yao, J., Liu, B., and Qin, F. (2011) Modular thermal sensors in temperature-gated transient receptor potential (TRP) channels. *Proc Natl Acad Sci U S A* 108: 11109-11114.
2. Bouquet, C., Soares, S., von Boxberg, Y., Ravaille-Veron, M., Propst, F., and Nothias, F. (2004) Microtubule-associated protein 1B controls directionality of growth cone migration and axonal branching in regeneration of adult dorsal root ganglia neurons. *J Neurosci* 24: 7204-7213.
3. Zhang, X. Y., Wen, J., Yang, W., Wang, C., Gao, L., Zheng, L. H., Wang, T., Ran, K., Li, Y., Li, X., Xu, M., Luo, J., Feng, S., Ma, X., Ma, H., Chai, Z., Zhou, Z., Yao, J., Zhang, X., and Liu, J. Y. (2013) Gain-of-function mutations in SCN11A cause familial episodic pain. *Am J Hum Genet* 93: 957-966.
4. Power, R. M., and Huisken, J. (2017) A guide to light-sheet fluorescence microscopy for multiscale imaging. *Nat Methods* 14: 360-373.
5. Wang, Y., Gao, Y., Tian, Q., Deng, Q., Zhou, T., Liu, Q., Mei, K., Liu, H., Ma, R., Ding, Y., Rong, W., Cheng, J., Yao, J., Xu, T. L., Zhu, M. X., and Li, Y. (2018) TRPV1 SUMOylation regulates nociceptive signaling in models of inflammatory pain. *Nat Commun* 9: 1529.

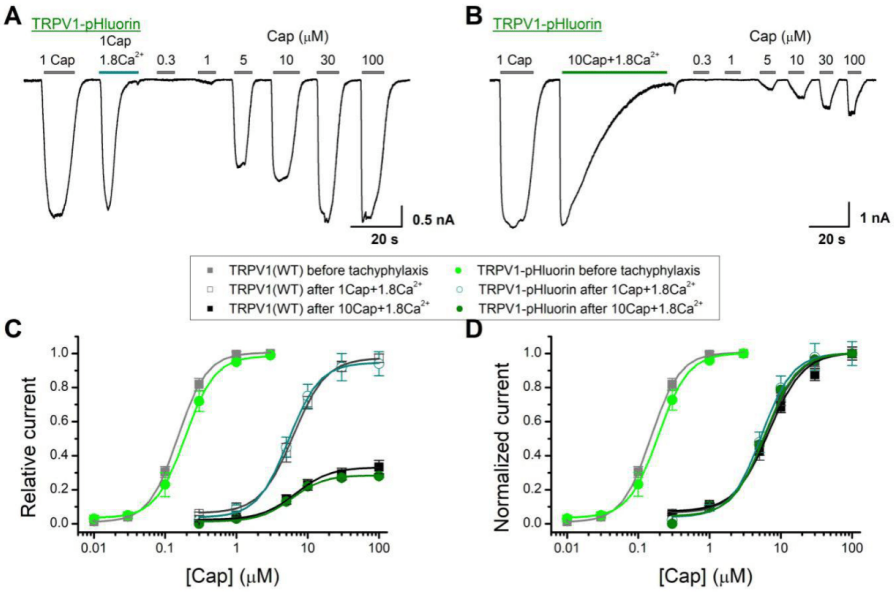

Fig. S1. TRPV1-pHluorin displays identical functional properties to wild-type TRPV1. (*A*-*B*) Tachyphylaxis induced by 1 μM and 10 μM capsaicin, respectively. Whole-cell recordings were made at V_h = -60 mV from HEK 293 cells transfected with TRPV1-pHluorin. Cells were bathed in Ca^{2+}-free solution, and the pipette solution contained no ATP. (*C*) Dose-response curves for TRPV1-pHluorin and wild-type TRPV1. Data were normalized to the initial 1 μM capsaicin reference response in each recording. Solid lines are fits to the Hill equation with EC50 = 0.19 ± 0.1 μM and n_H = 2.1 ± 0.1 for TRPV1-pHluorin before tachyphylaxis (*n* = 6), EC50 = 5.9 ± 0.4 μM and n_H = 2.0 ± 0.3 for TRPV1-pHluorin after 1 μM Cap + 1.8 Ca^{2+} stimulation (*n* = 7), and EC50 = 6.0 ± 0.5 μM and n_H = 1.9 ± 0.4 for TRPV1-pHluorin after 10 μM Cap + 1.8 Ca^{2+} stimulation (*n* = 7). For comparison, dose-response curves of wild-type TRPV1 are displayed on gray background. (*D*) The dose-response curves of defined conditions normalized to their intrinsic maximum. All electrophysiological recordings were from transiently transfected HEK 293 cells held at -60 mV. Cap, capsaicin. Error bars represent SEM.

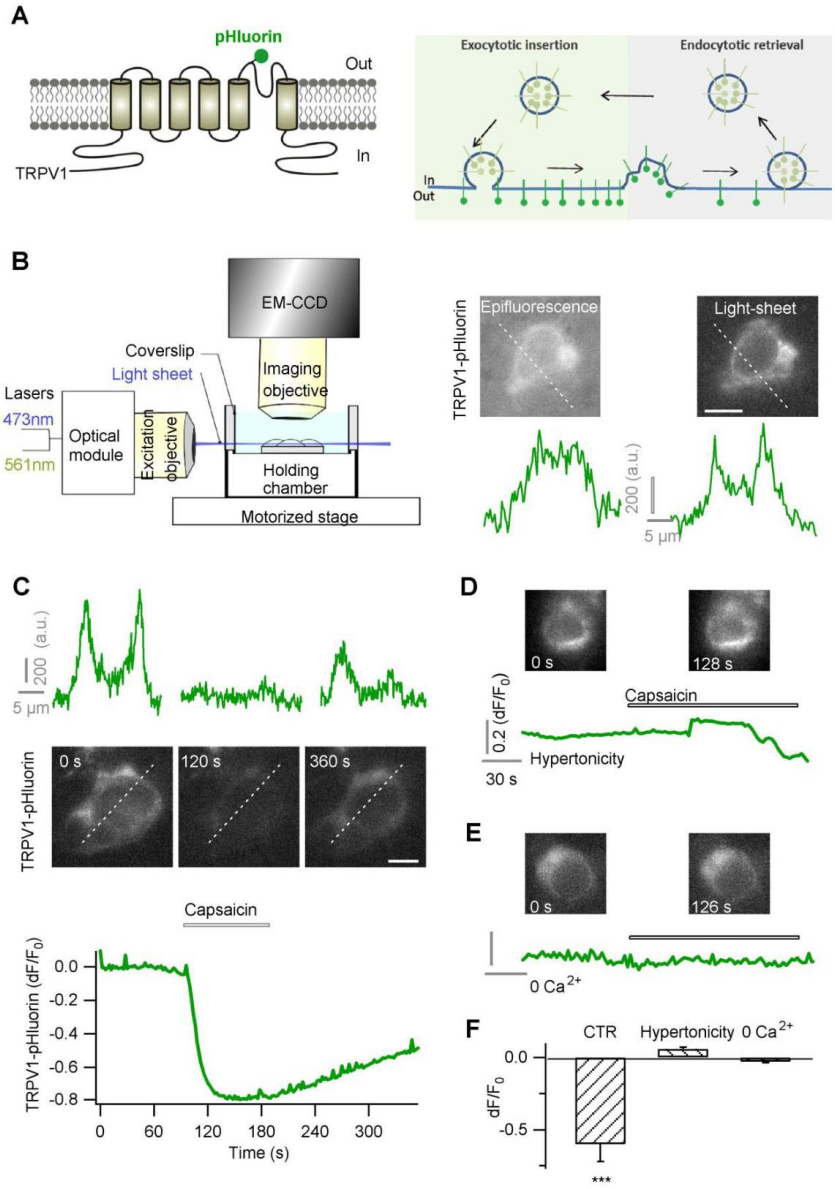

Fig. S2. Imaging TRPV1 exocytosis and endocytosis by TRPV1-pHluorin and light-sheet microscopy. (*A*) Illustration of TRPV1-pHluorin fusion protein. The high pH-dependence of pHluorin fluorescence allows to the dynamic imaging of TRPV1 exocytosis and endocytosis trafficking (right). (*B*) Light-sheet imaging reduces out-of-focus fluorescence and improves image contrast. The optical sectioning was

achieved by orthogonal light sheet generated by converging laser beam through the excitation objective (×10, 0.25NA). Linescan profile is shown for representative epifluorescence and light-sheet image, respectively. (*C*) TRPV1-pHluorin undergoes activity-dependent trafficking. High-dose capsaicin (30 μM) was applied to establish a maximal level of channel trafficking. (*D*) TRPV1-pHluorin endocytosis interfered by hypertonic solution. (*E*) Removing Ca^{2+} from extracellular solution inhibited both the exocytosis and endocytosis of TRPV1-pHluorin. (*F*) Endocytosis-induced TRPV1-pHluorin fluorescence diminution under different conditions, quantified as the drop fraction of the baseline at the time point of 60 s after the start of the stimulation [*n* = 6 cells for control (CTR), 9 cells for hypertonicity, 10 cells for 0 Ca^{2+}]. Scale bars, 10 μm.

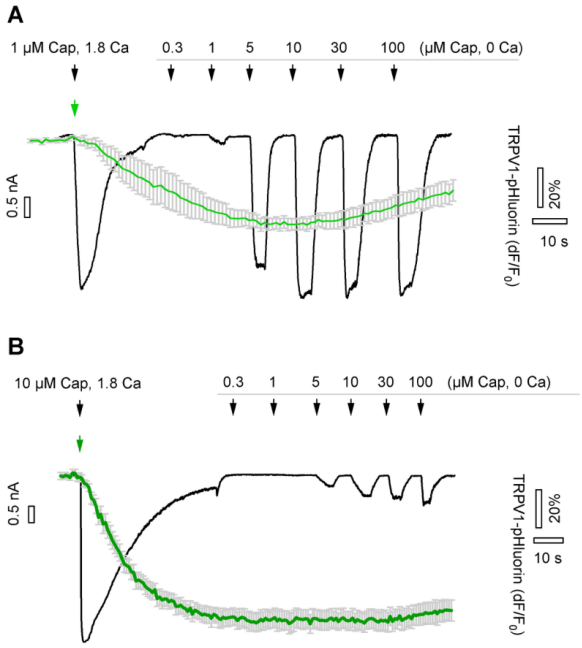

Fig. S3. Time courses of whole-cell currents and activity-gated recycling of TRPV1-pHluorin during tachyphylaxis induction. The typical whole-cell recording of HEK 293 cells expressing TRPV1-pHluorin is counter plotted with its trafficking fluorescence signals (taken from Fig 2), over the same time window. The reduction in whole-cell responses correlates with the extent of loss in TRPV1-pHluorin surface expression, for both 1 μM (A) and 10 μM (B) capsaicin stimulation.

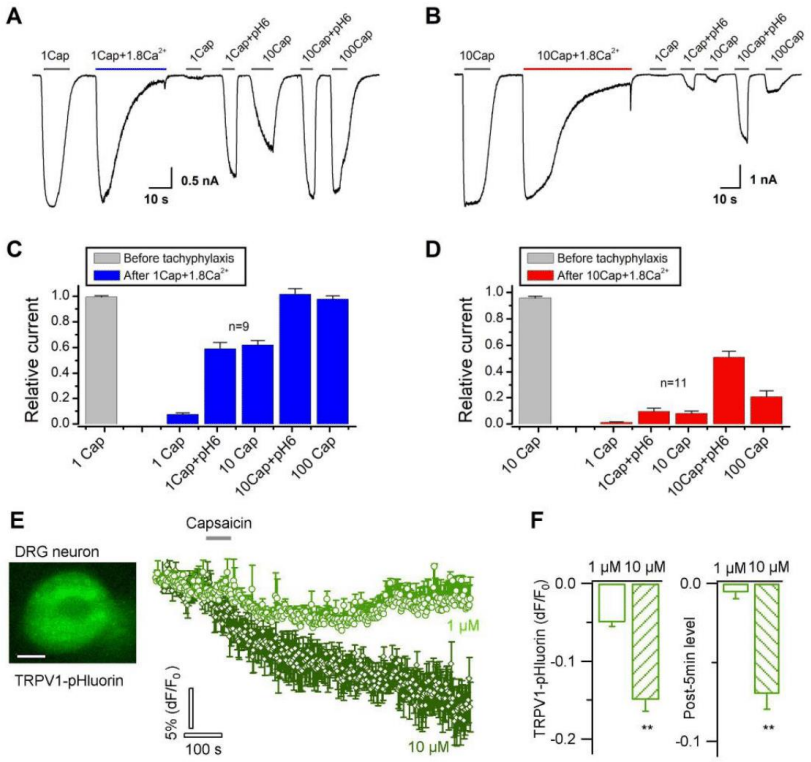

Fig. S4. TRPV1 undergoes strength-memorizing tachyphylaxis in DRG neurons. (*A-B*) Whole-cell currents recorded before (the first current as the reference), during and after 1 μM (*A*) or 10 μM capsaicin (*B*) stimulation with 1.8 mM Ca^{2+}. During high capsaicin-induced tachyphylaxis, stimulations of similar strengths evoked relatively weak whole-cell currents. This confirms the observations made in HEK 293 cells. (*C-D*) Average bars of current peak amplitude. Following tachyphylaxis induced by 1 μM capsaicin and 1.8 mM Ca^{2+} (*C*), 10 μM capsaicin remained to evoke an approximately half-maximum whole-cell current, while 10 μM capsaicin at pH 6 or 100 μM capsaicin gave a robust full maximum response (blue bars), relative to the reference responses obtained in pre-tachyphylaxis condition (gray bar). Yet after 10 μM Cap + 1.8 Ca^{2+} stimulation (*D*), the whole-cell current became not only irresponsive to 1 μM capsaicin but also to 10 μM capsaicin, and only partially responsive to 10 μM capsaicin plus pH 6 (51 ± 5% to the initial 1 μM capsaicin response, *n* = 8), and 100 μM capsaicin (21 ± 5% to the initial 1 μM capsaicin response, *n* = 16). (*E*) Light-sheet imaging of primary mouse DRG neurons expressing TRPV1-pHluorin, challenged by 1 μM (*n* = 6 neurons) and 10 μM capsaicin (*n* = 5 neurons) in the presence of external Ca^{2+} (1.8 mM), respectively. (*F*)

Comparison of capsaicin-induced maximal loss in TRPV1-pHluorin surface expression (*left*), and the TRPV1-pHluorin expression levels at 5 min after stimulation. Scale bar, 10 μm.

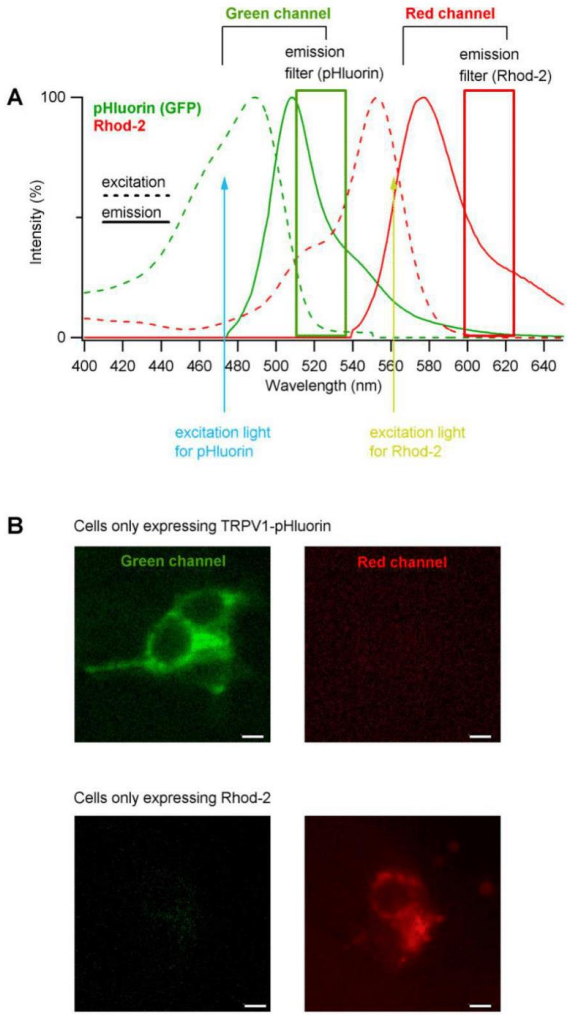

Fig. S5. Cross-talk control for dual-color imaging. (*A*) Filter set selected according to the normalized spectral profiles of GFP (for the pH mutant, pHluorin) and Rhod-2 (Ca^{2+} indicator; both adapted from Thermo Fisher Scientific). (*B*) Experimental validation of the absence of cross-talk for dual-color imaging TRPV1-pHluorin and Rhod-2. In cells expressing only one fluorophore (TRPV1-pHluorin or Rhod-2),

showed no significant cross-talk fluorescence signals to another imaging channel. Scale bars, 10 μm.

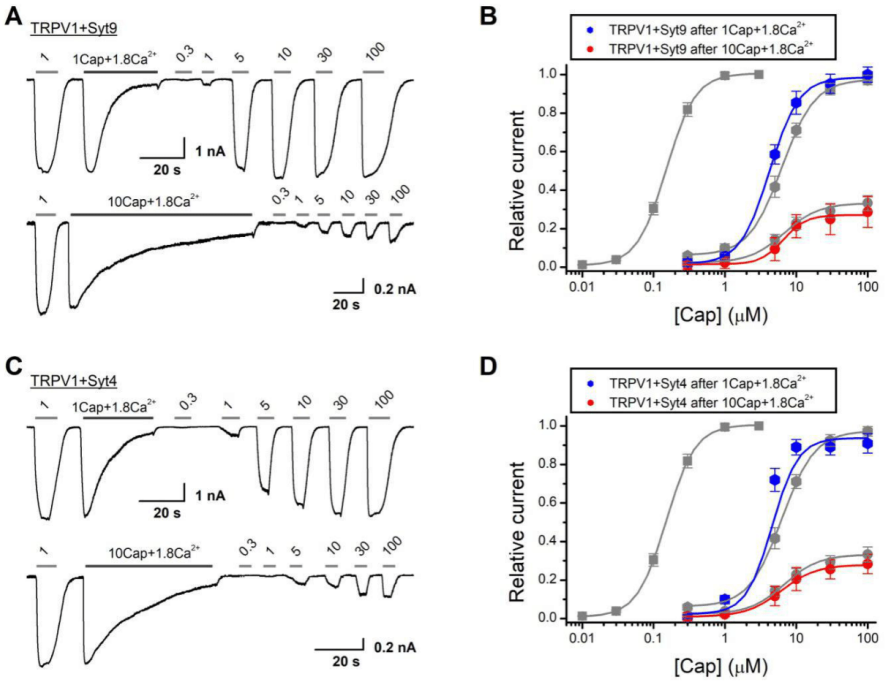

Fig. S6. Neither Syt9 nor Syt4 affects whole-cell current recovery during tachyphylaxis. (*A*) Whole cell recordings were made at V_h = -60 mV from HEK 293 cells transfected with TRPV1 and Syt9, and tachyphylaxis induced by 1 μM or 10 μM capsaicin, in the presence of 1.8 mM Ca^{2+}. (*B*) Dose-response curves with and without Syt9 (*n* = 6 for each). Data were normalized for each cell by its initial response to 1 μM capsaicin. The gray traces are without Syt9, and from left to right represent dose-response curves obtained before tachyphylaxis, during tachyphylaxis induced by 1 μM and 10 μM capsaicin, respectively. (*C* – *D*) Parallel experiments from cells cotransfected with TRPV1 and Syt4, in response to 1 μM (*n* = 6) or 10 μM capsaicin (*n* = 7). Cap, capsaicin. Error bars, SEM.

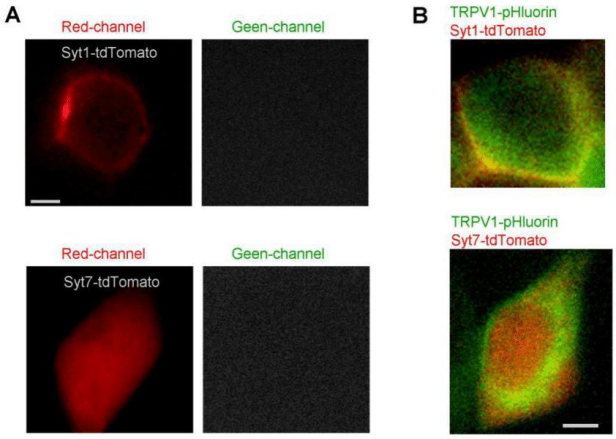

Fig. S7. Distinct subcellular distribution patterns for Syt1- and Syt7-tdTomato. The imaging protocol and same filter set were used as in Fig S5. (*A*) Absence of crosstalk from Syt1- and Syt7-tdTomato to TRPV1-pHluorin channel. HEK 293 cells only expressing Syt1/7-tdTomato were used. (*B*) Co-expression of TRPV1-pHluorin and Syt1- or Syt7-tdTomato in HEK 293 cells. Scale bars, 10 μm for *A* and 5 μm for *B*.

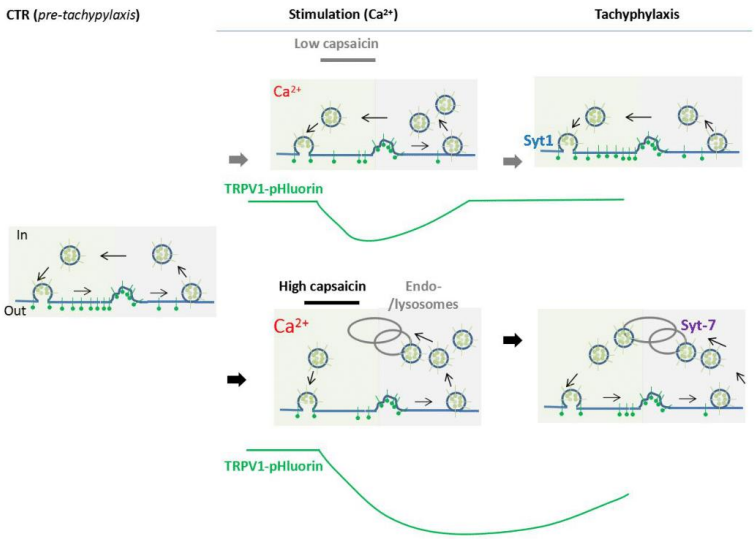

Fig. S8. Diagram illustrating Ca^{2+} signals, via synaptotagmin proteins, regulate the recycling of TRPV1 channels and whole-cell tachyphylaxis recovery.

List of publications, scientific communications, and rewards

Publications from the PhD study:

Herrera Moro Chao D, Kirchner MK, **Pham C**, Foppen E, Denis RGP, Castel J, Morel C, Montalban E, Hassouna R, Bui LC, Renault J, Mouffle C, Garcias-Caceres C, Tschöp MH, Li D, Martin C, Stern JE, Luquet S. Hypothalamic astrocytes control systemic glucose metabolism and energy balance. ***Cell Metabolism. 2022*** Oct 4;34(10):1532-1547.e6. doi: 10.1016/j.cmet.2022.09.002.

Pham C, Hérault K, Oheim M, Maldera S, Vialou V, Cauli B, Li D. Astrocytes respond to a neurotoxic amyloid fragment with state-dependent Ca^{2+} alteration and multiphasic transmitter release. ***Acta Neuropathol Commun. 2021*** Mar 16;9(1):44. doi: 10.1186/s40478-021-01146-1. PMID: 33726852; PMCID: PMC7968286.

Pham C, Moro DH, Mouffle C, Didienne S, Hepp R, Pfrieger FW, Mangin JM, Legendre P, Martin C, Luquet S, Cauli B, Li D. Mapping astrocyte activity domains by light sheet imaging and spatio-temporal correlation screening. ***Neuroimage. 2020*** Oct 15;220:117069. doi: 10.1016/j.neuroimage.2020.117069. Epub 2020 Jun 22. PMID: 32585347.

Tian Q, Hu J, Xie C, Mei K, **Pham C**, Mo X, Hepp R, Soares S, Nothias F, Wang Y, Liu Q, Cai F, Zhong B, Li D, Yao J. Recovery from tachyphylaxis of TRPV1 coincides with recycling to the surface membrane. ***PNAS***. ***2019*** Mar 12;116(11):5170-5175. doi: 10.1073/pnas.1819635116. Epub 2019 Feb 25. PMID: 30804201; PMCID: PMC6421460.

Manuscripts in preparation:

Pham C, et al., and Li D*. Aquaporin water channel regulates brain astrocyte volume homeostasis. In preparation 2022/**2023**.

Conference communications:

Oral communications:

Sept 2018 ***2nd thematic days of the neuroendocrinolgy society (SNE),*** **Paris, France**. Hypothalamic region-specific astrocyte regulation of glucose homeostasis and energy balance. Herrera Moro Chao D, **Pham C**, Foppen E, Le Thuc O, Denis R, Gangarossa G, Koekkoek L, Castel J, Morel C, Corsini S, Garcia-Caceres C, Martin C, Li D, Tschop M, Luquet S

Oct 2018 ***French Club of Glial Cells – Annual Meeting.*** Mapping astrocytes calcium domains by light-sheet imaging and spatio temporal correlative screening**. Pham C**, Li D

June 2019 ***BFA Young Researcher's meeting. Physiology: from basic to applied research,*** **Paris, France.** Hypothalamic region-specific astrocyte regulation of glucose homeostasis and energy balance**.** Herrera Moro Chao D, **Pham C**, Foppen E, Denis R, Castel J, Morel C, Chi-Bui Lihn, Koekkoek L, Bagci E, Berland C, Montalban E, Hassouna R, Gangarossa G, Le Thuc O, Garcia-Caceres C, Tschop M, Li D, Martin C, Luquet S

Poster communications:

July 2019 ***European Glia Meeting:*** Mapping astrocyte calcium domains by light sheet imaging and spatio-temporal correlation screening. **Pham C**, Herrera Moro D, Mouffle C, Didienne S, Hepp R, Pfrieger F W, Mangin JM, Legendre P, Martin C, Luquet S, Cauli B, Li D.

April 2019 ***EMBO Workshop: Organ Crosstalk in energy balance and metabolic disease.*** **Cadiz, Spain.** Hypothalamic region-specific astrocyte regulation of glucose homeostasis and energy balance. Herrera Moro Chao D, **Pham C**, Foppen E, Denis R, Castel J, Morel C, Koekkoek L, Bagci E, Berland C, Montalban E, Hassouna R, Gangarossa G, Le Thuc O, Garcia-Caceres C, Tschop M, Li D, Martin C, Luquet S

April 2018 ***2nd German-French Conference on Diabetes Research,*** **Berlin, Germany**. Hypothalamic region-specific astrocyte regulation of glucose homeostasis and energy balance. Herrera Moro Chao D, **Pham C**, Foppen E, Le Thuc O, Denis R, Gangarossa G, Koekkoek L, Castel J, Morel C, Corsini S, Garcia-Caceres C, Martin C, Li D, Tschop M, Luquet S

July 2018 ***International Congress of Neuroendocrinology,*** **Toronto, Canada.** Hypothalamic region-specific astrocyte regulation of glucose homeostasis and energy balance. Herrera Moro Chao D, **Pham C**, Foppen E, Le Thuc O, Denis R, Gangarossa G, Koekkoek L, Castel J, Morel C, Bagci E, Corsini S, Garcia-Caceres C, Martin C, Li D, Tschop M, Luquet S

Sept 2018 ***6th Helmholtz Diabetes Conference.*** **Munich, Germany.** Hypothalamic region-specific astrocyte regulation of glucose homeostasis and energy balance**.** Herrera Moro Chao D, **Pham C**, Foppen E, Le Thuc O, Denis R, Gangarossa G, Koekkoek L, Castel J, Morel C, Bagci E, Corsini S, Garcia-Caceres C, Martin C, Li D, Tschop M, Luquet S

Imaging Ca^{2+} signals in hypothalamic astrocytes in diet induced obesity. **Pham C**, Herrera Moro Chao D, Mouffle C, Garcia-Caceres C, Martin C, Tschop M, Luquet S, Li D

Sept 2018 ***2nd thematic days of the neuroendocrinolgy society (SNE).*** Imaging Ca^{2+} signals in hypothalamic astrocytes in diet induced obesity. **Pham C**, Herrera Moro Chao D, Mouffle C, Garcia-Caceres C, Martin C, Tschop M, Luquet S, Li D

Academic laureats from the PhD study:

France Alzheimer Foundation, Individual Fellowship, 2021-2022

Japan Society for the Promotion of Science (JSPS) – CNRS Summer program, 2022

Bibliography

Abramov AY, Canevari L, Duchen MR (2004) Calcium signals induced by amyloid beta peptide and their consequences in neurons and astrocytes in culture. Biochim Biophys Acta 1742:81–87.

Abudara V, Retamal MA, Del Rio R, Orellana JA (2018) Synaptic Functions of Hemichannels and Pannexons: A Double-Edged Sword. Front Mol Neurosci 11:435.

Agre P (2006) The aquaporin water channels. Proc Am Thorac Soc 3:5–13.

Amiry-Moghaddam M, Frydenlund DS, Ottersen OP (2004) Anchoring of aquaporin-4 in brain: molecular mechanisms and implications for the physiology and pathophysiology of water transport. Neuroscience 129:999–1010.

Appaix F, Girod S, Boisseau S, Römer J, Vial JC, Albrieux M, Maurin M, Depaulis A, Guillemain I, van der Sanden B (2012) Specific in vivo staining of astrocytes in the whole brain after intravenous injection of sulforhodamine dyes. PLoS One 7:1–13.

Aspelund A, Antila S, Proulx ST, Karlsen TV, Karaman S, Detmar M, Wiig H, Alitalo K (2015) A dural lymphatic vascular system that drains brain interstitial fluid and macromolecules. J Exp Med 212:991–999.

Badaut J, Ashwal S, Adami A, Tone B, Recker R, Spagnoli D, Ternon B, Obenaus A (2011) Brain water mobility decreases after astrocytic aquaporin-4 inhibition using RNA interference. J Cereb blood flow Metab Off J Int Soc Cereb Blood Flow Metab 31:819–831.

Badaut J, Fukuda AM, Jullienne A, Petry KG (2014) Aquaporin and brain diseases. Biochim Biophys Acta 1840:1554–1565.

Barres BA (2008) The Mystery and Magic of Glia: A Perspective on Their Roles in Health and Disease. Neuron 60:430–440 Available at: http://dx.doi.org/10.1016/j.neuron.2008.10.013.

Bazargani N, Attwell D (2016) Astrocyte calcium signaling: the third wave. Nat Neurosci

19:182–189 Available at: http://www.nature.com/doifinder/10.1038/nn.4201.

Benfenati V, Caprini M, Dovizio M, Mylonakou MN, Ferroni S, Ottersen OP, Amiry-Moghaddam M (2011) An aquaporin-4/transient receptor potential vanilloid 4 (AQP4/TRPV4) complex is essential for cell-volume control in astrocytes. Proc Natl Acad Sci U S A 108:2563–2568.

Bihan D Le, Iima M (2015) Diffusion Magnetic Resonance Imaging : What Water Tells Us about Biological Tissues. :1–13.

Binder DK, Papadopoulos MC, Haggie PM, Verkman AS (2004) In vivo measurement of brain extracellular space diffusion by cortical surface photobleaching. J Neurosci Off J Soc Neurosci 24:8049–8056.

Bindocci E, Savtchouk I, Liaudet N, Becker D, Carriero G, Volterra A (2017) Three-dimensional Ca $^{2+}$ imaging advances understanding of astrocyte biology. Science (80-) 356:eaai8185 Available at: http://www.sciencemag.org/lookup/doi/10.1126/science.aai8185.

Bloch O, Auguste KI, Manley GT, Verkman AS (2006) Accelerated progression of kaolin-induced hydrocephalus in aquaporin-4-deficient mice. J Cereb blood flow Metab Off J Int Soc Cereb Blood Flow Metab 26:1527–1537.

Brinker T, Stopa E, Morrison J, Klinge P (2014) A new look at cerebrospinal fluid circulation. Fluids Barriers CNS 11:10.

Brown PD, Davies SL, Speake T, Millar ID (2004) Molecular mechanisms of cerebrospinal fluid production. Neuroscience 129:955–968.

Bruno CA, O'Brien C, Bryant S, Mejaes JI, Estrin DJ, Pizzano C, Barker DJ (2021) pMAT: An open-source software suite for the analysis of fiber photometry data. Pharmacol Biochem Behav 201:173093.

Buckman LB, Thompson MM, Moreno HN, Ellacott KLJ (2013) Regional astrogliosis in the mouse hypothalamus in response to obesity. J Comp Neurol 521:1322–1333.

Burnett ME, Johnston HM, Green KN (2015) Structural characterization of the aquaporin inhibitor 2-nicotinamido-1,3,4-thiadiazole. Acta Crystallogr Sect C, Struct Chem 71:1074–1079.

Chen Z, Yuan Z, Yang S, Zhu Y, Xue M, Zhang J, Leng L (2022) Brain Energy Metabolism: Astrocytes in Neurodegenerative Diseases. CNS Neurosci Ther.

Chever O, Dossi E, Rouach N (2016) [Astrocyte control of neuronal synchrony: mind the GAP!]. Med Sci (Paris) 32:820–822.

Chever O, Lee C-Y, Rouach N (2014) Astroglial connexin43 hemichannels tune basal excitatory synaptic transmission. J Neurosci Off J Soc Neurosci 34:11228–11232.

Chiarini A, Dal Prà I, Armato U, Gardenal E, Gui L (2017) Amyloid β-Exposed Human Astrocytes Overproduce Phospho-Tau and Overrelease It within Exosomes, Effects Suppressed by Calcilytic NPS 2143—Further Implications for Alzheimer's Therapy. Front Neurosci 11:1–9 Available at: http://journal.frontiersin.org/article/10.3389/fnins.2017.00217/full.

Cousins O, Hodges A, Schubert J, Veronese M, Turkheimer F, Miyan J, Engelhardt B, Roncaroli F (2022) The blood-CSF-brain route of neurological disease: The indirect pathway into the brain. Neuropathol Appl Neurobiol 48:e12789.

Dallérac G, Zapata J, Rouach N (2018) Versatile control of synaptic circuits by astrocytes: where, when and how? Nat Rev Neurosci 19:729–743.

Daneman R, Prat A (2015) The blood-brain barrier. Cold Spring Harb Perspect Biol 7:a020412.

Debacker C, Djemai B, Ciobanu L, Tsurugizawa T, Le Bihan D (2020) Diffusion MRI reveals in vivo and non-invasively changes in astrocyte function induced by an aquaporin-4 inhibitor. PLoS One 15:e0229702.

Denizot A, Lyon I, Doctorale E (2019) Simulating calcium signaling in fine astrocytic processes To cite this version : HAL Id : tel-02406699 Simulation de la signalisation calcique dans les prolongements fins astrocytaires.

Drew PJ (2022) Neurovascular coupling: motive unknown. Trends Neurosci:1–11 Available at: https://doi.org/10.1016/j.tins.2022.08.004.

Escartin C et al. (2021) Reactive astrocyte nomenclature, definitions, and future directions. Nat Neurosci 24:312–325.

Fiacco TA, McCarthy KD (2018) Multiple Lines of Evidence Indicate That Gliotransmission Does Not Occur under Physiological Conditions. J Neurosci Off J Soc Neurosci 38:3–13.

Haj-yasein NN, Fluge G, Eilert-olsen M, Andreas G, Skare Ø (2011) reduces blood – brain water uptake and confers barrier function on perivascular astrocyte endfeet. 108:17815–17820.

Haj-Yasein NN, Vindedal GF, Eilert-Olsen M, Gundersen GA, Skare Ø, Laake P, Klungland A, Thorén AE, Burkhardt JM, Ottersen OP, Nagelhus EA (2011) Glial-conditional deletion of aquaporin-4 (Aqp4) reduces blood-brain water uptake and confers barrier function on perivascular astrocyte endfeet. Proc Natl Acad Sci U S A 108:17815–17820.

Hajdu SI (2003) A note from history: Discovery of the cerebrospinal fluid. Ann Clin Lab Sci 33:334–336.

Harada K, Kamiya T, Tsuboi T (2016) Gliotransmitter release from astrocytes: Functional, developmental, and pathological implications in the brain. Front Neurosci 9:1–9.

Harrison IF, Ismail O, Machhada A, Colgan N, Ohene Y, Nahavandi P, Ahmed Z, Fisher A, Meftah S, Murray TK, Ottersen OP, Nagelhus EA, O'Neill MJ, Wells JA, Lythgoe MF (2020) Impaired glymphatic function and clearance of tau in an Alzheimer's disease model. Brain 143:2576–2593.

Herrera Moro Chao D, Kirchner MK, Pham C, Foppen E, Denis RGP, Castel J, Morel C, Montalban E, Hassouna R, Bui LC, Renault J, Mouffle C, García-Cáceres C, Tschöp MH, Li D, Martin C, Stern JE, Luquet SH. Hypothalamic astrocytes control systemic glucose metabolism and energy balance. Cell Metab. 2022 Oct 4;34(10):1532-1547.e6. doi: 10.1016/j.cmet.2022.09.002. PMID: 36198294.

Heuser K, Enger R (2021) Astrocytic Ca(2+) Signaling in Epilepsy. Front Cell Neurosci 15:695380.

Huber VJ, Igarashi H, Ueki S, Kwee IL (2018) Aquaporin-4 facilitator TGN-073 promotes interstitial fluid circulation within the blood – brain barrier : [17 O] H 2 O JJVCPE MRI study. :697–703.

Huber VJ, Tsujita M, Nakada T (2009) Identification of Aquaporin 4 inhibitors using in vitro

and in silico methods. Bioorg Med Chem 17:411–417 Available at: http://dx.doi.org/10.1016/j.bmc.2007.12.040.

Igarashi H, Huber VJ, Tsujita M, Nakada T (2011) Pretreatment with a novel aquaporin 4 inhibitor, TGN-020, significantly reduces ischemic cerebral edema. Neurol Sci Off J Ital Neurol Soc Ital Soc Clin Neurophysiol 32:113–116.

Igarashi H, Tsujita M, Suzuki Y, Kwee IL, Nakada T (2013) Inhibition of aquaporin-4 significantly increases regional cerebral blood flow. :324–328.

Ikeshima-Kataoka H (2016) Neuroimmunological Implications of AQP4 in Astrocytes. Int J Mol Sci 17.

Iliff JJ, Wang M, Liao Y, Plogg BA, Peng W, Gundersen GA, Benveniste H, Vates GE, Deane R, Goldman SA, Nagelhus EA, Nedergaard M (2012) A paravascular pathway facilitates CSF flow through the brain parenchyma and the clearance of interstitial solutes, including amyloid β. Sci Transl Med 4:147ra111.

Jackson JG, Robinson MB (2018) Regulation of mitochondrial dynamics in astrocytes: Mechanisms, consequences, and unknowns. Glia 66:1213–1234.

Jarand ME, Anna BH, Wannan ET, Enger R, Jensen V, Pettersen KH, Nagelhus EA (2019) Astroglial endfeet exhibit distinct Ca 2 + signals during hypoosmotic conditions. :2399–2409.

Jeon H, Kim M, Park W, Lim JS, Lee E, Cha H, Ahn JS, Kim JH, Hong SH, Park JE, Lee E-J, Woo C-W, Lee S (2021) Upregulation of AQP4 Improves Blood-Brain Barrier Integrity and Perihematomal Edema Following Intracerebral Hemorrhage. Neurother J Am Soc Exp Neurother 18:2692–2706.

Jiang R, Diaz-Castro B, Looger LL, Khakh BS (2016) Dysfunctional Calcium and Glutamate Signaling in Striatal Astrocytes from Huntington's Disease Model Mice. J Neurosci 36:3453–3470 Available at: http://www.jneurosci.org/cgi/doi/10.1523/JNEUROSCI.3693-15.2016.

Jung JS, Bhat R V, Preston GM, Guggino WB, Baraban JM, Agre P (1994) Molecular characterization of an aquaporin cDNA from brain: candidate osmoreceptor and regulator of water balance. Proc Natl Acad Sci U S A 91:13052–13056.

Kessler J-P (2013) Control of cleft glutamate concentration and glutamate spill-out by perisynaptic glia: uptake and diffusion barriers. PLoS One 8:e70791.

Khakh BS, McCarthy KD (2015) Astrocyte calcium signaling: From observations to functions and the challenges therein. Cold Spring Harb Perspect Biol 7:1–17.

Kim JG et al. (2014) Leptin signaling in astrocytes regulates hypothalamic neuronal circuits and feeding. Nat Neurosci 17:908–910 Available at: http://www.nature.com/doifinder/10.1038/nn.3725.

Kitchen P, Salman MM, Halsey AM, Ahmed Z, Conner AC, Bill RM, Kitchen P, Salman MM, Halsey AM, Clarke-bland C, Macdonald JA (2020) Article Targeting Aquaporin-4 Subcellular Localization to Treat Central Nervous System Edema ll ll Article Targeting Aquaporin-4 Subcellular Localization to Treat Central Nervous System Edema. :784–799.

Lafrenaye AD, Simard JM (2019) Bursting at the Seams: Molecular Mechanisms Mediating Astrocyte Swelling. Int J Mol Sci 20.

Le Bihan D (2014) Diffusion MRI: What water tells us about the brain. EMBO Mol Med 6:569–573.

Lobello K, Ryan JM, Liu E, Rippon G, Black R (2012) Targeting Beta Amyloid : A Clinical Review of Immunotherapeutic Approaches in Alzheimer ' s Disease. 2012.

Louveau A, Plog BA, Antila S, Alitalo K, Nedergaard M, Kipnis J (2017) Understanding the functions and relationships of the glymphatic system and meningeal lymphatics. 127.

Louveau A, Smirnov I, Keyes TJ, Eccles JD, Rouhani SJ, Peske JD, Derecki NC, Castle D, Mandell JW, Lee KS, Harris TH, Kipnis J (2015) Structural and functional features of central nervous system lymphatic vessels. Nature 523:337–341.

Lundgaard I, Li B, Xie L, Kang H, Sanggaard S, Haswell JDR, Sun W, Goldman S, Blekot S, Nielsen M, Takano T, Deane R, Nedergaard M (2015) Direct neuronal glucose uptake heralds activity-dependent increases in cerebral metabolism. Nat Commun 6:6807.

Lundgaard I, Lu ML, Yang E, Peng W, Mestre H, Hitomi E, Deane R, Nedergaard M (2017) Glymphatic clearance controls state-dependent changes in brain lactate concentration. J Cereb blood flow Metab Off J Int Soc Cereb Blood Flow Metab 37:2112–2124.

MacAulay N, Zeuthen T (2010) Water transport between CNS compartments: contributions of aquaporins and cotransporters. Neuroscience 168:941–956.

Macey RI (1984) Transport of water and urea in red blood cells. Am J Physiol 246:C195-203.

Magistretti PJ, Allaman I (2018) Lactate in the brain: from metabolic end-product to signalling molecule. Nat Rev Neurosci 19:235–249.

Mesquita S Da, Fu Z, Kipnis J (2018) Perspective The Meningeal Lymphatic System : A New Player in Neurophysiology. Neuron 100:375–388 Available at: https://doi.org/10.1016/j.neuron.2018.09.022.

Mestre H et al. (2020a) Cerebrospinal fluid influx drives acute ischemic tissue swelling. Science 367.

Mestre H, Hablitz LM, Xavier ALR, Feng W, Zou W, Pu T, Monai H, Murlidharan G, Rivera RMC, Simon MJ, Pike MM, Pla V, Du T, Kress BT, Wang X, Plog BA (2018) Aquaporin-4-dependent glymphatic solute transport in the rodent brain. :1–31.

Mestre H, Mori Y, Nedergaard M (2020b) The Brain ' s Glymphatic System : Current Controversies. Trends Neurosci xx:1–9 Available at: https://doi.org/10.1016/j.tins.2020.04.003.

Mestre H, Tithof J, Du T, Song W, Peng W, Sweeney AM, Olveda G, Thomas JH, Nedergaard M, Kelley DH (n.d.) pulsations and is reduced in hypertension. Nat Commun Available at: http://dx.doi.org/10.1038/s41467-018-07318-3.

Mitchell JL, Mollan SP, Vijay V, Sinclair AJ (2019) Novel advances in monitoring and therapeutic approaches in idiopathic intracranial hypertension. Curr Opin Neurol 32:422–431.

Mola MG, Sparaneo A, Gargano CD, Spray DC, Svelto M, Frigeri A, Scemes E, Nicchia GP (2016) The speed of swelling kinetics modulates cell volume regulation and calcium signaling in astrocytes: A different point of view on the role of aquaporins. Glia 64:139–154.

Morton JS, Daly CJ, Jackson VM, McGrath JC (2007) Alpha(1A)-adrenoceptors mediate contractions to phenylephrine in rabbit penile arteries. Br J Pharmacol 150:112–120 Available at:

http://www.pubmedcentral.nih.gov/articlerender.fcgi?artid=2013850&tool=pmcentrez&rendertype=abstract.

Mucke L, Masliah E, Yu G, Mallory M, Rockenstein E (2000) High-Level Neuronal Expression of Aβ1–42 in Wild-Type..Synaptotoxicity without Plaque Formation.pdf. J Neurosci 20:4050–4058.

Murphy TR, Davila D, Cuvelier N, Young LR, Lauderdale K, Binder DK, Fiacco TA (2017) Hippocampal and Cortical Pyramidal Neurons Swell in Parallel with Astrocytes during Acute Hypoosmolar Stress. 11:1–19.

Nagai J, Yu X, Papouin T, Cheong E, Freeman MR, Monk KR, Hastings MH, Haydon PG, Rowitch D, Shaham S, Khakh BS (2021) Behaviorally consequential astrocytic regulation of neural circuits. Neuron 109:576–596.

Nagelhus EA, Ottersen OP (2013) Physiological roles of aquaporin-4 in brain. Physiol Rev 93:1543–1562.

Nakamura Y, Suzuki Y, Tsujita M, Huber VJ, Yamada K, Nakada T (2011) Development of a Novel Ligand, [C]TGN-020, for Aquaporin 4 Positron Emission Tomography Imaging. ACS Chem Neurosci 2:568–571.

Nedergaard M (2013) Neuroscience. Garbage truck of the brain. Science 340:1529–1530.

Nedergaard M, Goldman SA (2020) Glymphatic failure as a final common pathway to dementia. Science 370:50–56.

Nedergaard M, Rodr??guez JJ, Verkhratsky A (2010) Glial calcium and diseases of the nervous system. Cell Calcium 47:140–149.

Nielsen S, Nagelhus EA, Amiry-Moghaddam M, Bourque C, Agre P, Ottersen OP (1997) Specialized membrane domains for water transport in glial cells: high-resolution immunogold cytochemistry of aquaporin-4 in rat brain. J Neurosci Off J Soc Neurosci 17:171–180.

O'Shea TM, Burda JE, Sofroniew M V (2017) Cell biology of spinal cord injury and repair. J Clin Invest 127:3259–3270.

Pannasch U, Rouach N (2013) Emerging role for astroglial networks in information

processing: from synapse to behavior. Trends Neurosci 36:405–417.

Pannasch U, Vargová L, Reingruber J, Ezan P, Holcman D, Giaume C, Syková E, Rouach N (2011) Astroglial networks scale synaptic activity and plasticity. Proc Natl Acad Sci U S A 108:8467–8472.

Papadopoulos MC, Verkman AS (2013) Aquaporin water channels in the nervous system. 14 Available at: http://dx.doi.org/10.1038/nrn3468.

Pham C, Hérault K, Oheim M, Maldera S, Vialou V, Cauli B (2021) Astrocytes respond to a neurotoxic Aβ fragment with state‐dependent - Ca 2 + alteration and multiphasic transmitter release. Acta Neuropathol Commun:1–19 Available at: https://doi.org/10.1186/s40478-021-01146-1.

Plog BA, Nedergaard M (2018) The Glymphatic System in Central Nervous System Health and Disease: Past, Present, and Future. Annu Rev Pathol Mech Dis 13:annurev-pathol-051217-111018 Available at: http://www.annualreviews.org/doi/10.1146/annurev-pathol-051217-111018.

Popkin BM, D'Anci KE, Rosenberg IH (2010) Water, hydration, and health. Nutr Rev 68:439–458.

Rangroo Thrane V, Thrane AS, Plog BA, Thiyagarajan M, Iliff JJ, Deane R, Nagelhus EA, Nedergaard M (2013) Paravascular microcirculation facilitates rapid lipid transport and astrocyte signaling in the brain. Sci Rep 3:2582.

Rasmussen MK, Mestre H, Nedergaard M (2022) Fluid transport in the brain. Physiol Rev 102:1025–1151.

Roberts KF, Elbert DL, Kasten TP, Patterson BW, Sigurdson WC, Connors RE, Ovod V, Munsell LY, Mawuenyega KG, Miller-thomas MM, Moran CJ, Iii DTC, Derdeyn CP, Bateman RJ (2014) Amyloid- b Efflux from the Central Nervous System into the Plasma.

Rosu G, Catalin B, Balseanu TA, Laurentiu M, Claudiu M, Kumar-singh S, Daniel P (2020) Inhibition of Aquaporin 4 Decreases Amyloid A β 40 Drainage Around Cerebral Vessels.

Sakka L, Coll G, Chazal J (2011) Anatomy and physiology of cerebrospinal fluid. Eur Ann Otorhinolaryngol Head Neck Dis 128:309–316.

Savtchouk I, Volterra A (2018) Gliotransmission: Beyond Black-and-White. J Neurosci Off J Soc Neurosci 38:14–25.

Scheltens P, Strooper B De, Kivipelto M, Holstege H, Chételat G, Teunissen CE, Cummings J, Flier WM Van Der (2021) Seminar Alzheimer ' s disease. 397.

Shigetomi E, Patel S, Khakh BS (2016) Probing the Complexities of Astrocyte Calcium Signaling. Trends Cell Biol 26:300–312.

SIDEL VW, SOLOMON AK (1957) Entrance of water into human red cells under an osmotic pressure gradient. J Gen Physiol 41:243–257.

Simard M, Nedergaard M (2004) The neurobiology of glia in the context of water and ion homeostasis. Neuroscience 129:877–896.

Slezak M, Göritz C, Niemiec A, Frisén J, Chambon P, Metzger D, Pfrieger FW (2007) Transgenic Mice for Conditional Gene Manipulation in Astroglial Cells. Glia 51:523–532.

Smith AJ, Verkman AS (2019) CrossTalk opposing view: Going against the flow: interstitial solute transport in brain is diffusive and aquaporin-4 independent. J Physiol 597:4421–4424.

Smith AJ, Yao X, Dix JA, Jin B-J, Verkman AS (2017a) Test of the "glymphatic" hypothesis demonstrates diffusive and aquaporin-4-independent solute transport in rodent brain parenchyma. Elife 6.

Smith AJ, Yao X, Dix JA, Jin B, Verkman AS (2017b) Test of the ' glymphatic ' hypothesis demonstrates diffusive and aquaporin-4- independent solute transport in rodent brain parenchyma. :1–16.

Sofroniew M V., Vinters H V. (2010) Astrocytes: Biology and pathology. Acta Neuropathol 119:7–35.

Spector R, Robert Snodgrass S, Johanson CE (2015) A balanced view of the cerebrospinal fluid composition and functions: Focus on adult humans. Exp Neurol 273:57–68.

Tait MJ, Saadoun S, Bell BA, Papadopoulos MC (2008) Water movements in the brain: role of aquaporins. Trends Neurosci 31:37–43.

Takano T, Kang J, Jaiswal JK, Simon SM, Lin JH-C, Yu Y, Li Y, Yang J, Dienel G, Zielke HR, Nedergaard M (2005) Receptor-mediated glutamate release from volume sensitive channels in astrocytes. Proc Natl Acad Sci U S A 102:16466–16471.

Tian Q, Hu J, Xie C, Mei K, Pham C, Mo X, Hepp R, Soares S, Nothias F, Wang Y, Liu Q, Cai F, Zhong B, Li D, Yao J. Recovery from tachyphylaxis of TRPV1 coincides with recycling to the surface membrane. Proc Natl Acad Sci U S A. 2019 Mar 12;116(11):5170-5175. doi: 10.1073/pnas.1819635116. Epub 2019 Feb 25. PMID: 30804201; PMCID: PMC6421460.

Toft-bertelsen TL, Larsen BR (2020) Clearance of activity-evoked K + transients and associated glia cell swelling occur independently of AQP4 : A study with an isoform-selective AQP4 inhibitor. :1–14.

Trillo-Contreras JL, Ramírez-Lorca R, Villadiego J, Echevarría M. Cellular Distribution of Brain Aquaporins and Their Contribution to Cerebrospinal Fluid Homeostasis and Hydrocephalus. Biomolecules. 2022 Mar 31;12(4):530. doi: 10.3390/biom12040530. PMID: 35454119; PMCID: PMC9025855.

Verkhratsky A (2019) Astroglial Calcium Signaling in Aging and Alzheimer's Disease. Cold Spring Harb Perspect Biol 11.

Verkhratsky A, Butt A (2013) Glial Physiology and Pathophysiology. Glial Physiol Pathophysiol.

Verkhratsky A, Nedergaard M (2018) Physiology of Astroglia. Physiol Rev 98:239–389 Available at: http://www.physiology.org/doi/10.1152/physrev.00042.2016.

Verkman AS, Smith AJ, Phuan P-W, Tradtrantip L, Anderson MO (2017) The aquaporin-4 water channel as a potential drug target in neurological disorders. Expert Opin Ther Targets 21:1161–1170.

Vincent M, Gaudin M, Lucas-Torres C, Wong A, Escartin C, Valette J. Characterizing extracellular diffusion properties using diffusion-weighted MRS of sucrose injected in mouse brain. NMR Biomed. 2021 Apr;34(4):e4478. doi: 10.1002/nbm.4478. Epub 2021

Jan 27. PMID: 33506506; PMCID: PMC7988537.

von Bartheld CS, Bahney J, Herculano-Houzel S (2016) The search for true numbers of neurons and glial cells in the human brain: A review of 150 years of cell counting. J Comp Neurol 524:3865–3895.

Wilhelmsson U, Bushong EA, Price DL, Smarr BL, Phung V, Terada M, Ellisman MH, Pekny M (2006) Redefining the concept of reactive astrocytes as cells that remain within their unique domains upon reaction to injury. Proc Natl Acad Sci U S A 103:17513–17518.

Xie L, Kang H, Xu Q, Chen MJ, Liao Y, Thiyagarajan M, O'Donnell J, Christensen DJ, Nicholson C, Iliff JJ, Takano T, Deane R, Nedergaard M (2013) Sleep drives metabolite clearance from the adult brain. Science 342:373–377.

Xue C, Lin TY, Chang D (2017) Thioflavin T as an amyloid dye : fibril quantification , optimal concentration and effect on aggregation.

Zamanian JL, Xu L, Foo LC, Nouri N, Zhou L, Giffard RG, Barres BA (2012) Genomic analysis of reactive astrogliosis. J Neurosci 32:6391–6410.

Zhang H, Verkman AS (2010) Microfiberoptic measurement of extracellular space volume in brain and tumor slices based on fluorescent dye partitioning. Biophys J 99:1284–1291.